

Important Notice

This copy may be used only for the purposes of research and private study, and any use of the copy for a purpose other than research or private study may require the authorization of the copyright owner of the work in question. Responsibility regarding questions of copyright that may arise in the use of this copy is assumed by the recipient.

UNIVERSITY OF CALGARY

Interpretation of well-log, VSP, seismic streamer, and OBS data at the
White Rose oilfield, offshore Newfoundland

By

Jessica María Jaramillo Sarasty

A THESIS

SUBMITTED TO THE FACULTY OF GRADUATE STUDIES
IN PARTIAL FULFILMENT OF THE REQUIREMENTS FOR THE
DEGREE OF MASTER OF SCIENCE

DEPARTMENT OF GEOLOGY AND GEOPHYSICS

CALGARY, ALBERTA

DECEMBER, 2005

© Jessica María Jaramillo Sarasty 2005

UNIVERSITY OF CALGARY
FACULTY OF GRADUATE STUDIES

The undersigned certify that they have read, and recommend to the Faculty of Graduate Studies for acceptance, a thesis entitled "Interpretation of well-log, VSP, seismic streamer, and OBS data at the White Rose oilfield, offshore Newfoundland" submitted by Jessica María Jaramillo Sarasty in partial fulfillment of the requirements for the degree of Master of Science.

*Supervisor, Dr. Robert R. Stewart,
Department of Geology and Geophysics*

*Dr. Laurence R. Lines,
Department of Geology and Geophysics*

*Dr. Donald C. Lawton,
Department of Geology and Geophysics*

*External Examiner Dr. Brij B. Maini,
Department of Chemical and Petroleum Engineering*

Date

ABSTRACT

The petrophysical analysis in this thesis is based on dipole sonic (V_p and V_s), density, gamma-ray, and porosity logs (density porosity and neutron porosity). In general, velocity increases as total porosity decreases. V_p/V_s decreases slightly when total porosity decreases. V_s shows a high correlation with porosity. In addition, we find that Castagna's "mudrock" relationship predicts V_s from V_p reasonably well in the clastic section. Better fits can be achieved by dividing the lithologies into formations. In general, Faust's relationship makes a fair prediction of V_s , although for a better fit with the well data, different constants are required from the original relationship. The results were encouraging (Jaramillo and Stewart, 2003).

A multi-offset-VSP dataset was acquired in Husky Energy's H-20 well in the White Rose field. This survey generated several outputs including corridor stacks and CDP mapping of PP and CCP mapping of PS data. The interpretation of these results shows that the best correlations are between the PS synthetic seismograms and the PS offset VSP data. PS images from these synthetic seismograms at the top of the Avalon Formation, show higher amplitude over the adjacent signals. Synthetic and field data indicated that converted-wave (PS) data might be useful in mapping the Avalon reservoir at White Rose (Jaramillo et al., 2002).

During the summer of 2002, an ocean-bottom seismometer test line was conducted over Husky Energy's L-08 well in the White Rose oilfield. For this survey, 21 seismometer/hydrophone ocean-bottom (OBS) instruments were used as receivers to record the data. An airgun was used as the seismic source. The correlation between the PP and PS synthetics from well L-08 and the OBS data (vertical and radial components) gave confidence to the interpretation of the resultant PP and PS seismic sections. After matching both radial and vertical component seismic sections, the events on both sections became correlated. The V_p/V_s values obtained from the seismic are related to the values from well L-08. There are some V_p/V_s anomalies going laterally on the seismic sections. In general, the values decrease with depth (Jaramillo and Stewart, 2004).

ACKNOWLEDGEMENTS

I would like to thank my Supervisor, Dr. Robert R. Stewart, for his support and guidance throughout this project. Husky Energy Inc. generously provided the seismic data used in this thesis. David Emery and Larry Mewhort from Husky Energy provided many insights during this work. Dr. Keith Louden from Dalhousie University conducted the seismic OBS experiment from which I analyzed. Dr. Peter Cary from Sensor Geophysical processed the OBS data. Dr. Brian Russell provided insights to the Hampson-Russell software and gave his time generously to explain the underlying theory.

Special thanks to Kevin Hall for help in everyday computer problems. Richard Xu and Carlos Montaña assisted me in understanding the software packages. Special thanks go to Louise Forgues, for her emotional and administrative support. Mark Kirkland performed the valuable job of correcting grammar in this thesis.

I am thankful to the CREWES Project and Sponsors for providing me with financial support during my studies.

Kelly Fries, Laurie Vaughan, Faye Nicholson, and Cathy Hubbell of the Department of Geology and Geophysics generously helped me in the administrative and university procedures. Sandy Blazina was always there to listen to me and lend support.

I can never be grateful enough to my parents, Zamarino and Guiomar for the encouraging support that helping me through difficult times and for believing in me.

I would like to thank Dr. Laurence R. Lines, Dr. Donald C. Lawton, Dr. Brij B. Maini and Dr Ronald C. Hinds, for taking time to read my thesis, and for their useful suggestions.

DEDICATION

To my beloved parents Zamarino y Guiomar

TABLE OF CONTENTS

Approval page	ii
Abstract	iii
Acknowledgements	iv
Dedication	v
Table of Contents	vi
List of Tables	x
List of Figures	xiv
List of Equations	xxx
CHAPTER 1. INTRODUCTION	1
1.1 Objectives	2
1.2 Field location	3
1.3 History of the White Rose field	5
1.4 Imaging challenges at White Rose field	7
1.5 Geology	8
1.5.1 Regional Setting of Grand Banks Basin	8
1.5.2 Jeanne d’Arc Basin	11
1.5.3 Jeanne d’Arc Basin’s Stratigraphy	12
1.5.4 White Rose field’s Lithologies	12
1.5.5 Avalon Formation	13
1.5.6 Avalon Reservoir Pools	14
CHAPTER 2. WELL-LOG ANALYSIS	19
2.1 H-20 well-log analysis	21
2.2 Study of Empirical relationships	23
2.2.1 Vp versus depth	23
2.2.2 Vs versus depth	24
2.2.3 Vp/Vs versus depth	24
2.2.4 Actual Vp versus Vp estimated from the Faust’s relationship	25
2.2.5 Actual Vs versus Vs estimated from the Faust’s relationship	30
2.2.6 Actual Vs versus Vs estimated from the Castagna’s relationship	37

2.2.7 Actual Vp, Actual Vs, Actual Vp/Vs versus GR	45
2.2.8 Actual ρ versus ρ estimated from the Gardner's relationship using Vp..	49
2.2.9 Actual ρ versus ρ estimated from the Gardner's relationship using Vs..	54
2.2.10 Vp, Vs from Gardner relationship using ρ	57
2.2.11 Vp, Vs, Vp/Vs versus ϕ_D	60
2.2.12 Vp, Vs, Vp/Vs versus ϕ_N	64
2.2.13 ϕ_N versus ϕ_D	66
2.2.14 Multivariate analysis	68
CHAPTER 3. VSP INTERPRETATION	73
3.1 VSP survey	73
3.2 Interpretation	76
3.2.1 Tie of PP synthetic seismograms with PP offset VSP field data	76
3.2.2 Tie of PS synthetic seismograms with PS offset VSP-CCP data	77
3.2.3 PP synthetic seismogram with the walk-above VSP (PP) field data	78
3.2.4 Walk-above VSP field data (PP) with the seismic section (PP)	82
3.2.5 PP synthetic seismograms with the seismic section (PP)	82
CHAPTER 4. CONVERTED-WAVE OBS INTERPRETATION	87
4.1 SCREECH survey	87
4.1.1 Survey Equipment	88
4.1.2 Acquisition and Geometry	88
4.1.3 Interpretation	89
4.2 Acquisition and Geometry of the 4-C Ocean-Bottom Seismometer (OBS)	
survey	89
4.2.1 4C ocean-bottom seismometer (OBS) survey	93
4.2.2 Processing of the OBS data	95
4.2.3 Interpretation	96
4.2.4 Correlation	112
4.2.5 Vp/Vs analysis	116

5. CONCLUSIONS	123
5.1 Well-Log Analysis	123
5.2 VSP Interpretation	123
5.3 OBS interpretation	124
6. FUTURE WORK	125
7. REFERENCES	127
APPENDIX A	Introduction	133
APPENDIX B	Well log analysis	139
APPENDIX C	VSP interpretation	158
APPENDIX D	Converted-wave OBS interpretation	162

LIST OF TABLES

Table 1.1:	Summary of the White Rose oilfield. (Modified from Husky Energy Inc, 2005.).	5
Table 1.2:	White Rose pools information. (Modified after Husky Energy, 2002.).	15
Table 2.1:	Wells analyzed and crossplots assembled. Key: ✓ shows which relationships were investigated in the well.	21
Table 2.2:	General velocity trends for Vp and Vs logs.	22
Table 2.3:	Behaviour of Vp/Vs ratio versus depth for H-20 and L-08 wells ..	25
Table 2.4:	Formation age used on Faust's relationship.	26
Table 2.5:	Constants used to predict Vp from Faust's relationship for all wells. The RMS from using Faust's constant and the RMS error from using the derived constant gives the accuracy of the derived constant. The derived constant is per well.	29
Table 2.6:	Constants used to predict Vs from Faust's relationship for wells H-20 and L-08. The RMS error from using Faust's constant and the RMS error from using the derived constant show the accuracy of the derived constant. The derived constant is per well.	31
Table 2.7:	RMS error values for each well. These RMS values accord to the constant used to derive Vp and Vs. The constants are approaching Faust's relationship using a 125.3 constant, the derived constants are per well. Key: ♦ This log is not present in this well; * Poor RMS results; ✱ Good RMS results	36
Table 2.8:	Constants (used to predict Vp and Vs from Faust) and velocity values for wells H-20 and L-08.	37
Table 2.9:	Vp/Vs values obtained from Faust constants and velocities, using data from wells H-20 and L-08.	37
Table 2.10:	RMS analysis for the different Vs curves obtained from well H-20. The RMS value is based on the percentage error between the original curve and the derived curve. Key: ✱ indicates good RMS results.	42

Table 2.11:	RMS analysis for the different Vs curves obtained in well L-08. The RMS value is based on the percentage error between the original curve and the derived curve. Key: ✕ indicates good RMS Results.	42
Table 2.12:	General behaviour of GR versus Vp for each Formation on each well.	46
Table 2.13:	General trend of GR versus Vp/Vs for each Formation.	48
Table 2.14:	Constants used to predict ρ from Vp using Gardner's relationship for all wells. The RMS from using Gardner's constant and the RMS error from using the derived constant gives the accuracy of the derived constant. The derived constant is per well. Key: ✕ indicates good RMS results.	50
Table 2.15:	Constants used to predict ρ from Vs using Gardner's relationship for wells H-20 and L-08. The RMS from using Gardner's constant and the RMS error from using the derived constant give the accuracy of the derived constant. The derived constant is per well. Key: ✕ Indicates good RMS results.	56
Table 2.16:	Total depth of the wells with the depth of the section that was analyzed.	58
Table 2.17:	Constants used in approaching Vp and Vs from Gardner's relationship using density. The RMS value shows the root mean square error between the new relationship and the original values. Key: ♦ Data was not acquired on this well; ✕ Good RMS results. .	60
Table 2.18:	Constants used in the multivariate analysis to derive Vp and Vs. .	70
Table 4.1:	General behaviour of Vp/Vs, showing the general trend found in each Formation for well L-08 and for the OBS seismic data. Key: ♦ indicates the Formation that is directly beneath the Base of Tertiary unconformity.	122
Table B.1:	Constants used to predict Vp from Faust's relationship for all wells. There were just two constants per well (for the Tertiary and for the Cretaceous sections).	141

Table B.2:	Faust's constants used to predict V_p for each well's Formations. Well N-22 had the closest results to the Faust constant (125.3) in the Wyandot, Petrel, Nautilus, Eastern Shoals, White Rose and Jeanne d'Arc Formations. Key: ♦ This Formation is not present on this well; • Formation at the bottom of the well.	143
Table B.3:	Constants used to predict V_s for wells H-20 and L-08 Formations. There were just two constants per well.	145
Table B.4:	Constants used to predict V_s for Formations in wells H-20 and L-08. Constants were derived for each Formation. Key: ♦ This Formation is not present in this well. These constants could be lithology indicators	147
Table B.5:	Gardner constant used to predict ρ from V_p . Key: ♦ This Formation is not present on the well; blue shading: Good RMS results per Formation; yellow shading: Bad RMS results per Formation.	150
Table B.6:	Constants used to predict ρ from Gardner's relationship for all wells using V_p and V_s . Two constants were derived per well (Tertiary and Cretaceous constants). Also the RMS value is shown for comparison between wells. Key: ♦ This Formation is not present on the well; blue shading: Good RMS results per Formation (Tertiary or Cretaceous); yellow shading: Bad RMS results per Formation (Tertiary or Cretaceous).	152
Table B.7:	Gardner's constant used to predict ρ from V_s . Key: ♦ data was not acquired on this Formation.	153

LIST OF FIGURES

Figure 1.1:	Location of White Rose oilfield, Newfoundland (Modified from Encarta.msn.com, 2004).	4
Figure 1.2:	Regional setting of Jeanne d’Arc Basin (Modified after Husky Oil, Operations 2001).	4
Figure 1.3:	The White Rose Avalon pools and wells (Modified after Husky Oil Operations, 2001).	6
Figure 1.4:	White Rose Avalon oilfield and wells (Modified after Husky Oil Operations, 2001).	7
Figure 1.5:	Stratigraphy of the White Rose field. (From Deutsch/Meehan - Husky Oil, 2000, in Husky Oil Operations, 2001).	9
Figure 1.6:	Location of Grand Banks Basins and White Rose oilfield, (Modified from Husky Oil Operations, 2001).	11
Figure 1.7:	Sea Rose Floating Production, Storage and Offloading (FPSO) vessel (Modified from Husky Energy Inc, 2004).	17
Figure 2.1:	Locations of the White Rose wells that are analyzed in this chapter (Modified after Husky Oil Operations, 2001).	19
Figure 2.2:	Logs from well H-20: Vp, left, and Vs, right, log curves	22
Figure 2.3:	Logs from well H-20: Panel (a) — gamma ray log curve; Panel (b) —RHOB (Actual ρ) log curve.	23
Figure 2.4:	Vp versus depth for well N-22. A velocity increase with depth is the general trend observed on the different wells studied.	24
Figure 2.5:	Panel (a) — Vp/Vs versus depth for well H-20; Panel (b) — Vp/Vs versus Depth for well L-08.	26
Figure 2.6:	Panel (a) — actual Vp and Faust Vp for well A-90: RMS error of the Vp Faust curve is ± 1344.12 m/s; Panel (b) — percentage error between the Actual Vp curve and the Faust Vp curve for well A-90; Panel (c) — actual Vp and Faust Vp for well H-20: RMS error of the Vp Faust curve is ± 398.01 m/s; Panel (d) — percentage error between the Actual Vp curve and the Faust Vp curve for well H-20. The panels show the results of applying the original Faust	

	relationship to the well log data. The Vp Faust curves on both panels were derived using a Faust constant of 125.3.	28
Figure 2.7:	Panel (a) — actual Vp and Faust Vp (curves A and B) versus depth for well A-90; Panel (b) — percentage error between the actual Vp curve and the Faust Vp curve A (derived from 125.3 as the constant): RMS error is ± 1344.12 m/s; Panel (c) — percentage error between the actual Vp curve and the Faust Vp curve B (derived using 132.38 as the constant). RMS error is ± 846.06 m/s.	29
Figure 2.8:	Data from well H-20: Panel (a) — actual Vp and Faust Vp (curves A and B) versus depth. Panel (b) — percentage error between the actual Vp curve and the Faust Vp curve A (derived using 125.3 as the constant): RMS error is ± 398.01 m/s; Panel (c) — percentage error between the actual Vp curve and the Faust Vp curve B (derived using 128.90 as the constant): RMS error is ± 387.45 m/s.	30
Figure 2.9:	Data from well H-20: Panel (a) — actual Vs and Faust Vs (curves A and B) versus depth; Panel (b) — percentage error between the actual Vs curve and the Faust Vs curve A (derived using 70 as the constant): RMS error is ± 444.48 m/s; Panel (c) — percentage error between the actual Vs curve and the Faust Vs curve B (derived using 65.53 as the constant): RMS value is ± 429.80 m/s...	32
Figure 2.10:	Data from well L-08: Panel (a) — actual Vs and Faust Vs (curves A and B) versus depth; Panel (b) — percentage error between the actual Vs curve and the Faust Vs curve A (derived using a constant of 70): RMS error is ± 444.48 m/s; Panel (c) — percentage error between the actual Vs curve and the Faust Vs curve B (derived using a constant of 59.67): RMS value is ± 433.81 m/s.	33
Figure 2.11:	Results from well H-20. Panel (a) — actual Vp and Faust Vp (curves A and B) versus depth. The Vp curve A is derived from Faust, using the 125.3 constant. The Vp curve B is derived from Faust, using 128.90 as the constant; Panel (b) — actual Vs and	

Faust Vs (curves A and B) versus depth. The Vs curve A is derived from Faust, using 70 as the constant. The Vs curve B is derived from Faust, using 65.53 as the constant; Panel (c) — the Vp curve A is the result of comparing the actual Vp and the Vp derived from Faust, using the 125.3 constant; Vs curve A is the result of comparing the actual Vs and the Vs derived from Faust, using the using the 70 constant; Panel (d) — the Vp curve A is the result of comparing the actual Vp and the Vp derived from Faust, using the 128.90 constant; Vs curve A is the result of comparing the actual Vs and the Vs derived from Faust, using the 65.53 constant.

34

Figure 2.12: Results from well L-08: Panel (a) — Vp curve A is the result from comparing the actual Vp and the Vp derived from Faust, using the 125.3 constant. The Vs curve A is the result of comparing the actual Vs and the Vs derived from Faust, using the 70 constant. Panel (b) — Vp curve B is the result from comparing the actual Vp and the Vp derived from Faust, in this case using $C_s=59.67$. The Vs curve B is the result of comparing the actual Vs and the Vs derived from Faust.

36

Figure 2.13: Panel (a) — actual Vs versus actual Vp for well H-20. The data falls into the original Castagna’s mudrock line. Panel (b) — actual Vs versus actual Vp for well L-08. The data falls the into original Castagna’s mudrock line.

39

Figure 2.14: Data from well H-20: Panel (a) — actual Vs and Castagna Vs (mudrock empirical relation) versus depth. Panel (b) — percentage error between the actual Vs curve and the Vs Castagna curve.

40

Figure 2.15: Data from well L-08: Panel (a) — actual Vs and Castagna Vs (mudrock empirical relation) versus depth. Panel (b) — percentage error between the Actual Vs curve and the Vs Castagna curve.

41

Figure 2.16: Data from well H-20. The details of the Figure are explained before in page 40.

43

Figure 2.17:	Data from well L-08. The details of the Figure are explained before in page 41.	44
Figure 2.18:	Panel (a) — GR versus actual Vp for the Nautilus Formation in each well from the area. Panel (b) — GR versus actual Vp for the Avalon Formation in each well from the area. In general, as the Formations (Avalon and Nautilus) grade upward from siltstone into sandstone, the velocity increases.	45
Figure 2.19:	Panel (a) — GR versus actual Vp for well H-20. Panel (b) — GR versus actual Vp for well L-08. As the Formations upgrade from siltstones to sandstones, the velocities increase. Both wells exhibit similar, general trends for each Formation. Both of these wells are located on the South Avalon Pool.	47
Figure 2.20:	Panel (a) — Vp/Vs versus GR for well H-20. Panel (b) — Vp/Vs versus GR for well L-08. Note that the Tertiary Formation keeps a siltstone range of values as the well goes deeper. The differentiation of Formations is noticeable. In both wells, the relationships behave quite similarly: as Vp/Vs decreases, GR decreases.	48
Figure 2.21:	Data from the Avalon Formation from well E-09. Panel (a) — actual Vp versus actual ρ and Gardner ρ data from well E-09. Panel (b) — actual Vp versus actual ρ and Gardner ρ . The Avalon fits better to the relationship than the other Formations.	50
Figure 2.22:	Panel (a) — actual ρ and Gardner's ρ versus actual Vp for well H-20 (2772–3271 m). Panel (b) — actual ρ and Gardner's ρ versus actual Vp for well L-08.	51
Figure 2.23:	Panel (a) — Actual ρ versus depth. Panel (b) — actual ρ and Gardner ρ (derived using Gardner constant). The RMS error is $\pm 58.79 \text{ kg/m}^3$. Panel (c) — percentage error between these two ρ versus depth. The data is from the bottom of well H-20 showing the Avalon and Eastern Shoals Formations.	53
Figure 2.24:	Density versus velocity, crossplot for well H-20. Actual ρ and velocity values versus the ρ predicted from Gardner's rule. The field values are for the bottom section of the well (from 2772	

	m to 3271 m), where actual ρ was acquired.	53
Figure 2.25:	Data from well L-08. Panel (a) — actual ρ , and Gardner ρ (derived using V_p and a 310 constant) versus depth. Panel (b) — percentage error between these two ρ	54
Figure 2.26:	Panel (a) — actual ρ versus Gardner ρ (derived using V_s and $a=350$ and 352.73 derived constant) for well H-20. Panel (b) — actual ρ versus Gardner ρ (derived using V_s and $a=350$ and 386.02 derived constant) for well L-08.	55
Figure 2.27:	Data from well L-08. Panel (a) — actual ρ and Gardner ρ (derived using V_s and $a=350$ and 386.02 derived constant) versus depth. Panel (b) — percentage error between actual ρ and Gardner ρ (derived using 350 as the constant) versus depth. The RMS error is $\pm 261.76 \text{ kg/m}^3$. Panel (c) — percentage error between actual ρ and Gardner ρ (derived using 386.02 as the constant) versus depth. The RMS error is $\pm 141.59 \text{ kg/m}^3$	56
Figure 2.28:	Data from well H-20 showing the Avalon Formation. Panel (a) — actual V_p versus depth. Panel (b) — actual V_p and Gardner V_p (derived using a constant of 310) versus depth. Panel (c) — percentage error between these two V_p curves versus depth. ...	58
Figure 2.29:	Data from well J-49. Panel (a) — actual V_p and Gardner V_p (derived from ρ using constants of 310 and 314.80) versus depth. Panel (b) — percentage error between actual ρ and Gardner ρ (derived using 310 as the constant) versus depth. The RMS error is $\pm 1223.84 \text{ m/s}$. Panel (c) — percentage error between actual V_p and Gardner V_p (derived using 314.80 as the constant) versus depth. The RMS error is $\pm 1056.81 \text{ m/s}$	59
Figure 2.30:	Data from well L-08. Panel (a) — actual V_s and Gardner V_s (derived using constants of 350 and 386.02) versus depth. Panel (b) percentage error between actual V_s and Gardner V_s (derived using 350 as the constant) versus depth. The RMS error is $\pm 760.15 \text{ m/s}$. Panel (c) percentage error between actual V_s and Gardner V_s (derived using 386.02 as the constant) versus depth.	

	The RMS error is ± 395.97 m/s.	60
Figure 2.31:	Well L-08 Vp versus ϕ_D , assuming a sandstone matrix.	62
Figure 2.32:	Well L-08 Vp versus ϕ_D , assuming a limestone matrix.	63
Figure 2.33:	Well L-08 Vp/Vs versus ϕ_D , assuming a sandstone matrix.	64
Figure 2.34:	Well L-08 Vp versus ϕ_N , assuming a sandstone matrix.	65
Figure 2.35:	Well L-08 Vp/Vs versus ϕ_N	66
Figure 2.36:	Well L-08 density porosity (ϕ_D) versus neutron porosity (ϕ_N), overlain on a chart from Western Atlas (1985) The details of the Figure are explained in page 68.	67
Figure 2.37:	Well log curves from well L-08, from a section of Nautilus shale. Panel (a) — actual Vp versus depth. Panel (b) — actual Vs versus depth. Panel (c) — actual GR versus depth. Panel (d) — actual ϕ_N versus depth. Panel (e) — actual ϕ_D versus depth.	69
Figure 2.38:	Data from a section of Nautilus shale from well L-08. Panel (a) — actual Vp and derived Vp (using a multivariate analysis) versus depth. Panel (b) — percentage error between these two Vp curves versus depth. RMS error ± 213.52 m/s.	70
Figure 2.39:	The data is from a section of Nautilus shale from well L-08. Panel (a) — actual Vs and derived Vs (using a multivariate analysis) versus depth. Panel (b) — percentage error between these two Vs curves versus depth. The RMS error is ± 178.77 m/s.	71
Figure 2.40:	Data from a section of Nautilus shale from well L-08. Panel (a) — actual Vs, derived Vs (using a multivariate analysis), and Castagna Vs (using his mudrock relationship) versus depth. Panel (b) — percentage error between the two derived Vs curves and the actual Vs versus depth. The RMS error is ± 178.77 m/s for the derived Vs (using multivariate analysis) and ± 206.78 m/s for Castagna Vs (using the mudrock relationship).	72
Figure 2.41:	Data from a section of Nautilus shale from well L-08. Vs, derived Vs (using Emerge Software analysis), derived Vs (using a multivariate analysis), and Castagna Vs (using his mudrock relationship) versus depth.	72

Figure 3.1:	Location of well H-20 (Modified after Husky Oil , Operations 2001).	73
Figure 3.2:	Details of the H-20 offset VSP survey showing the north-south seismic line (1.8 to 3 seconds TWT) intersecting well H-20. (Modified after Emery, 2001).	75
Figure 3.3:	Details of the H-20 walk-above VSP showing the north-south seismic line (1.8 to 3 seconds TWT) intersecting well H-20. (Modified after Emery, 2001).	75
Figure 3.4:	Result from matching the PP synthetic seismogram and the offset VSP section. Key: Eocene EOCN, South Mara Smara, Base Tertiary Btrt, Nautilus Naut, Avalon Aval, Eastern Shoals Eshl. ...	79
Figure 3.5:	Result from matching the PS synthetic seismogram and the Offset VSP section. Key: Eocene EOCN, South Mara Smara, Base Tertiary Btrt, Nautilus Naut, Avalon Aval, Eastern Shoals Eshl.	80
Figure 3.6:	In this composite figure, Panels (a) to (c) show the results from matching the PP synthetic seismogram with the walk-above VSP section, using the Gardner ρ value (derived from Gardner, Figure 2.23). Panel (d) is a zoom of the dashed area in the Panels (a) and (b); the stacked trace section is from the PP synthetic seismogram. Key: Eocene EOCN, South Mara Smara, Base Tertiary Btrt, Nautilus Naut, Avalon Aval, Eastern Shoals Eshl. ..	81
Figure 3.7:	Comparison between PP synthetic seismogram, offset VSP PP section (Panel a), Offset VSP PS section (Panel b) and PS synthetic seismogram for well H-20. Key: Eocene EOCN, South Mara Smara, Base Tertiary Btrt, Nautilus Naut, Avalon Aval, Eastern Shoals Eshl.	82
Figure 3.8:	Comparison between walk-above VSP PP, PP stacked trace section (results from using Rhob and Rhga logs), and Offset VSP PP surveys for well H-20. Key: Eocene EOCN, South Mara Smara, Base Tertiary Btrt, Nautilus Naut, Avalon Aval, Eastern Shoals Eshl.	83
Figure 3.9:	Comparison between the walk-above VSP (P-wave) and PP seismic section (1.8 to 3 sec TWT).	84

Figure 3.10:	Result from matching the PP synthetic seismogram and the PP seismic section (black is a peak and red is a trough). Key: Eocene EOCN, South Mara Smara, Base Tertiary Btrt, Nautilus Naut, Avalon Aval, Eastern Shoals Eshl.	85
Figure 3.11:	Composite figure showing a comparison of PS synthetics: high frequency (45Hz) versus low frequency (30Hz) (Panels (a) and (c)). Panel (d): the events of interest in a close-up comparison of the stacked trace sections from each of the synthetic seismograms of Panels (a) and (c). Key: Eocene EOCN, South Mara Smara, Base Tertiary Btrt, Nautilus Naut, Avalon Aval, Eastern Shoals Eshl.	86
Figure 4.1:	Location of SCREECH survey, showing three transects of the survey across the Newfoundland continental margin. (Modified from odp.tamu.edu).	88
Figure 4.2:	Vertical component seismic section at station 3090 (See Appendix D for location of stations). We note that the reflector at 4000 ms could be related to the Base of Tertiary event (Modified from Stewart and et al., 2001).	90
Figure 4.3:	Radial component seismic section at station 3090 (See Appendix D for location of stations). We note that the reflector at 6000 ms could be related to the Base of Tertiary event and may correspond to the event at 4000 ms in Figure 4.2 (Modified from Stewart and et al., 2001).	91
Figure 4.4:	Showing the Hudson 2002-011 Line 1 and Hudson 2002-011 Line 2 (point D on the map), from the FLAME 2002 scientific expedition. (Modified from Jackson et al., 2002).	92
Figure 4.5:	Location of source lines (red) and approximate position of 21 OBS receivers (blue). (Hall and Stewart, 2002).	92
Figure 4.6:	Receiver locations of the 21 OBS units, laterally exaggerated. (Modified from Hall and Stewart, 2002).	93
Figure 4.7:	Receiver and source location (Modified from Hall and Stewart, 2002).	94

Figure 4.8:	Dalhousie ocean-bottom seismometer (OBS), (Modified from www.phys.ocean.dal.ca/seismic , 2002).	94
Figure 4.9:	Air gun array, (Modified from Jackson et al., 2002).	95
Figure 4.10:	Location of well L-08 at the White Rose field. (Modified after Husky Oil Operations Ltd, 2001).	98
Figure 4.11:	Results from correlating the PP and PS synthetics, from wells H-20 and L-08.	99
Figure 4.12:	Result from matching the PP and PS synthetics from well L-08. ...	100
Figure 4.13:	CDP grid displayed using Kingdom suite software showing the location of well L-08. There were 35 east-west inlines and 216 north-south crosslines.	101
Figure 4.14:	Well logs from well L-08 (P wave, S wave, Vp/Vs, ρ , GR tops of the sequence).	102
Figure 4.15:	Well L-08 PP synthetic and vertical component sections, showing Inline 19 in a W-E direction. The horizons have been defined (TrtE, South Mara, Base of Tertiary, Nautilus, Avalon, and Eastern Shoals) after tying the well L-08 with the seismic. The data was flattened at the Base of Tertiary unconformity to facilitate the interpretation.	104
Figure 4.16:	Time slices of each of the events interpreted on the vertical component seismic section. The horizons defined are: Tertiary E, South Mara, Base of Tertiary, Nautilus, Avalon, and Eastern Shoals events. Well L-08 is shown on each time slice.	105
Figure 4.17:	Streamer P-seismic section from White Rose PGS-97 3D survey. Well L-08 is shown, along with the South Mara, Base of Tertiary, Nautilus, Avalon, and Eastern Shoals events. Uplifting of the Avalon and Eastern Shoals Formations can be seen, due to faults in the stratigraphy creating a complex structural area. (Modified from Emery, 2001).	106
Figure 4.18:	PP time thickness maps between the main horizons (Tertiary E, South Mara, Base of Tertiary, Nautilus, Avalon and Eastern Shoals) of the survey. Well L-08 is shown on each time thickness map.	107

Figure 4.19:	Well L-08 PP synthetic and hydrophone component section showing Inline 19. The horizons defined (TrtE, South Mara, Base of Tertiary, Nautilus, Avalon and Eastern Shoals) after tying the well L-08 with the seismic. The data was flattened at the Base of Tertiary unconformity to facilitate the interpretation.	108
Figure 4.20:	Time slices of each of the events interpreted on the hydrophone component seismic section. The horizons defined are Tertiary E, South Mara, Base of Tertiary, Nautilus, Avalon, and Eastern Shoals events. Well L-08 is shown on each time slice.	109
Figure 4.21:	Hydrophone time thickness maps on P time between the main horizons (Tertiary E, South Mara, Base of Tertiary, Nautilus, Avalon and Eastern Shoals) of the survey. Well L-08 is shown on each time thickness map.	111
Figure 4.22:	Well L-08 PS synthetic and radial component section showing Inline 19. The horizons were defined (TrtE, South Mara, Base of Tertiary, Nautilus, Avalon, and Eastern Shoals) after tying well L-08 with the seismic. The data was flattened at the Base of Tertiary unconformity to facilitate the Interpretation.	112
Figure 4.23:	Time slices of each of the events interpreted on the radial component (PS-wave) seismic section. The horizons defined are Tertiary E, South Mara, Base of Tertiary, Nautilus, Avalon and Eastern Shoals events. Well L-08 is shown on each time slice. ...	113
Figure 4.24:	PS time thickness maps between the main horizons (Tertiary E, South Mara, Base of Tertiary, Nautilus, Avalon, and Eastern Shoals) of the survey. Well L-08 is shown on each time thickness map.	114
Figure 4.25:	Radial component (Panel 1) and vertical component (Panel 2) seismic sections mapped on PP time, showing the different horizons defined (TrtE, South Mara, Base of Tertiary, Nautilus, Avalon, and Eastern Shoals) after tying the GR well log. Well L-08 is annotated on the seismic, showing Inline 19 for both sections.	115
Figure 4.26:	Correlation between the OBS P data and the Streamer P data.	

	Showing the correlation between the different horizons (TrtE, South Mara, Base Tertiary, Nautilus, Avalon and Eastern Shoals) with well L-08.	116
Figure 4.27:	Radial component (Panel (a)) and pressure component (Panel (b)) seismic sections mapped on PP time, showing Inline 19 for both sections and with the different horizons defined (TrtE, South Mara, Base of Tertiary, Nautilus, Avalon, and Eastern Shoals) after tying the GR well log. Well L-08 is annotated on the seismic..	117
Figure 4.28:	Vp/Vs analysis after matching the PP section with the PS seismic section, showing the horizons (Tertiary E, South Mara, Base of Tertiary, Nautilus, Avalon, and Eastern Shoals) and well L-08 with gamma ray log.	118
Figure 4.29:	Apparent average interval Vp/Vs maps for each horizon (Tertiary E, South Mara, Base of Tertiary, Nautilus, Avalon, and Eastern Shoals). Well L-08 is shown on each Vp/Vs map. The inline and xline are gridding onto 25 x 25 bin spacing. Refer to Table 4.1 for Vp/Vs comparison.	119
Figure 4.30:	Vp/Vs versus depth Avalon Formation, from well L-08. ...	122
Figure B.1:	Data from well A-90. Panel (a) — actual Vp and Faust Vp using 125.3 (for the entire well) and Vp using derived constants (a constant for the Tertiary Formations and a constant for the Cretaceous Formations) versus depth. Panel (b) — percentage error between the actual Vp curve and the Faust Vp (derived from the 125.3 constant). The RMS error is ± 1344.12 m/s. Panel (c) — percentage error between the actual Vp curve and the Faust Vp curve derived using two constants. The Tertiary Formations with constant $C_p=107.39$ and an RMS error of ± 238.79 m/s. The Cretaceous Formations with a constant $C_p=169.20$ and RMS error ± 631.71 m/s.	140
Figure B.2:	Data from well H-20. Panel (a) — actual Vp and Faust Vp using 125.3 (for the entire well) and Vp using derived constants (a constant for the Tertiary Formations and a constant for the	

Cretaceous Formations) versus depth. Panel (b) — percentage error between the actual Vp curve and the Faust Vp (derived from the 125.3 constant). The RMS error is ± 398.01 m/s. Panel (c) — percentage error between the actual Vp curve and the Faust Vp curve derived using two constants. The Tertiary Formations with constant $C_p=116.89$ and an RMS error of ± 127.53 m/s. The Cretaceous Formations with a constant $C_p=139.59$ and an RMS error of ± 397.60 m/s. 141

Figure B.3: Results from well H-20. Panel (a) — actual Vp, Faust Vp using 125.3 (for the entire well) and Vp using derived constants per Formation ($C_p=116.89$ Tertiary; $C_p=118.04$ South Mara; $C_p=144.34$ Petrel/Base of Tertiary; $C_p = 135.34$ Nautilus; $C_p = 140.91$ Avalon). Panel (b) — percentage error between the actual Vp curve and the Faust Vp (derived from the 125.3 constant). The RMS error is ± 398.01 m/s. Panel (c) — percentage error between the actual Vp curve and the Faust Vp curve derived using several constants. The RMS error is ± 120.23 m/s (Tertiary), ± 238.80 m/s (South Mara), ± 298.11 m/s (Petrel/Base of Tertiary), ± 398.63 m/s (Nautilus), and ± 401.59 m/s (Avalon). 142

Figure B.4: Data from well H-20. Panel (a) — actual Vs and Faust Vs using 70 (for the entire well) and Vs using derived constants (a separate constant for the Tertiary and the Cretaceous Formations) versus depth. Panel (b) — percentage error between the actual Vs curve and the Faust Vs (derived from using 70 as the constant). The RMS error is ± 444.48 m/s. Panel (c) — percentage error between the actual Vs curve and the Faust Vs curve derived using two constants: the Tertiary Formations with constant $C_p=49.60$ and an RMS error of ± 98.26 m/s and the Cretaceous Formations with a constant $C_p=79.79$ and an RMS error of ± 299.74 m/s. 145

Figure B.5: Data from well L-08. Panel (a) — actual Vs and Faust Vs using 70 (for the entire well) and Vs using derived constants (separate

constants for the Tertiary and Cretaceous Formations) versus depth. Panel (b) — percentage error between the actual Vs curve and the Faust Vs (derived from using 70 as the constant). The RMS error is ± 508.53 m/s. Panel (c) —percentage error between the actual Vs curve and the Faust Vs curve derived using two constants. The Tertiary Formations with a constant $C_p=45.11$ and an RMS error of ± 153.93 m/s. The Cretaceous Formations with a constant $C_p=75.96$ and an RMS error of ± 47.83 m/s. 146

Figure B.6: Results from well H-20. Panel (a) — actual Vs, Faust Vs using 70 (for the entire well) and Vs using derived constants per Formation ($C_s=49.03$ Tertiary; $C_s =58.13$ South Mara; $C_s =74.09$ Petrel/Base of Tertiary; $C_s =73.27$ Nautilus; $C_s =85.17$ Avalon). Panel (b) — percentage error between the actual Vs curve and the Faust Vs (derived from the 70 constant). The RMS error is ± 444.48 m/s. Panel (c) — percentage error between the actual Vs curve and the Faust Vs curve derived using several constants. RMS errors are: ± 76.87 m/s (Tertiary), ± 199.92 m/s (South Mara), ± 173.76 m/s (Petrel/Base of Tertiary), ± 228.17 m/s (Nautilus), and ± 268.18 m/s (Avalon). 147

Figure B.7: Results from well L-08. Panel (a) — actual Vs and Faust Vs using 70 (for the entire well) and Vs using derived constants per Formation ($C_s=44.40$ Tertiary; $C_s =58.01$ South Mara; $C_s =72.32$ Petrel/Base of Tertiary; $C_s =72.04$ Nautilus; $C_s =82.21$ Avalon). Panel (b) — percentage error between the actual Vs curve and the Faust Vs (derived from the 70 constant). The RMS is error ± 508.53 m/s. Panel (c) — percentage error between the actual Vs curve and the Faust Vs curve derived using several constants. RMS errors are: ± 133.03 m/s (Tertiary), ± 222.02 m/s (South Mara), ± 150.52 m/s (Petrel/Base of Tertiary), ± 152.41 m/s (Nautilus), and ± 163.79 m/s (Avalon). 148

Figure B.8: Results from well E-09. Panel (a) — actual ρ , Gardner ρ (derived from V_p) using derived constants per Formation ($a=348.66$ (Tertiary), $a =329.48$ (South Mara), $a =328.69$ (Wyandot), a

=328.19 (Nautilus), $a = 301.49$ (Ben Nevis), $a = 301.91$ (Avalon), $a = 327.36$ (Eastern Shoals), $a = 317.50$ (Hibernia), $a = 334.82$ (Fortune Bay), and $a = 318.74$ (Jeanne d'Arc)). Panel (b) — green curve shows the percentage error between the Gardner ρ curve and the Gardner ρ (derived from a least square constant of 320.25); dark blue curve shows percentage error between the Gardner ρ curve and the Gardner ρ curve derived using several constants. The RMS errors are: $\pm 73.56 \text{ kg/m}^3$ (Tertiary), $\pm 44.93 \text{ kg/m}^3$ (South Mara), $\pm 33.18 \text{ kg/m}^3$ (Wyandot), $\pm 45.86 \text{ kg/m}^3$ (Nautilus), $\pm 87.24 \text{ kg/m}^3$ (Ben Nevis), $\pm 90.83 \text{ kg/m}^3$ (Avalon), $\pm 68.14 \text{ kg/m}^3$ (Eastern Shoals), $\pm 110.11 \text{ kg/m}^3$ (Hibernia), $\pm 51.14 \text{ kg/m}^3$ (Fortune Bay), and $\pm 114.70 \text{ kg/m}^3$ (Jeanne d'Arc)....

151

Figure B.9: Results from Well N-22. Panel (a) — actual ρ and Gardner ρ (from V_p) using derived constants (a separate constant for the Tertiary and Cretaceous Formations) versus depth. Panel (b) — percentage error between the actual V_s curve and the Gardner ρ curve derived using two constants. The Tertiary Formations with a constant of $a = 326.71$, and RMS error of $\pm 87.11 \text{ kg/m}^3$. The Cretaceous Formations with a constant of $a = 320.95$ and RMS error of $\pm 223.91 \text{ kg/m}^3$.

153

Figure B.10: Results from well L-08. Panel (a) — actual ρ and Gardner ρ (derived from V_s) using derived constants per Formation ($a=401.96$ (Tertiary), $a = 388.87$ (South Mara), $a = 385.99$ (Petrel/Base of Tertiary), $a = 382.59$ (Nautilus), $a = 340.63$ (Avalon), and $a = 362.01$ (Eastern Shoals)). Panel (b) — percentage error between the Gardner ρ curve and the Gardner ρ (derived from several constants). RMS errors are: $\pm 42.28 \text{ kg/m}^3$ (Tertiary), $\pm 68.98 \text{ kg/m}^3$ (South Mara), $\pm 39.58 \text{ kg/m}^3$ (Petrel/Base of Tertiary), $\pm 53.52 \text{ kg/m}^3$ (Nautilus), $\pm 39.49 \text{ kg/m}^3$ (Avalon), and $\pm 28.74 \text{ kg/m}^3$ (Eastern Shoals).

154

Figure B.11: Results from well L-08. Panel (a) — actual ρ and Gardner ρ (from V_s) using two derived constants (once constant for the Tertiary

Formations and another for the Cretaceous Formations) versus depth. Panel (b) — percentage error between the actual ρ curve and the Gardner ρ curve derived using two constants. The Tertiary Formations with a constant $a=401.34$ has an RMS error of $\pm 46.28 \text{ kg/m}^3$. The Cretaceous Formations with a constant $a=367.11$ and an RMS error of $\pm 149.68 \text{ kg/m}^3$ 155

Figure C.1: Result from matching the PP synthetic seismogram and the offset VSP section, using the Gardner ρ value (curve RHGA in Figure 2.23). Key: Eocene EOCN, South Mara Smara, Base Tertiary Btrt, Nautilus Naut, Avalon Aval, Eastern Shoals Eshl. 159

Figure C.2: Result from matching the PS synthetic seismogram and the Offset VSP section, using the Gardner ρ value (curve RHGA in Figure 2.23). Key: Eocene EOCN, South Mara Smara, Base Tertiary Btrt, Nautilus Naut, Avalon Aval, Eastern Shoals Eshl. 160

Figure C.3: Results from matching the PP synthetic seismogram and the PP seismic section, using the Gardner ρ value (curve RHGA in Figure 2.23). (Black is a peak and red is a trough.) Key: Eocene EOCN, South Mara Smara, Base Tertiary Btrt, Nautilus Naut, Avalon Aval, Eastern Shoals Eshl. 161

Figure D.1: Location of seismic lines and receivers 3090, 3100, 3110 and 3250 SCREECH survey (Modified from Keith and Louden, 2000.). 162

Figure D.2: Common receiver gathers for the hydrophone (pressure sensor) at locations 3090, 3100, 3110 and 3250. (Modified from Stewart et al., 2001). 163

Figure D.3: Common receiver gathers for the vertical component (V1) at locations 3090, 3100, 3110 and 3250. (Modified from Stewart et al., 2001). 163

Figure D.4: Common receiver gathers for the horizontal component (H1) at locations 3090, 3100, 3110 and 3250. (Modified from Stewart et al., 2001). 163

Figure D.5: Common receiver gathers for the horizontal component (H2) at

locations 3090, 3100, 3110 and 3250. (Modified from Stewart
et al., 2001). 164

LIST OF EQUATIONS

Equation 2.1	$V_p = C_p (TZ)^{1/6}$ <p> V_p Compressional velocity (m/s) C_p Constant 125.3 T Formation age Z Depth of burial (m) </p> 25
Equation 2.2	$V_s = C_s (TZ)^{1/6}$ <p> V_s Shear velocity (m/s) C_s Constant 70 T Formation age Z Depth of burial (m) </p> 30
Equation 2.3	$\frac{C_p}{C_s} = \frac{\bar{V}_p}{\bar{V}_s}$ <p> \bar{V}_p Compressional velocity (m/s) \bar{V}_s Shear velocity (m/s) C_p Constant used to derive V_p C_s Constant used to derive V_s </p> 37
Equation 2.4	$V_s = \frac{(V_p - 1360)}{1.16}$ <p> V_s Shear velocity (m/s) V_p Compressional velocity (m/s) </p> 37
Equation 2.5	$V_s = \frac{V_p}{1.9}$ <p> V_s Shear velocity (m/s) V_p Compressional velocity (m/s) </p> 38
Equation 2.6	$V_s = -0.05509V_p^2 + 1.0168V_p - 1.0305$ <p> V_s Shear velocity (m/s) V_p Compressional velocity (m/s) </p> 38
Equation 2.7	$\rho = a\alpha^m$ <p> ρ Density (kg/m³) a Constant of 310 α Compressional velocity (m/s) m Constant of 0.25 </p> 49

Equation 2.8	$\rho = aV_s^m$	54
	ρ Density (kg/m ³) a Constant of 350 or derived constant V_s Shear velocity (m/s) m Constant of 0.25		
Equation 2.9	$V_p = 10^{\frac{\log \rho - \log a}{m}}$	57
	V_p Compressional velocity (m/s) ρ Density (kg/m ³) a Constant of 310 or derived constant m Constant of 0.25		
Equation 2.10	$V_s = 10^{\frac{\log \rho - \log a}{m}}$	58
	V_s Compressional velocity (m/s) ρ Density (kg/m ³) a Constant of 350 or derived constant m Constant of 0.25		
Equation 2.11	$\rho_b = \phi \cdot \rho_f + (1 - \phi) \rho_m$	61
	ρ_b Bulk density, or density log reading (kg/m ³) ϕ Porosity ρ_f Density of the fluid (kg/m ³) ρ_m Density of the matrix, zero porosity (kg/m ³)		
Equation 2.12	$\phi_D = \frac{\rho_m - \rho_b}{\rho_m - \rho_f}$	61
	ϕ_D Density-porosity ρ_m Density of the matrix, zero porosity (kg/m ³) ρ_f Density of the fluid (kg/m ³) ρ_b Bulk density, or density log reading (kg/m ³)		
Equation 2.13	$V_p = a + bV_s + cGR + d\phi_N + e\phi_D$	69
	V_p Compressional velocity V_s Shear velocity GR Gamma Ray ϕ_N Neutron-porosity ϕ_D Density-porosity a, b, c, d, e Constants derived from the multivariate analysis for V_p curve		

Equation 2.14 $V_s = a + bV_p + cGR + d\phi_N + e\phi_D$ 69

V_p Compressional velocity
 V_s Shear velocity
 GR Gamma Ray
 ϕ_N Neutron-porosity
 ϕ_D Density-porosity
 a, b, c, d, e Constants derived from the multivariate analysis for V_s curve

Equation B.1 $V_{si} = a_0 + a_1V_{pi} + a_2GR_i + a_3\phi_{Ni} + a_4\phi_{Di}$ 156

V_{si} Shear velocity (m/s)
 V_{pi} Compressional velocity (m/s)
 GR_i Gamma Ray (API)
 ϕ_{Ni} Neutron-porosity (pu)
 ϕ_{Di} Density-porosity (pu)
 a_0, a_1, a_2, a_3, a_4 Constants

Equation B.2 $E^2 = \frac{1}{N} \sum_{i=1}^N (V_{si} - a_0 - a_1V_{pi} - a_2GR_i - a_3\phi_{Ni} - a_4\phi_{Di})^2$ 156

E Error
 N Number of samples
 V_{si} Shear velocity (m/s)
 V_{pi} Compressional velocity (m/s)
 GR_i Gamma Ray (API)
 ϕ_{Ni} Neutron-porosity (pu)
 ϕ_{Di} Density-porosity (pu)
 a_0, a_1, a_2, a_3, a_4 Constants

Equation B.3
$$\begin{bmatrix} V_{s1} \\ V_{s2} \\ V_{s3} \\ \vdots \\ V_{sN} \end{bmatrix} = \begin{bmatrix} 1 & V_{p1} & GR_1 & \phi_{N1} & \phi_{D1} \\ 1 & V_{p2} & GR_2 & \phi_{N2} & \phi_{D2} \\ 1 & V_{p3} & GR_3 & \phi_{N3} & \phi_{D3} \\ \vdots & \vdots & \vdots & \vdots & \vdots \\ 1 & V_{pN} & GR_N & \phi_{NN} & \phi_{DN} \end{bmatrix} \begin{bmatrix} a_0 \\ a_1 \\ a_2 \\ a_3 \\ a_4 \end{bmatrix}$$
 157

$V_{s(1,2,3,...N)}$ Shear velocity (m/s) i^{th} samples
 $V_{p(1,2,3,...N)}$ Compressional velocity (m/s) i^{th} samples
 $GR_{(1,2,3,...N)}$ Gamma Ray (API) i^{th} samples
 $\phi_{N(1,2,3,...N)}$ Neutron-porosity (pu) i^{th} samples
 $\phi_{D(1,2,3,...N)}$ Density-porosity (pu) i^{th} samples
 a_0, a_1, a_2, a_3, a_4 Constants

Equation B.4 $V_s = PA$ 157

V_s Nx1 matrix
 P Nx5 matrix
 A 5x1 matrix

Equation B.5

$$A = (P^T P)^{-1} P^T V_s$$

..... 157

- A* Matrix with unknown constants
- P* Matrix with known values
- P^T* Transpose of matrix with known values (*V_p*, *GR*, *φ_b*, and *φ_N*)
- V_s* Matrix with *V_s* values

CHAPTER 1. INTRODUCTION

Conventional seismic streamer acquisition and processing for imaging hydrocarbon reservoirs has matured, but not always with unqualified success. The use of multi-component seismic data has been successfully applied by the petroleum industry in offshore surveys, trying to decrease the technical risk of exploring for structural and stratigraphic targets (Hanson et al., 1999). In the North Sea, the use of ocean-bottom cable (OBC) surveys has produced useful images. Off the east coast of Canada, the geology and seismic imaging problems have some similarities to those of the North Sea reservoirs. The White Rose field exploration experienced several imaging problems which will be examined later in the thesis. A solution to some of the problems could lie with the generation of converted waves. Ocean-bottom seismometers (OBS) are used to record converted waves in an attempt to obtain a better image from the subsurface and to avoid some of the imaging problems of the area of study (MacLeod et al., 1999).

S-wave logging is a relatively new logging method, thus the majority of vintage wells do not have S-wave velocity surveys. With the advent of converted-wave exploration and AVO, the industry has turned to shear-wave velocity (V_s) values for exploration purposes (Stewart et al, 2003). How can we obtain V_s from the old surveys? One of the first widely used methods was Castagna's (1985) relationship, to predict V_s from compressional-wave velocity (V_p). One objective of this thesis is to evaluate V_s based on Castagna's relationship and V_p from Gardner et al.,'s (1974), Faust's (1951) and Pickett's (1963a) relationships. These relationships are shown below:

$$V_s = \frac{(V_p - 1360)}{1.16} \quad \text{(Castagna's relationship)}$$

where: V_s Shear velocity (m/s)
 V_p Compressional velocity (m/s)

$$\rho = a\alpha^m \quad (\text{Gardner's relationship})$$

where: ρ Density (kg/m^3)
 a Constant of 310
 α Compressional velocity (m/s)
 m Constant of 0.25

$$V_p = C_p (TZ)^{1/6} \quad (\text{Faust's relationship})$$

where: V_p Compressional velocity (m/s)
 C_p Constant 125.3
 T Formation age
 Z Depth of burial (m)

$$V_s = \frac{V_p}{1.9}, \quad (\text{Pickett's relationship})$$

where: V_s Shear velocity (m/s)
 V_p Compressional velocity (m/s)

These empirical relationships could be used for further converted-wave survey design, processing, and interpretation of the White Rose field. Particularly in the subsea environment, where the compressional response can be poor at some intervals, the interest in shear waves is growing (Caldwell, 1999). In fluids, shear waves do not propagate and as no commercial seafloor shear-source exists at this point, the only way to commercially acquire a usable shear-wave response is to capture PS conversion from horizontal receivers set on the ocean-floor bottom (Garotta, 2000). For this case, an analysis of the 3D-4C data from the OBS survey that took place in the White Rose field in the summer of 2002 is also an objective of this work.

1.1 Objectives

Correlation of all the available logs from White Rose oilfield. To establish the petrophysics trend of the White Rose field. I analyze a six well log data sets (A-90, E-09, H-20, J-49, L-08, and N-22) from the White Rose oilfield offshore and use

dipole sonic (V_p and V_s), density (ρ), porosity (ϕ) and Gamma Ray (GR) logs, in an attempt to understand the petrophysical characteristics of the field. In addition, the work in this thesis evaluates and suggests how V_p , V_s , ρ , GR, lithology relate to each other using the field data.

Application of empirical relationships: Faust's (1951), Gardner et al.'s (1974) and Castagna's (1985), to find V_p , V_s and ρ from actual data from the White Rose field.

Interpretation of PP and PS VSP data from well H-20 of the White Rose field.

Interpretation of White Rose streamer (PP seismic section) and OBS (using vertical, radial and hydrophone seismic sections) data.

This thesis is organized as follows:

- Summary of the geology and history of the White Rose region
- Summary of the various rock properties found at White Rose
- Interpretation of surface seismic P-P and P-P VSP data
- Generation of P-P synthetics
- Interpretation of P-S VSP data
- Generation of P-S synthetics
- Analysis of well log data
- Interpretation of OBS seismic data
- Analysis of the V_p/V_s results from the OBS data

1.2 Field location

The White Rose field is located on the northeastern edge of the Jeanne d'Arc Basin, approximately 350 km southeast of St. John's, Newfoundland (Figure 1.1).

The White Rose field is 50 km from both the Hibernia and Terra Nova oilfields. The water depth is about 120 m. The field is a complex faulted region (Figure 1.2) located above the deep-seated Amethyst salt ridge and the White Rose diapir, and situated in the hanging wall of the Voyager Fault. The target reservoir is the Avalon sandstone.

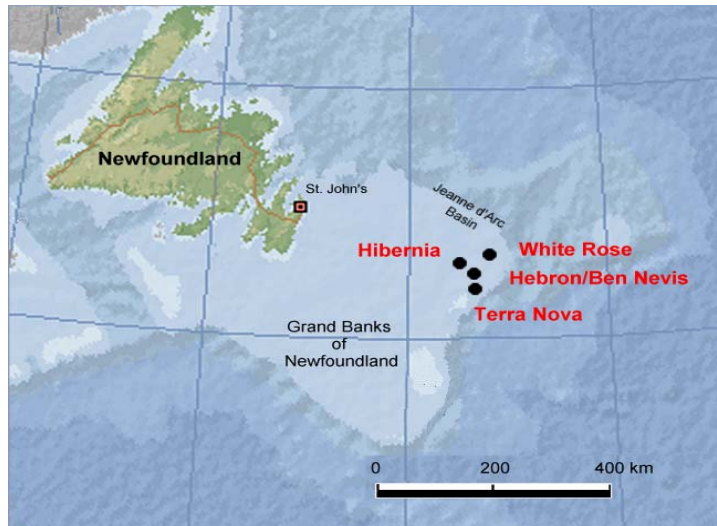


Figure 1.1: Location of White Rose oilfield, Newfoundland. (Modified from Encarta.msn.com, 2004.)

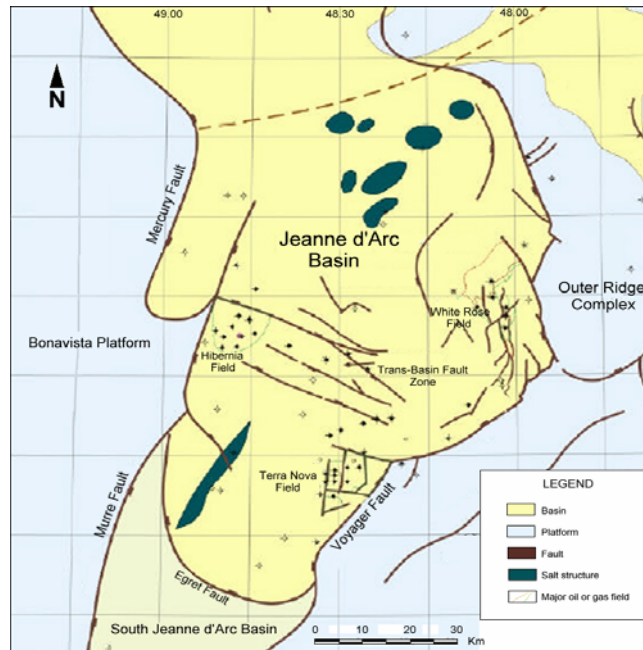


Figure 1.2: Regional setting of Jeanne d'Arc Basin. (Modified after Husky Oil Operations Ltd, 2001.)

The oilfield (Table 1.1) is estimated to have approximately 750 MMBbls oil in place and 2 Tcf gas (Enachescu et al., 1999). The field is the third largest field within the Jeanne d'Arc basin. The field contains three major Avalon Formation pools (Figure 1.3): the South, North and West Avalon pools. All three pools are oil accumulations overlain by a gas cap and underlain by a water leg. The three pools have been penetrated by various wells. These wells are described in the following section.

Discovery	1984, White Rose N-22 well, gas 1988, White Rose E-09 well, oil
Water depth	120 m
Reservoir area	40 km ²
Reservoir depth	2,875 m subsea
API gravity	30°
Production formation	Avalon Formation (Early Cretaceous)
Reservoir character	Well-sorted, fine-grained sandstone
Recoverable Reserves	200–250 million barrels
Estimated development wells	19–21 production and injection (water and gas) wells
Wells to first oil	Up to 10 production and injection wells
Peak annual production	100,000 barrels/day
Partners	Husky Oil (72.5%) and Petro-Canada (27.5%).
Production life	12–15 years
Field development	Subsea wells tied back to the SeaRose FPSO (Floating, Production, Storage and Offloading) vessel

Table 1.1: Summary of the White Rose oilfield. (Modified from Husky Energy Inc, 2005.)

1.3 History of the White Rose field

The drilling history of the White Rose oilfield (Figure 1.4) according to Husky Oil Operations Ltd (2001) is summarized below:

The White Rose field is operated by Husky Energy Inc, and is located within the Newfoundland offshore area. During 1984 and 1986, the first three wells were drilled on the White Rose domal area (N-22, J-49 and L-61). Oil and gas were encountered in all wells. Based on these positive results, the White Rose E-09 well was then drilled in 1987. The well was drilled into a separate structure on the southern flank of the complex. It was the first well drilled in the South Avalon region and encountered over 90 m of net oil pay. The 90-m discovery paved the way to future commercial development.

Wells L-08 and A-17 were drilled into the South Avalon Oil Pool in 1999. These wells yielded important information on the extent and quality of the reservoir originally encountered by the E-09 well. Well N-30 was drilled in the northern part of the field. Information from this well assisted in the delineation of the pool first encountered by the N-22 well. The H-20 well was drilled in 2000 to further evaluate the northern extent of the South Avalon pool.

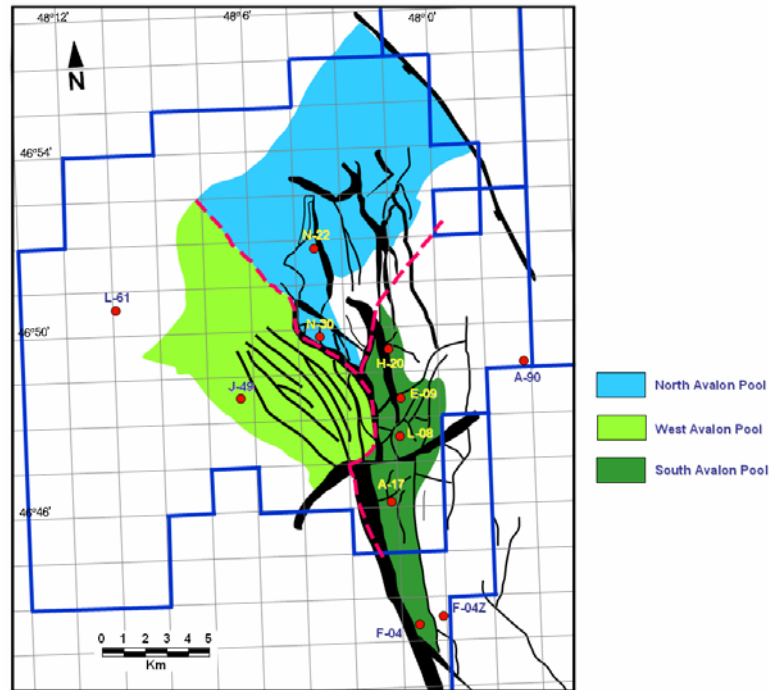


Figure 1.3: The White Rose Avalon pools and wells (Modified after Husky Oil Operations Ltd, 2001).

In 2003, wells F-04 and F-04Z were drilled in the White Rose area (Figure 1.4). The results obtained from well F-04 implied that the reservoir characteristics are comparable to the South Avalon Pool. Well F-04Z will help to delineate the structure (Husky Energy Inc, 2003).

A development plan was put into place. Four wells have been drilled, including an oil producer (well B 07 2) that underwent testing and three water injectors. Following an analysis of the pressure measurements and flow rate, the production capability of the well is estimated to be between 25,000 and 35,000 barrels per day (Husky Energy Inc, 2004).

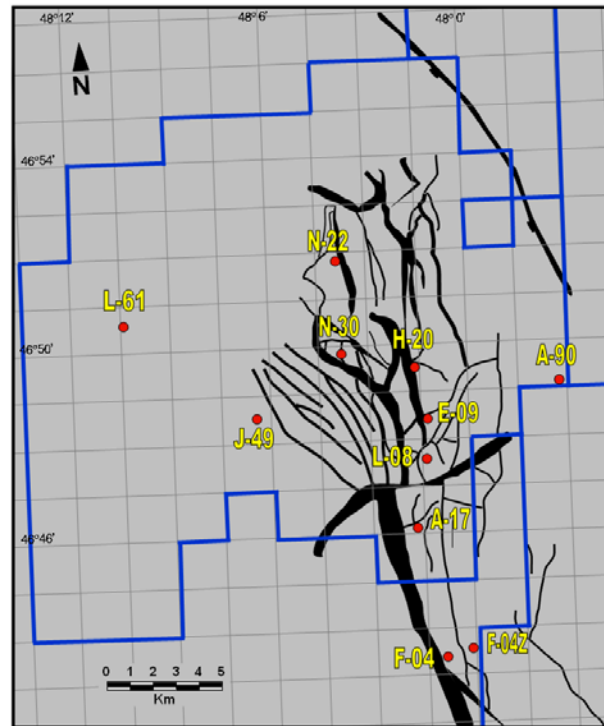


Figure 1.4: White Rose Avalon oilfield and wells (Modified after Husky Oil Operations Ltd, 2001).

1.4 Imaging challenges at White Rose field

According to Hoffe et al., (2000), a number of difficulties have been found in seismic surveys in the White Rose field. The imaging challenges are:

- **Hard water bottom.** The water bottom is approximately 125 m deep. The occurrence of high ocean-bottom reflection coefficients creates serious water-column reverberations. This hard water bottom is due to the presence of glacial deposits of large boulder/cobble fields. Another probable cause could be a hardpan surface created during the Grand Banks' aerial exposure over successive periods of glaciation (Hoffe et al., 2000).
- **Strong P-wave impedance contrast at the base of the Tertiary creates strong multiples.** The erosional unconformity at the Tertiary-Cretaceous boundary within the White Rose field (Figure 1.5) has a

strong seismic impedance contrast. The reflection coefficient at this interface is large and significant energy is reflected from it. The reflection then becomes trapped in other layers, including the water column, and produces more strong multiples. The Base of Tertiary interferes with the upgoing primary reflections from the multiple event at the Avalon reservoir level. This degrades the final seismic image of the reservoir.

- **Poor P-wave impedance contrast at the zone of interest.** The top of the Avalon Formation is a sandstone unit with overlying by siltstone. Shales of the Nautilus Formation overlie this unit. The resulting P-wave impedance contrast between these two formations is minimal. The outcome is that the top of Avalon reflector is quite weak.
- **Presence of gas clouds.** Faults from extensional movements affect the reservoir level, breaking the Base of Tertiary unconformity and forming gas clouds by up-dip leakage of gas along the fault structures. The presence of vapour gas and dispersed gas in fine clastics (Tertiary sediments) can obscure and distort the reservoir seismic image. These gas clouds have an attenuating effect on the final stacked PP section. According to Emery (2001), the seismic signal loses frequency because it is scattered and attenuated when passing through the Tertiary zone; this results in weaker seismic reflectors below the gas cloud.

1.5 Geology

1.5.1 Regional Setting of Grand Banks Basin

The Grand Banks of Newfoundland shown in Figure 1.6 outline a wide continental shelf. The shelf is the easternmost outcrop of the North American continental plate. The Grand Banks area is delimited by the Cumberland Belt-Flemish Cap (CBFC) Paleozoic lineament to the North, the Newfoundland Transform Fault Zone (NTFZ) to the South, the Bonavista Platform to the West, and the Continent-Ocean Boundary (COB) to the East (Husky Oil Operations Ltd, 2001).

The subsurface components of this area are a sequence of five interconnected sedimentary basins (Figure 1.6). The five basins are the South Whale Subbasin (Scotian Basin) and the Whale, Horseshoe, Carson, and Jeanne d'Arc basins. These basins contain deformed rocks dating from the Late Triassic through to the Tertiary. The Mesozoic basins and the Paleozoic and Precambrian rocks that lie beneath and surround the basins were subject to periods of deformation and erosion throughout the Late Jurassic and Early Cretaceous. An important peneplain created the Avalon Unconformity. This peneplain covers the central Grand Banks and thick clastic deposits on the flanks of the Grand Banks. Gradual regional subsidence during the Late Cretaceous and Tertiary resulted in a thin and undisturbed cover of fine-grained marine shelf deposits (McAlpine, 1990). There were three rifting periods of the Grand Banks (Hoffe et al., 2000), which were:

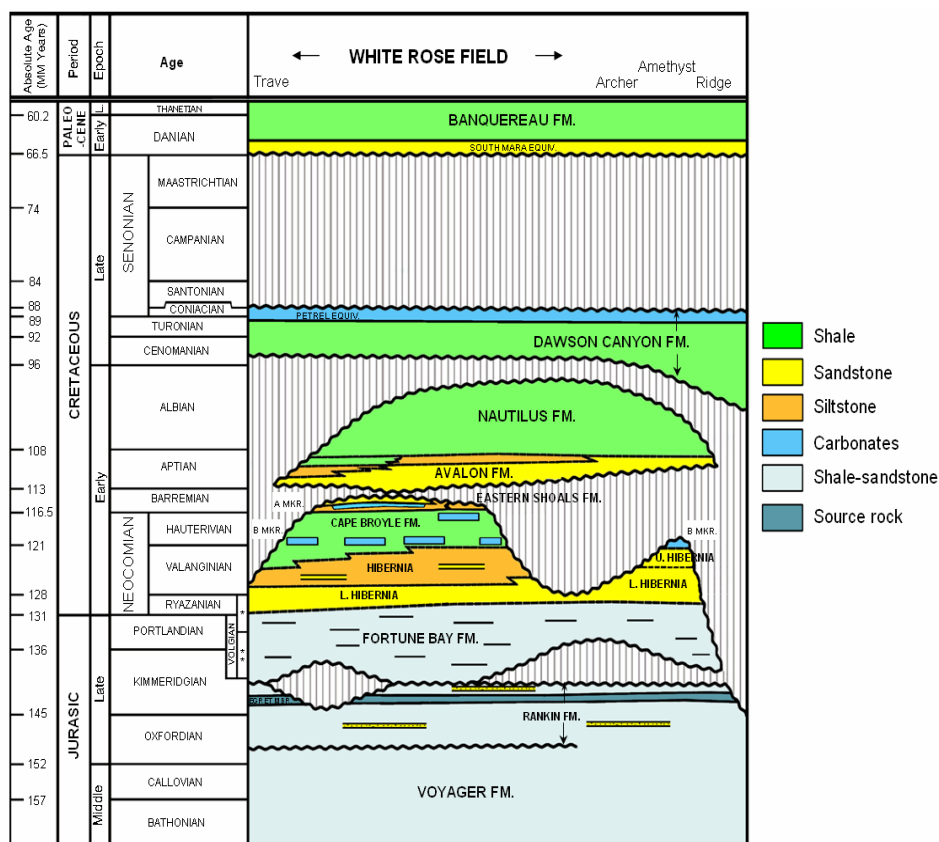


Figure 1.5. Stratigraphy of the White Rose field. (From Deutsch/Meehan-Husky Oil, 2000, in Husky Oil Operations Ltd, 2001.)

- **Late Triassic to Early Jurassic:** The northeast–southwest trending basins began to develop through rifting between North America and Africa
- **Late Jurassic to Late Early Cretaceous:** Separation of Iberia from the Grand Banks. This episode led to the formation of the Avalon Unconformity (a major erosional peneplain).
- **Late-Cretaceous:** Detachment of Labrador and Greenland occurred.

During Late Cretaceous and Tertiary times, inter-rift subsidence and final thermal subsidence deepened the basin and provided a thick cover of fine clastics. The presence of mobile salt during the Late Triassic caused more complexity in the structure of the basin.

The structural history of the basin is linked with the development of structural styles that can be attributed to six consecutive rifting periods that are closely related to six depositional sequences (Hoffe et al., 2000). According to Grant and McAlpine (1990), the six sequences are:

- Aborted Rift (Late Triassic to Early Jurassic): ~ 225–197 Ma
- Epeiric Basin (Early to Late Jurassic): ~ 197–153 Ma
- Late Rift (Late Jurassic to Neocomian): ~ 153–118 Ma
- Transition to Drift, Phase I (Barremian to Cenomanian): ~ 118–105 Ma
- Transition to Drift: Phase II (Late Cretaceous and Paleocene): ~ 105–58 Ma
- Passive Margin (Tertiary to Quaternary): ~ 58–3 Ma

Appendix A gives a more detailed description of the six structural styles and sequences.

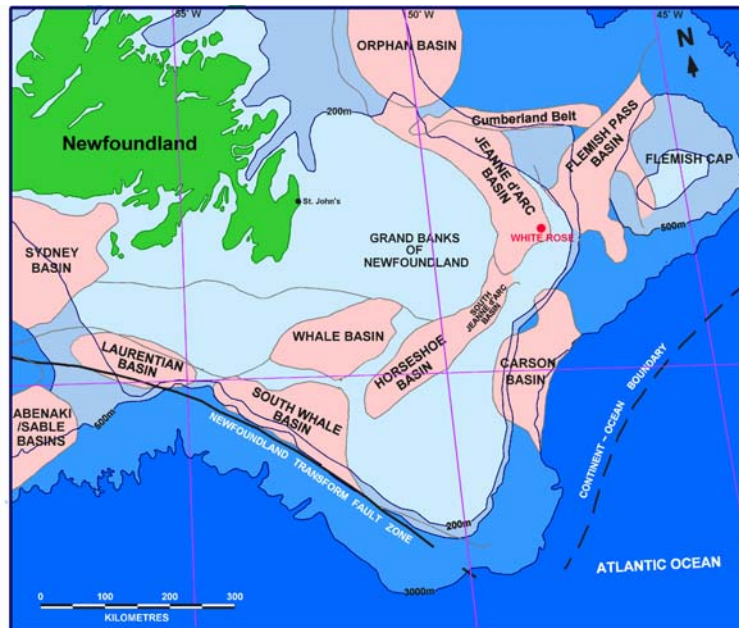


Figure 1.6. Location of Grand Banks Basins and White Rose oilfield (Modified from Husky Oil Operations Ltd, 2001).

1.5.2 Jeanne d'Arc Basin

The Jeanne d'Arc Basin (Figures 1.2 and 1.6) is located in the northeastern part of the Grand Banks of Newfoundland. The Basin is a Mesozoic failed-rift basin. The basin is 20 km deep according to the interpretation of deep multi-channel seismic data (Grant and McAlpine, 1990). The basin encompasses an area of approximately 10,500 km². The basin outline is an elongated trough with a north-northwest south-southeast trend, and enclosed by the Murre Fault to the west, the CBFC lineament to the north, the Voyager fault zone to the east, and the Egret fault to the south (Husky Oil Operations Ltd, 2001).

The sedimentary evolution of the Basin (Appendix A) is related to the structural framework of the basin and to the regional tectonic episodes linked to the break-up of Pangaea. Two periods of rifting were dominated by the deposition of evaporites and coarse clastics, respectively. The periods are separated by a period of non-tectonism, characterized by the deposition of fine clastics and limestones. A two-stage transition to a passive continental margin followed as fine clastics and minor chalky limestones were deposited (McAlpine, 1990).

Major reserves of oil have been discovered in the Jeanne d'Arc Basin and, most notably, in the Hibernia field. The oil was generated after the continental break-up, in shales deposited at the end of the tectonically quiet period. The oil is now trapped mainly in stacked sandstone reservoirs deposited during the second period of rifting (McAlpine, 1990).

1.5.3 Jeanne d'Arc Basin's stratigraphy

The Jeanne d'Arc Basin, is perhaps the most studied of all the Grand Banks basins due to its hydrocarbon potential. The Early Mesozoic break-up of Pangaea was a complex process which resulted in the formation of a number of fault-bounded Mesozoic rift basins, one of which was the Jeanne d'Arc Basin (Husky Oil Operations Ltd, 2001).

1.5.4 White Rose field's lithologies

The following is a brief description of the proven reservoir lithologies (Figure 1.6) of the White Rose field. A more complete description of the Formations is given in Appendix A. According to the Geological Survey of Canada (2000) and Hoffe et al. (2000), the main Formations present in the Jeanne d'Arc Basin from older to younger are:

- **Hibernia Formation (Tithonian–Berriasian):** Composed of alternating thick sandstones and thinner interbedded shales. It is subdivided into an upper and a lower unit.
- **Catalina Formation (Late Berriasian–Valanginian):** Consists of thinly bedded sequences of sandstones, siltstones, shales, and a minor amount of limestones.
- **Eastern Shoals Formation (Hauterivian–Barremian):** Consists of massive calcareous sandstone/oolitic limestone sequence and a thick sequence of interbedded sandstone and siltstone.
- **Avalon Formation (Barremian–Late Aptian):** The main target of exploration, consisting of a complex siliciclastic sequence, and described

in more detail in section 1.5.5.

- **Ben Nevis Formation (Late Aptian–Late Albian):** Composed of interbedded shales, sandstones, and local coal beds.

1.5.5 Avalon Formation

The Avalon sandstones were deposited during the Early Cretaceous (Aptian). The Formation consists of stacked aggradational shoreface sandstone units, culminating in an upward-fining shaly siltstone. Most of the sandstones were deposited as middle-to-upper shoreface sandstones. The upper shoreface sandstones were subsequently reworked as storm deposits to a middle-to-lower shoreface position.

The Avalon Formation is a complex and variable siliciclastic series, divisible into three subunits, displaying a coarsening upward pattern (McAlpine, 1990). A typical unit thickness is included in the description:

- **Basal subunit (42 m):** This is termed a "red mudstone" sequence, and is characterized by varicoloured shales containing interbedded sandstones.
- **Middle subunit (37 m):** This subunit has thicker sandstone beds, along interbedded grey shales.
- **Upper subunit (46 m):** The upper subunit contains a slightly coarsening upward, sandstone-dominated unit, with siltstone at the top.

The boundary between the Avalon Formation and the Eastern Shoals Formation is sharp. The contact with the Ben Nevis Formation is sharp and unconformable at the basin margins and over major structures, becoming disconformable to conformable toward the basin axis. The Avalon Formation grades laterally into the Nautilus Shale. The environment of deposition was a flat, low-lying coastal plain containing salty lagoons and swamps bordering a large, tidal-dominated shallow estuary (McAlpine, 1990).

At the White Rose and North Ben Nevis oilfield, production is contained in the Avalon sandstones. The economically important sandstone accumulations took

place in the southeastern part of the field with thickness of up to 350 m of sandstone (wells E-09, L-08, and A-17).

The major reservoir facies in the White Rose field (Husky Oil Operations Ltd, 2001) are:

- Sandstones with more than 15% porosity, which are the main flow units in the reservoir having an average permeability of greater than 100 mD; and
- Sandstones with porosities between 10 and 15%, having permeabilities ranging between 10 to 50 mD.
- Sandstones with less than 10% porosity are non-reservoir.

1.5.6 Avalon Reservoir Pools

According to reservoir pressure data contained in Husky Oil Operations Ltd's 2001 public reports, a few major faults (West Amethyst, Central, and Twin faults), and a low structural trend oriented north-northeast, divides the White Rose field into three main pools (Figure 1.3):

- **West Avalon Pool:** The pool was explored with well J-49. The pool is positioned between the West Amethyst, Central, and North J-49 faults, and the crestal erosional edge has an area approximately of 16 km². The trap is structural.
- **North Avalon Pool:** This pool has been addressed using wells N-22 and N-30. It is located on the southeastern flank of the White Rose Diapir, and is defined by the Central Fault, White Rose Diapir erosional edge, Trave Fault, and the southeastern end of the Trave Syncline. The pool has an area of about 10 km². Wells N-22 and N-30 were used to show that the trap is structural, but a stratigraphic element may be present toward the northwest, where the Avalon sandstone may be absent due to truncation or onlap.
- **South Avalon Pool:** The most significant pool, has 350 m of sandstone

with over 100 m of net oil pay. This pool was explored with wells E-09, L-08, A-17, and H-20. It is located to the east of the Amethyst Ridge and Central Fault, and limited by the East Amethyst, Central and Twin faults to the west, and by a structural dip toward the north and east. The pool has an area of approximately 18 km². The trap is structural, but may have a significant stratigraphic component. This pool is geologically complicated.

All three pools contain oil accumulations overlain by a gas cap and underlain by a water leg. Gas-oil contacts have been evaluated in all three pools. Oil-water contacts have only been drilled in the West and South Avalon pools. A brief summary of reservoir properties is listed in Table 1.2.

Delineation wells F-04 and F-04Z (Figures 1.3 and 1.4) are located at the southern end of the oilfield, on a separate geological structure. The results from well F-04 suggest that the reservoir characteristics are comparable to the characteristics in the South Avalon Pool. Well F-04Z will help to delineate the structure. The potential hydrocarbon volumes are estimated to be 200–250 billion cubic feet of natural gas and 60–90 million barrels of oil in place (Husky Energy Inc, 2003).

	South Avalon	North Avalon	West Avalon
Gas-oil contact (m subsea)	2872	3014	3064
Oil-water contact (m subsea)	3009	3073	3127
GAS CAP			
Original gas cap in place (10⁹ m³)	14	50	34
Gas pay area (m²)	12 x 10 ⁶	35 x 10 ⁶	23 x 10 ⁶
Porosity average (%) (net sands)	15.1	14.6	14.6
Permeability average (mD) (net sands)	110	83	83
OIL LEG			
Original oil in place (10⁶ m³)	124	29	39
Recoverable oil (10⁶ m³)	36.0	6.7	8.9
Oil pay area (m²)	18 x 10 ⁶	10 x 10 ⁶	16 x 10 ⁶
Porosity average (%) (net sands)	15.7	15.0	14.7
Permeability average (mD) (net sands)	127	95	87

Table 1.2: White Rose pools information. (Modified after Husky Energy, 2002.)

According to Husky Energy Inc (2004), four wells (an oil producer and three water injectors) have been drilled to date. The oil producer well, White Rose B 07 2 is a horizontal well (with a horizontal section of approximately 1,200 metres) that

underwent testing in the summer of 2004. The pressure measurements and flow rate information obtained during the test indicate that the productive capability of the well through permanent production facilities is between 25,000 and 35,000 barrels per day. During the test, oil flowed to the surface at a rate of more than 9,000 barrels per day, the maximum allowed by test facilities on the rig.

The Sea Rose Floating Production, Storage and Offloading (FPSO) vessel (Figure 1.7), built in South Korea, will produce oil from the White Rose oilfield off the coast of Newfoundland and Labrador. In February 2004, a 14,000 nautical mile journey began from South Korea to Marystown, Canada. Installation of the topsides, and hook up and commissioning took place in Marystown, Newfoundland. The Sea Rose FPSO was built on the design concepts of performance, safety, and reliability, which required to operate off the east coast of Canada. An ice-strengthened hull and a detachable mooring system have been incorporated in the design to ensure safe operations on the Grand Banks. The double-hulled construction was based on a proven Samsung tanker design concept and has a storage capacity of 940,000 barrels of oil. This is about 10 days of production capacity. The successful completion and deployment of the FPSO will lead to first oil in late 2005 or early 2006 (Husky Energy Inc, 2005).

Also built in South Korea was the first of two shuttle tankers (the Heather Knutsen and the Jasmine Knutsen). Each has a crude oil capacity of one million barrels. The vessels have bow-loading systems and are designed to load in tandem from the stern of the Sea Rose FPSO. The process to load the vessels will take about 24 hours. The shuttle tankers will transport oil from the White Rose field to market destinations on the east coast of Canada and the United States (Husky Energy Inc, 2005).

The SeaRose FPSO reached the White Rose oilfield in late August 2005. The vessel was connected to a subsea production system and will go through about three months of offshore hook-up and commissioning in preparation for first oil (Husky Energy Inc, 2005).



Figure 1.7: Sea Rose Floating Production, Storage and Offloading (FPSO) vessel (Modified from Husky Energy Inc, 2004).

CHAPTER 2. WELL-LOG ANALYSIS

This chapter examines well log analyses conducted on different wells (A-90, E-09, H-20, J-49, L-08, and N-22) that have been drilled in the White Rose area (Figure 2.1). These are not the only wells in the area (there are also wells L-61, A-17, N-30, and the more recently drilled F-04, F-04Z and B 07 2), but the six wells used in this study have the most complete data.

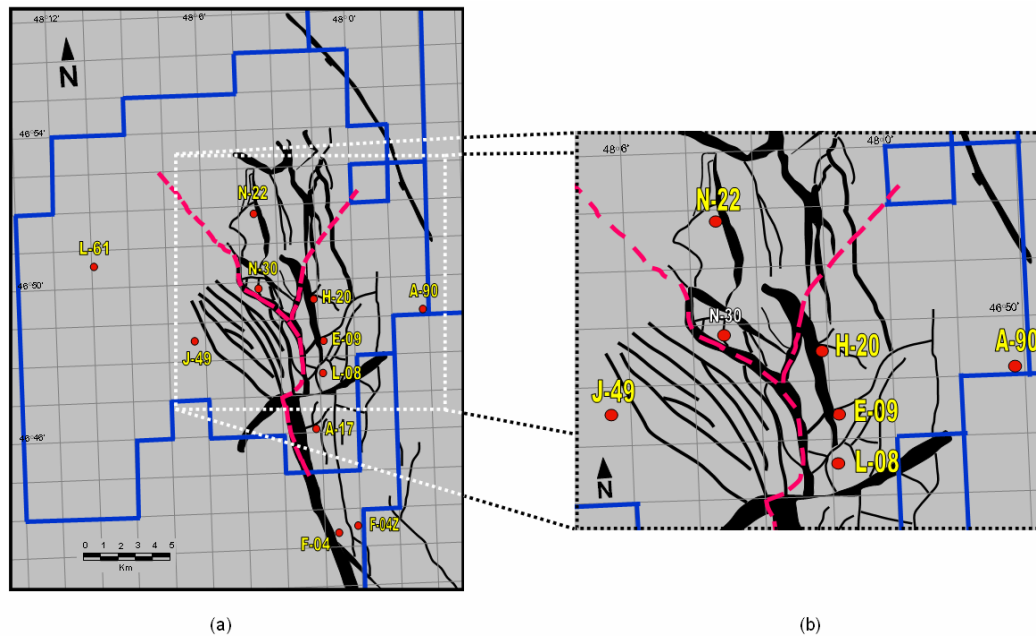


Figure 2.1: Locations of the White Rose wells that are analyzed in this chapter (Modified after Husky Oil Operations Ltd, 2001).

The well log analyses examine relationships among the selected wells of the White Rose field. Moreover, the analyses provide a detailed look into the data relationships between wells H-20 and L-08. In these wells, we were able to review both V_p and V_s log data.

The empirical relationships between V_p , V_s , ρ , GR and ϕ logs in the study area are explored. The different correlations examined are (Jaramillo and Stewart, 2002; 2003):

- V_p and V_s versus depth;

- V_p and V_s versus GR;
- V_p/V_s versus depth;
- V_p/V_s versus GR;
- Actual V_p versus V_p estimated from Faust's relationship;
- Actual V_s versus V_s estimated from Faust's relationship;
- Actual V_s versus V_s estimated from Castagna's relationship;
- Actual ρ versus ρ from Gardner's relationship using V_p ;
- Actual ρ versus ρ from Gardner's relationship using V_s .
- Actual V_p , V_s , V_p/V_s versus ϕ_D
- Actual V_p , V_s , V_p/V_s versus ϕ_N
- ϕ_N versus ϕ_D

The H-20 and L-08 wells were the only two wells with V_s data. Table 2.1 summarizes these relationships. In addition, some porosity logs (density porosity and neutron porosity) in the petrophysical analysis of the White Rose area were studied (Jaramillo and Stewart, 2003). To this end, this study concentrates on well L-08, which is the well in the middle of the 3D-4C OBS survey area. The 3D-4C OBS survey took place in the summer of 2002 and it is studied in Chapter 4.

The lithologies studied are reviewed in section 1.5.4 and Appendix A. The geological formations involved in the analysis are:

- Banquereau Formation, a shale (the term used for this Formation in the analysis is Tertiary Formation: the Tertiary E unit is included in the Banquereau Formation);
- South Mara Formation (glauconitic silty fine sandstone);

- Dawson Canyon Formation (marl and calcareous shale);
- Petrel member (argillaceous limestone);
- Nautilus Formation (siltstone and shale);
- Avalon Formation (very fine to grained sandstone, siltstone and shale);
- Eastern Shoals Formation (interbedded shale, siltstone, sandstone and limestone).

	A-90	E-09	H-20	J-49	L-08	N-22
Vp and Vs versus depth	Vp✓	Vp✓	Vp✓Vs✓	Vp✓	Vp✓Vs✓	Vp✓
Vp and Vs versus GR	Vp✓	Vp✓	Vp✓Vs✓	Vp✓	Vp✓Vs✓	Vp✓
Vp/Vs versus depth			✓		✓	
Vp/Vs versus GR			✓		✓	
Actual Vp versus Faust Vp	✓	✓	✓	✓	✓	✓
Actual Vs versus Faust Vs			✓		✓	
Actual Vs versus Castagna Vs			✓		✓	
Actual ρ versus Gardner's ρ from Vp		✓	✓	✓		✓
Actual ρ versus Gardner's ρ from Vs			✓		✓	
Actual Vp versus Gardner's Vp from ρ		✓	✓	✓	✓	✓
Actual Vs versus Gardner's Vs from ρ			✓		✓	
Vp, Vs, Vp/Vs versus ϕ_D					✓	
Vp, Vs, Vp/Vs versus ϕ_N					✓	
ϕ_N versus ϕ_D					✓	

Table 2.1: Wells analyzed and crossplots assembled. Key: ✓ shows which relationships were investigated in the well.

2.1 H-20 well-log analysis

The White Rose H-20 well was drilled during the second quarter of 2000, with the intention of delineating the northern limit of the South Avalon Pool. Following the drilling, a multi-offset Vertical Seismic Profiling (VSP) study was conducted. The details of the VSP survey are reviewed in section 3.1.

Log data from well H-20, discussed in this section, are: gamma ray log (GR); the delta-t shear (P- and S-mode Shear Dipole Tool-SDT) log; the delta-t compressional (P- and S-mode Shear Dipole Tool-SDT) log; and the bulk density log

(Figures 2.2 and 2.3). In Figure 2.2, the log curves resulting from the transformed ΔT compressional into P-wave velocity (V_p), and the transformed ΔT shear into S-wave velocity (V_s) are shown. We note a general increase in velocity with depth (Table 2.2).

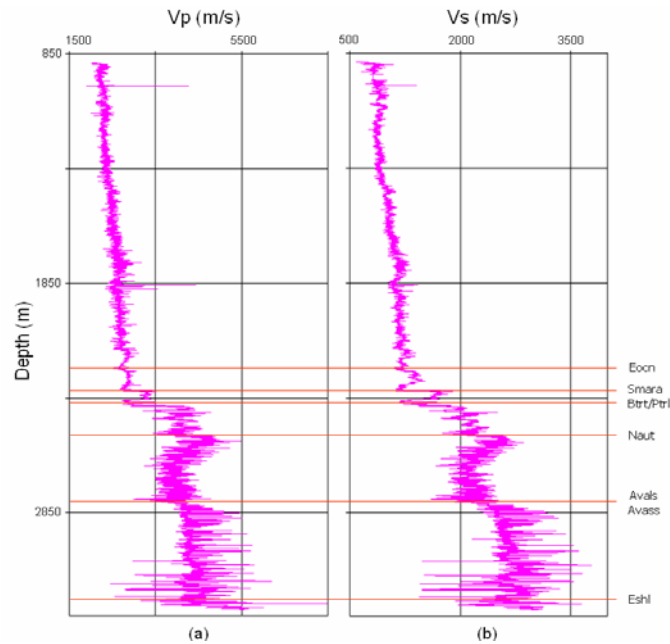


Figure 2.2: Logs from well H-20: V_p , left, and V_s , right, log curves.

Well	V_p (m/s)	V_s (m/s)
A-90	1300-6000	No data available
E-09	1100-6300	No data available
H-20	2100-5600	780-3200
J-49	1860-5300	No data available
L-08	2100-5400	650-3000
N-22	2100-5600	No data available

Table 2.2: General velocity trends for V_p and V_s logs.

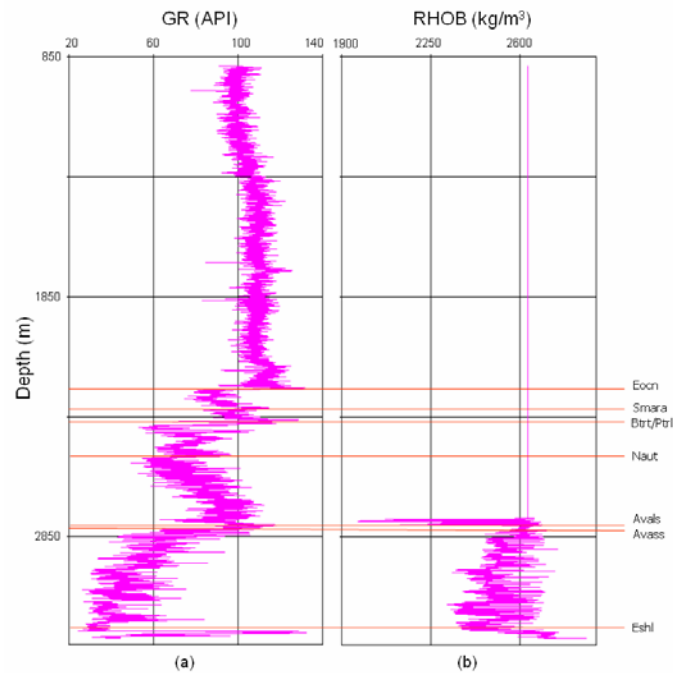


Figure 2.3: Logs from well H-20: Panel (a) — gamma ray log curve; Panel (b) — RHOB (Actual ρ) log curve.

2.2 Study of empirical relationships

In attempting to understand the petrophysical behaviour of the oilfield, and also to identify how some petrophysical properties relate to each other, I analyzed well log data from wells A-90, E-09, H-20, J-49, L-08, and N-22. With this information, I consider general rock property values as well as the empirical relationships between the dipole sonic (V_p and V_s), ρ , ϕ , and GR logs for the wells. These analyses are listed in Table 2.1.

2.2.1 V_p versus depth

P and S velocities generally increase with increasing confining pressure (Yilmaz, 2001). All wells in the study area have a general increase of V_p with depth (Figure 2.4). Some portions of the curves do show velocity decreases that are generally due to a local change in lithology, or perhaps the presence of a compressible free gas replacing liquids in the pore space that could make the P-wave velocity considerably reduced (Castagna et al., 1993).

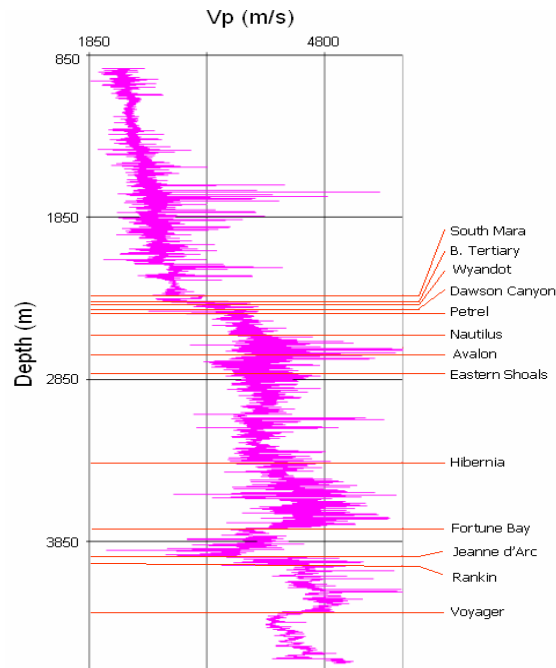


Figure 2.4: Vp versus depth for well N-22. A velocity increase with depth is the general trend observed on the different wells studied.

In general, the Cretaceous Formations have higher velocity values (up to ~6300 m/s) and are related to the Jeanne d'Arc and Eastern Shoals Formations (up to ~5600 m/s); the lower velocity values are from the Nautilus (down to ~3100 m/s) and Rankin (down to ~2750 m/s) Formations. The Tertiary Formations show mid-range Vp velocities up to ~4800 m/s.

2.2.2 Vs versus depth

The Vs data used in this section is from the L-08 and H-20 wells (Figure 2.1). There is a general increase of Vs with depth in both of the wells. Similar to the Vp log curves, the Vs log curves occasionally have velocity decreases, partially due to the local changes in lithology.

2.2.3 Vp/Vs versus depth

This analysis was conducted on wells H-20 and L-08. A decrease of Vp/Vs with depth is observed (Figure 2.5). Shallow values are in the 2.5–3.5 range. Deeper values are closer to ~1.6. Within lithological Formations we observe some increase of the Vp/Vs values. The increase of pressure and temperature could generate bulk

porosity reductions, phase changes, cementation, and additional diagenetic changes that could result in compressional and shear velocity gradients (Castagna et al., 1993). From an analysis of the gradients of V_p/V_s in some other areas with similar lithology to the White Rose field, we found that in the Grane Field in the North Sea (Avseth et al., 2001) and in the northern region of the Gulf of Mexico (DeAngelo, et al., 2003), that V_p/V_s decreases with depth.

The average V_p/V_s values found at the wells H-20 and L-08 are shown in Table 2.3. These values pertain to the Tertiary (above Base of Tertiary unconformity) and Cretaceous Formations (from the Base of Tertiary unconformity to the bottom of the wells).

	V_p/V_s	
	H-20	L-08
Tertiary: top of well to Base of Tertiary	~2.61–2.20	~3.18–1.82
Cretaceous: Base of Tertiary to bottom of well	~1.94–1.63	~1.88–1.63
Bottom of well	3271 m	3118 m
Base of Tertiary	2384 m	2316 m

Table 2.3: Behaviour of V_p/V_s ratio versus depth for H-20 and L-08 wells.

2.2.4 Actual V_p versus V_p estimated from Faust's relationship

Faust's empirical relationship (shown in Equation 2.1, below) predicts compressional velocities as a function of geological time (Table 2.4) and depth of burial of the rock (Faust, 1951). This section compares the predicted V_p from the Faust relationship with measured or actual V_p values. Faust (1951) worked with 500 velocity datasets measured from surveys in Canada and the United States. His velocity study was concentrated on shale and sand sections. The conclusion from his study was that the V_p velocity increases with depth and age of the shales and sandstones, and that this increase is greater in the shallower Formations. The data studied was from old Ordovician rocks to Post-Eocene Formations.

$$V_p = C_p (TZ)^{1/6}, \quad (2.1)$$

where: V_p Compressional velocity (m/s)
 C_p Constant 125.3
 T Formation age (millions of years)
 Z Depth of burial (m)

Age (my)	Formation	Age (my)	Formation
	Tertiary	118	Eastern Shoals
55	South Mara	118	White Rose
65	Wyandot	122	Hibernia
75	Dawson Canyon	125	Lower Hibernia
88	Petrel Member	128	Fortune Bay
92	Nautilus	138	Jeanne d'Arc
105	Ben Nevis	152	Rankin
115	Avalon	152	Voyager

Table 2.4: Formation age used on Faust's relationship.

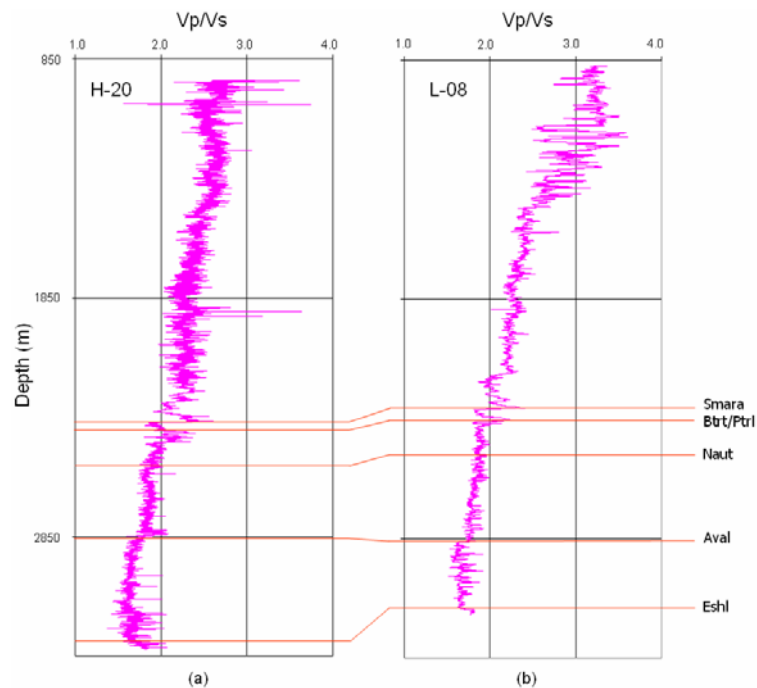


Figure 2.5: Panel (a) — Vp/Vs versus depth for well H-20; Panel (b) — Vp/Vs versus depth for well L-08.

For my study, the result obtained using Faust's equation gave very approximate estimates for the Tertiary Formations, and significantly underestimates the Cretaceous Formations (Figure 2.6). In general, the Faust Vp relationship provides only an approximate trend in this case. It was necessary to segment the wells into their main Formations and try to evaluate the best-fit Vp curve using

Faust's equation. To obtain the constants, different approaches were used. The analysis and results of these approaches are in Appendix B.

Faust's relationship was not acquired for the Formations at the bottom of the well. This is because the age of the rocks below the top of the Formation is unknown.

The main idea behind using the different constants for each Formation was to see how accurate the relationship was for the area. However, it is important to be able to have one only constant for an area instead of several constants. In this case (Figures 2.7 and 2.8), I derived one constant per well (Table 2.5). These new constants were derived from the actual Vp log curve and from the Faust relationship.

In Figures 2.7 and 2.8, the curve using the Faust constant ($C_p=125.3$) is labelled "curve A" and the curve with the derived constant is labelled "curve B". Each predicted curve is compared with the actual Vp log curve (Panels (b) and (c) on both Figures). After the comparison, there were negative results (when the values from curve A or B were below the values of the actual Vp log curve), and positive results (when the values from curve A or B were above the values of the actual Vp log curve).

After comparing both RMS error values (Figures 2.7 and 2.8, Table 2.5), we can conclude that original Cp curve data constant ($C_p=125.3$) works best for the younger Tertiary Formations. The derived constant, $C_p=132.38$, works better for the Cretaceous Formations. However, we have a better fit for the Cretaceous Formations if we examine each Formation independently, and then determine an independent constant for the Tertiary section (Appendix B). Tertiary sediments are mostly clastics. In the Cretaceous Formations, there is limestone present. In general, the results obtained from the clastic base Faust equation have to be looked at with caution since the Faust equation was formulated using clastic data.

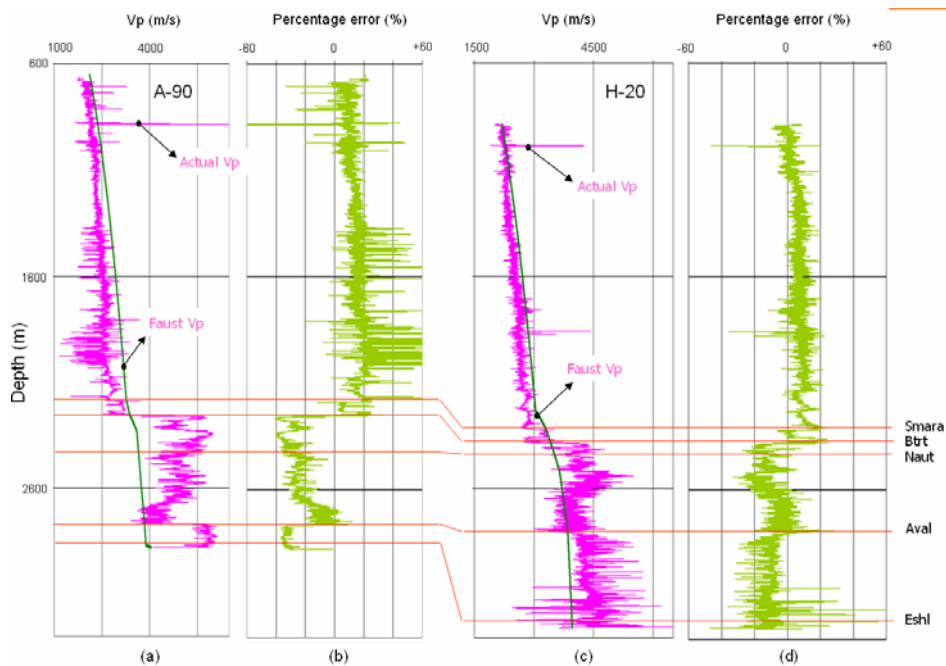


Figure 2.6: Panel (a) — actual Vp and Faust Vp for well A-90: RMS error of the Vp Faust curve is ± 1344.12 m/s; Panel (b) — percentage error between the Actual Vp curve and the Faust Vp curve for well A-90; Panel (c) — actual Vp and Faust Vp for well H-20: RMS error of the Vp Faust curve is ± 398.01 m/s; Panel (d) — percentage error between the Actual Vp curve and the Faust Vp curve for well H-20. The panels show the results of applying the original Faust relationship to the well log data. The Vp Faust curves on both panels were derived using a Faust constant of 125.3.

Including the results from the Appendix B, the results from deriving Vp from the Faust relationship can be divided in four groups:

- using the constant 125.3 for the entire wells, the best result is in well H-20;
- using the derived constant for the well, the best results are in wells L-08, N-22, and H-20;
- using just two constants (one for the Tertiary Formations and one for the Cretaceous Formations), well H-20 shows good results. Wells L-08, H-20, N-22, and J-49 have the best results. Poorer results came from wells A-90, and E-09 (Appendix B);
- using a constant per Formation and per well, the best result is well N-22 (Appendix B).

Well	Faust Constant	RMS error \pm (m/s)	Constants derived	RMS error \pm (m/s)
A-90	125.3	1344.12	132.38	846.06
E-09	125.3	546.16	127.53	542.83
H-20	125.3	398.01	128.90	387.45
J-49	125.3	445.15	126.06	444.64
L-08	125.3	381.07	120.50	360.54
N-22	125.3	389.89	123.74	387.31

Table 2.5: Constants used to predict Vp from Faust's relationship for all wells. The RMS from using Faust's constant and the RMS error from using the derived constant gives the accuracy of the derived constant. The derived constant is per well.

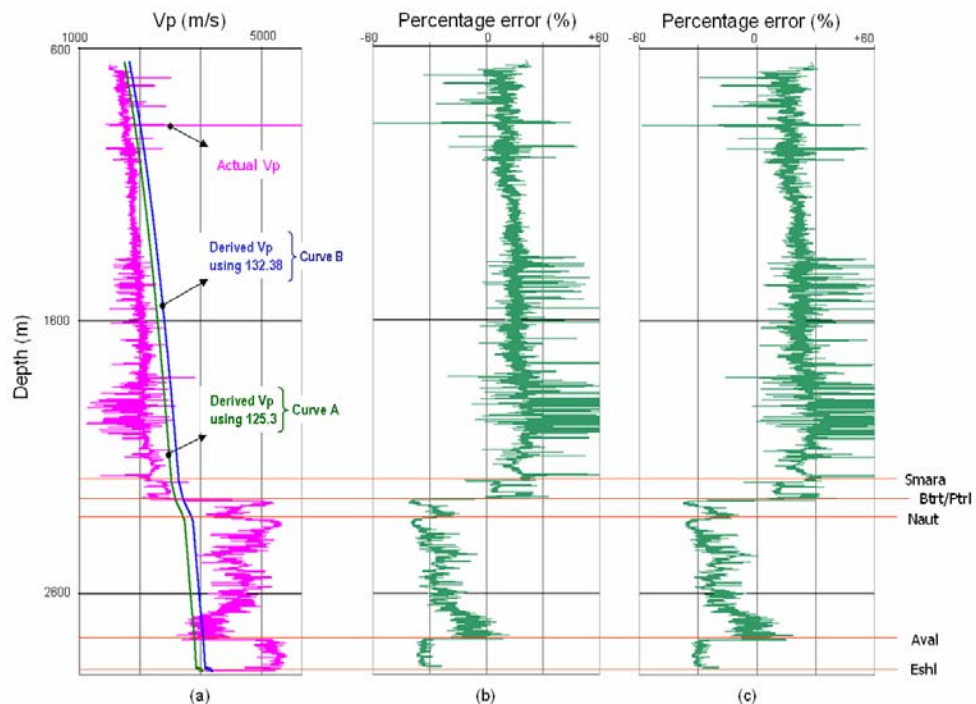


Figure 2.7: Panel (a) — actual Vp and Faust Vp (curves A and B) versus depth for well A-90; Panel (b) — percentage error between the actual Vp curve and the Faust Vp curve A (derived from 125.3 as the constant): RMS error is ± 1344.12 m/s; Panel (c) — percentage error between the actual Vp curve and the Faust Vp curve B (derived using 132.38 as the constant). RMS error is ± 846.06 m/s.

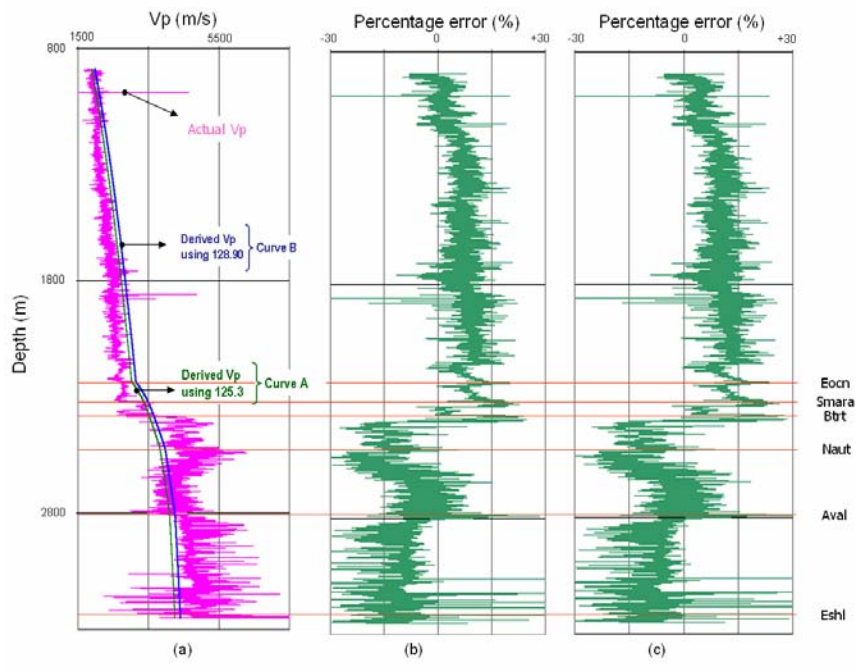


Figure 2.8: Data from well H-20: Panel (a) — actual Vp and Faust Vp (curves A and B) versus depth. Panel (b) — percentage error between the actual Vp curve and the Faust Vp curve A (derived using 125.3 as the constant): RMS error is ± 398.01 m/s; Panel (c) — percentage error between the actual Vp curve and the Faust Vp curve B (derived using 128.90 as the constant): RMS error is ± 387.45 m/s.

2.2.5 Actual Vs versus Vs estimated from Faust’s relationship

We explored the possibility of predicting Vs using a relationship similar to the one used to predict Vp from Faust (1951), Equation 2.2. The “Vs Faust equation” attempts to predict shear velocities as a function of geological time and depth of burial of the rock. We explored this relationship in wells H-20 and L-08 where the shear velocity was acquired (Figures 2.9 and 2.10). A general constant of $C_s=70$ was used to start the analysis. This constant showed good results for both wells. The constants for each well (Table 2.6) were derived from the log Vs curve and from the Faust relationship.

$$V_s = C_s (TZ)^{1/6}, \quad (2.2)$$

where: V_s Shear velocity (m/s)
 C_s Constant 70
 T Formation age (millions of years)
 Z Depth of burial (m)

The results obtained using Faust equation gave a better Vs curve for the Cretaceous Formations with $C_p=70$. For the Tertiary Formations, the derived Cs worked better. However, the results from both the Tertiary and Cretaceous Formations should be taken with caution (Figures 2.9 and 2.10 and Table 2.6). The quality of these results (Figures 2.9 and 2.10) could also be due to the observation that the sequence is mainly clastic but still contains limestones that can affect the determination of the constant. The best results were found in well H-20. Well L-08 had a fair result for the Tertiary Formations. The final results showed a gross velocity average.

As we did with the Vp analysis, the most important criterion for using different constants for each Formation was to see how precise the relationship could be for the area of study (Appendix B). Still, it is essential to be able to have only one constant for the area as a replacement for several constants (Table 2.6).

In Figures 2.9 and 2.10, the curve using the Faust constant ($C_s=70$) is labelled “curve A” and the derived constant curve is labelled “curve B”. Each predicted curve is compared with the actual Vs log curve (Panels (b) and (c) on Figures 2.9 and 2.10). After the comparison, there were negative results (when the values from curve A or B were below the values of the actual Vs log curve), and positive results (when the values from curve A or B were above the values of the actual Vs log curve). After this procedure, the results obtained were encouraging. The RMS errors (Table 2.6) showed that the best results are from using the derived constants.

Well	Faust Constant	RMS error \pm (m/s)	Constants derived	RMS error \pm (m/s)
H-20	70	444.48	65.53	429.80
L-08	70	508.53	59.67	433.81

Table 2.6: Constants used to predict Vs from Faust’s relationship for wells H-20 and L-08. The RMS error from using Faust’s constant and the RMS error from using the derived constant show the accuracy of the derived constant. The derived constant is per well.

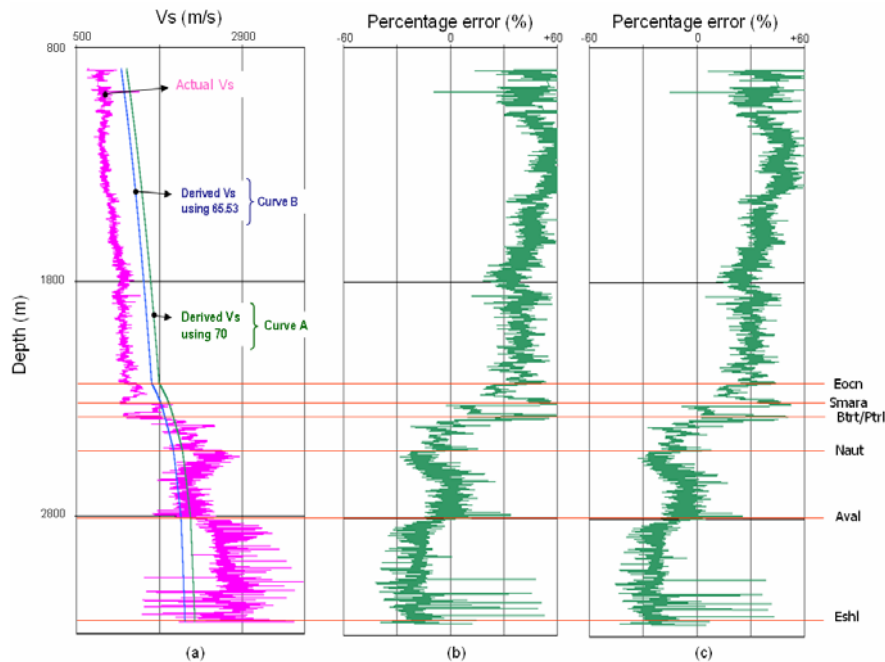


Figure 2.9: Data from well H-20: Panel (a) — actual Vs and Faust Vs (curves A and B) versus depth; Panel (b) — percentage error between the actual Vs curve and the Faust Vs curve A (derived using 70 as the constant): RMS error is ± 444.48 m/s; Panel (c) — percentage error between the actual Vs curve and the Faust Vs curve B (derived using 65.53 as the constant): RMS value is ± 429.80 m/s.

In Figures 2.11 and 2.12, we compare the percentage errors for Vp and Vs (using the derived curves A and B). We can conclude that the use of the Faust equation is a reliable method for deriving Vs. For Vs, we found better results in the Cretaceous Formations than for the Tertiary Formations. Nonetheless, the use of Faust's equation is a very approximate method to derive Vs and therefore should be used with caution.

In Figures 2.11 (Panels (c) and (d)) and 2.12 (Panels (a) and (b)), we can see that the main difference in percentage errors is in the Tertiary Formations for both Vp and Vs curves. In Figure 2.11 Panel (d) has a lower percentage error than Panel (c). In Panel (b) of Figure 2.12, the percentage error is lower when we compare it with Panel (a). Panel (d) in Figure 2.11 and Panel (b) in Figure 2.12 show the results after using the constants (Tables 2.4 and 2.5) on the wells.

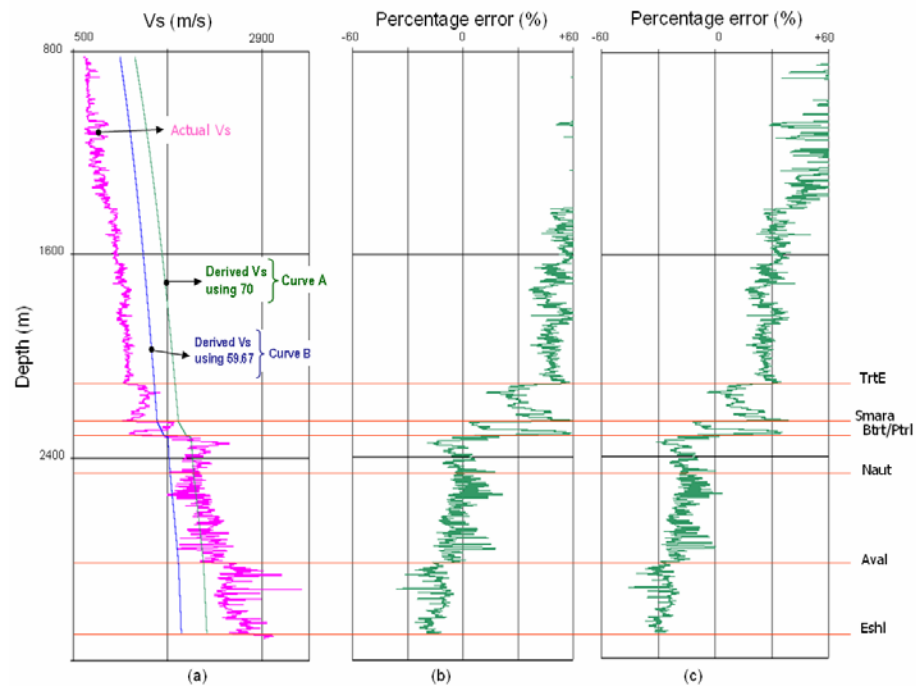


Figure 2.10: Data from well L-08: Panel (a) — actual Vs and Faust Vs (curves A and B) versus depth; Panel (b) — percentage error between the actual Vs curve and the Faust Vs curve A (derived using a constant of 70): RMS error is ± 444.48 m/s; Panel (c) — percentage error between the actual Vs curve and the Faust Vs curve B (derived using a constant of 59.67): RMS value is ± 433.81 m/s.

Including the results from Appendix B, the results from deriving Vs from the Faust relationship can be divided in four groups:

- using the constant 70 for the entire wells, the best result is from well H-20;
- using the derived constant per well, the better result is from well H-20
- using just two constants (one for the Tertiary Formations and one for the Cretaceous Formations) wells H-20 and L-08 have good results (Appendix B);
- using a constant per Formation and per well, both wells L-08 and H-20 showed good results (Appendix B).

Faust (1951) used an interval of 1000 feet as a standard measurement. According to Faust, the relationship between velocity to depth and geologic time

tended to be ambiguous with the use of shorter intervals, implying errors of measurements and variations in lithology. All the sections indicated as calcareous were eliminated. In his paper, the anomalous values found on the Tertiary rocks are associated with an unusually high degree of cementation.

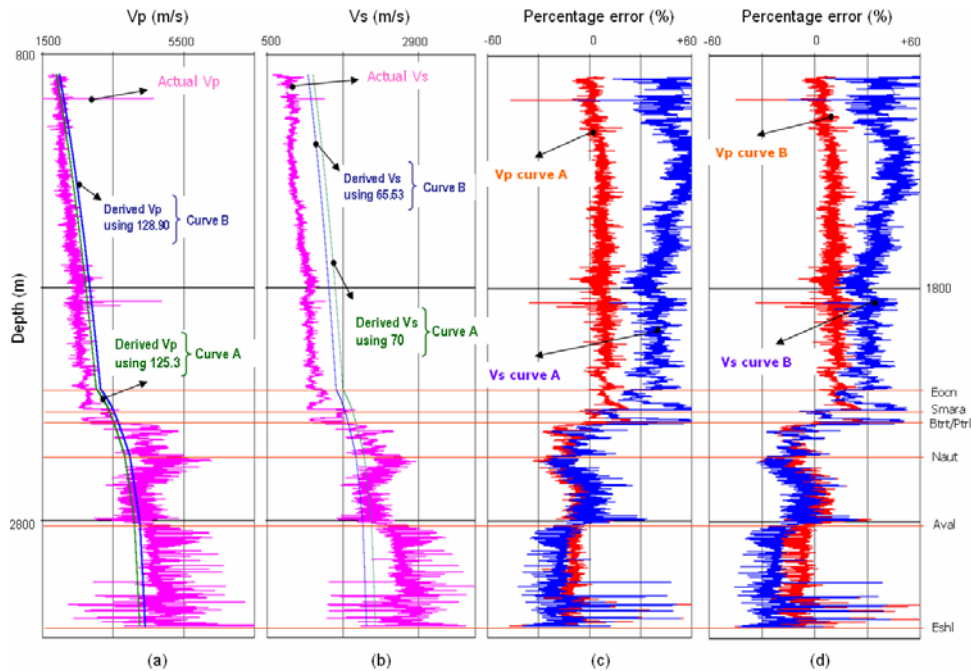


Figure 2.11: Results from well H-20. Panel (a) — actual Vp and Faust Vp (curves A and B) versus depth. The Vp curve A is derived from Faust, using the 125.3 constant. The Vp curve B is derived from Faust, using 128.90 as the constant; Panel (b) — actual Vs and Faust Vs (curves A and B) versus depth. The Vs curve A is derived from Faust, using 70 as the constant. The Vs curve B is derived from Faust, using 65.53 as the constant; Panel (c) — the Vp curve A is the result of comparing the actual Vp and the Vp derived from Faust, using the 125.3 constant; Vs curve A is the result of comparing the actual Vs and the Vs derived from Faust, using the using the 70 constant; Panel (d) — the Vp curve A is the result of comparing the actual Vp and the Vp derived from Faust, using the 128.90 constant; Vs curve A is the result of comparing the actual Vs and the Vs derived from Faust, using the 65.53 constant.

Our study used the entire well data to apply the Faust relationship, which include calcareous sections within the clastics (this made it difficult to eliminate a calcareous section). We had a variety of results, this variety could be due to the age of the rocks, and how pressure and temperature affect each rock.

After considering the results (also from the Appendix B) of deriving Vp and Vs using Faust's relationship we can conclude:

- When using Faust's constant (125.3) for the entire well, the Tertiary section is overestimated and the Cretaceous section is underestimated. The results should be viewed with caution (Figures 2.6: Panels (a) and (c); Figure 2.7: Panel (a); Figure 2.8: Panel (a); Figure 2.9: Panel (a); Figure 2.10: Panel (a); Figure 2.11: Panels (a) and (b));
- When using the derived constant for the entire well, the results are similar to the results using the 125.3 constant. The velocities at the Tertiary section are overestimated and the velocities at the Cretaceous section are underestimated. The results are similar to, but improve on, those using the 125.3 constant. However, the approach should be used with caution (Figures 2.6: Panels (a) and (c); Figure 2.7: Panel (a); Figure 2.8: Panel (a); Figure 2.9: Panel (a); Figure 2.10: Panel (a); Figure 2.11: Panels (a) and (b));
- When using a constant for the Tertiary section and another constant for the Cretaceous section, the results are reasonable. Nonetheless, in various parts of the sections, the curves are either underestimated or overestimated (Appendix B);
- Using a constant for each Formation in the well, the results are satisfactory (Appendix B).

If we base our analysis on the RMS error values (Table 2.7) from Vp and Vs results, we can say that the best prediction is for wells H-20 and L-08. We found that the analysis shows a smaller RMS error in these wells. The use of the relationship is an approximate approach for both Vp and Vs velocities but in general the better results come from the Vp curve. As we see, RMS error values vary per well; however, a RMS error value depends on the depth, age of burial of the rock, and also on the type of rock, due to the response of the Vp and Vs curves to the lithology, so this relationship should be used with caution.

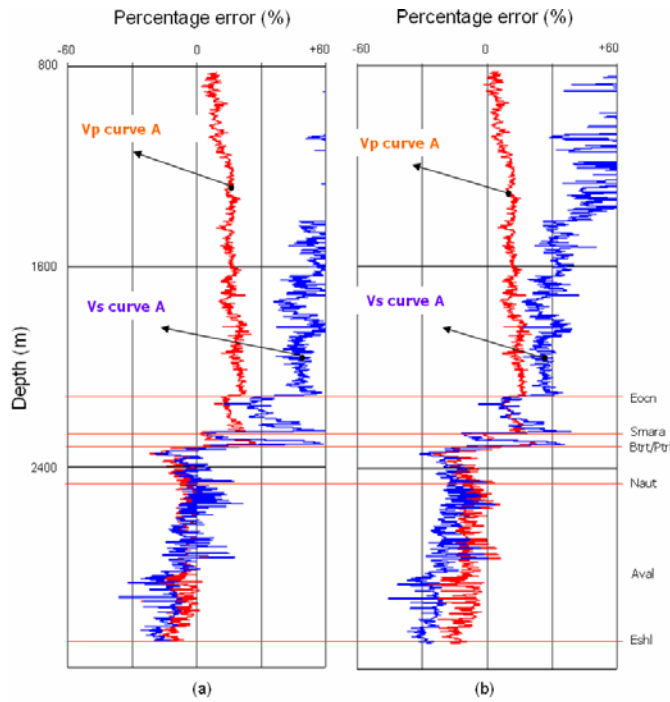


Figure 2.12: Results from well L-08: Panel (a) — Vp curve A is the result from comparing the actual Vp and the Vp derived from Faust, using the 125.3 constant. The Vs curve A is the result of comparing the actual Vs and the Vs derived from Faust, using the 70 constant. Panel (b) — Vp curve B is the result from comparing the actual Vp and the Vp derived from Faust, in this case using Cs=59.67. The Vs curve B is the result of comparing the actual Vs and the Vs derived from Faust.

Well	RMS error± (m/s)			
	Vp from Faust		Vs from Faust	
	125.3 constant	Derived constant	70 constant	Derived constant
A-90	1344.12*	846.06*	♦	♦
E-09	546.16	542.83	♦	♦
H-20	398.01	387.45	444.48✕	429.80✕
J-49	445.15	444.64	♦	♦
L-08	381.07✕	360.54✕	508.53*	433.81*
N-22	389.89	387.31	♦	♦

Table 2.7: RMS error values for each well. These RMS values accord to the constant used to derive Vp and Vs. The constants are approaching Faust’s relationship using a 125.3 constant, the derived constants are per well. Key: ♦ This log is not present in this well; * Poor RMS results; ✕ Good RMS results

Following the analysis using the Faust equation and obtaining the derived constants in well H-20 and L-08, we compared the best fit “derived constants” (Cp and Cs) with the corresponding actual average velocity values Vp and Vs (Table 2.8). For this analysis we used the derived constants used on well H-20 and L-08. The resultant relationship shown below (Equation 2.3 and Table 2.9) gave

reasonable V_p and V_s values for wells H-20 and L-08 that indicated the results obtained from the Faust equation were reliable. The $\overline{V_p}/\overline{V_s}$ values are the average values present in the wells.

$$\frac{C_p}{C_s} = \frac{\overline{V_p}}{\overline{V_s}}, \quad (2.3)$$

where: $\overline{V_p}$ Average compressional velocity (m/s)
 $\overline{V_s}$ Average shear velocity (m/s)
 C_p Constant used to derive V_p
 C_s Constant used to derive V_s

Well	Constants		Actual Average Velocity	
	P-wave	S-wave	P-wave	S-wave
H-20	128.90	65.53	3168.67	1565.79
L-08	120.50	59.67	3022.34	1454.52

Table 2.8: Constants (used to predict V_p and V_s from Faust) and velocity values for wells H-20 and L-08.

Well	C_p/C_s	V_p/V_s
H-20	1.97	2.02
L-08	2.02	2.08

Table 2.9: V_p/V_s values obtained from Faust constants and velocities, using data from wells H-20 and L-08.

2.2.6 Actual V_s versus V_s estimated from Castagna's relationship

We used Castagna's (1985) mudrock equation (Equation 2.4) to derive V_s from V_p . Prior to applying Equation 2.4 to the data; we plotted the actual V_p and V_s along Castagna's mudrock line to determine how well the prediction of this data would fit our actual data (Figure 2.13). As shown in Figure 2.13, most of the well's data falls on the Castagna mudrock line. This gave us an initial degree of confidence in applying this formula to our data. In both wells, the Eastern Shoals (calcareous sandstone/oolitic limestone sequence) data does not fall at all into the mudrock line.

$$V_s = \frac{(V_p - 1360)}{1.16}, \quad (2.4)$$

where: V_s Shear velocity (m/s)
 V_p Compressional velocity (m/s)

Castagna's equation could only be checked for wells H-20 and L-08 (Figures 2.14 and 2.15). After applying the equation, the prediction of Vs for the entire well gave satisfactory results. One reason for the quality of the fit is probably due to the predominance of clastic strata as per Castagna's assumptions.

Where some carbonate content was present (Dawson Canyon calcareous shale, Petrel Member limestone and Eastern Shoals sandstone/limestone), Castagna's mudrock equation worked better than expected. We kept on searching for a better approach to this velocity predictor for the carbonate lithology, using Pickett's empirical relationship for limestones (1963a). Pickett's equation is shown as Equation 2.5.

$$V_s = \frac{V_p}{1.9}, \quad (2.5)$$

where: V_s Shear velocity (m/s)
 V_p Compressional velocity (m/s)

Equation 2.5 was empirically derived using laboratory core data to predict Vs for carbonates. Castagna (1993) based his carbonate equation on Pickett's equation and a least-squared polynomial fit to the data (Equation 2.6); this limestone empirical relationship gives better results for the limestone section of our well than when using the mudrock equation

$$V_s = -0.05509V_p^2 + 1.0168V_p - 1.0305, \quad (2.6)$$

where: V_s Shear velocity (m/s)
 V_p Compressional velocity (m/s)

Castagna's relationship (1993) for limestone contain three constants (-0.05509, 1.0168, and 1.0305) and Vp to predict shear velocities. Figures 2.14 and 2.15 show the results after applying the Castagna relationship to our data. The Vs results are satisfactory on well H-20 (Figure 2.16) where the Eastern Shoals formation are sandstone and limestone. We can appreciate that the Vs curve derived using Castagna's empirical relationship for limestone is more accurate than Castagna's Vs derived solely for clastics. On well L-08 (Figure 2.17), the results are more encouraging for the Petrel member. On the same well, the resultant Vs values from Castagna's mudrock equation for clastics is higher than the actual Vs values.

On the same well, the results for the Eastern Shoals Formation are reasonable. The Castagna-derived V_s for limestones is more realistic than the Castagna V_s for clastics.

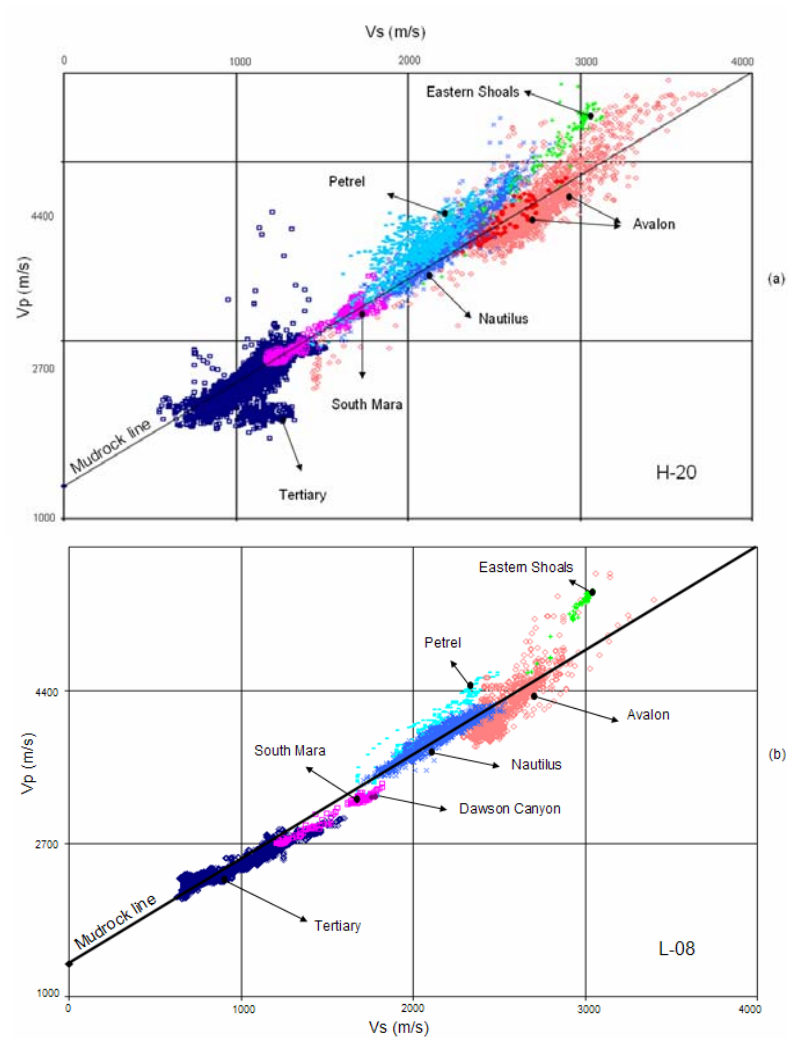


Figure 2.13: Panel (a) — actual V_s versus actual V_p for well H-20. The data falls close to the original Castagna's mudrock line. Panel (b) — actual V_s versus actual V_p for well L-08. The data falls the into original Castagna's mudrock line.

To support Figures 2.16 and 2.17, we have the RMS error values of these new curves (Table 2.10 and 2.10). Following are the details of Figures 2.16 and 2.17. In both figures we have three rows (1, 2, 3) and three columns (a, b, c).

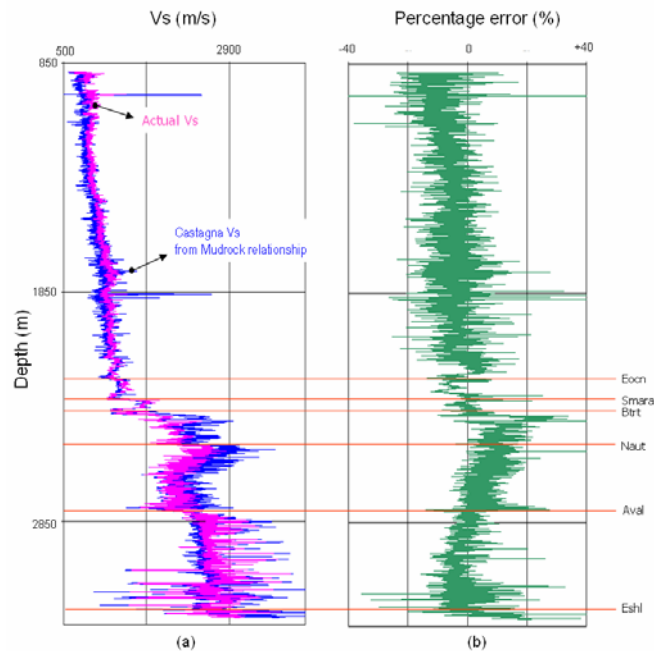


Figure 2.14: Data from well H-20: Panel (a) — actual Vs and Castagna Vs (mudrock empirical relation) versus depth. Panel (b) — percentage error between the actual Vs curve and the Vs Castagna curve.

The data from Figure 2.16 is from the well H-20. Row (1) column (a) shows actual Vs and Castagna Vs (derived from Castagna's mudrock relationship) versus depth. Row (1) column (b) shows actual Vs and Castagna Vs (derived from Castagna's limestone relationship) versus depth. Row (1) column (c) shows actual Vs and Castagna Vs (derived from Pickett's relationship) versus depth.

Row (2) column (a) provides a closer look at the Petrel Formation, actual Vs and Castagna Vs (derived from Castagna's mudrock relationship) versus depth. Row (2) column (b) provides a closer look at the Petrel Formation, actual Vs and Castagna Vs (derived from Castagna's limestone relationship) versus depth. Row (2) column (c) is a closer look at the Petrel Formation, actual Vs and Castagna Vs (derived from Pickett's relationship) versus depth.

Row (3) column (a) provides a closer look to the Eastern Shoals Formation, actual Vs and Castagna Vs (derived from Castagna's mudrock relationship) versus depth. Row (2) column (b) is a closer look to the Eastern Shoals Formation, actual Vs and Castagna Vs (derived from Castagna's limestone relationship) versus depth. Row (2) column (c) provides a closer look at the Eastern Shoals Formation, actual

Vs and Castagna Vs (derived from Pickett's relationship) versus depth.

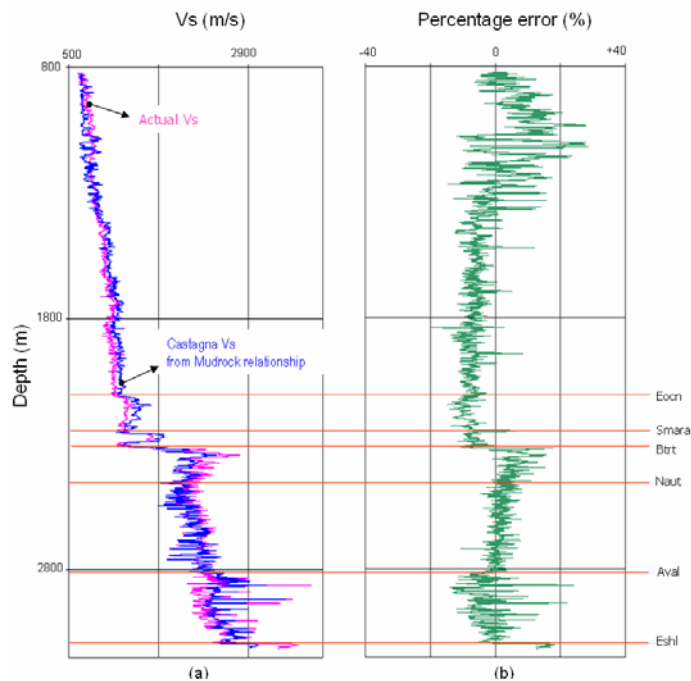


Figure 2.15: Data from well L-08: Panel (a) — actual Vs and Castagna Vs (mudrock empirical relation) versus depth. Panel (b) — percentage error between the Actual Vs curve and the Vs Castagna curve.

In Table 2.10, we can see that the best result for the entire well H-20 is using Castagna's mudrock equation. For the Eastern Shoals Formation, Castagna's limestone relationship does a better job than Pickett's relationship. Petrel Member is better analyzed by Pickett's relationship. The best result for the entire well uses Castagna's mudrock equation.

The data shown in Figure 2.17 is from well L-08. Row (1) column (a) shows actual Vs and Castagna Vs (derived from Castagna's mudrock relationship) versus depth. Row (1) column (b) shows actual Vs and Castagna Vs (derived from Castagna's limestone relationship) versus depth. Row (1) column (c) shows actual Vs and Castagna Vs (derived from Pickett's relationship) versus depth.

Row (2) column (a) is a closer look at the Petrel Formation, actual Vs and Castagna Vs (derived from Castagna's mudrock relationship) versus depth. Row (2) column (b) is a closer look at the Petrel Formation, actual Vs and Castagna Vs (derived from Castagna's limestone relationship) versus depth. Row (2) column (c) is

a closer look to the Petrel Formation, actual Vs and Castagna Vs (derived from Pickett's relationship) versus depth.

Row (3) column (a) is a closer look at the Eastern Shoals Formation, actual Vs and Castagna Vs (derived from Castagna's mudrock relationship) versus depth. Row (3) column (b) is a closer look at the Eastern Shoals Formation, actual Vs and Castagna Vs (derived from Castagna's limestone relationship) versus depth. Row (3) column (c) provides a closer look at the Eastern Shoals Formation, actual Vs and Castagna Vs (derived from Pickett's relationship) versus depth.

Vs derived from	Thickness (m)	RMS error \pm (m/s)		
		Mudrock relationship	Castagna's limestone relationship	Pickett's relationship
All Formations	2382.77	145.00 ✖	182.18	276.06
Petrel	138.50	288.96	147.70	115.56 ✖
Eastern Shoals	20.33	466.01	127.21 ✖	150.75

Table 2.10: RMS analysis for the different Vs curves obtained from well H-20. The RMS values accord to the relationship used to derive Vs. Key: ✖ indicates good RMS results.

Table 2.11, shows the RMS values for the entire well L-08, and also the carbonate Formations present in the well (Petrel and Eastern Shoals). The best result for the entire well uses Castagna's mudrock equation. For the Petrel Formation and the Eastern Shoals Formation, Castagna's limestone relationship gives a better result than Pickett's relationship.

Vs derived from	Thickness (m)	RMS error \pm (m/s)		
		Mudrock relationship	Castagna's limestone relationship	Pickett's relationship
All Formations	2293.25	107.31 ✖	175.83	305.48
Petrel	148.88	152.48	51.89 ✖	165.86
Eastern Shoals	21	509.05	162.75 ✖	688.58

Table 2.11: RMS analysis for the different Vs curves obtained in well L-08. The RMS values accord to the relationship used to derive Vs. Key: ✖ indicates good RMS results

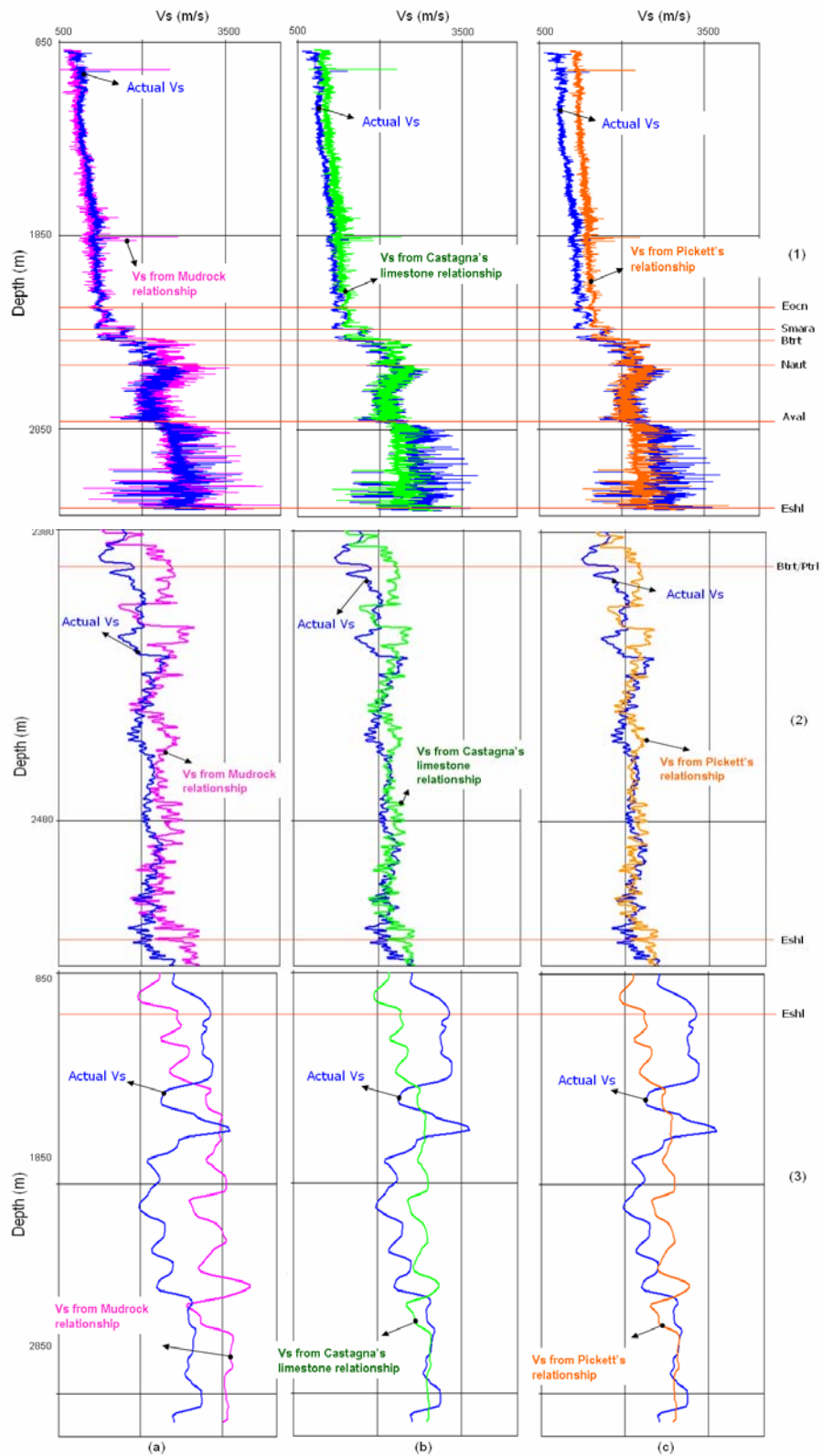


Figure 2.16: Data from well H-20. The details of the Figure are explained in page 40.

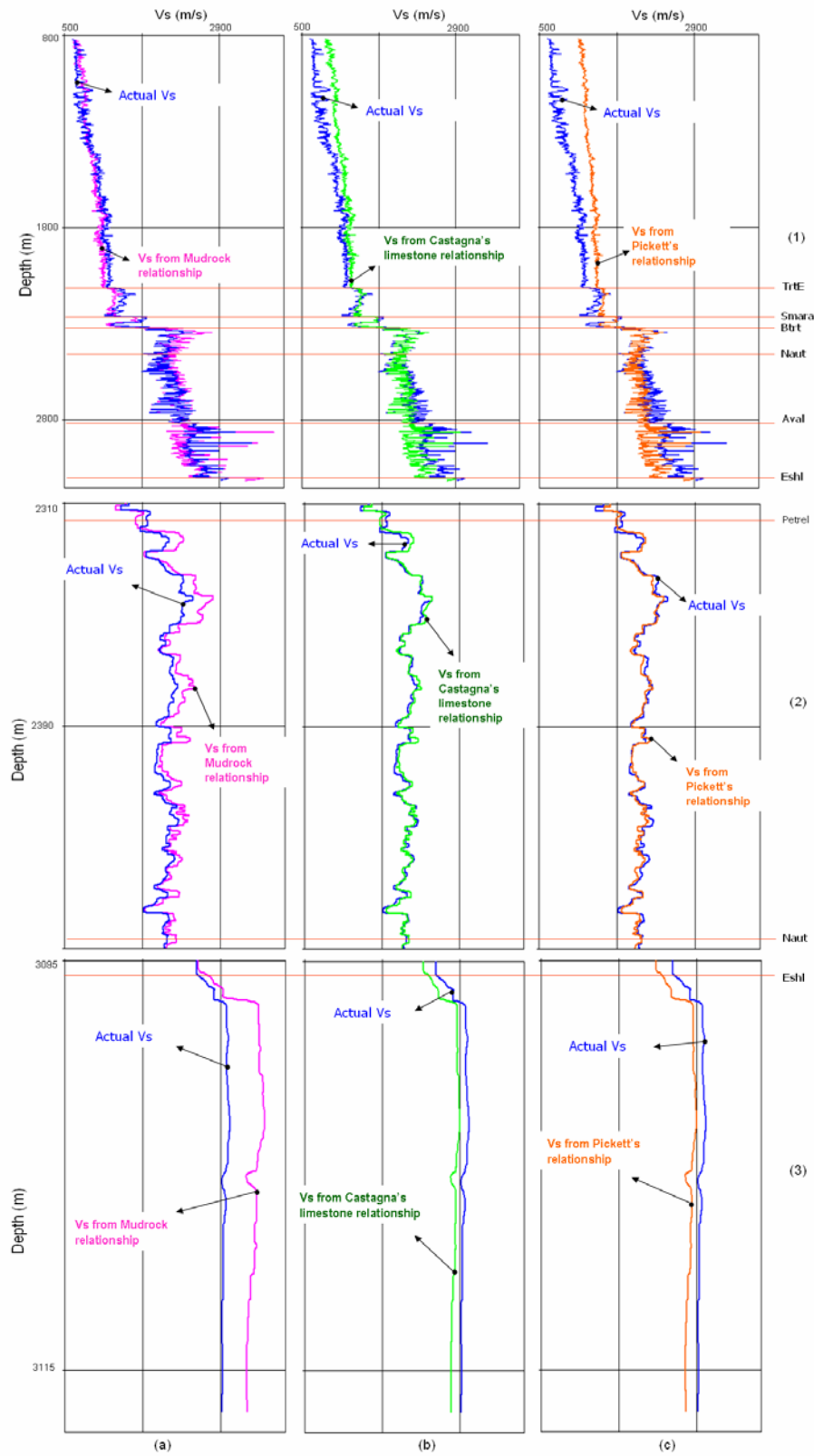


Figure 2.17: Data from well L-08. The details of the Figure are explained in page 41.

2.2.7 Actual Vp, Actual Vs, Actual Vp/Vs versus GR

The gamma ray results on the wells show a common trend for the corresponding lithology. As we go from shales and limestones into sandstones, the velocities increase. Figure 2.18 shows this general trend on the different wells within the Nautilus and Avalon Formations.

It can be observed from Table 2.12 that the Tertiary Formation and the Fortune Bay Formation have lower Vp values (1100–2300 m/s) than the other Formations displayed in the table. The Cretaceous rocks have a high range of Vp values (3900–6200 m/s).

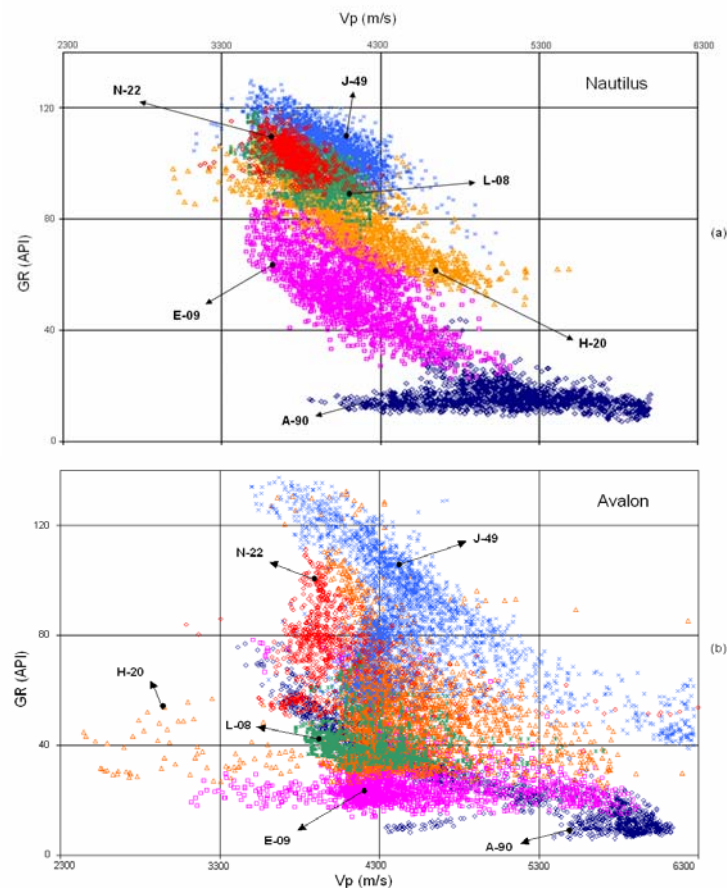


Figure 2.18: Panel (a) — GR versus actual Vp for the Nautilus Formation in each well from the area. Panel (b) — GR versus actual Vp for the Avalon Formation in each well from the area. In general, as the Formations (Avalon and Nautilus) grade upward from siltstone into sandstone, the velocity increases.

In Figure 2.19, wells H-20 and L-08 have similar velocity ranges. The GR trend is reacting to lithology. The general behaviour of the well is for the Tertiary Formation to have increasing Vp with a constant range of GR values. The Nautilus Formation tends to have decreasing GR values with increasing Vp values. The Avalon Formation has a variable range of GR values (in H-20, the values range from 28–129 and on L-08 from 31–71) that decrease as the P velocity increases.

Formation	Lithology	GR (API)	Vp (m/s)
Tertiary	Shale	20–140	1100–3500
South Mara	Sandstone-siltstone	28–128	2700–4800
Wyandot	Chalk	11–111	2900–5800
Dawson Canyon	Sandstone-shale	53–99	3100–3900
Petrel Member	Limestone	53–136	2600–4500
Nautilus	Shale-mudstone	22–129	3300–5000
Avalon	Sandstone-shale	6–137	2500–6200
Eastern Shoals	Calcareous sandstone-siltstone	7–126	3200–6000
White Rose	Shale	44–136	3500–5400
Hibernia	Sandstone-shale	6–135	3200–5600
Lower Hibernia	Sandstone	53–141	3400–5300
Fortune Bay	Shale-siltstone- sandstone	40–121	2300–4400
Jeanne d'Arc	Sandstone-shale	13–160	2900–5700
Rankin	Limestone	31–110	2800–5400
Voyager	Sandstone-shale-limestone	80–118	4000–5100

Table 2.12: General behaviour of GR versus Vp for each Formation on each well.

The variability of the GR, Vp, and Vs in the Avalon Formation could be indicative of porosity and shale content. This knowledge might have an impact on how the interface between the Nautilus and the Avalon is identified on the seismic data.

Table 2.13 shows the values for each lithologic Formation in the H-20 and L-08 wells. In Figure 2.20, one can observe a general trend on both wells in the Vp/Vs versus GR relationship: Vp/Vs increases with increasing GR values. Over the entire wells, the general trends have a decrease in Vp/Vs as depth increases (Avalon and Eastern Shoals Formations). The GR values for the wells show a trend with different lithologies. The Vp/Vs values also correspond to changes in lithology. High Vp/Vs values (3.5–4.0) are related to the Tertiary Formation (shallow rocks), which correlate with high GR values (60–130, Banquereau shales). As the depth increases,

the GR values decrease (going from shales-limestones-sandstones) and Vp/Vs decreases. Probably mostly due to lithology, age, and compaction/pressure.

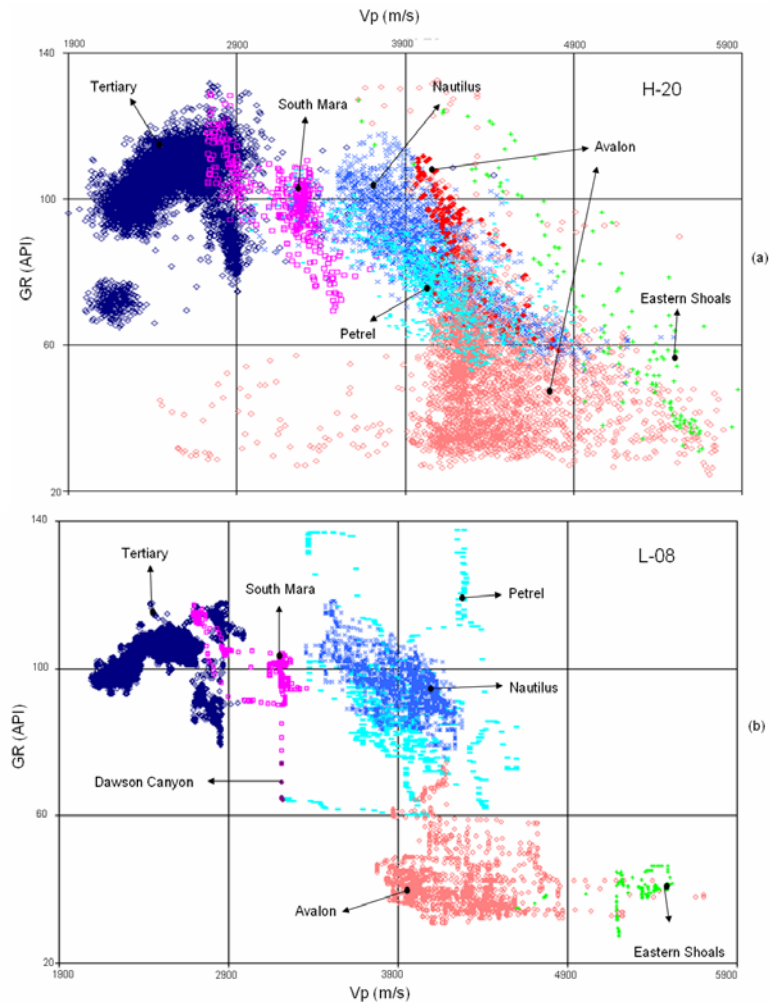


Figure 2.19: Panel (a) — GR versus actual Vp for well H-20. Panel (b) — GR versus actual Vp for well L-08. As the Formations upgrade from siltstones to sandstones, the velocities increase. Both wells exhibit similar, general trends for each Formation. Both of these wells are located on the South Avalon Pool.

In general (as shown in Figure 2.20, and Table 2.13), the Vp/Vs values decrease with depth and the GR values depend on lithology. If we compare the Nautilus and Avalon GR and Vp/Vs values, we notice that the GR values for the Nautilus shales have a range of 60–120 and for the Avalon Formation 22–137. Their Vp/Vs values are also similar to each other (1.59–2.06 versus 1.52–2.00). These different ranges overlay each other and therefore could make it difficult to distinguish between the two lithologies based exclusively on Vp/Vs and GR.

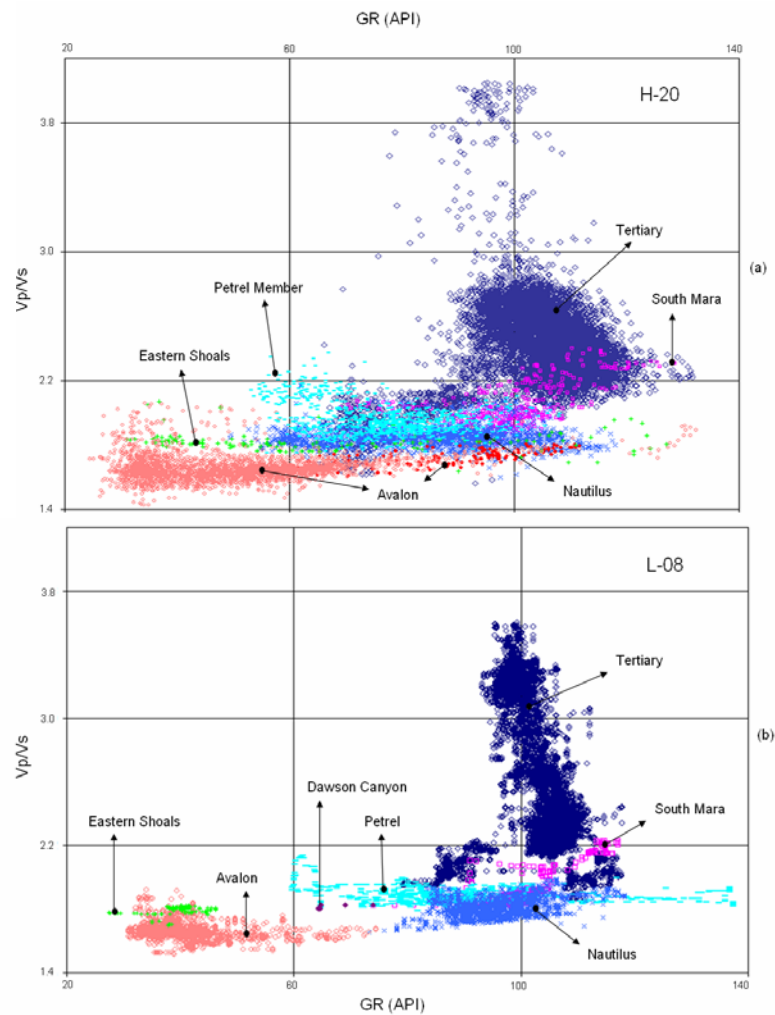


Figure 2.20: Panel (a) — V_p/V_s versus GR for well H-20. Panel (b) — V_p/V_s versus GR for well L-08. Note that the Tertiary Formation keeps a siltstone range of values as the well goes deeper. The differentiation of Formations is noticeable. In both wells, the relationships behave quite similarly: as V_p/V_s decreases, GR decreases.

Formation	H-20		L-08	
	GR (API)	V_p/V_s	GR (API)	V_p/V_s
Tertiary	65–130	1.63–4.00	84–117	1.84–3.59
South Mara	62–120	1.79–2.29	90–116	1.81–2.21
Petrel Member	54–107	1.77–2.33	60–140	1.81–2.23
Nautilus	58–117	1.59–2.06	78–117	1.67–1.98
Avalon	28–129	1.51–2.00	31–71	1.52–1.91
Eastern Shoals	30–117	1.76–1.84	32–46	1.70–1.81

Table 2.13: General trend of GR versus V_p/V_s for each Formation.

2.2.8 Actual ρ versus ρ from Gardner's relationship using V_p

In using Gardner's equation (Equation 2.7), ρ (density in kg/m^3) can be derived from V_p and Gardner's constants, a and m . Gardner et al. (1974) gives values for a and m of 310 and 0.25, respectively. This section compares the predicted ρ from Gardner's equation with actual ρ values. We apply this relationship to all well data where a ρ log was acquired.

$$\rho = a\alpha^m, \quad (2.7)$$

where: ρ Density (kg/m^3)
 a Constant of 310
 α Compressional velocity (m/s)
 m Constant of 0.25

Faust (1953) concludes that, in general, velocity and density will increase with depth and the age of formations. Gardner et al. (1974) state that consecutively deeper layers may vary significantly in composition and porosity with additional marked local changes in velocity and density that will end the gradual increase of velocity and density with depth. In our study, we experienced this situation, which is why we approached the relationship in a different way, using a constant per formation, as explained in Appendix B.

Well A-90 did not have a density log. For wells E-09 (Figure 2.21) and well H-20 (Figure 2.22, Panel (a)), where the ρ prediction was done for the section of the well where ρ was acquired, Wells J-49, L-08 (Figure 2.22, Panel (b)), and N-22, Gardner's equation had difficulties predicting ρ using 310 as constant. There is significant scatter in the data. In this case, the wells were segmented into different Formations for a better approach to the relationship. The constants used and the results for each Formation are in Appendix B.

To derive a new and more suitable constant per well, we derived the constant from the actual density value and the function from Gardner's equation ($a\alpha^m$). With these new constants we were able to fit the data (Table 2.14). Also, with the help of the RMS error values we were able to corroborate where the relationship worked better.

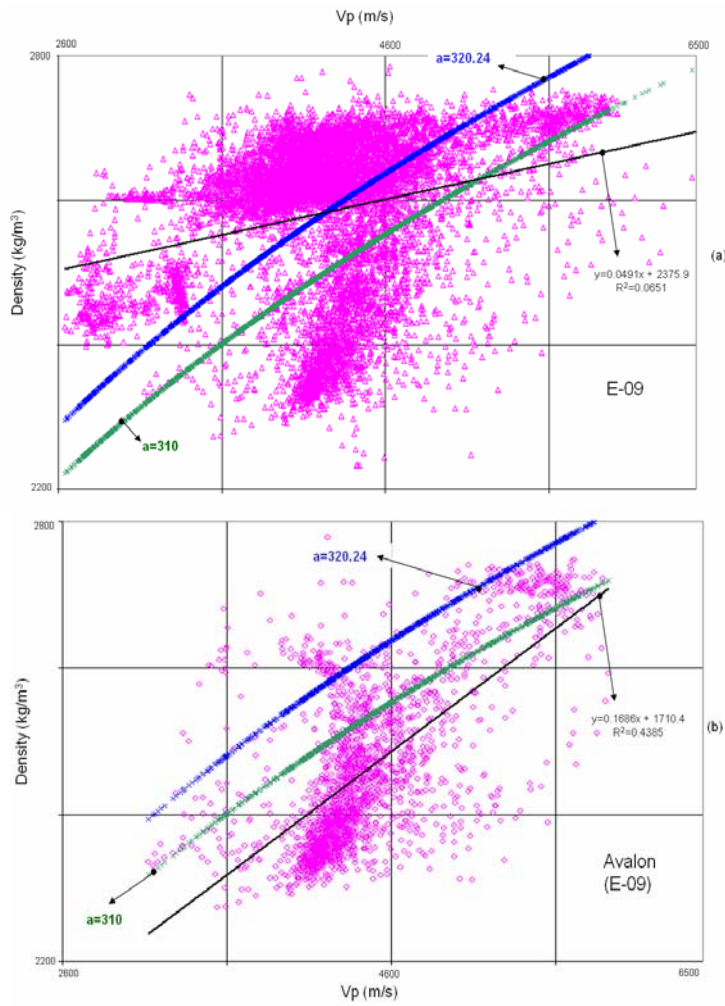


Figure 2.21: Data from the Avalon Formation from well E-09. Panel (a) — actual Vp versus actual ρ and Gardner ρ , data from well E-09. Panel (b) — actual Vp versus actual ρ and Gardner ρ . The Avalon fits better to the relationship than the other Formations.

Well	Gardner Constant	RMS error \pm (m/s)	Constants derived	RMS error \pm (m/s)
E-09	310	144.61	320.24	118.64 ✖
H-20	310	58.79	310.14	58.79
J-49	310	247.06	314.80	244.21 ✖
L-08	310	112.25	319.31	88.65 ✖
N-22	310	124.41	318.76	104.61 ✖

Table 2.14: Constants used to predict ρ from Vp using Gardner's relationship for all wells. The RMS from using Gardner's constant and the RMS error from using the derived constant gives the accuracy of the derived constant. The derived constant is per well. Key: ✖ indicates good RMS results

The RMS error values (Table 2.14) show that the best results use the derived constant. For well H-20 (Figure 2.22, Panel (a)), using both Gardner's constant and the derived constant give similar results and RMS error values of ± 58.79 m/s.

As shown for well L-08 in Figure 2.22, Panel (b), Gardner's rule has difficulty predicting ρ . There are three clusters in the data. However, the RMS error values (Table 2.14) are considered reasonable.

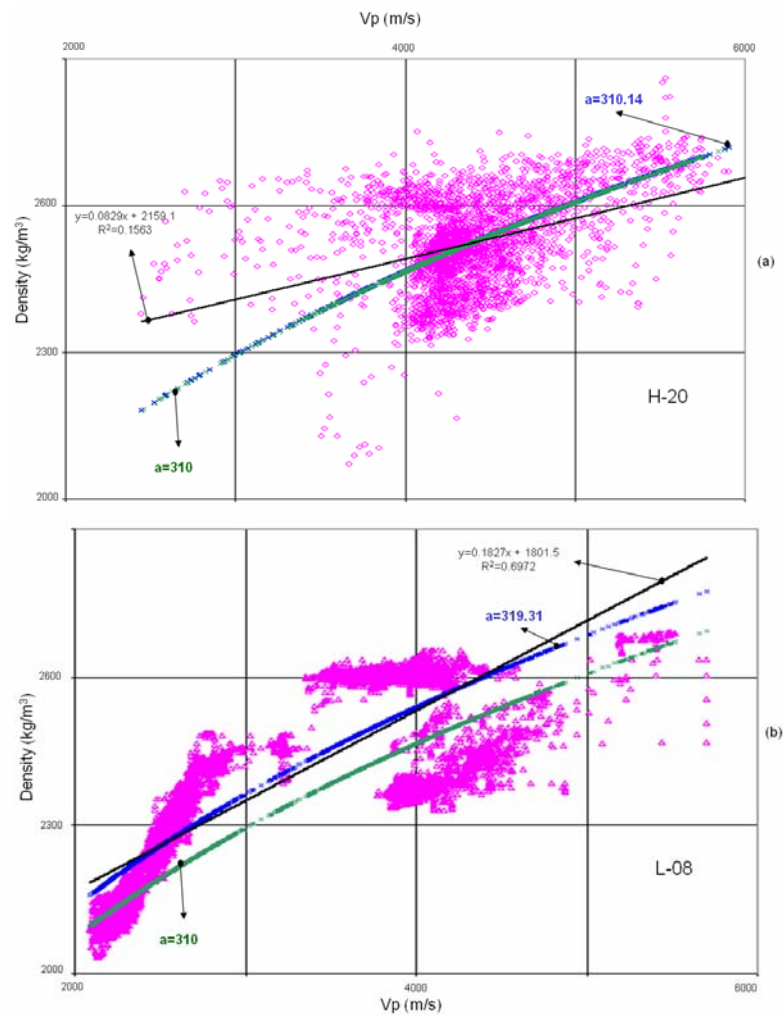


Figure 2.22: Panel (a) — actual ρ and Gardner's ρ versus actual Vp for well H-20 (2772–3271 m). Panel (b) — actual ρ and Gardner's ρ versus actual Vp for well L-08.

Gardner's rule was applied to the bottom section (2772–3271 m) of well H-20 where the values of ρ and P velocity were acquired (Figure 2.23). The upper part of well H-20 (2772 m to 824 m), was set to be constant at a value of 2642 kg/m^3 . In Figure 2.24, a trend was determined between Vp and ρ . Gardner's equation,

assumes clastics rocks. The linear fit gives a poor correlation coefficient of 0.15% and there is considerable density scatter (clastics and carbonates units). This percentage occurs both on the trend of the results from Gardner's rule and the trend of the best fit line (Figure 2.24). The predicted values from Gardner's equation show an reasonable fit with the actual data using $a=310$. The RMS error value for this constant is $\pm 58.79 \text{ kg/m}^3$. For example, as shown in Figure 2.21, we determined that using a Gardner's constant $a=320.24$ gives a better fit to the data from well E-09. In Figure 2.21, note the different trend line slopes when using $a=310$ and $a=320.24$. As shown in Figure 2.24, the predicted density values using Gardner's equation were expected to be better. The predicted density results from well L-08 were lower in magnitude than the actual values (Figure 2.25).

According to Castagna et al. (1993), the use of Gardner's equation has a tendency to overvalue the density for sandstones and undervalue the density for shales. Our results show a different trend. The shales tend to have an underestimation in the density values like Castagna's, but the density of the sandstones do not have a general trend. From the five wells that were analyzed (E-09, H-20, J-49, L08, and N-22), six Formations were treated as sandstones (South Mara, Avalon, Eastern Shoals, Hibernia, Lower Hibernia, and Jeanne d'Arc). It is important to remember that these Formations are not an absolute package of sandstones; we can find shales, limestones, and siltstones within these Formations. This variation in lithology within the "sandstone Formations" and also porosity should explain why the final density results do not show a general trend (the values are undervalued and overvalued for this group of rocks). The final Castagna's results came from the Gulf of Mexico and not Eastern Canada. This may be a reason why the results were fair. The presence of carbonates could also mislead the predicted values.

As was noted at the beginning of the section, the velocity and density properties depend on different factors. In Appendix B, the analysis by breaking down the wells into their main Formations, we can conclude that the results were reasonable. Also the results after using a constant per Tertiary Formations and one for the Cretaceous Formations were also quite similar. The results should be taken with sufficient caution, keeping in mind the different lithologies that are involved in

the analysis.

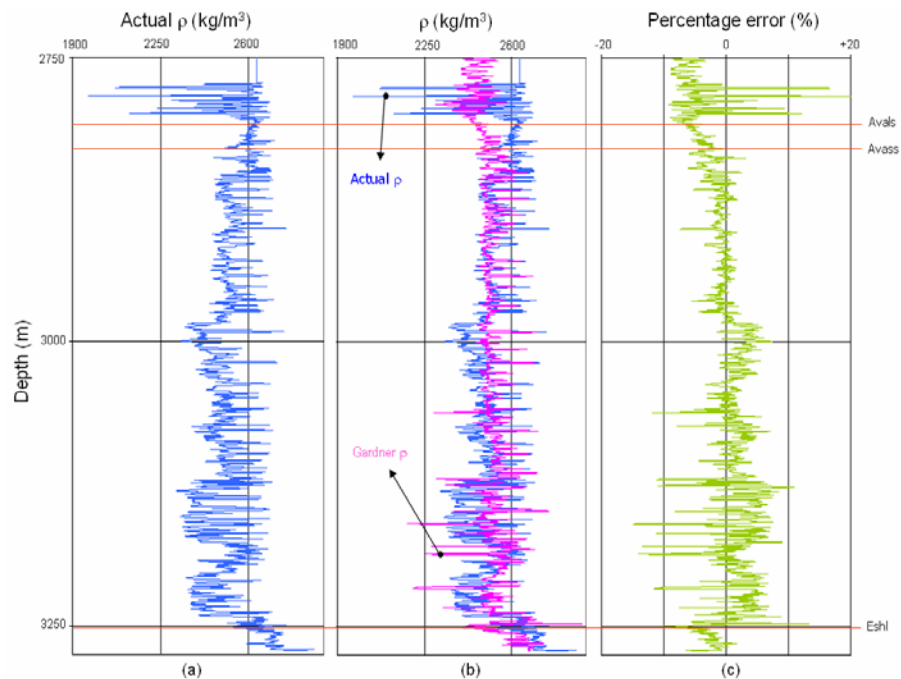


Figure 2.23: Panel (a) — Actual ρ versus depth. Panel (b) — actual ρ and Gardner ρ (derived using Gardner constant). The RMS error is $\pm 58.79 \text{ kg/m}^3$. Panel (c) — percentage error between these two ρ versus depth. The data is from the bottom of well H-20 showing the Avalon and Eastern Shoals Formations.

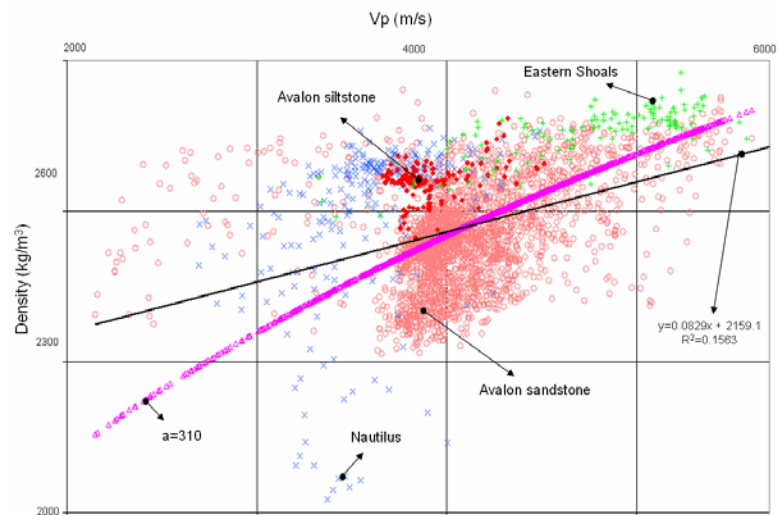


Figure 2.24: Density versus velocity, crossplot for well H-20. Actual ρ and velocity values versus the ρ predicted from Gardner's rule. The field values are for the bottom section of the well (from 2772 m to 3271 m), where actual ρ was acquired.

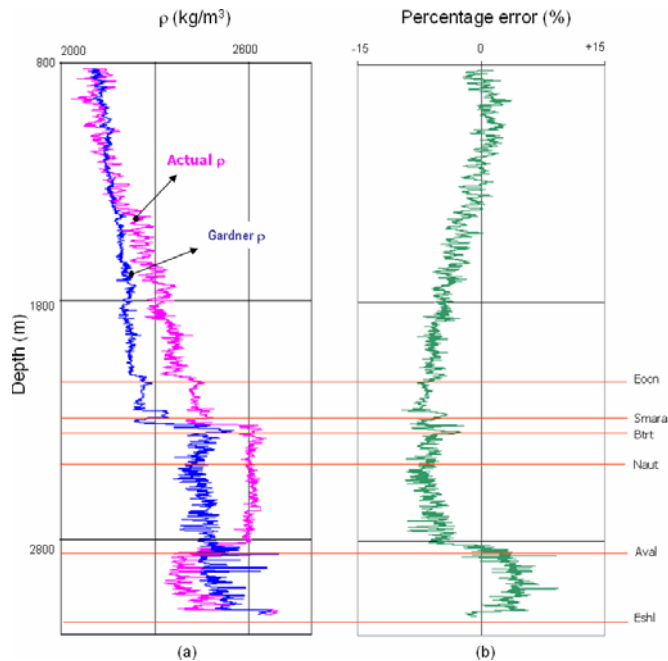


Figure 2.25: Data from well L-08. Panel (a) — actual ρ , and Gardner ρ (derived using V_p and a 310 constant) versus depth. Panel (b) — percentage error between these two ρ .

2.2.9 Actual ρ versus ρ from Gardner's relationship using V_s

We evaluated the prediction of ρ using V_s . This new approach (Equation 2.8) is based on Gardner et al.'s equation (1974), (Equation 2.7). This section compares the predicted ρ from Equation 2.8 with the actual ρ value. We performed this comparison for all the data on well L-08 and for the data from the bottom section of well H-20 (2272–3271 m).

$$\rho = aV_s^m, \quad (2.8)$$

where: ρ Density (kg/m^3)
 a Constant of 350 or derived constant
 V_s Shear velocity (m/s)
 m Constant of 0.25

As $V_s < V_p$, we expected the new constants to be higher. A constant of $a = 350$ was used with well H-20 (RMS error $\pm 70.57 \text{ kg/m}^3$), and with well L-08 (RMS error $\pm 261.76 \text{ kg/m}^3$), which is different from Gardner's original relationship. Deriving the constant, we found that well H-20 has a similar 350 constant (352.73), and well L-08 uses a 386.02 constant (Table 2.15) and Figures 2.26 and 2.27. The exponent

$m = 0.25$ was used (Figure 2.26), and the results for the entire wells were marginal (Figure 2.27). In this case, to improve the results we segmented the well data into lithological Formations and used a different constant per Formation (Appendix B). This segmentation of the data was also done in evaluating the V_p to ρ relationships. Even though we used different constants for each Formation, the outcome was fair.

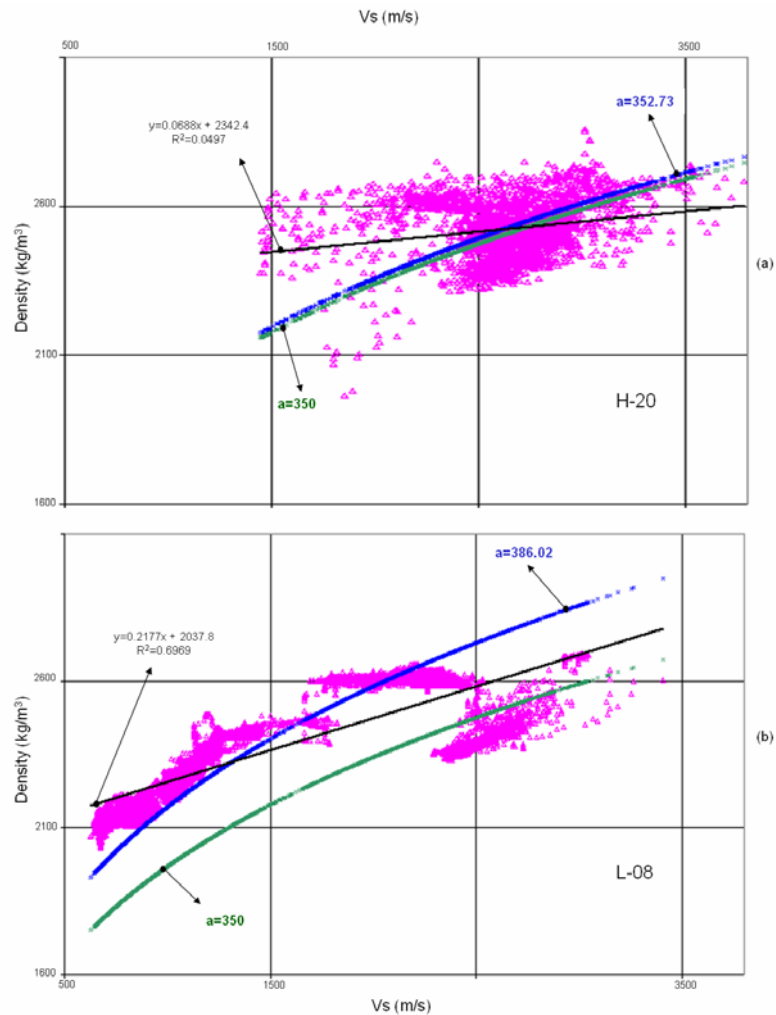


Figure 2.26: Panel (a) — actual ρ versus Gardner ρ (derived using V_s and $a=350$ and 352.73 derived constant) for well H-20. Panel (b) — actual ρ versus Gardner ρ (derived using V_s and $a=350$ and 386.02 derived constant) for well L-08.

Velocity and density properties depend on different factors, including type of rock, porosity, mineral composition, and fluid properties. These factors in turn are affected by overburden pressure, fluid pressure, microcracks, age, and depth of burial (Gardner, 1974). This could explain why the poor results using V_s to derive ρ

with a constant of 350. That is why, after our analysis breaking down the wells into their main Formations, we can conclude that we have reasonable results (Appendix B). For well H-20 the results after using the 310 constant are reasonable. To derive ρ from Vs, for well H-20 we used a constant of 352.73 and for well L-08 a constant of 386.02 (Table 2.15).

Well	Gardner Constant	RMS error \pm (m/s)	Constants derived	RMS error \pm (m/s)
H-20	350	70.57	352.73	69.47 ✖
L-08	350	261.76	386.02	141.59 ✖

Table 2.15: Constants used to predict ρ from Vs using Gardner’s relationship for wells H-20 and L-08. The RMS from using Gardner’s constant and the RMS error from using the derived constant give the accuracy of the derived constant. The derived constant is per well. Key: ✖ indicates good RMS results.

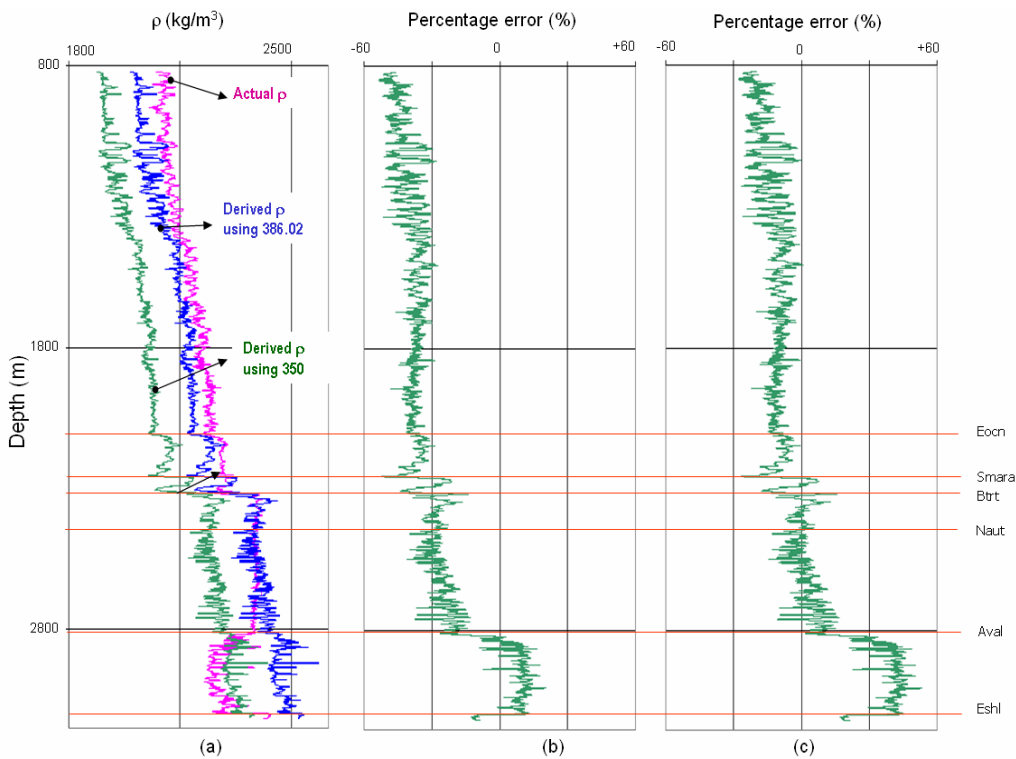


Figure 2.27: Data from well L-08. Panel (a) — actual ρ and Gardner ρ (derived using Vs and $a=350$ and 386.02 derived constant) versus depth. Panel (b) — percentage error between actual ρ and Gardner ρ (derived using 350 as the constant) versus depth. The RMS error is ± 261.76 kg/m³. Panel (c) — percentage error between actual ρ and Gardner ρ (derived using 386.02 as the constant) versus depth. The RMS error is ± 141.59 kg/m³.

2.2.10 Vp, Vs from Gardner relationship using ρ

Since Gardner's rule (Equation 2.7) has some predictive value, we explored the possibility of predicting Vp and Vs as a function of ρ . This analysis is based on Gardner's (1974) work. The "Vp Gardner relationship" (Equation 2.9) was used to predict compressional velocities, given ρ . For this case, we based our analysis on the results obtained from the previous section where we derived ρ from Vp and Vs. The constants used in this analysis are the same constants used in the previous section (Tables 2.13 and 2.14). The constant a was changed and $m=0.25$ was kept the same. We explored the use of the relationship (Equation 2.9) in wells E-09, H-20, J-49, L-08, and N-22. Well A-90 did not have ρ log to work with.

$$V_p = 10^{\frac{\log \rho - \log a}{m}}, \quad (2.9)$$

where: V_p Compressional velocity (m/s)
 ρ Density (kg/m³)
 a Constant 310 or derived constant
 m Constant 0.25

After deriving Vp from Gardner's relationship, the results were favourable in some parts of the wells (Figures 2.28 and 2.29), and overall the results were fair for the five wells. The highest RMS error value for Vp is on well J-49 (± 1056.81 m/s). However, this value is better than the RMS error from the constant 310 (± 1223.84 m/s). Each well has its own constant which are different from the 310 constant used in the previous relationship where we derived ρ from Vp. We cannot compare the results between wells due to the different sections involved in the study (Table 2.16).

The "Vs Gardner relationship" can be used to predict Vs velocities, given ρ (Equation 2.10). In this case, the results were not as good as expected in most parts of the wells (Figures 2.29 and 2.30). The constants were $a=350$ for well H-20 and well L-08 and m was kept as 0.25.

$$V_s = 10^{\frac{\log \rho - \log a}{m}}, \quad (2.10)$$

where: V_s Shear velocity (m/s)
 ρ Density (kg/m^3)
 a Constant 350 or derived constant
 m Constant 0.25

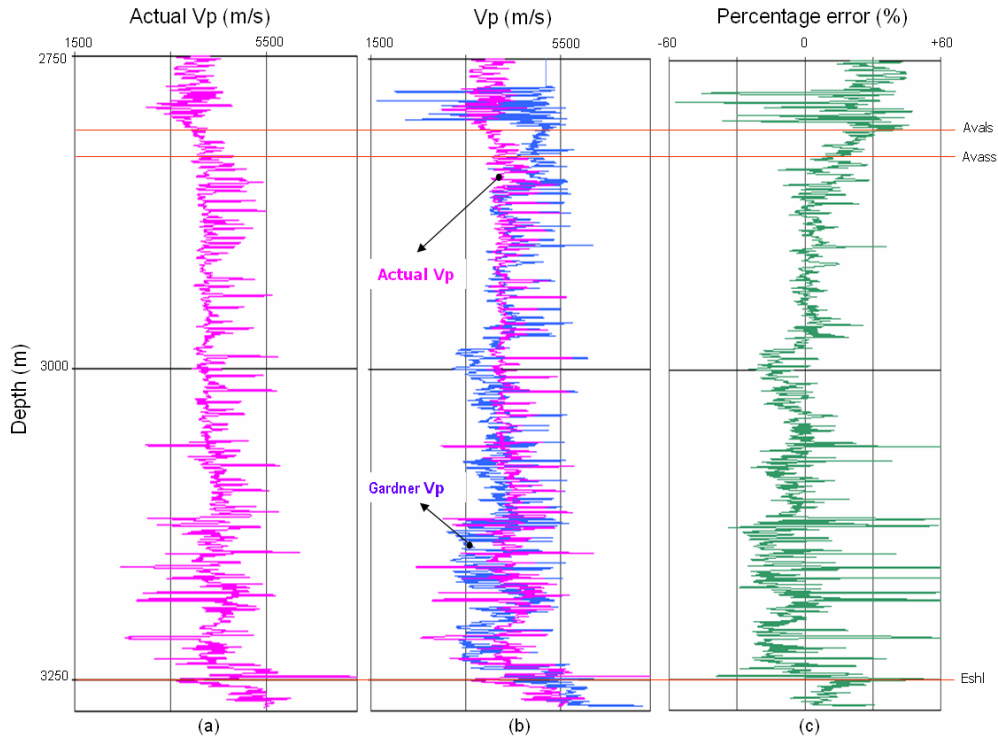


Figure 2.28: Data from well H-20 showing the Avalon Formation. Panel (a) — actual Vp versus depth. Panel (b) — actual Vp and Gardner Vp (derived using a constant of 310) versus depth. Panel (c) — percentage error between these two Vp curves versus depth.

Well	Total Well (m)	Section analyzed (m)
E-09	3178.00	1620.01
H-20	2447.54	504.74
J-49	3871.72	3068.88
L-08	2293.25	2293.25
N-22	3669.94	3669.94

Table 2.16: Total depth of the wells with the depth of the section that was analyzed.

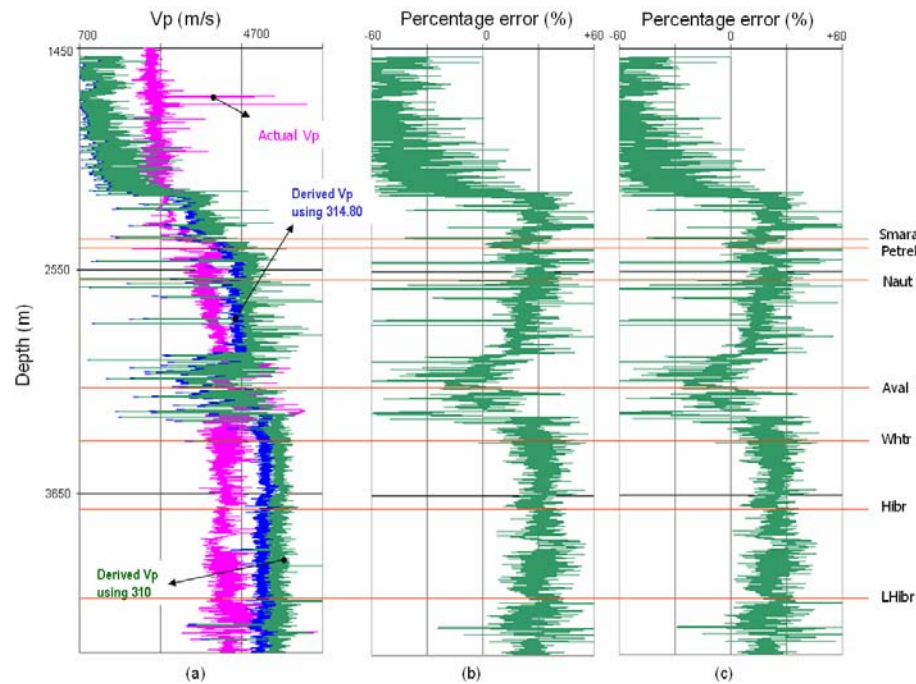


Figure 2.29: Data from well J-49. Panel (a) — actual Vp and Gardner Vp (derived from ρ using constants of 310 and 314.80) versus depth. Panel (b) — percentage error between actual ρ and Gardner ρ (derived using 310 as the constant) versus depth. The RMS error is ± 1223.84 m/s. Panel (c) — percentage error between actual Vp and Gardner Vp (derived using 314.80 as the constant) versus depth. The RMS error is ± 1056.81 m/s.

For the Vs analysis in wells H-20 and L-08, the best results are observed in well H-20 where we used a derived constant of 352.73; the correlation was applied to the bottom part of the well where we had ρ data (Table 2.16). As we see on Table 2.16, the section explored in well H-20 was 504.74 m of 2447.54 m and in well L-08, 2293.25 m (that is, the entire well). With this large difference of sections, it is very difficult to imply that one RMS is better than the other. What we can say is that the RMS obtained on both wells in the Vs analysis gave better results than the RMS obtained in the Vp analysis (Table 2.17).

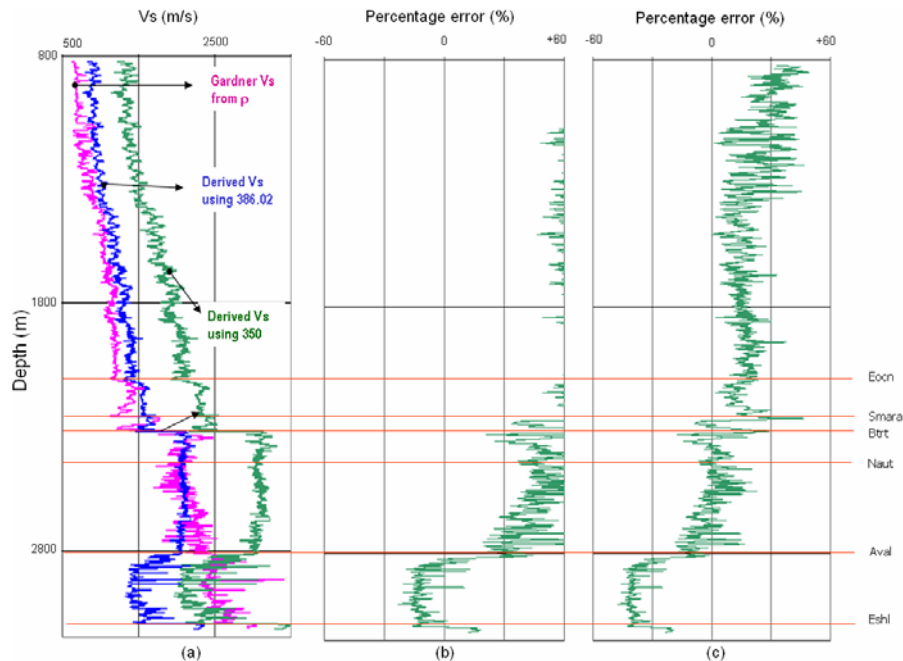


Figure 2.30: Data from well L-08. Panel (a) — actual Vs and Gardner Vs (derived using constants of 350 and 386.02) versus depth. Panel (b) percentage error between actual Vs and Gardner Vs (derived using 350 as the constant) versus depth. The RMS error is ± 760.15 m/s. Panel (c) percentage error between actual Vs and Gardner Vs (derived using 386.02 as the constant) versus depth. The RMS error is ± 395.97 m/s.

Well	Vp from Gardner				Vs from Gardner			
	Gardner Constant	RMS \pm (m/s)	Derived Constants	RMS \pm (m/s)	Gardner Constant	RMS \pm (m/s)	Derived Constants	RMS \pm (m/s)
E-09	310	1021.28	320.24	742.68	♦	♦	♦	♦
H-20	310	477.82	310.14	476.87	350	350.96	352.73	336.05 ✱
J-49	310	1223.84	314.80	1056.81	♦	♦	♦	♦
L-08	310	693.11	319.31	495.15	350	760.15	386.02	395.97 ✱
N-22	310	1020.77	318.76	717.04	♦	♦	♦	♦

Table 2.17: Constants used in approaching Vp and Vs from Gardner's relationship using density. The RMS value shows the root mean square error between the new relationship and the original values. Key: ♦ Data was not acquired on this well; ✱ Good RMS results.

2.2.11 Vp, Vs, Vp/Vs versus ϕ_D

To better understand the area of interest (Avalon sandstone), we need to know more about the lithology and ϕ of the area. Our first requirement is to know the bulk density of the formation. The bulk density is a function of the density of the minerals (matrix) and the volume (porosity) of the free fluids (Rider, 2002).

The density log measures the bulk density changes in the subsurface formations. The density tool uses a focused radioactive source and two detectors. The source emits high-energy gamma rays into the formation. Some of the gamma rays collide with atoms of the formation material and the energy is progressively absorbed. The collision between the gamma rays and the electrons (dislodged from the atoms) produce a loss of energy and scatter in all directions. This reaction is Compton scattering and depends only on the electron density of the formation. The electron density is correlated to bulk density. This is the basic concept of the standard density measurement (Dewan, 1983). Dense formations have a strong attenuation, meaning that only a small amount of gamma rays travel back to the tool's detectors. Formations of lower density allow a higher number of gamma rays to reach the tool's detectors and be recorded (Hilchie, 1982a).

Density porosity or ϕ_D is derived using the bulk density (Equation 2.11). In this study, Equation 2.12 was used.

The rock type must be known before porosity can be determined from the density. The density of the matrix of sandstone and limestone is 2650 kg/m^3 and 2710 kg/m^3 , respectively. The density of the fluid is 1000 kg/m^3 for fresh water (Hilchie, 1982b).

For example, when we are using density-porosity (ϕ_D) in a sandstone matrix, we are referring to the transformation of bulk density into ϕ_D using a value of 2650 kg/m^3 (Equation 2.12). For limestone formations (Eastern Shoals), a limestone matrix was used to derive porosity. On the other hand, for formations with lithologies known to be sandstone (Avalon Formation), a sandstone matrix was used to derive porosity.

$$\rho_b = \phi \cdot \rho_f + (1 - \phi) \rho_m ; \quad (2.11)$$

$$\phi_D = \frac{\rho_m - \rho_b}{\rho_m - \rho_f} , \quad (2.12)$$

where: ϕ_D Density-porosity
 ρ_m Density of the matrix, zero porosity (kg/m^3)
 ρ_f Density of the fluid (kg/m^3)
 ρ_b Bulk density, or density log reading (kg/m^3)

In the case of a sandstone matrix (Figure 2.31), the total porosity increases as the velocity decreases. The Avalon Formation shows a pattern with a linear regression of $y = -6846x + 5214.3$, $R^2 = 0.5792$. In the shallow part of the well, there is some data that does not exhibit the same behaviour as the Banquereau shale (Tertiary Formation). This could be due to problems with log measurements through the casing. The Nautilus shale behaves somewhat differently from the Banquereau shale (Tertiary Formation) but still shows a general trend.

As we go from shallow and porous Formations (Tertiary and South Mara), the velocity starts to increase and the porosity starts to decrease (Nautilus and Avalon). The Avalon shows the porous part (sandstone) and the siltstone part (nonporous section) that could be related to the negative porosity values present. Also the negative values could be indicative of calcite lime in the matrix (2710 kg/m^3).

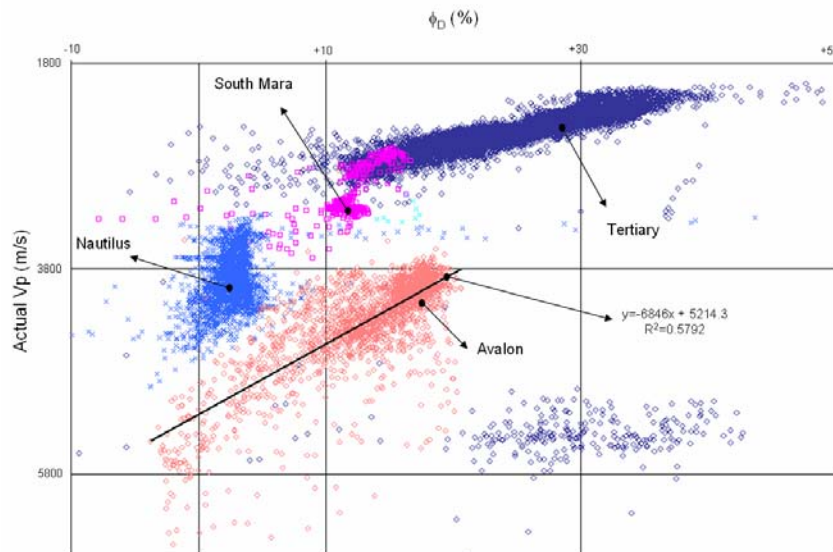


Figure 2.31: Well L-08 Vp versus ϕ_D , assuming a sandstone matrix.

In the case where the matrix was limestone (Figure 2.32), the behaviour was similar to the ϕ_D value derived using a sandstone matrix. Dawson Canyon Formation (calcareous shale) has a high ϕ_D percentage with low Vp, but we can not rely on this result because of insufficient data. The Petrel Member (limestone) shows a range of porosity of 1 to 10%. The porosity decreases as P velocity increases. Also there are some high porosity values up to 20%, but the lack of sufficient data in this area make

it impossible to rely in this value. The Eastern Shoals (calcareous sandstone-siltstone) data show that as we progress deeper in the well, the porosity becomes less than 5% and we find higher velocities; the lack of high porosity could be due to compaction of the rock.

Petrel Member and Eastern Shoals Formation have a linear regression of $y = -9470.4x + 4487.3$ $R^2 = 0.3991$ and, $y = -6673.9x + 5430.9$ $R^2 = 0.6135$, respectively (Figure 2.32). In general, the P velocity decreases with increasing porosity.

The ϕ_D relationship for Vs is derived in the same manner as for Vp (see Equation 2.12). In this case there is not enough data to work with; we do not have data for the Tertiary and the South Mara Formation, but we can still gain a general idea of the trend of this relationship. We have a section of the Nautilus and the entire Avalon Formation. In the analysis for the sandstone matrix case, the total porosity increases as the velocity decreases. The Avalon formation shows a pattern with a linear regression for $y = -3989.8x + 3118.8$, $R^2 = 0.6854$. The Nautilus formation exhibits a trend, but still has lower velocity with general porosity values up to 5%. As we observed on the Vs plots, there are some negative porosity values. These may be indicative of calcite lime in the matrix (2710 kg/m^3).

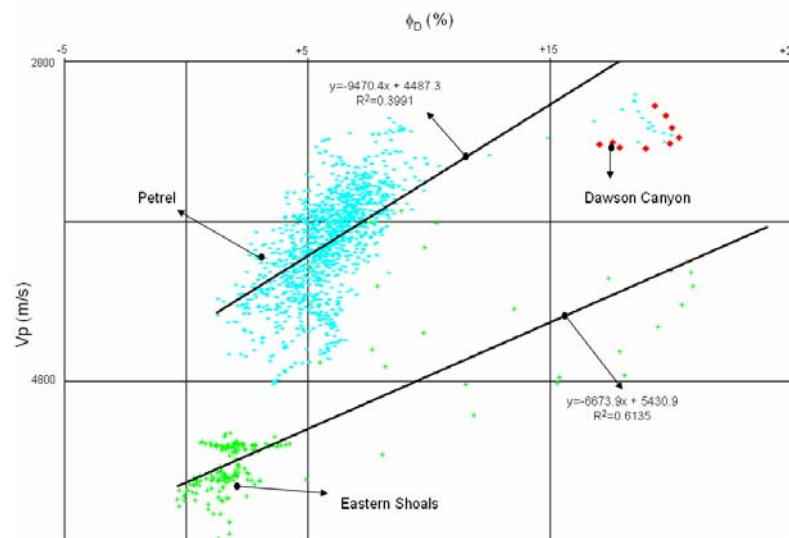


Figure 2.32: Well L-08 Vp versus ϕ_D , assuming a limestone matrix.

In the sandstone and limestone matrix case, the behaviour of the data is similar for the Vp data. The data show a linear regression where $y = -3066.7x + 3011.9$, $R^2 = 0.534$. In general, the Vs velocity decreases with increasing porosity.

This analysis was done in the section of the Nautilus and Avalon Formations with a sandstone matrix. For similar lithologies, the Vp/Vs is either unchanged or slightly increases with porosity. For limestone, there was no data to work with. However, the Nautilus shale shows a slight increase in Vp/Vs when porosity increases. This could be caused by the presence of bound water on the formation. In Figure 2.33 (sandstone matrix), the linear regression shows $y = -0.0716x + 1.6726$, $R^2 = 0.0019$. The trend in the limestone matrix is $y = -0.6557x + 1.7891$, $R^2 = 0.2159$. The Avalon Formation shows a range of Vp/Vs between 1.51-2.03. On a limestone matrix, the Eastern Shoals show that Vp/Vs decreases as total porosity increases.

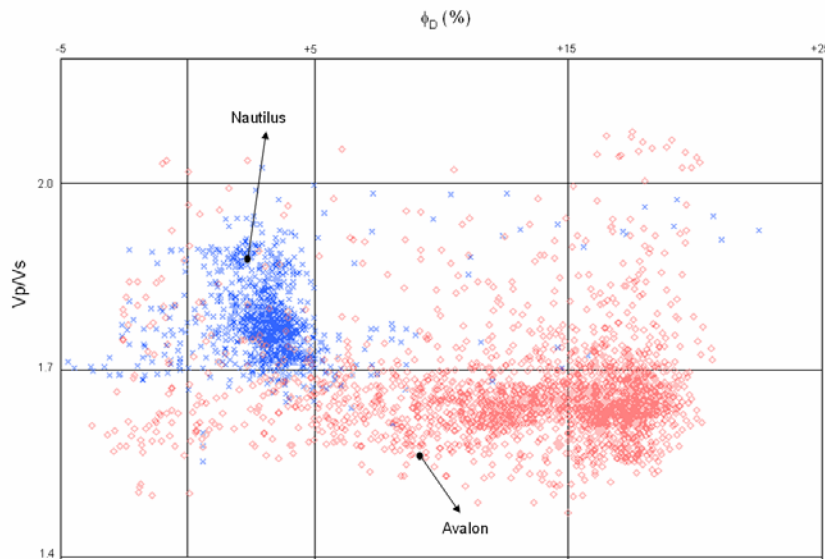


Figure 2.33: Well L-08 Vp/Vs versus ϕ_D , assuming a sandstone matrix.

2.2.12 Vp, Vs, Vp/Vs versus ϕ_N

The neutron log is a porosity well log that measures hydrogen density. A low hydrogen density suggests low liquid-filled porosity (Sheriff, 1999). Much of the hydrogen present in a formation is in the water (bound, crystallized, or free pore water) and oil. Since one or both of these fluids are present in the pores of the rocks,

we can establish the porosity by counting the hydrogen atoms (Johnson and Pile, 2002).

Usually the neutron log is recorded using a limestone matrix calibration. When the formation is sandstone or dolomite, a correction is required to relate the limestone porosity to the proper matrix. To do this correction we need to know the matrix of the formation. With the use of tables or empirical calibrations (see the neutron-density chart in section 2.2.13, ϕ_N versus ϕ_D), we can obtain the real porosities for these lithologies (Rider, 2002).

For the relationship evaluated using Figures 2.34 and 2.35, we assumed a sandstone matrix. The general trend is a decrease of V_p with increasing neutron porosity. The Nautilus shale shows high porosity values. This may be unrealistic, and likely due to bound water (Rider, 2002).

For the V_s versus ϕ_N relationship, we assumed a sandstone matrix. The general trend is a decrease in velocity as the neutron porosity increases. The general trend of the Avalon data is a linear regression where $y = -5805.2x + 3157$, $R^2 = 0.6774$. As for V_p versus ϕ_N , the Nautilus shale shows high porosity values. This could be due to bound water (shale has a large number of hydrogen atoms since water molecules are bound to the clay) — Johnson and Pile (2002).

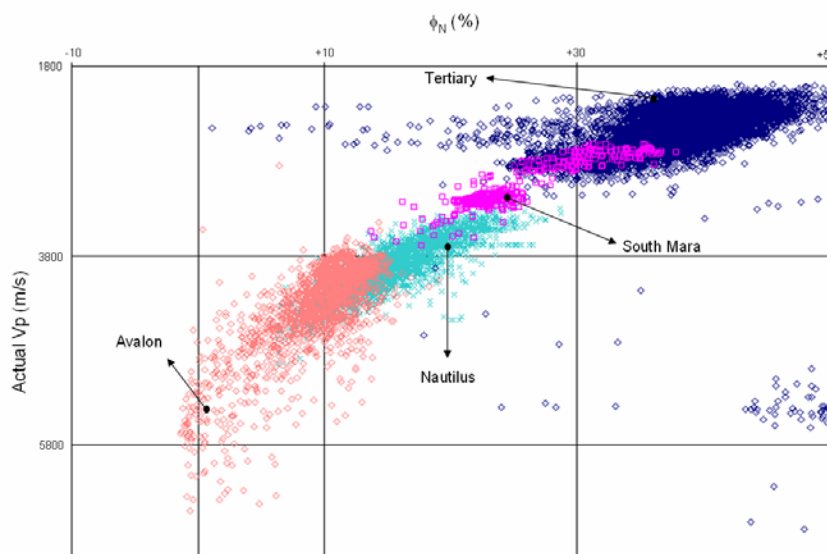


Figure 2.34: Well L-08 V_p versus ϕ_N , assuming a sandstone matrix.

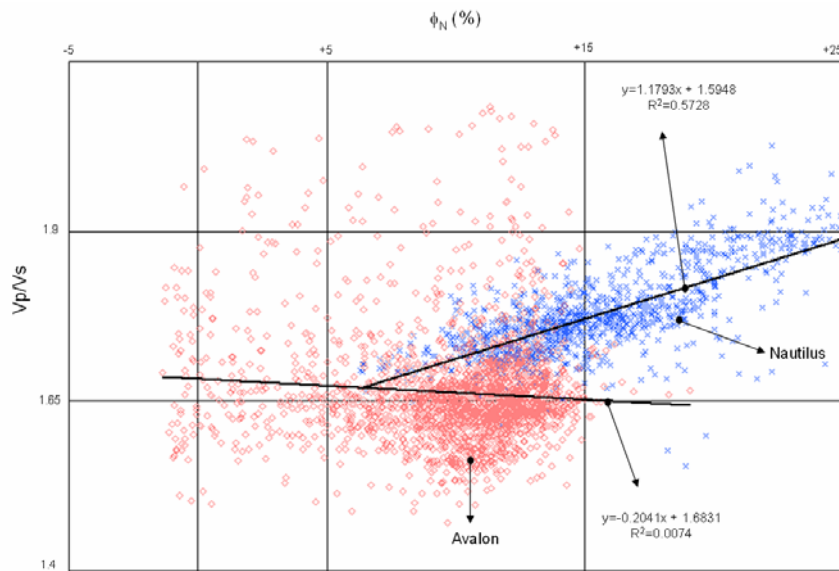


Figure 2.35. Well L-08 Vp/Vs versus ϕ_N .

For the Vp/Vs versus ϕ_N we can appreciate scattered data. The relationship for the Nautilus shale shows an increase when ϕ_N increases. The Avalon shows a general trend of maintaining a low Vp/Vs value while the ϕ_N increases. The general trend of the Avalon data (Figure 2.35), shows a linear regression of $y = -0.2041x + 1.6831$, $R^2 = 0.0074$. The general range (including the scattered data) for Vp/Vs values for Nautilus is ~ 1.68 - 1.96 , and Avalon ~ 1.51 - 2.04 .

2.2.13 ϕ_N versus ϕ_D

When we work with neutron and density logs, it is important to remember that there are some effects that will affect the final porosity value. The effect due to a hydrocarbon presence implies that some gas or light hydrocarbons can cause the density log to show an increase in the porosity value. Conversely, the porosity value will decrease on the neutron log (Schlumberger, 1987).

Let's consider the shale effect on the density porosity versus neutron porosity crossplot. The presence of shales and clays in sandstone units (shaly sandstones) causes a problem with the interpretation of density porosity and neutron porosity. The presence of non-effective shales (kaolinite and chlorite), means there is zero cation exchange capacity between the clay's adsorbed water and formation water.

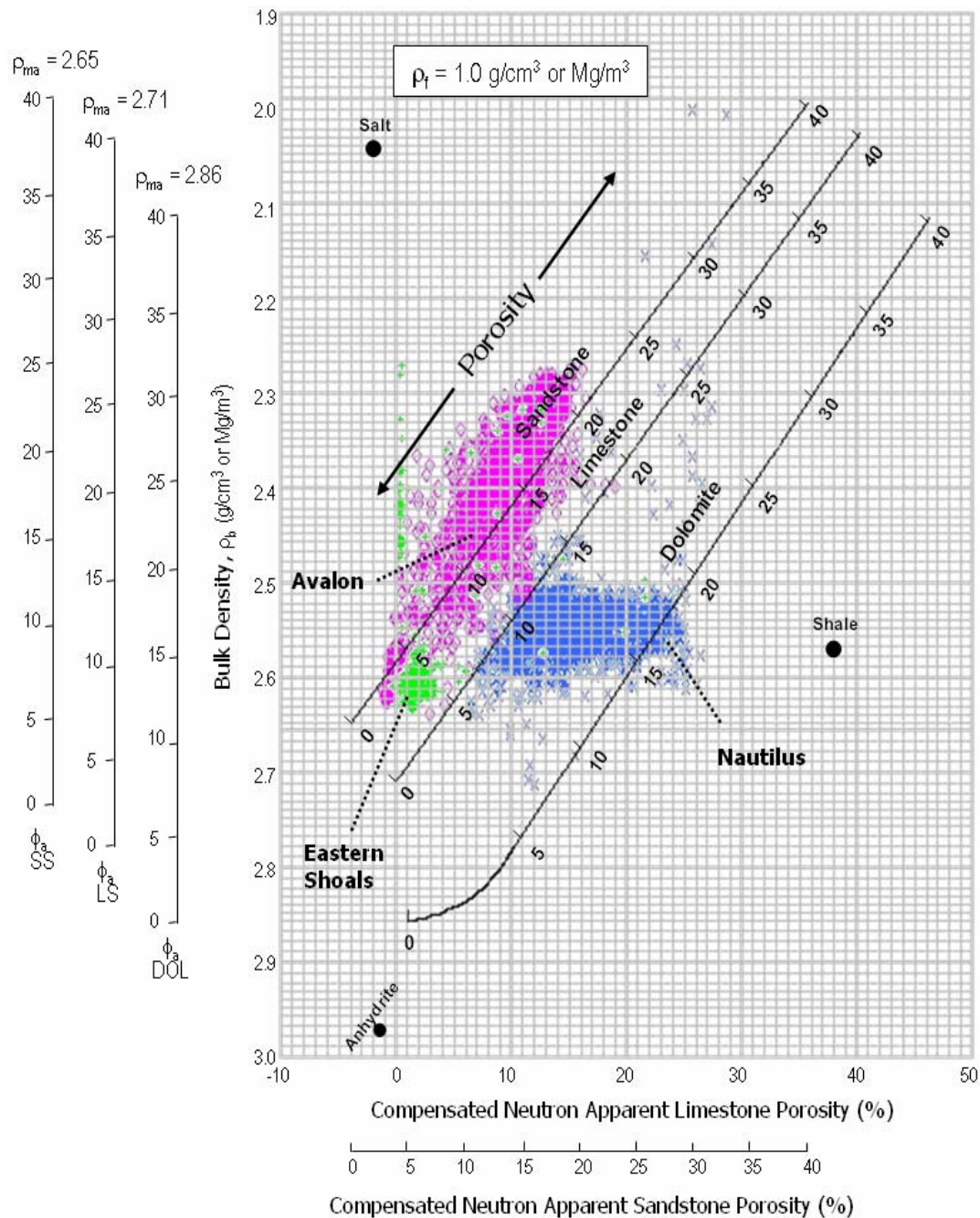


Figure 2.36: Density porosity versus neutron porosity (well L-08), overlain on a chart from Western Atlas (1985). The details of the Figure are explained in page 68.

This process occurs along the clay surfaces (Asquith, 1990) and influences the neutron log to a higher degree than the density log and the cloud of data shifts to higher apparent neutron porosities. This is seemingly due to the large amount of

water linked with these shales. This shift is, of course, wrong since the shale point should not move (Hilchie, 1982).

The neutron-density chart (Figure 2.36) can be used to differentiate between the common reservoir rocks (sandstone, limestone, dolomite), shale and some evaporites. At any point on the chart, we will have points of intersection for the lithology and the porosity. The three lines correspond to density and neutron porosity variation for values of porosity between 0 and 40 PU (porosity units) for the three main rock types. At the sandstone line, there is 0% shale, and at the shale point there is 100% shale. In between, there is a series of parallel lines to the sandstone line that represent, from left to right, an increasing percentage of shale (Hilchie 1982).

As shown in Figure 2.35 and 2.36, the Nautilus shale points cluster. If we look at the position of the sandstone line and the 100% shale point, it can be estimated that the Nautilus shale range lies between 20 to 80%. This is consistent with the known geology of the area. The Avalon Formation follows the sandstone line of the chart. The Avalon and Eastern Shoals ϕ_N increases when ϕ_D increases; for the Nautilus shale, the ϕ_N increases with an increase in ϕ_D that it is not as evident as it is in the ϕ_N . However, the porosity values are high for the Nautilus; this could be apparent porosity due to the presence of bound water.

2.2.14 Multivariate analysis

As a more detailed approach to studying the data, we explored a multivariate analysis in well L-08. According to Russell (2004), the main purpose of the multivariate analysis is to predict a target sonic log with the combination of seismic attributes. In our case, our target log to derive using the multivariate analysis is V_p and V_s log curves. The attributes are V_p , V_s , GR, ϕ_N , and ϕ_D .

In this case, we do not have other well logs for comparison, so we enlist the help of an algorithm and Matlab software to work with one well and five log curves (attributes) that will help to generate the constants needed for the analysis (Appendix B). This well was chosen due to the data present. The attributes that the well has are V_p , V_s , GR, ϕ_N , and ϕ_D (Figure 2.36). We will work with Equations 2.13 and 2.14.

$$V_p = a + bV_s + cGR + d\phi_N + e\phi_D, \quad (2.13)$$

$$V_s = a + bV_p + cGR + d\phi_N + e\phi_D, \quad (2.14)$$

where: V_p Compressional velocity
 V_s Shear velocity
 GR Gamma Ray
 ϕ_N Neutron-porosity
 ϕ_D Density-porosity
 a, b, c, d, e Constants derived from the multivariate analysis

The constants (Table 2.18) generated after the multivariate analysis were used on the Equations 2.13 and 2.14 to obtain V_p and V_s from several attributes (V_p , V_s , GR , ϕ_N , and ϕ_D).

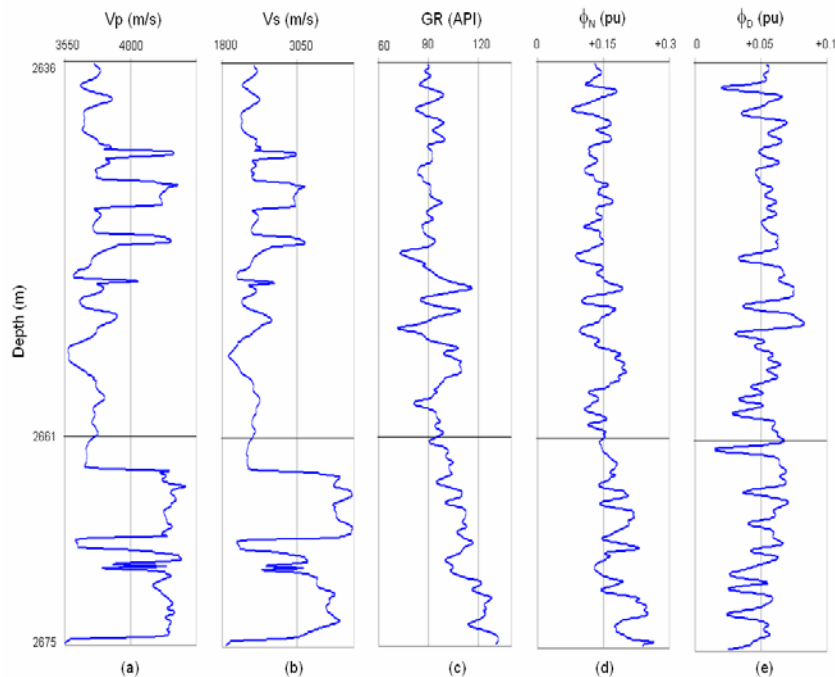


Figure 2.37: Well log curves from well L-08, from a section of Nautilus shale. Panel (a) — actual V_p versus depth. Panel (b) — actual V_s versus depth. Panel (c) — actual GR versus depth. Panel (d) — actual ϕ_N versus depth. Panel (e) — actual ϕ_D versus depth.

The main purpose of this analysis is to predict V_p and V_s using more than one attribute, as we did in the previous sections. The results were encouraging. For this analysis we are using only the section where all the attributes coincide. This

section (Figure 2.37), which is found in the Nautilus shale of well L-08, is about 39 m thick.

Constant	To derive Vp	To derive Vs
<i>a</i>	1635.6	-1280.5
<i>b</i>	1.1	0.8
<i>c</i>	1.7	1.7
<i>d</i>	-1718.4	1229.7
<i>e</i>	805.1	-554.6

Table 2.18: Constants used in the multivariate analysis to derive Vp and Vs.

After applying the constants in Equations 2.13 and 2.14, the results were encouraging (Figures 2.38 and 2.39). The results for the Vp log curve (Figure 2.38) shows that the percentage error between the actual Vp and the derived Vp is between about -11 and +9%. The RMS value shows that the deviation is ± 213.52 m/s. The graphic shows the good results from this multivariate analysis.

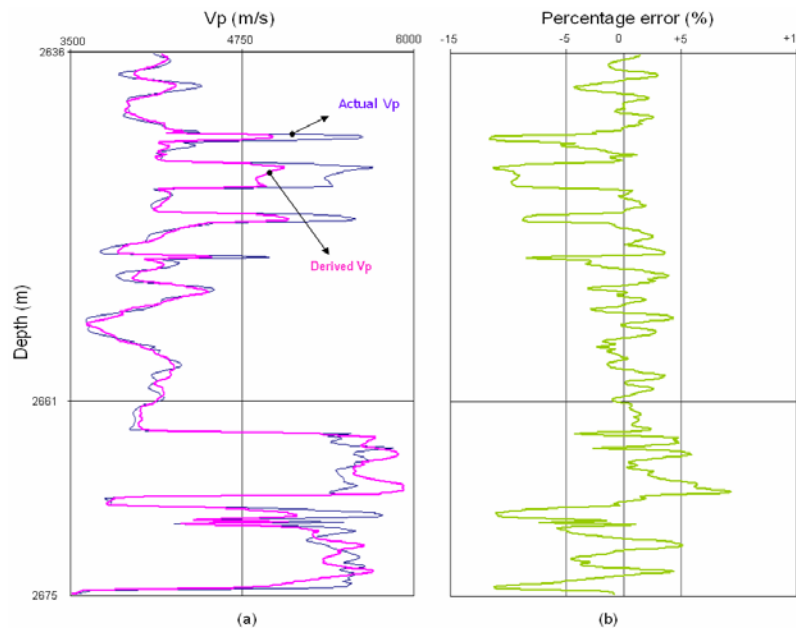


Figure 2.38: Data from a section of Nautilus shale from well L-08. Panel (a) — actual Vp and derived Vp (using a multivariate analysis) versus depth. Panel (b) — percentage error between these two Vp curves versus depth. RMS error ± 213.52 m/s.

Figure 2.39 shows the Vs results. The range of percentage error is about -13 to +18%. The RMS error is ± 178.77 m/s. If we compare the results obtained in the

same area when we applied Castagna's mudrock relationship, we can see that the multivariate analysis works better (Figure 2.40).

The approach used on Figure 2.40 to derive V_s (using Castagna's mudrock relationship and multivariate analysis) has some similarity due to the fact that both relationships use V_p log data. Still, with Castagna's mudrock equation, we only used one attribute (V_p) and with the multivariate analysis we used four attributes (V_p , GR, ϕ_N , and ϕ_D). The results using the mudrock relationship haven't drifted too far from the original values. The results using multivariate analysis gave us more confidence in the study.

A different approach to multivariate analysis, using Hampson-Russell's Emerge Software, was undertaken. Due to the fact that we just had one well with the required data, the approach gave a derived V_s very closely matching the actual V_s (Figure 2.41). To be able to do a statistical analysis, it is necessary to have more well logs with the required data to study.

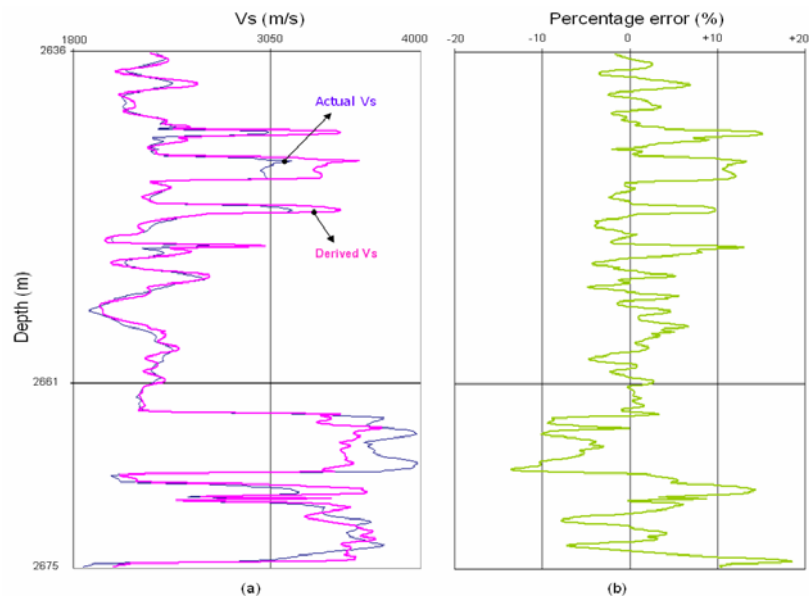


Figure 2.39: The data is from a section of Nautilus shale from well L-08. Panel (a) — actual V_s and derived V_s (using a multivariate analysis) versus depth. Panel (b) — percentage error between these two V_s curves versus depth. The RMS error is ± 178.77 m/s.

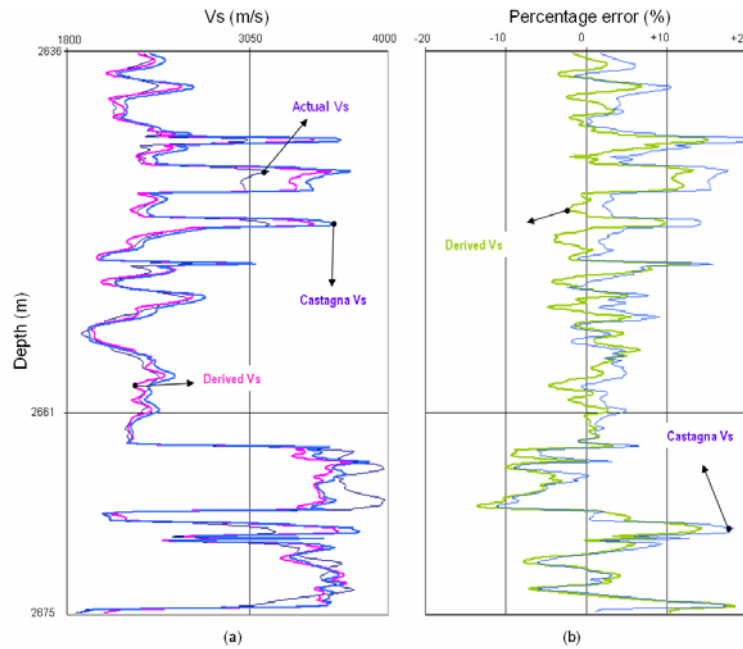


Figure 2.40: Data from a section of Nautilus shale from well L-08. Panel (a) — actual Vs, derived Vs (using a multivariate analysis), and Castagna Vs (using his mudrock relationship) versus depth. Panel (b) — percentage error between the two derived Vs curves and the actual Vs versus depth. The RMS error is ± 178.77 m/s for the derived Vs (using multivariate analysis) and ± 206.78 m/s for Castagna Vs (using the mudrock relationship).

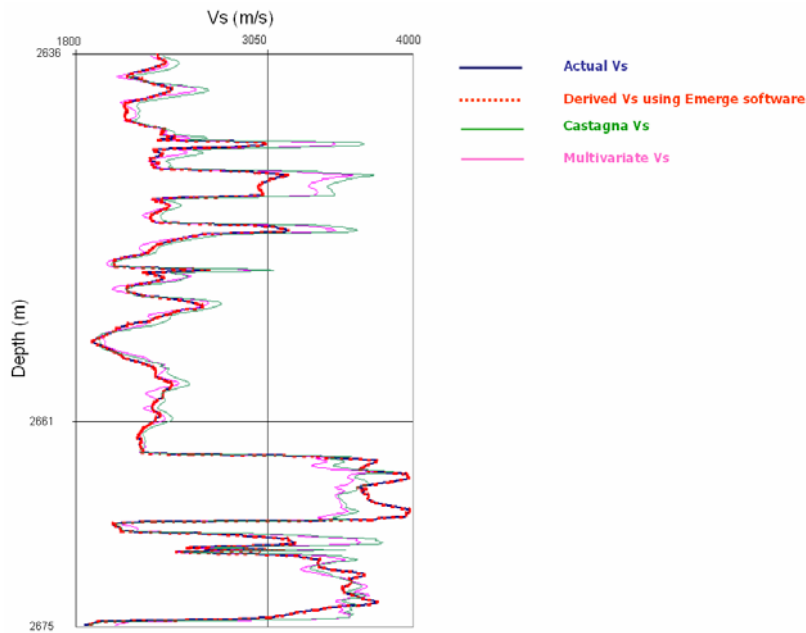


Figure 2.41: Data from a section of Nautilus shale from well L-08. actual Vs, derived Vs (using Emerge Software analysis), derived Vs (using a multivariate analysis), and Castagna Vs (using his mudrock relationship) versus depth.

CHAPTER 3. VSP INTERPRETATION

3.1 VSP survey

The White Rose H-20 well (location shown in Figure 3.1) was drilled during the summer of 2000 with the objective of delineating the northern limit of the South Avalon Pool. Following the drilling, a vertical seismic profile (VSP) program was conducted. Some of the reasons for the acquisition of the VSP data were (Hoffe et al., 2000):

- To determine the existence of minor faults in the Avalon reservoir and the influence of the faults on the interpretation.
- To explore the application of the ocean-bottom cable (OBC) survey for the White Rose field using VSP-determined values.
- To evaluate if PS waves (as seen in the VSP data) can yield a clearer image of the reservoir.

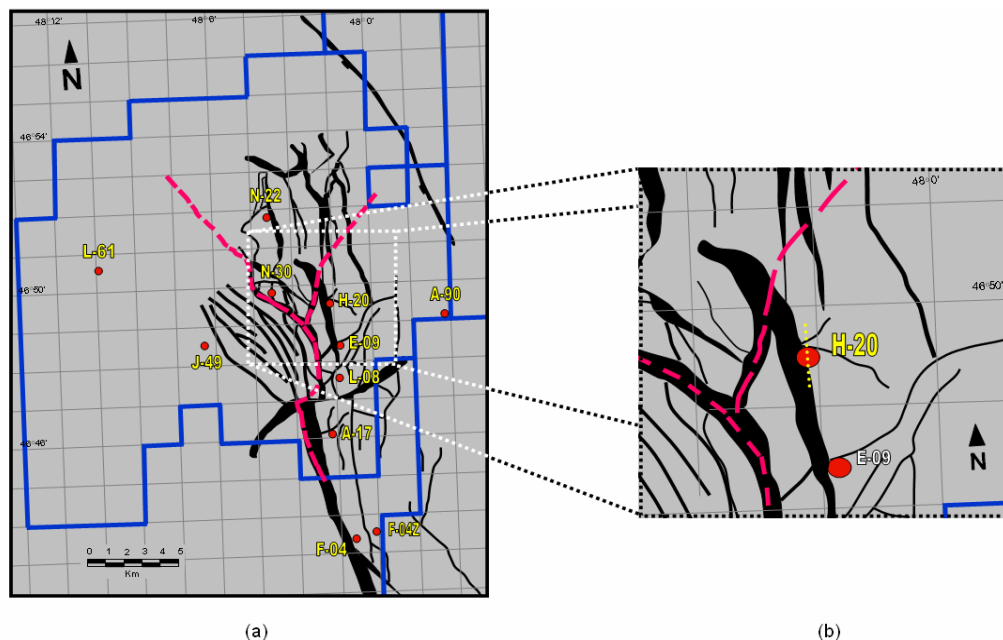


Figure 3.1: Location of well H-20 (Modified after Husky Oil Operations, 2001).

The processing of the VSP dataset was conducted by Schlumberger, Canada and their processing generated several outputs such as (1) the corridor stack, (2)

VSP-CDP map of the PP, and (3) VSP-CCP map of the PS data. In this section, I will review the analysis of the well logs and the correlation of the reflected P (P-P) and converted S (P-S) synthetic seismograms to the seismic data. The correlations will be shown for:

- PP synthetic seismograms to the PP offset VSP data;
- PP synthetic seismogram to the walk-above VSP (PP only) data;
- PP synthetic seismograms to the seismic section (PP only);
- PS synthetic seismograms to the PS (S) offset VSP data;
- walk-above VSP P-wave data to the P wave seismic section.

Two VSP datasets resulted from the acquisition of the VSP. They were the offset and walk-above VSP. The geometry of each of the surveys acquired in the study area are described below:

- **H-20 offset-VSP.** The acquisition geometry of the well H-20 offset VSP survey (Figure 3.2) had a fixed source offset placed 1000 m north of the H-20 well. The VSP receivers (three-component triaxial sondes) were located between 2080 and 2500 m measured depth (in the vertical part of well H-20) during the recording of the VSP data.
- **H-20 walk-above VSP.** The geometry of the walk-above VSP survey (Figure 3.3) had a moving source. The source offset distance was between 40 and 250 m from the well location. These source offsets were placed vertically above the geophones located at a depth range of 1660–3280 m. The source was placed vertically above the geophones within the deviated well. When the receiver was moved further away from the well head, the source was moved to be vertically above the geophones.

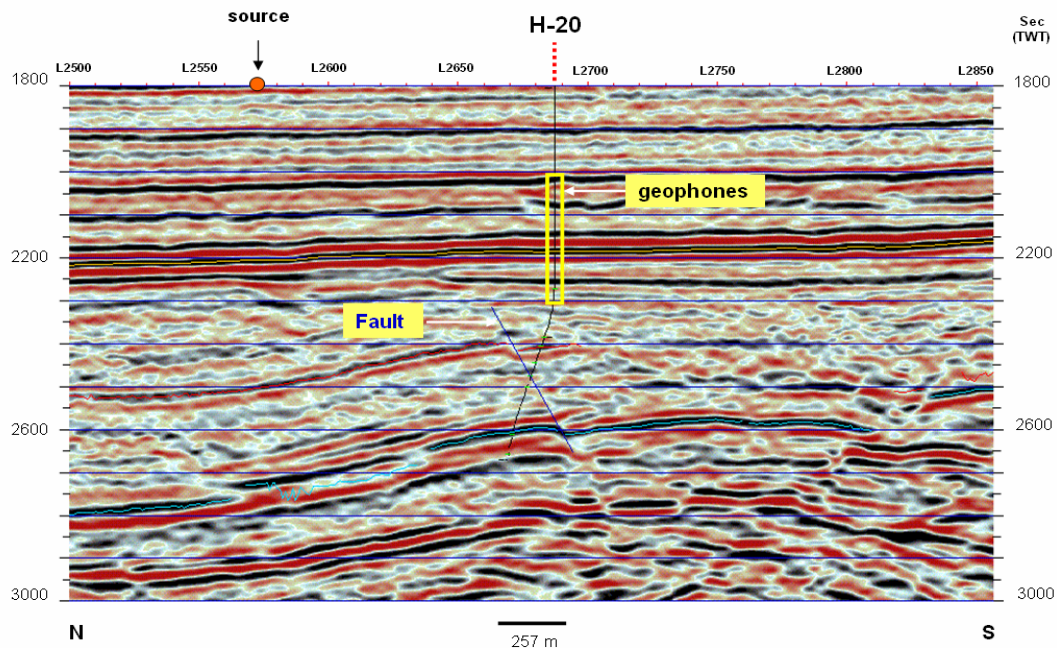


Figure 3.2: Details of the H-20 offset VSP survey showing the north-south seismic line (1.8 to 3 seconds TWT) intersecting well H-20. (Modified after Emery, 2001.)

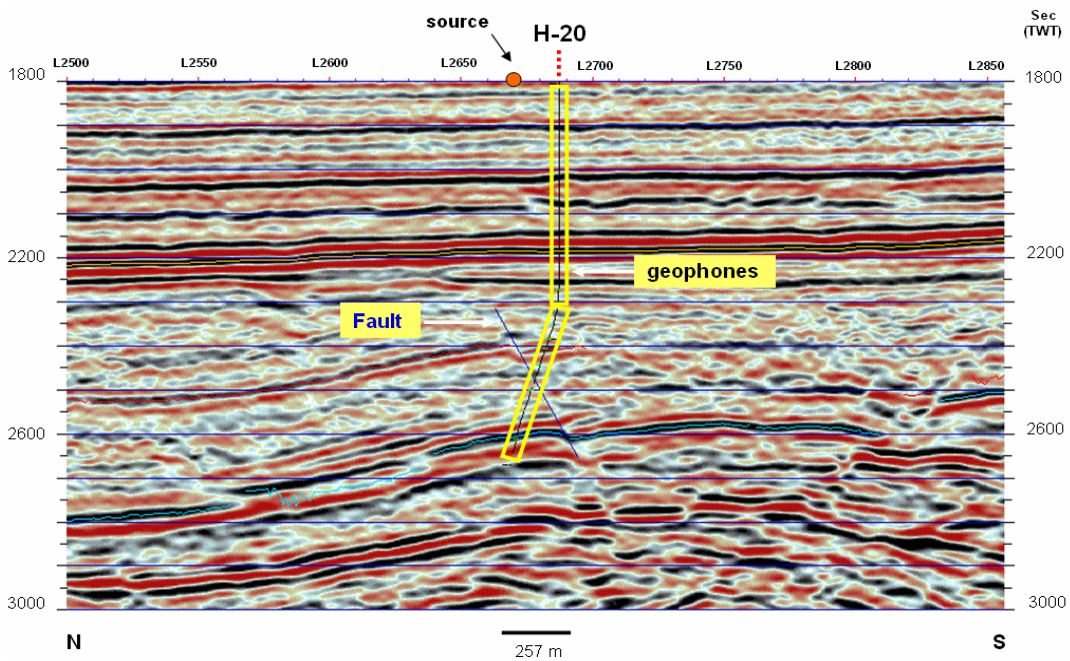


Figure 3.3: Details of the H-20 walk-above VSP showing the north-south seismic line (1.8 to 3 seconds TWT) intersecting well H-20. (Modified after Emery, 2001.)

3.2 Interpretation

Schlumberger Canada processed the VSP data for Husky Energy Inc. Synthetic seismograms were calculated using the CREWES software package SYNTH (Larsen et al., 1997). For the synthetic seismograms, a suitable wavelet was chosen that would match the surface seismic wavelet. The wavelet used in the synthetic seismogram generation was a Ricker wavelet with a frequency of 45 Hz.

The next step is to match the synthetic seismogram with the P-P seismic section and with the P wave and PS VSP data. The procedure is described below.

3.2.1 Tie of PP synthetic seismograms with PP offset VSP field data.

The matching of the PP synthetic seismogram with the PP VSP-CDP transformed data section (Figures 3.4) shows a good correlation. The events correlated are described as follows:

- **Eocene (EOCN):** The Eocene is a significant event in the synthetic surface seismic display (Panel (a)). The modelled offsets were from 0 (synthetic seismogram) to 2000 m (the offset in the VSP).
- **South Mara (Smara):** The South Mara event is easy to interpret in the synthetic seismic section. In the synthetic seismic section, the amplitude starts to lessen in amplitude from 1200 m to 2000 m offset. In the VSP-CDP data, the South Mara is a strong event. The South Mara events near the 0 offset distance begin to exhibit distortion at the inner VSP offsets.
- **Base of Tertiary Unconformity (Btrt):** This is a strong event on both sections. The VSP-CDP events show NMO problems at shallow depths (Panel (a)). The neighbouring amplitudes decrease with offset in the synthetic seismogram.
- **Nautilus (Naut):** The event is also easy to recognize on the synthetic. The amplitude on both data sections (Panels (a) and (b)) is a strong peak and decreases slightly with offset in the synthetic seismogram. The formation event in the VSP-CDP section shows events that can be

correlated to several subunits of the Nautilus shale between the Nautilus and the Avalon events. In the VSP-CDP data, the subunit events are possibly contaminated by mode-converted residual SV events.

- **Avalon (Aval):** The top of this formation is a siltstone. This is in contact with the basal unit of the Nautilus, which is a silty sandstone that grades upward into siltstone. The low amplitude events are associated with this event. The acoustic impedances of the various layers of the Avalon results in low reflection coefficients. In the synthetic seismogram, the Avalon sandstone reflection event is powerful; however, the VSP-CDP reflections are less clear.
- **Eastern Shoals (Eshl):** This is a clear event seen in both Panels (a) and (b) (Figure 3.4).

3.2.2 Tie of PS synthetic seismograms with PS offset VSP-CCP data

Figure 3.5 shows the correlation of the P-S synthetic seismogram with the same reflections seen on the VSP-CCP, as described below:

- **Eocene (EOCN):** The shallow Eocene in Panel (a) shows a much lower amplitude than the same event in the VSP-CCP section.
- **South Mara (Smara):** The South Mara events correlate in Panels (a) and (b). On the synthetic seismogram, the reflection amplitude increases with offset. The VSP-CCP data show less amplitude change.
- **Base of Tertiary Unconformity (Btrt):** This is a strong event on the synthetic and real data (Panels (a) and (b)). The amplitude increases with offset in the synthetic seismogram, since the shear waves have small reflections at near offset.
- **Nautilus (Naut):** The top is easy to recognize on the real data. The amplitude of the event on Panels (a) and (b) is strong and increases with offset. The three subunits of the Nautilus shale are interpretable in these panels.

- **Avalon (Aval):** As shown in the PP analysis, the reflection coefficient between the Nautilus silty sandstone and the Avalon siltstone is low. However, in this analysis (PS synthetic seismogram and S-VSP section), the match is clearer. The predicted ρ value shows minor improvement on the event. At the base of the Avalon Formation one can see events probably related to the basal subunit that has shales interbedded with sandstones.
- **Eastern Shoals (Eshl):** It is easy to follow the event on the synthetic seismogram, but in the VSP-CCP section the interpretation is not clear.

3.2.3 PP synthetic seismogram with the walk-above VSP (PP) data

Figure 3.6 is the result of comparing the PP synthetic seismogram events (using the constant ρ value) and the walk-above VSP-CDP transformed VSP section. In the synthetic seismogram section, the Eocene, South Mara, Base of Tertiary Unconformity, and the Nautilus Shale events have high amplitude. In the walk-above VSP data these events are difficult to follow. This is due to the lack of VSP fold near the surface.

The Avalon Formation has the same problem. The interface between the Nautilus shale and the top of the Avalon sandstone is again difficult to observe. The Avalon event amplitude is low, due to the near constant lithology and the event in the VSP section is not easily defined. The walk-above VSP is still providing a low-fold event. The Eastern Shoals event is easy to follow on both sections (Panels (a) and (b) in Figure 3.6).

Figure 3.7, shows a correlation between PP synthetic seismogram, offset VSP PP section (Panel a), Offset VSP PS section (Panel b) and PS synthetic seismogram for well H-20, where one section supports the other.

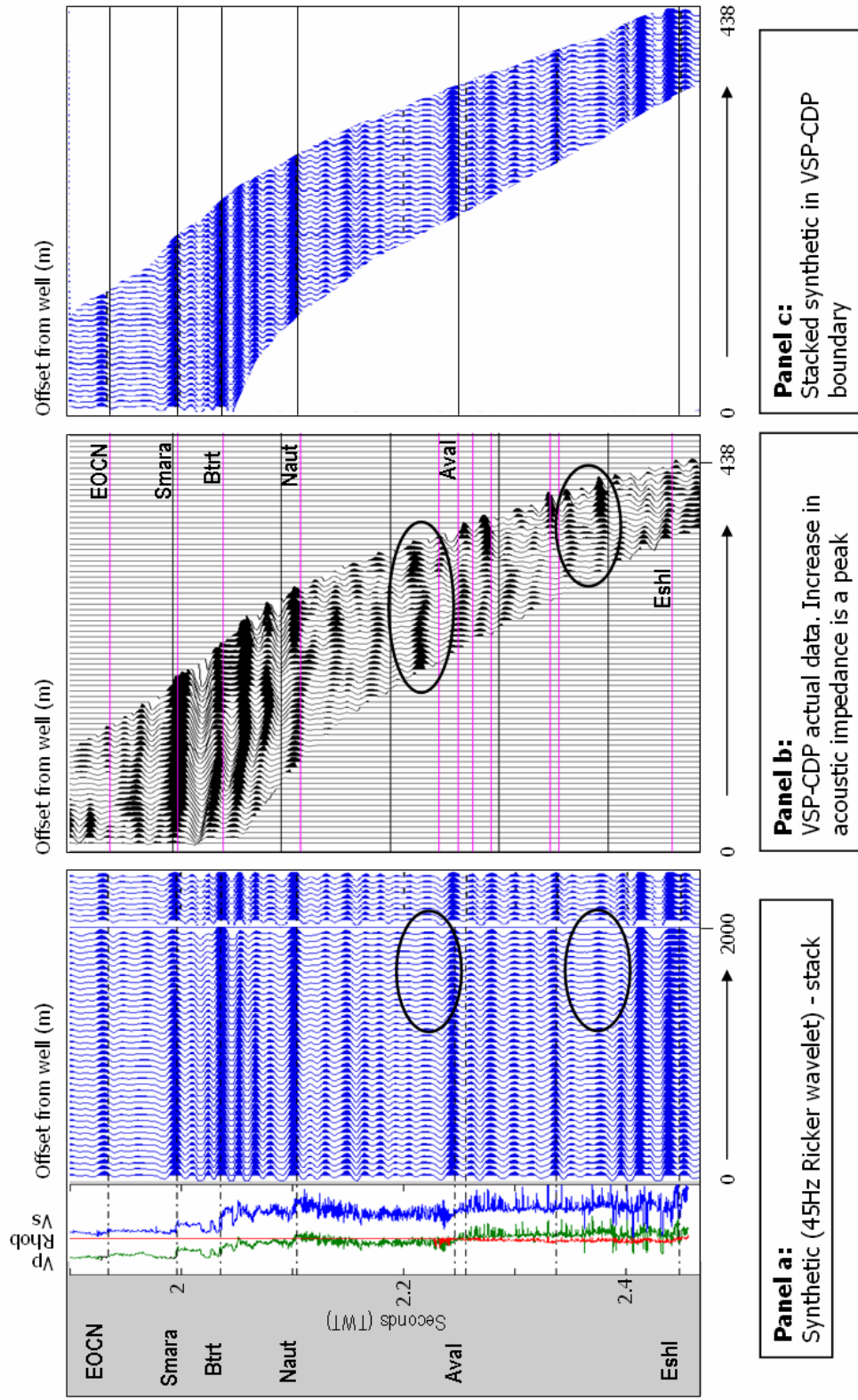


Figure 3.4: Result from matching the PP synthetic seismogram and the offset VSP section. Key: Eocene EOCN, South Mara Smara, Base Tertiary Btrt, Nautilus Naut, Avalon Aval, Eastern Shoals Eshl.

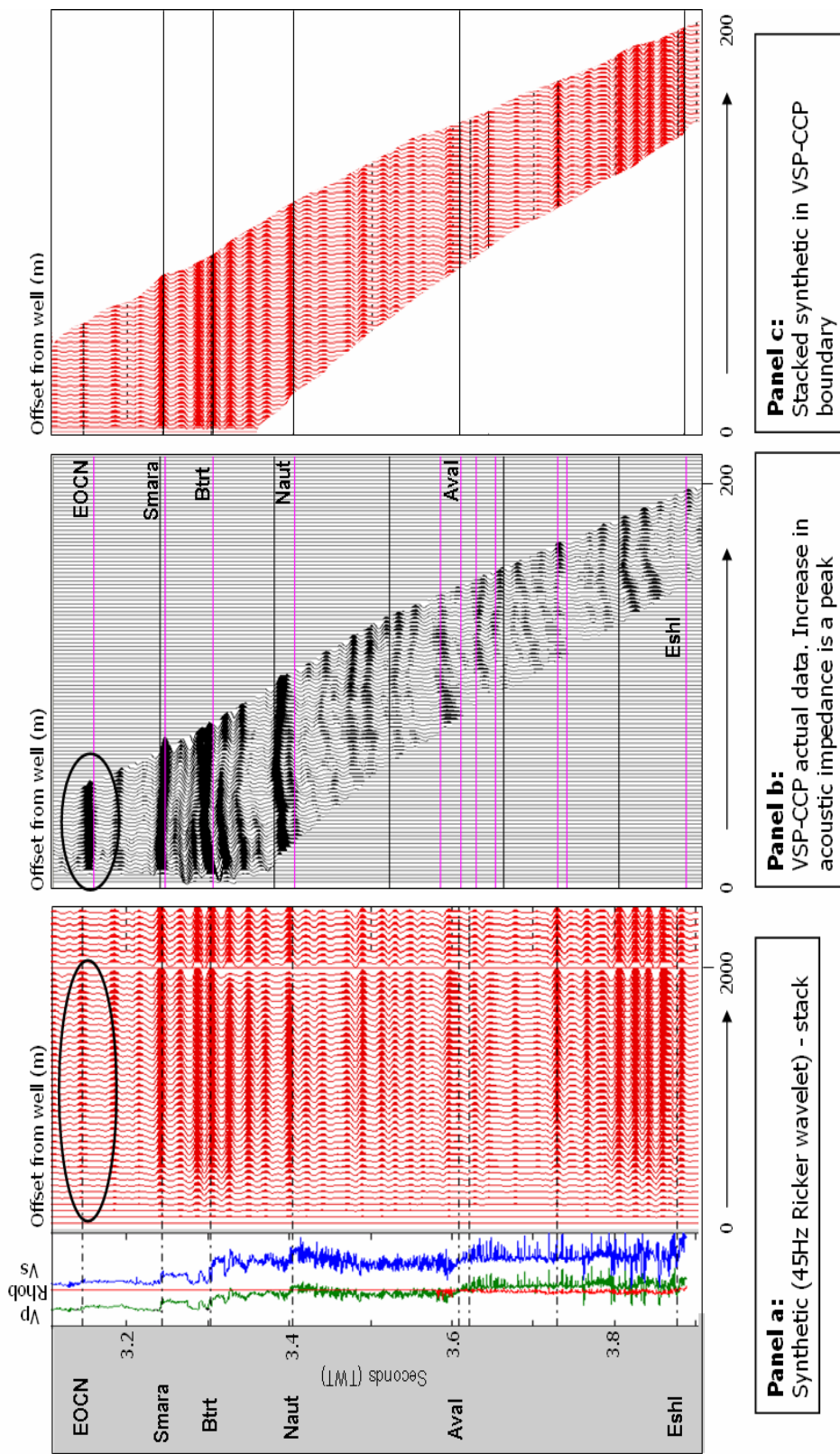


Figure 3.5: Result from matching the PS synthetic seismogram and the Offset VSP section. Key: Eocene EOCN, South Mara Smara, Base Tertiary Btrt, Nautilus Naut, Avalon Aval, Eastern Shoals Eshl.

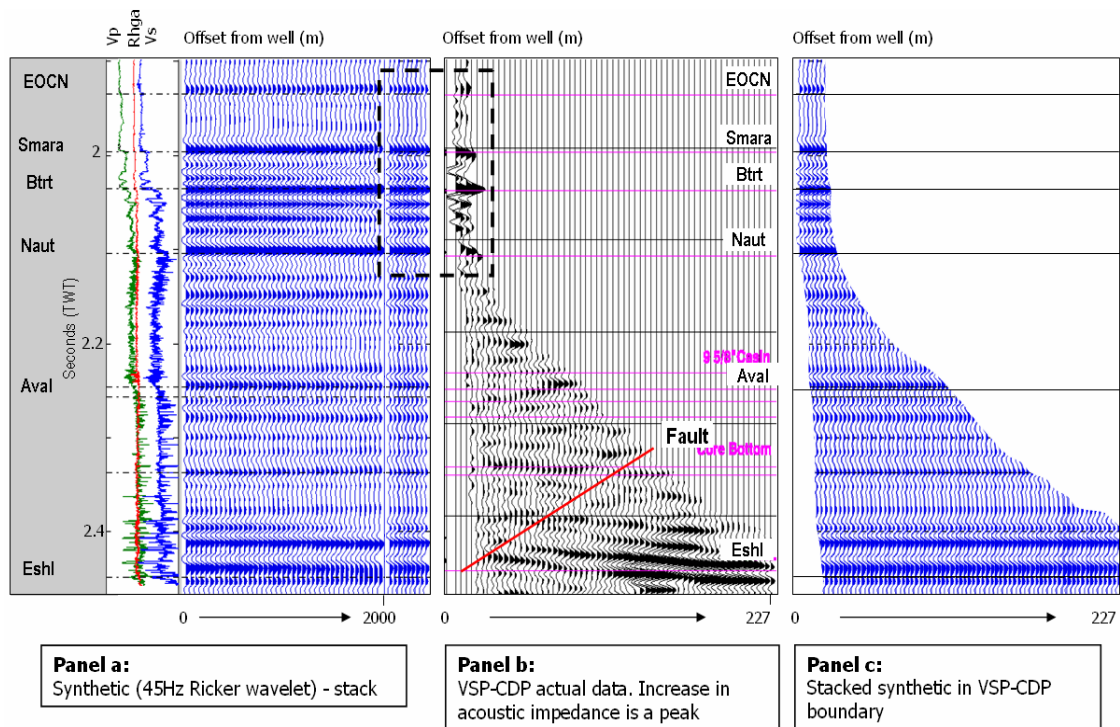


Figure 3.6: In this composite figure, Panels (a) to (c) show the results from matching the PP synthetic seismogram with the walk-away VSP section, using the Gardner ρ value (derived from Gardner, Figure 2.23). Panel (d) is a zoom of the dashed area in the Panels (a) and (b); the stacked trace section is from the PP synthetic seismogram. Key: Eocene EOCN, South Mara Smara, Base Tertiary Btrt, Nautilus Naut, Avalon Aval, Eastern Shoals Eshl.

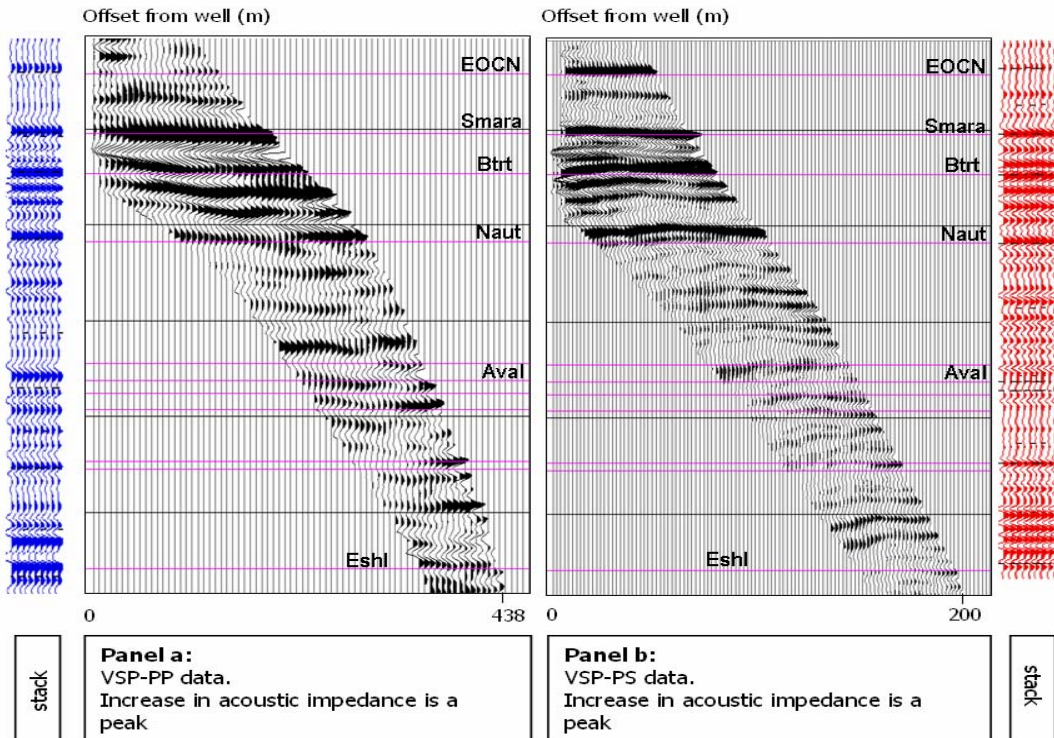


Figure 3.7: Comparison between PP synthetic seismogram, offset VSP PP section (Panel a), Offset VSP PS section (Panel b) and PS synthetic seismogram for well H-20. Key: Eocene EOCN, South Mara Smara, Base Tertiary Btrt, Nautilus Naut, Avalon Aval, Eastern Shoals Eshl.

3.2.4 Walk-above VSP data (PP) with the seismic section (PP)

Figure 3.8, shows a comparison between the Offset VSP (PP) and the Walk-above VSP (PP) data results. All the events (Eocene, South Mara, Base Tertiary Unconformity, and the Nautilus Shale) can be followed from one section to another one. However, the Walk-above VSP (PP) data do not have enough data on the upper section of the well, still we can correlate the events.

3.2.5 PP synthetic seismograms with the seismic section (PP)

In Figure 3.9, in the comparison between the walk-above VSP (P wave) and the PP seismic section, the correlation is reasonable. It is possible to postulate a fault crossing the Avalon sandstone reservoir. However, the interface between the

Nautilus shale and the top of the Avalon sandstone (which is a siltstone) is difficult to observe.

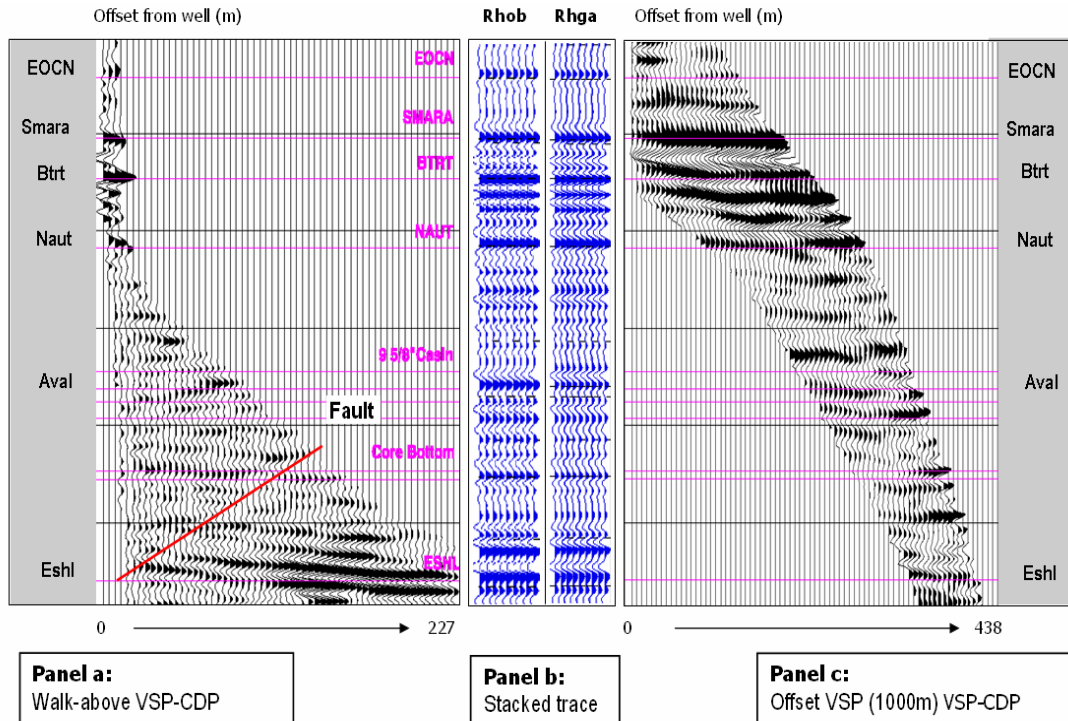


Figure 3.8: Comparison between walk-above VSP PP, PP stacked trace section (results from using Rhob and Rhga logs), and Offset VSP PP surveys for well H-20. Key: Eocene EOCN, South Mara Smara, Base Tertiary Btrt, Nautilus Naut, Avalon Aval, Eastern Shoals Eshl.

As a final comparison, Figures 3.10 shows the PP synthetic seismogram and the PP seismic section. The comparison of the synthetic seismogram and seismic section data in Panel (b), shows that the tops in the synthetic seismogram correlate well with the seismic section.

The PS section (Figure 3.5) assists in the correlation of the zones of interest (the interface between the Nautilus and Avalon formations). The PP correlation was less clear for the lithological correlation. The difficulty in defining the boundary between the Nautilus shale with the Avalon siltstone still remains.

Bearing in mind the different imaging challenges present at the White Rose field (section 1.4), converted waves (Stewart et al., 2003) may help to differentiate sand/shale boundaries, sharpen the definition of interfaces with low P-wave impedance boundaries, and improve imaging through gas zones. A 4C ocean-bottom sensor (OBS) survey, and the generation of shear waves would increase the quality of the image of the reservoir.

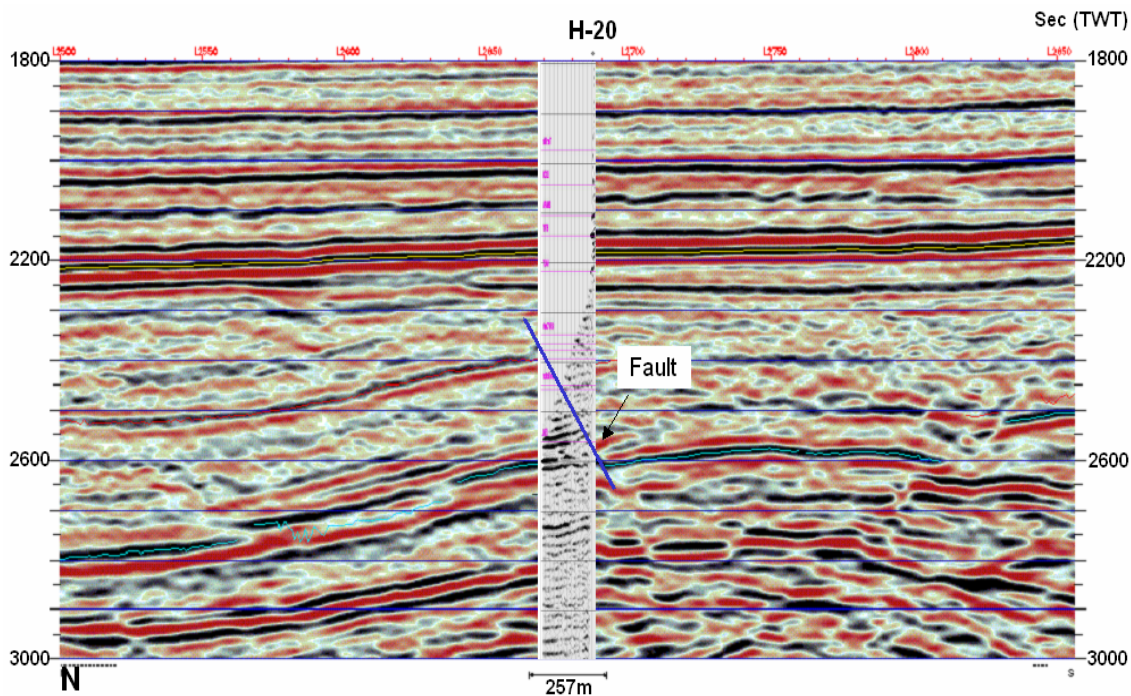
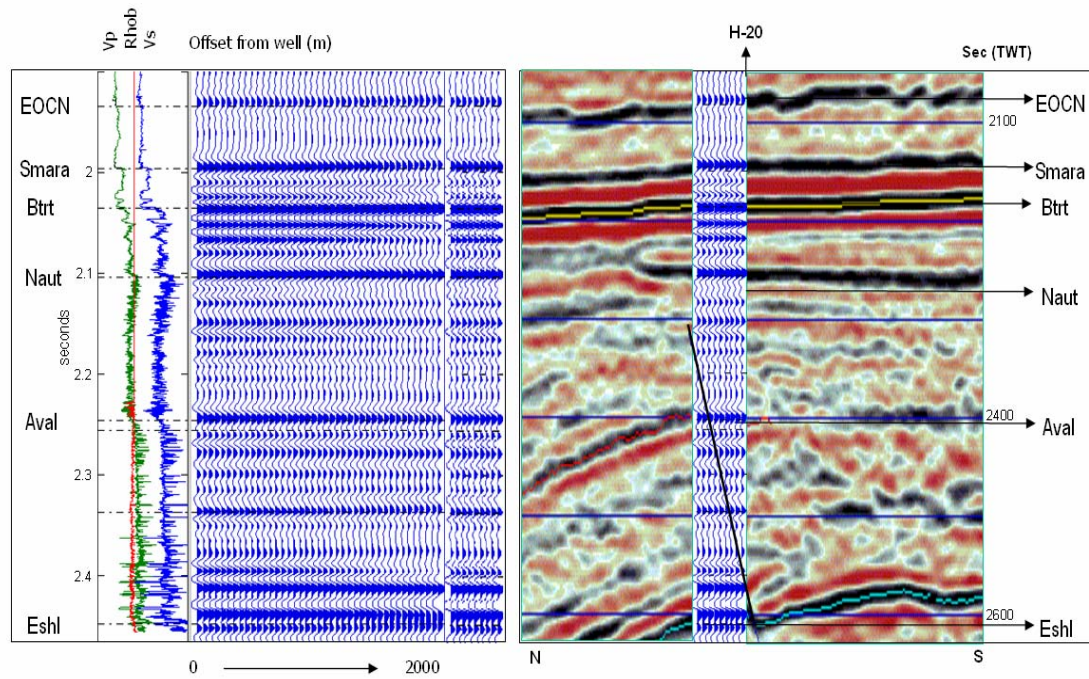


Figure 3.9: Comparison between the walk-above VSP (P-wave) and PP seismic section (1.8 to 3 sec TWT).

Let us consider a situation where the OBS survey PS appears to have lower frequency content than the PP. Isaac and Lawton (1995) observed that, in general, PS seismic sections have about half the frequency content of PP seismic sections (60 Hz versus 30 Hz). Figure 3.11 compares synthetic seismograms with higher and lower frequency content (45-Hz Ricker wavelet versus 30-Hz Ricker wavelet). Under these circumstances, the top of the Avalon Formation can still be identified.



Panel a:
Synthetic (45Hz Ricker wavelet) - stack

Panel b:
North South PP Seismic section and Synthetic seismogram

Figure 3.10: Result from matching the PP synthetic seismogram and the PP seismic section (black is a peak and red is a trough). Key: Eocene EOCN, South Mara Smara, Base Tertiary Btrt, Nautilus Naut, Avalon Aval, Eastern Shoals Eshl.

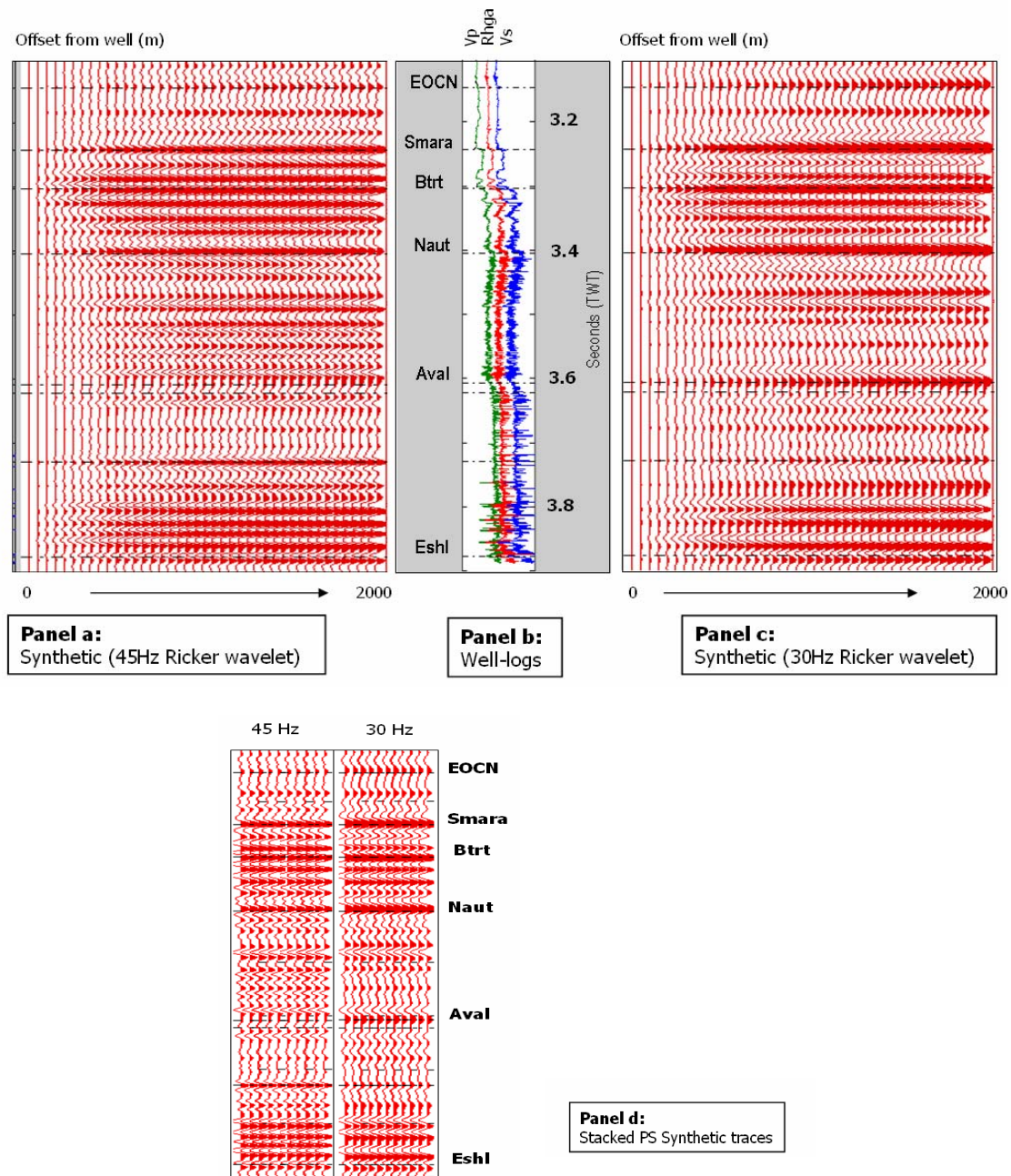


Figure. 3.11: Composite figure showing a comparison of PS synthetics: high frequency (45Hz) versus low frequency (30Hz) (Panels (a) and (c)). Panel (d): the events of interest in a close-up comparison of the stacked trace sections from each of the synthetic seismograms of Panels (a) and (c). Key: Eocene EOCN, South Mara Smara, Base Tertiary Btrt, Nautilus Naut, Avalon Aval, Eastern Shoals Eshl.

CHAPTER 4. CONVERTED-WAVE OBS INTERPRETATION

4.1 SCREECH survey

During the summer of 2000, Dalhousie University in Halifax (Nova Scotia) and other institutes acquired ocean-bottom seismometer/hydrophone (OBS/H) transect survey data off the east coast of Canada as part of the SCREECH (Studies of Continental Rifting and Extension on the Eastern Canadian Shelf) project (Louden and Funck, 2000). The Canadian east coast has interpretation difficulties due to complicated geology and seismic imaging. The challenges are similar to those experienced in the North Sea (Hoffe et al, 2000), where the use of multi-component seismic data has resulted in several fascinating and motivating images (Caldwell, 1999).

Multi-VSP surveys (offset-VSP and Walk-Above-VSP) have been conducted in well H-20 of the White Rose oilfield (Chapter 3). The interpretation panels produced using shear-wave (P-S) data showed improvement in interpretability over the conventional P-P data (D. Emery, Husky Energy, pers. comm.; Stewart et al., 2001).

The cost of acquiring an OBC survey is high, with mobilization fees being a main expense. As an alternative, four-component (4C) seismic measurements using ocean-bottom seismometer nodes were acquired by an international consortium of research groups (Canada: Dalhousie University and Memorial University; Denmark: Danish Lithosphere Centre; and USA: Woods Hole Oceanographic Institution and University of Wyoming) as part of their study of the Atlantic Continental Margin (Louden and Funck, 2000).

The field study took place (Figure 4.1) in the Eastern Canadian Shelf (Newfoundland Basin, Flemish Cap, and Grand Banks) during the summer of 2000. According to Louden and Funck (2000), the objectives for this survey were mainly for continental margin studies.

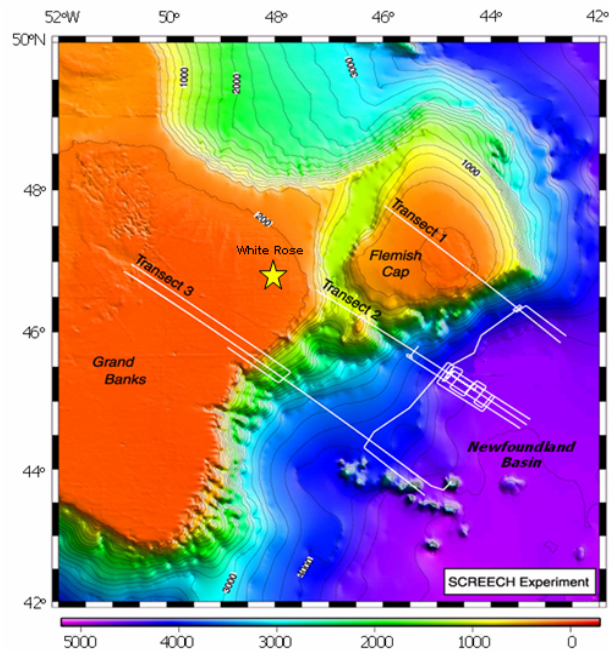


Figure 4.1. Location of SCREECH survey, showing three transects of the survey across the Newfoundland continental margin. (Modified from odp.tamu.edu).

4.1.1 Survey equipment

To acquire this survey, 2 ships were used. The R/V Oceanus deployed and recovered the 4C-OBS/H and the R/V Ewing was the source vessel. The instruments were deployed in water depths exceeding 4000 m. An 8540 cu. in. air gun array provided the acoustic source for the OBS/H and the multi-channel seismic (MCS) data was recorded on a 480-channel, 6-km long streamer (Louden and Funck, 2000). The equipment used to acquire the wide-angle data for the survey consisted of 29 ocean-bottom receivers.

4.1.2 Acquisition and geometry

The program was divided into three transects (Figure 4.1). This was done in an attempt to minimize transit times and maximize the survey recording time. This thesis looks at the third transect. On each transect, the OBS line was shot at a 200-metre shot spacing to reduce noise from previous shot. After the Ewing shot each

OBS line, the Oceanus retrieved the instruments and moved onto the next transect while the Ewing returned along the transect shooting the MCS (multi-channel seismic) line at a 50-metre shot spacing. In deeper water, the OBS/H array was closely spaced (usually 9–12 km), while over the thick continental crust of Flemish Cap and the Grand Banks, the array was more widely spaced (20–50 km) (Louden and Funck, 2000).

4.1.3 Interpretation

A preliminary analysis of the 4C receiver gathers (from the 2000 SCREECH survey) on transect 3 was conducted (Stewart et al, 2001). The vertical and radial migrated seismic sections showed the area of interest (Figures 4.2 and 4.3). We were able to identify a strong event that could be the Base of Tertiary unconformity. From this point, the identification of several events on the sections motivated the development of the OBS seismic survey in 2002.

4.2 Acquisition and geometry of the 4C ocean-bottom seismometer (OBS) survey

During May 2002, Dalhousie University and the Geological Survey of Canada (GSC) acquired a MARIPROBE crustal refraction line (2002-11 Line 1, Figure 4.4) using 4C OBS. During the same survey, a second line was shot with much smaller receiver spacing over White Rose (2002-11 Line 2, Figure 4.4).

Due to time limitations, it was decided to shoot a 2D seismic line centred on Husky Energy's L-08 well. Twenty-one OBS instruments were used to acquire the survey (2002-11 Line 2). The instruments were deployed over the ocean floor approximately 50 m apart to form a 1 km east-west line of receivers. The receivers drifted to the bottom through approximately 125 m of water. This deployment took about one hour. A total of 12 east-west source lines (each line being 8 km long) were acquired in a spiral pattern (Figure 4.5) starting above the OBS positions (Figure 4.6) at a rate of one line every 75 minutes, with a 1966 cu. in., 1650–1800 psi, 5 airgun

array. The source interval was 50 m and the source line interval varied from 50 m to 200 m. Retrieval of the instruments took around ten and a half hours (Hall and Stewart, 2003), and data were successfully downloaded from twenty of the twenty-one OBS. One OBS failed to record any signal at all. Dalhousie University, Sensor Geophysical, and CREWES processed the data.

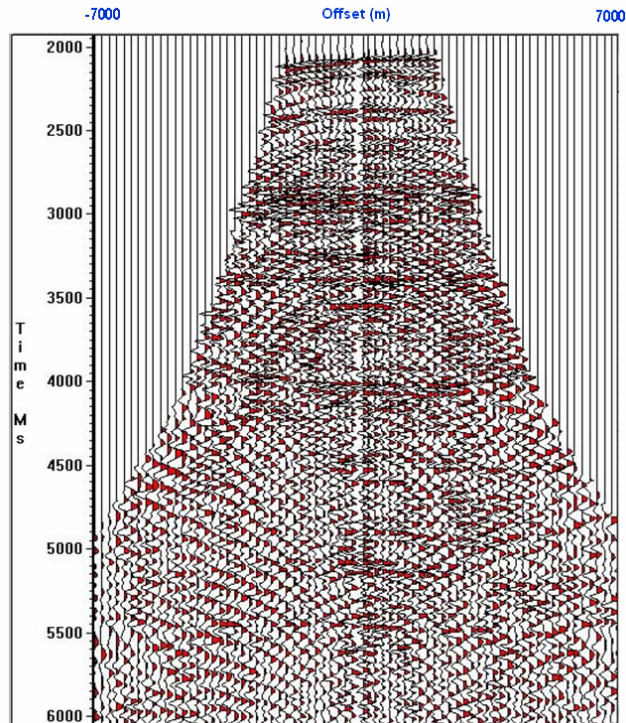


Figure 4.2. Vertical component seismic section at station 3090 (See Appendix D for location of stations). We note that the reflector at 4000 ms could be related to the Base of Tertiary event (Modified from Stewart and et al., 2001).

Each OBS carries a hydrophone and an oil-filled three-component geophone package. These instruments are attached to steel weights with rope, and dropped into the water to sink to the sea floor (Hall and Stewart, 2002).

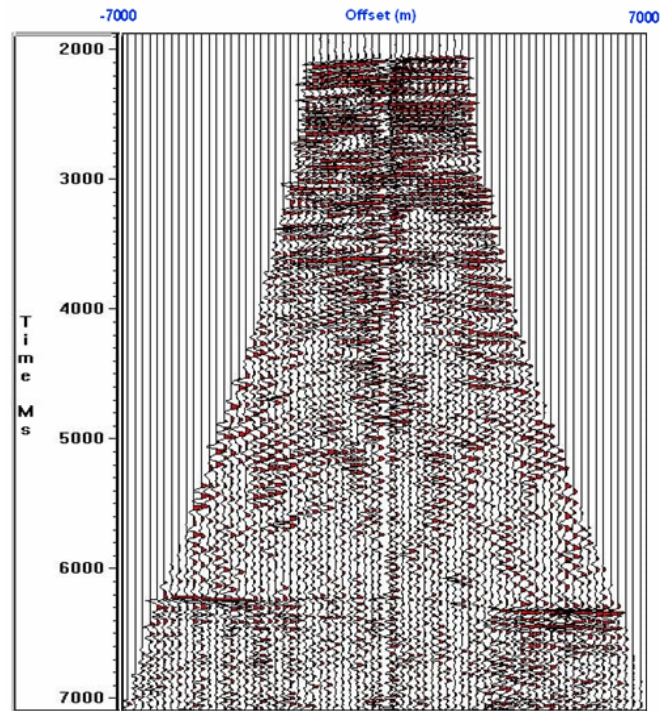


Figure 4.3. Radial component seismic section at station 3090 (See Appendix D for location of stations). We note that the reflector at 6000 ms could be related to the Base of Tertiary event and may correspond to the event at 4000 ms in Figure 4.2 (Modified from Stewart and et al., 2001).

The accuracy in positioning depends on water depth and local water currents. The positions of the drop points are known from GPS, and the final location point (Figure 4.6 and 4.7) of the OBS's were calculated with a technique that reduced the difference between the actual and predicted first-break times (assuming a constant water velocity of 1500 m/s throughout the water column). The instruments moved south from the drop points, drifting anywhere from 10 to 20m to their final locations on the sea floor (Cary and Stewart, 2003).

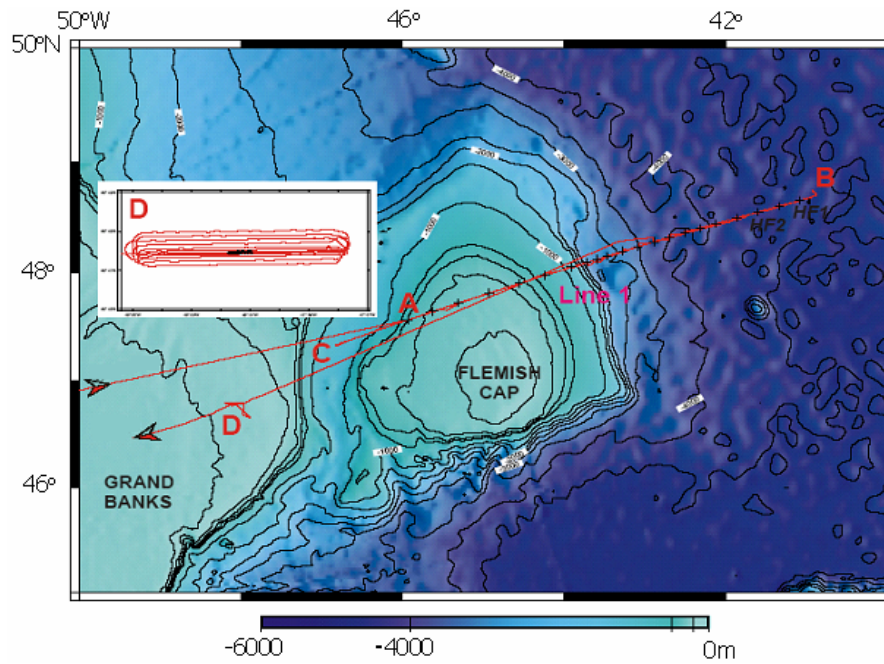


Figure 4.4: Showing the Hudson 2002-011 Line 1 and Hudson 2002-011 Line 2 (point D on the map), from the FLAME 2002 scientific expedition. (Modified from Jackson et al., 2002).

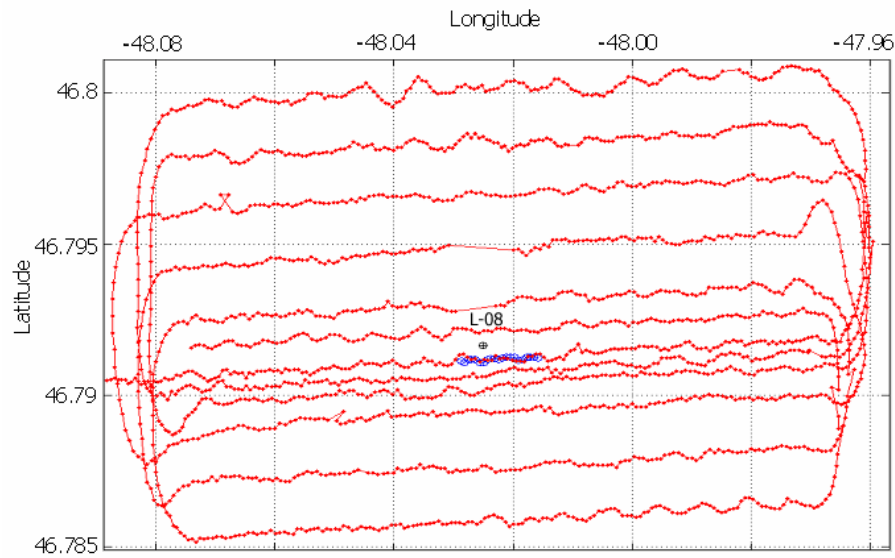


Figure 4.5: Location of source lines (red) and approximate position of 21 OBS receivers (blue). (Hall and Stewart, 2002).

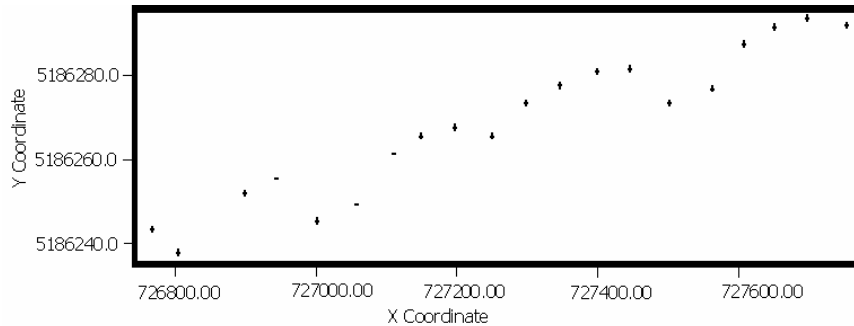


Figure 4.6: Receiver locations of the 21 OBS units, laterally exaggerated. (Modified from Hall and Stewart, 2002)

4.2.1 4C ocean-bottom seismometer (OBS) survey

The survey consisted of 21 OBS units (Figure 4.8) (normally used in crustal refraction experiments) deployed over 1 km with 12 sources lines from a towed air gun (Figure 4.9). There were numerous problems with the data. However, some promising final sections were achieved for both PP waves (vertical channel) and PS waves (radial channels). It has been stated that the final images show substantial promise for multi-component marine data in the White Rose area (Cary and Stewart, 2003).

The Avalon reservoir at the White Rose field is difficult to image using conventional marine seismic data. This is due to the effect of high amplitude water-column and peg-leg multiples. Another reason is the occurrence of gas clouds contained in the sediments (Hoffe et al., 2000). A multi-component ocean-bottom survey may possibly resolve these problems, since dual-sensor summation can be used to decrease the effect of out-of-plane multiples and converted waves are, in general, insensitive to the presence of gas (Hoffe et al., 2000).

To our knowledge, a 4C ocean-bottom cable (OBC) survey has not been conducted off the east coast of Canada. This may be due to the expense of the survey. However, Dalhousie University conducted ocean-bottom seismometer (OBS) surveys for deep crustal seismological research. The process of obtaining several shot gathers from a deep deployment in the summer 2000 cruise of the Dalhousie

OBS, showed energy on both the vertical and radial geophones. With these encouraging results, a four-component ocean-bottom seismometer (OBS) survey was acquired over White Rose oilfield using the Dalhousie OBS. The OBS survey was acquired during May/June of 2002 by Dalhousie University in a joint effort with the CREWES Project at the University of Calgary and Husky Energy Inc.

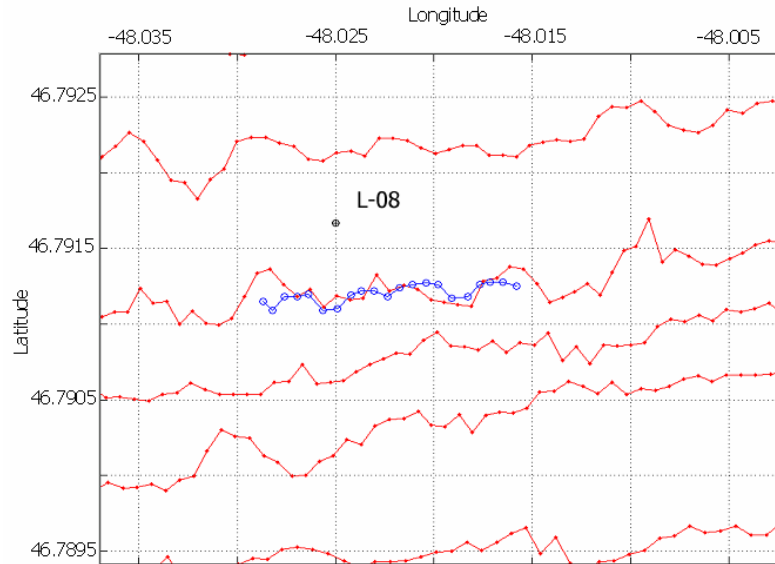


Figure 4.7: Receiver and source location. (Modified from Hall and Stewart, 2002)

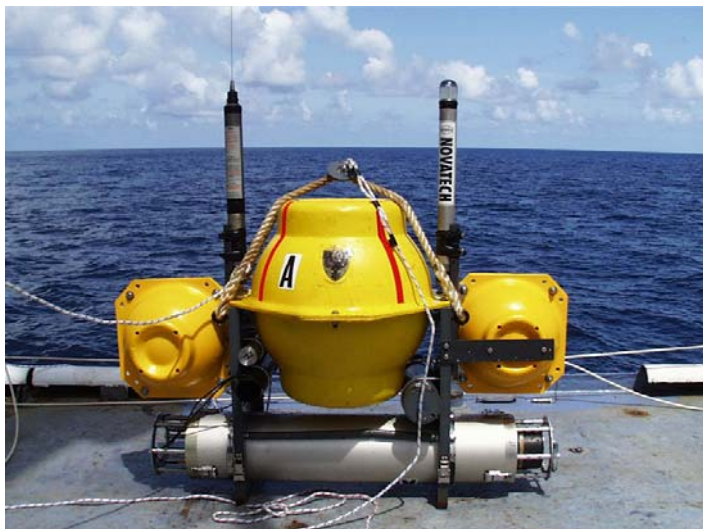


Figure 4.8: Dalhousie ocean-bottom seismometer (OBS). (Modified from www.phys.ocean.dal.ca/seismic, 2002)

The acquisition was performed with Dalhousie's ocean bottom seismometers. Until this survey, the instruments had not been used in shallow crustal exploration. According to Cary and Stewart (2003), some severe problems did occur with the quality of the data acquired, with several different types of noise being present.

The quality of the final stacks (section 4.2.3 Interpretation) gave encouraging results. The most reliable image came from the vertical component of the geophone, without the use of the hydrophone data. The horizontal components of the geophone show strong converted-wave reflection events. This study clearly shows that high-quality images are achievable with marine multi-component OBS data off the east coast of Canada.



Figure 4.9: Air gun array. (Modified from Jackson et al., 2002)

4.2.2 Processing of the OBS data

According to Cary and Stewart (2003), during the processing stage of the data, the polarity of the data for all components was kept equal with the recorded polarity.

There were numerous problems with the data, but some promising final sections were achieved for both PP waves (vertical channel) and PS waves (radial

channel). Processes applied to the data included data clipping repair, F-K and tau-p filtering, PP and PS stacking, and post-stack migration. The final images show substantial promise for multi-component marine data in the White Rose area (Cary and Stewart, 2003).

4.2.3 Interpretation

Before we start the interpretation of the OBS data, we need to do a correlation of the well log data from well H-20 (Chapter 3) and well L-08 (Figure 4.10). This would lend confidence to the interpretation of the different horizons on the OBS seismic sections. First, the synthetic seismograms from both wells were compared. In this case, we used a 45-Hz Ricker wavelet for both wells. The interpretation is in Figure 4.11, Panels (a) and (b).

- **Eocene (EOCN)-Tertiary E event (TrtE):** From the H-20 synthetic, the Eocene event is a strong peak which keeps almost the same amplitude with offset; on the PS synthetic the event increases amplitude with offset. In the L-08 synthetics, the event is strong in both PP and PS modes but less strong than the H-20's results. These two events are difficult to match.
- **South Mara (Smara):** The South Mara event is easy to identify in both wells, having a strong peak. In well H-20, the amplitude is constant on the PP section, and on the PS section the amplitude increases with offset. In well L-08, the amplitude decreases with offset for the P wave and increases with offset for the S wave. The events are easy to correlate.
- **Base of Tertiary Unconformity (Btrt):** The Base of Tertiary unconformity is our event guide, as the strongest event is the seismogram. On both wells, the event is constant on the PP synthetic and increases amplitude with offset in the PS seismogram. The event is very easy to correlate between wells.

- **Nautilus Shale (Naut):** The Nautilus shale has a strong response in well H-20, exhibiting increasing amplitude with offset. The event in the well L-08 is not as strong as well H-20 but still recognizable. In well L-08, the event decreases in amplitude with offset. The event can be match between wells.
- **Avalon Formation (Aval):** The Avalon formation shows a strong event in well H-20. The event increases in amplitude with offset for the P and S sections. In well L-08, the event is not easy to identify. The amplitude of the event is not strong and the event is related to a zero crossing of the trace in the P and S seismograms. It was not possible to correlate the event between wells.
- **Eastern Shoals (Eshl):** This event is strong in both wells. On the P seismograms from both wells, the amplitude increases with offset. The PS seismograms in both wells show that the event decreases its amplitude with offset. The Eastern Shoals event is correlated between wells.

It is important to remember that the distance in a straight line between these two wells is close to 4 km. This could be one of the reasons for the difficulty in correlating the Avalon Formation between them, as well as the complexity of the structures present in the area. Below the Tertiary unconformity, the presence of several regional faults affects the sequence, as do the compaction processes that took place in the area, affecting the lithological units in some manner at each location.

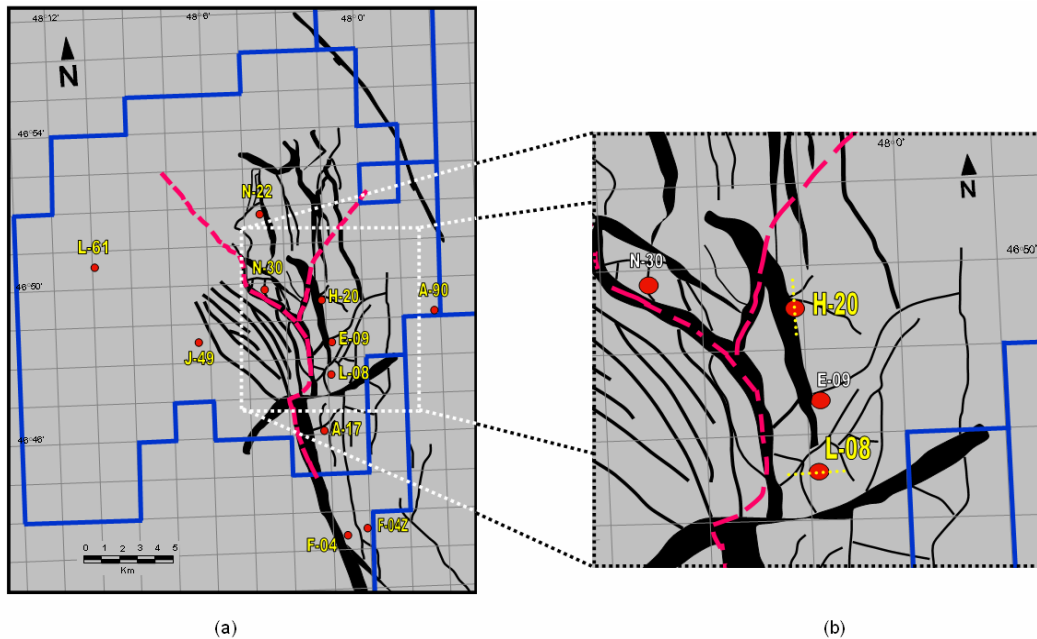


Figure 4.10: Location of well L-08 at the White Rose field. (Modified after Husky Oil Operations Ltd, 2001)

After the correlation between H-20 and L-08 wells, we applied a bandpass filter (4/8 25/30) to our 45-Hz Ricker wavelet seismograms to obtain a better result (Figures 4.12). The analysis of the interpretation is in Figure 4.12, Panels (a) and (b).

- **Tertiary E event (TrtE):** This event is strong in both panels. The amplitude is kept constant with offset for the P section. An increase in amplitude with offset is seen in the PS section.
- **South Mara (Smara):** The South Mara is a strong event and easy to identify. The amplitude is also kept constant, with an increase in amplitude with offset in the PS seismogram.
- **Base of Tertiary Unconformity (Btrt):** This event has a strong response with the bandpass applied. The amplitude increases with offset on both synthetics.

- **Nautilus Shale (Naut):** This event is not evident in the P seismogram. On the PS seismogram, the event is defined as a zero crossing and as a peak, but is still difficult to distinguish.
- **Avalon Formation (Aval):** The results are good; we can see the event on both sections. The P seismogram shows an event that decreases its amplitude with offset but can be seen at ~1000 m offset. The PS synthetic shows a better reflector that is easy to follow.
- **Eastern Shoals (Eshl):** The Eastern Shoals is also a strong event. The amplitude increases with offset and we can correlate both synthetics easily.

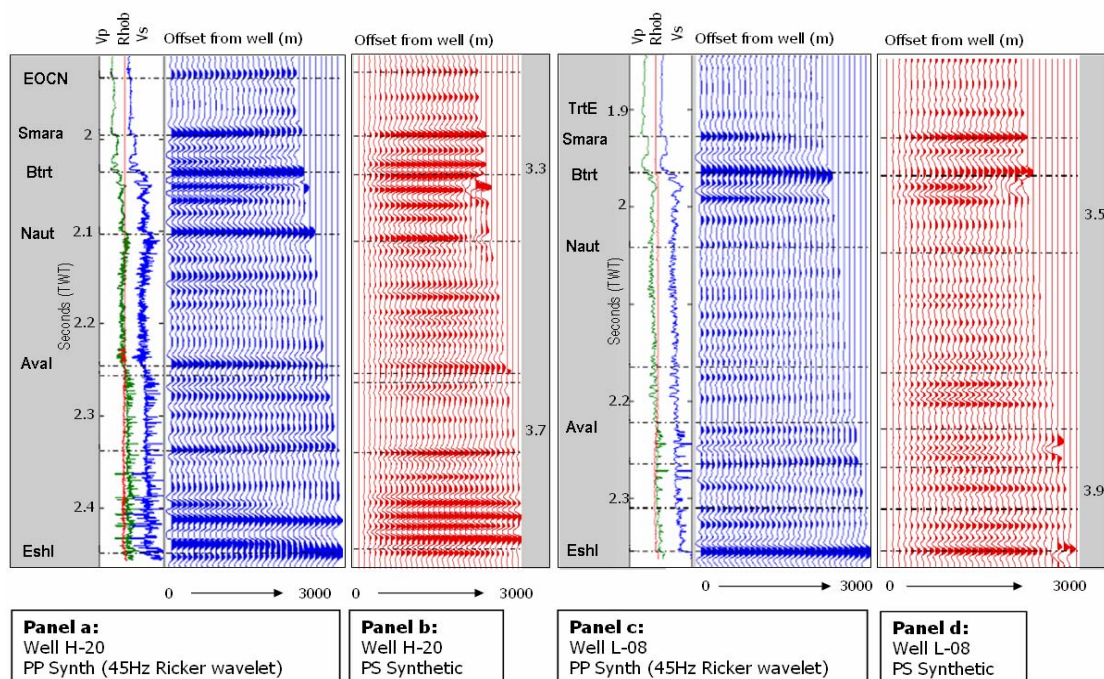


Figure. 4.11: Results from correlating the PP and PS synthetics from wells H-20 and L-08.

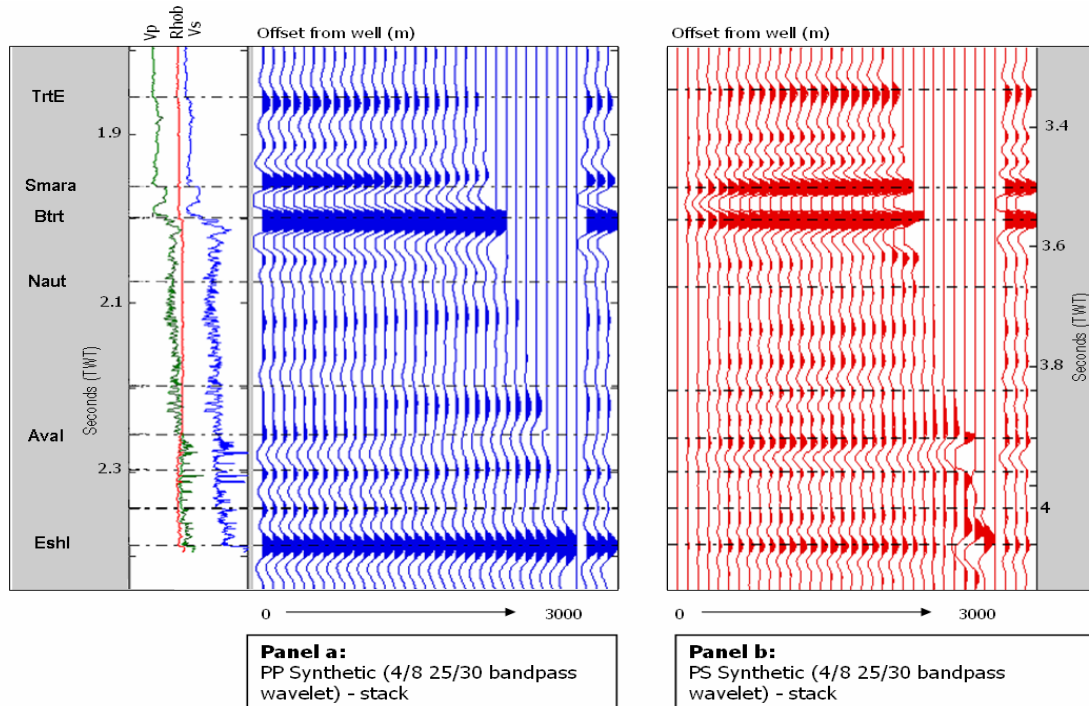


Figure 4.12: Result from matching the PP and PS synthetics from well L-08.

After doing the interpretation and correlation of these two wells (L-08 and H-20, Figures 4.11 and 4.12) we can start with the OBS interpretation. These correlations between wells will help in the process of correlation between the well L-08 and the OBS seismic data.

The data used to do the converted-wave interpretation is from the White Rose oilfield 3D-4C (ocean-bottom seismometer) OBS survey that took place in summer 2002.

There are three non-migrated (structure) and migrated post-stack seismic datasets, respectively, for a total of six post-stack datasets. The respective stacks were recorded by vertical, horizontal (or radial), and hydrophone (or pressure) components (section 4.2.3 Interpretation). The recorded two-way traveltime for the hydrophone (pressure), vertical and horizontal (radial) components are 6.0, 6.0, and 12.0 seconds respectively. All of the datasets were recorded with a 2.0 ms sample

interval. This study concentrated on the migrated post-stack data (section 4.2.3 Interpretation). The bin size was set at 25x25 m, inline (N-S Line 1-216), crossline (E-W Line 1-35), (Figure 4.13). The survey took place over a complex structure in the White Rose field (Figure 4.10).

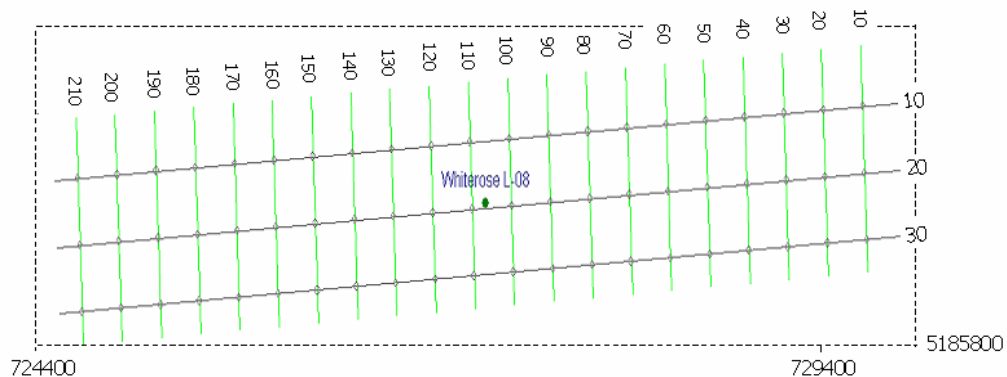


Figure 4.13: CDP grid displayed using Kingdom suite software showing the location of well L-08. There were 35 east-west inlines and 216 north-south crosslines.

During the interpretation stage of the project, we used Hampson-Russell PROMC software. This software is designed to help in the analysis and interpretation of multi-component seismic data. The OBS data and the L-08 well data (V_p , V_s , GR, and ρ — Figure 4.14) were loaded to start the interpretation. After loading the OBS data (vertical, radial and hydrophone components data), well L-08 was tied, to lend more confidence to the horizons defined on the OBS data.

Before the interpretation started, the Base of Tertiary unconformity event was flattened to facilitate an improved image of the horizons below this event. The horizons were picked on the seismic sections. The interpretation of the seismic data began with the correlation of the Base of Tertiary unconformity on both sections (well log data and seismic) and from that point the other events were correlated — in this case, Tertiary formation, South Mara, Nautilus, Avalon, and Eastern Shoals. On the seismic, the presence of a strong and continuous event below the Eastern Shoals was also noticeable, which we called Horizon. This event was used as a

complementary guide to help define the main events (Tertiary E, South Mara, Base of Tertiary, Nautilus, Avalon, and Eastern shoals).

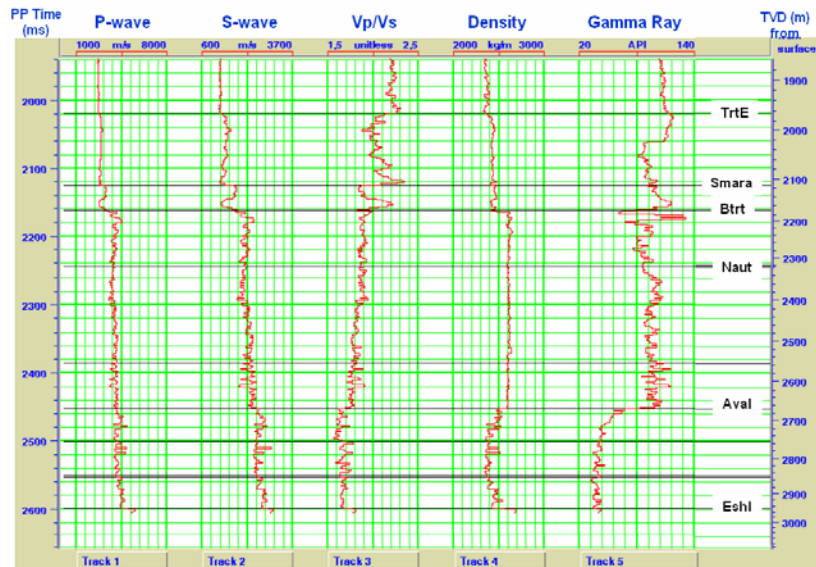


Figure 4.14: Well logs from well L-08 (P wave, S wave, Vp/Vs, ρ , GR, tops of the sequence).

► PP (Vertical component) interpretation

The data found in this component is clear (Figure. 4.15): there are some seismic events that can be followed along the survey without difficulty (South Mara, Base of Tertiary, and Nautilus). The analysis is seen in Figure 4.15. In general, the seismic section shows that the Tertiary events are continuous, with strong seismic signatures. Below the Tertiary unconformity, events can be followed; however, there is a lot of disturbance in the Avalon and Eastern Shoals events. This could be due to imaging, structural factors, unattenuated multiples or out of line energy.

After tying the L-08 well log to the OBS vertical seismic data, we used the PP synthetic seismogram (4/8 25/30 bandpass wavelet; Figure 4.12, Panel (a)) to help us obtain a better correlation of the horizons, which are defined as follows:

- **South Mara and Base of Tertiary unconformity:** are the two events that have a strong seismic signature along the survey. Both events are strong and display a flat horizon;
- **Nautilus:** this event can be interpreted as a “flat horizon”. Analyzing the data from north to south we can observe that the top is affected by some compressional faults on the west side of the survey, the presence of these thrust faults is more evident on the east side of the survey than on the west side, where the faults do not affect the event as much.
- **Avalon:** this event appears as a continuous horizon that in some parts seems to disappear into an upper event. This disturbance could be due to imaging, structural factors, unattenuated multiples or out of line energy. In other parts, it is easy to follow.
- **Eastern Shoals:** the event can be followed, although in some parts there are some break-ups in the event which could indicate faulting events or imaging problems.

After comparing the seismic vertical component data and the PP synthetic (Figure. 4.15), a good correlation between the Tertiary E, South Mara, Tertiary Unconformity and Eastern Shoals was found. The results for the Avalon, and Nautilus are not as good as the other events, but are encouraging. As noted previously, the Base of Tertiary event was flattened; however, the events below this unconformity shows a certain uplift on the west side that could be due to the effect of the faults that surround the area where well L-08 is located (Figure 4.15).

On Figure 4.16, the time slice for each event shows the general behaviour of the events along the survey. In general, the trend of the events show a smaller time value on the west side of the survey which agree with the trend found in the area of well L-08 on the White Rose - PGS 97 3D survey (Figure 4.17). The events above the Tertiary unconformity and below show a generally flat sequence that has a minor uplift on the west side of the survey. The uplift of Avalon and Eastern Shoals is

greater (Figure 4.16).

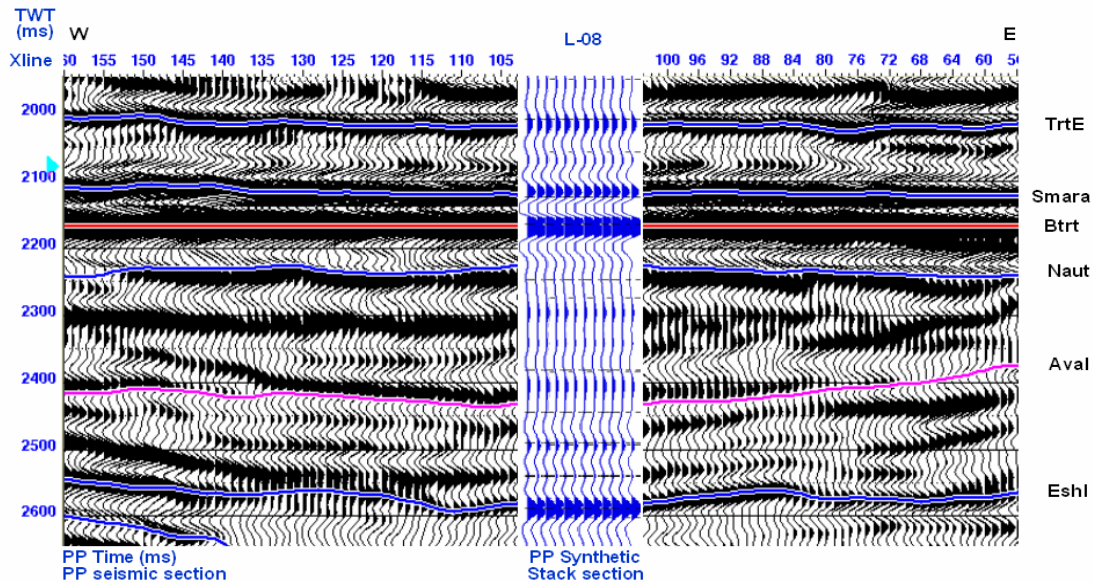


Figure 4.15: Well L-08 PP synthetic and vertical component sections, showing Inline 19 in a W-E direction. The horizons have been defined (TrtE, South Mara, Base of Tertiary, Nautilus, Avalon, and Eastern Shoals) after tying the well L-08 with the seismic. The data was flattened at the Base of Tertiary unconformity to facilitate the interpretation.

Figure 4.18 shows the different time thickness maps for the P seismic section: the Tertiary E (~85–127 ms), Avalon (~73–177 ms), and Eastern Shoals (~38–125 ms) thickness maps have a very similar time variation. South Mara (~42–64 ms) and Base of Tertiary (~43–81 ms) have a small time variation showing thin horizons. The Nautilus map shows the largest time variation ~129–245 ms, being the thickest horizon.

► Hydrophone (pressure component) interpretation

This component (Figure. 4.19) shows clear seismic results, most of the horizons being easy to follow. The seismic result shows a very approachable section where the Tertiary events are identified easily and that can be followed from E to W. The Cretaceous horizons are easy to follow, although they seem to be affected by faulting. Even so, almost the entire event can be followed along the seismic section.

The quality of these sections could be due to the increase sensitivity of the hydrophone to the reflected waves.

After tying the L-08 well log to the OBS horizontal seismic data, we used a PP synthetic seismogram (4/8 25/30 bandpass wavelet; Figure 4.12, Panel (a)). The following analysis refers to Figure 4.19:

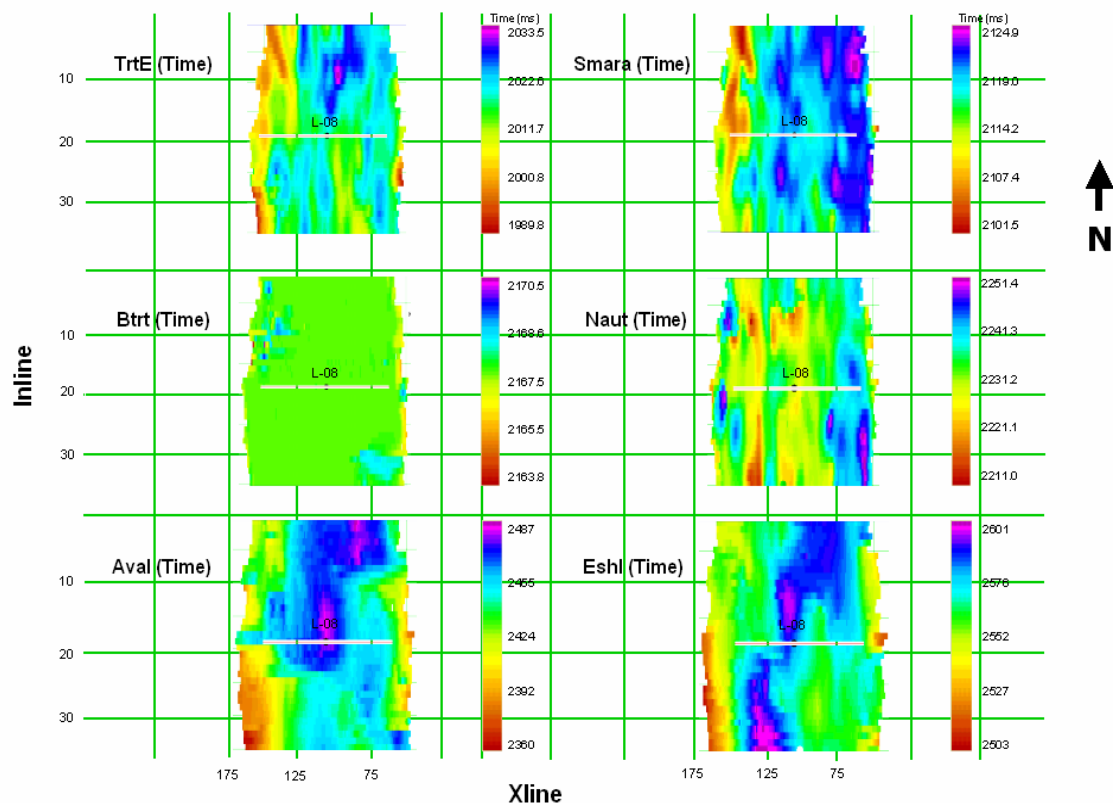


Figure 4.16: Time slices of each of the events interpreted on the vertical component seismic section. The horizons defined are: Tertiary E, South Mara, Base of Tertiary, Nautilus, Avalon, and Eastern Shoals events. Well L-08 is shown on each time slice.

- South Mara and Base of Tertiary unconformity:** both events are easy to identify. Still, the Base of Tertiary event has stronger impedance than the South Mara event. These events can be seen as flat features, very similar to those seen on the vertical and radial components. The Base of Tertiary event is not as strong as it is on the vertical component; this is similar to the response of the radial component, allowing us to have better

reflections from the Avalon event. These results, along with the similar results from the PS component, give an improved image of the reservoir over that obtained if we just used the PP results. Both events can be followed easily along the survey.

- **Nautilus:** is a continuous event. This event shows up better on this component than on the vertical or radial components. The amplitude is strong and it seems to be affected by some faults on the NE side of the survey.
- **Avalon:** can be followed along the section. The amplitude is strong. It seems to be some faults affecting the event. This component shows an improved image of the horizon.

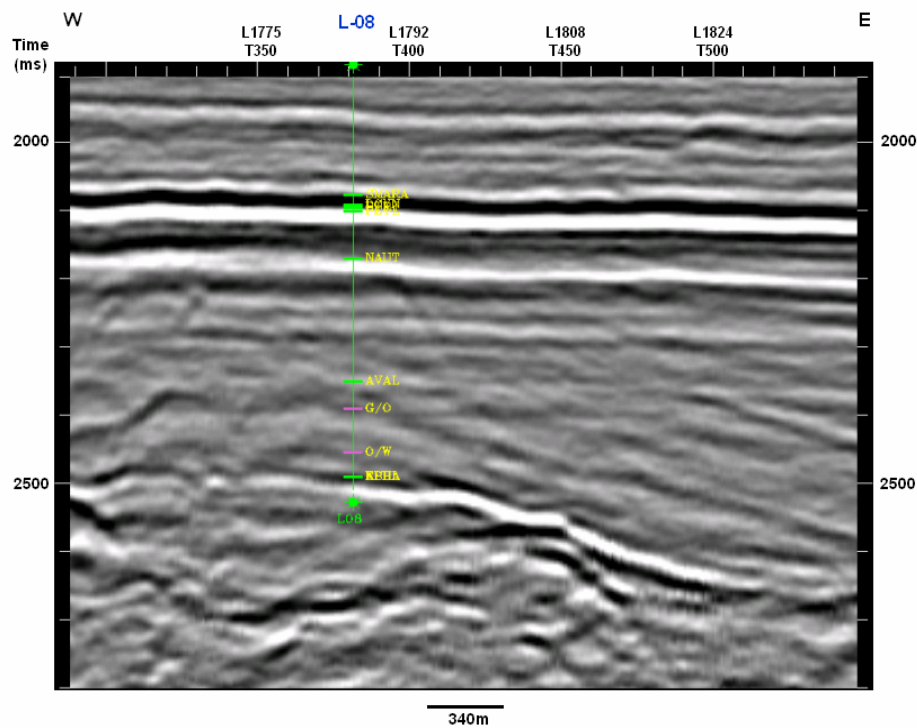


Figure. 4.17: Streamer P-seismic section from White Rose PGS-97 3D survey. Well L-08 is shown, along with the South Mara, Base of Tertiary, Nautilus, Avalon, and Eastern Shoals events. Uplifting of the Avalon and Eastern Shoals Formations can be seen, due to faults in the stratigraphy creating a complex structural area. (Modified from Emery, 2001).

- **Eastern Shoals:** is only seen in the SW part of the section, where there is continuous and strong amplitude that reduces until nearly disappearing. On the PP section, this event does not appear to be affected by faults. For that reason, the disappearance of the event could be due to imaging problems.

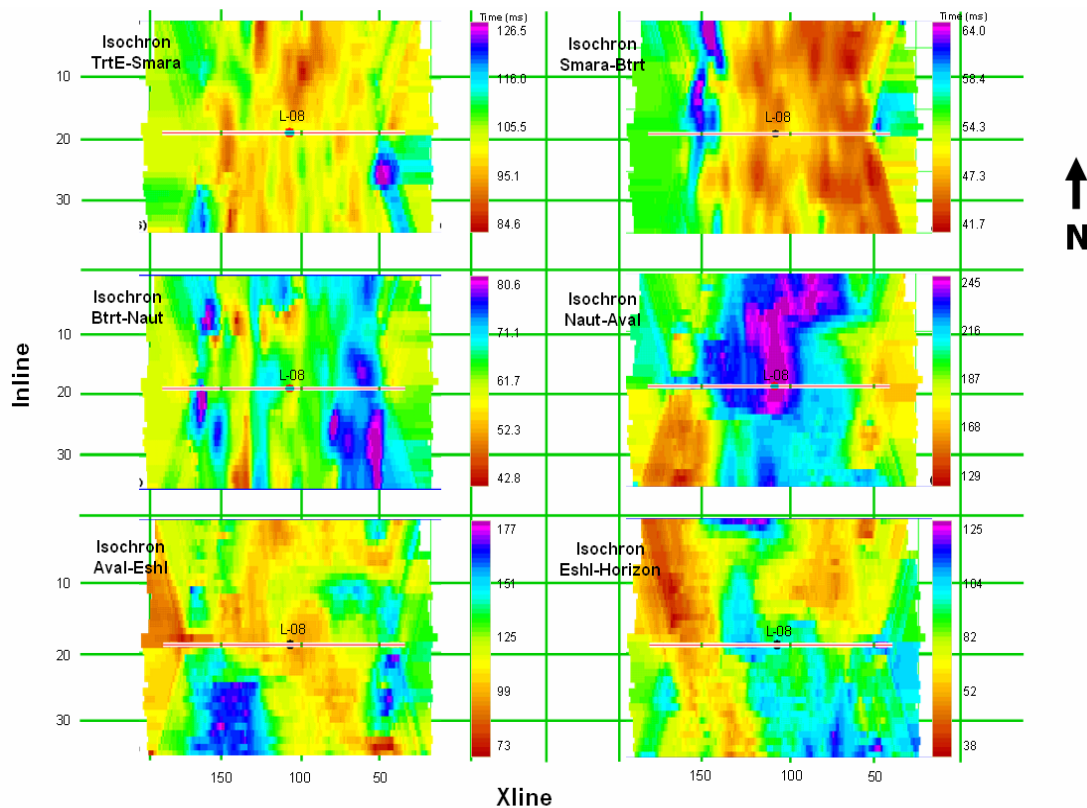


Figure. 4.18: PP time thickness maps between the main horizons (Tertiary E, South Mara, Base of Tertiary, Nautilus, Avalon and Eastern Shoals) of the survey. Well L-08 is shown on each time thickness map.

The results from the comparison between the seismic pressure component data and the PP synthetic (Figure. 4.19), are similar to those obtained from the PP section (Figure. 4.15). It is possible to match the Tertiary events and the Eastern Shoals event. The other events (Nautilus and Avalon) could appear to be shifted due to sonic stretch.

In addition time-slice analysis was conducted on this component (Figure 4.20). The general behaviour of the events along the survey can be seen. The Tertiary E, South Mara, Tertiary Unconformity, and Nautilus are smooth events with slight uplift; Avalon, and Eastern Shoals show a subtle uplift of the events.

For the hydrophone seismic section, the thickness maps are on P time (Figure 4.21). Tertiary E (~82–116 ms), Base of Tertiary (~64–120 ms), Avalon (~99–180 ms) and Eastern Shoals (~67–144 ms) thickness maps show a very similar time variation. South Mara (~41–59 ms) is the thinnest horizon. The Nautilus map is the thickest horizon with a large time variation ~140–225 ms.

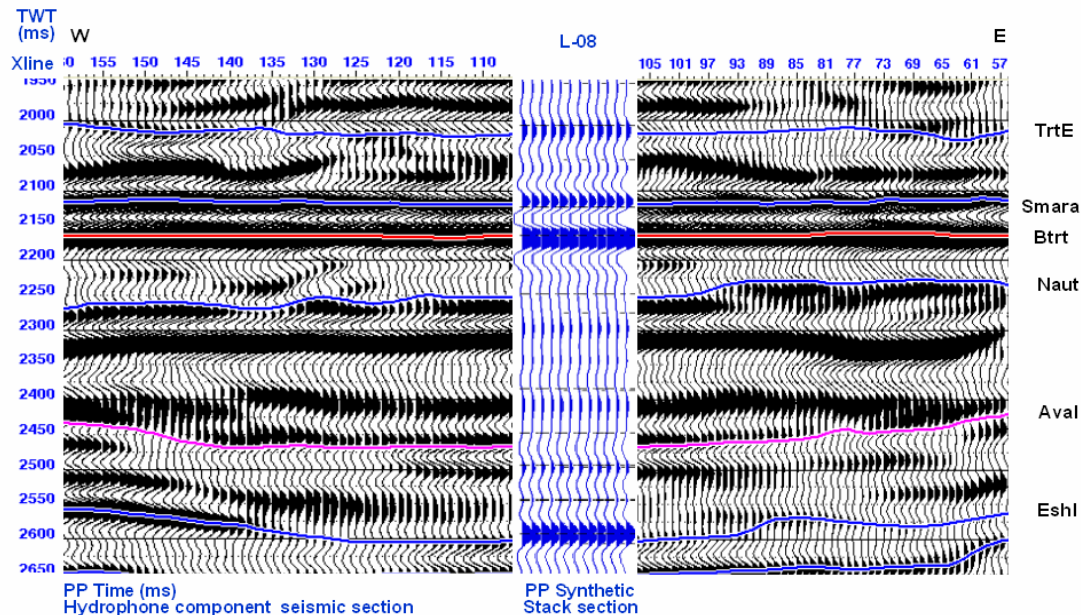


Figure 4.19: Well L-08 PP synthetic and hydrophone component section showing Inline 19. The horizons defined (TrtE, South Mara, Base of Tertiary, Nautilus, Avalon and Eastern Shoals) after tying the well L-08 with the seismic. The data was flattened at the Base of Tertiary unconformity to facilitate the interpretation.

► PS (Radial component) interpretation

This component (Figure. 4.22) reveals complex seismic results. Most of the horizons are difficult to follow but, in general, the final outcome is reasonable. The Tertiary events show some irregularities; they are not continuous as in the PP

seismic section. The amplitude of the Tertiary events is lower than the amplitude found in the PP seismic section. For the Cretaceous events, below the Nautilus (~4100 ms PS time) the horizons cannot be easily defined: there is irregularity that could be due to the imaging or to the presence of faults that are affecting the horizons (for example, around 2400 ms on the W side of the PP section Figure 4.15) and that make it difficult to follow the events (Avalon and Eastern Shoals Formations).

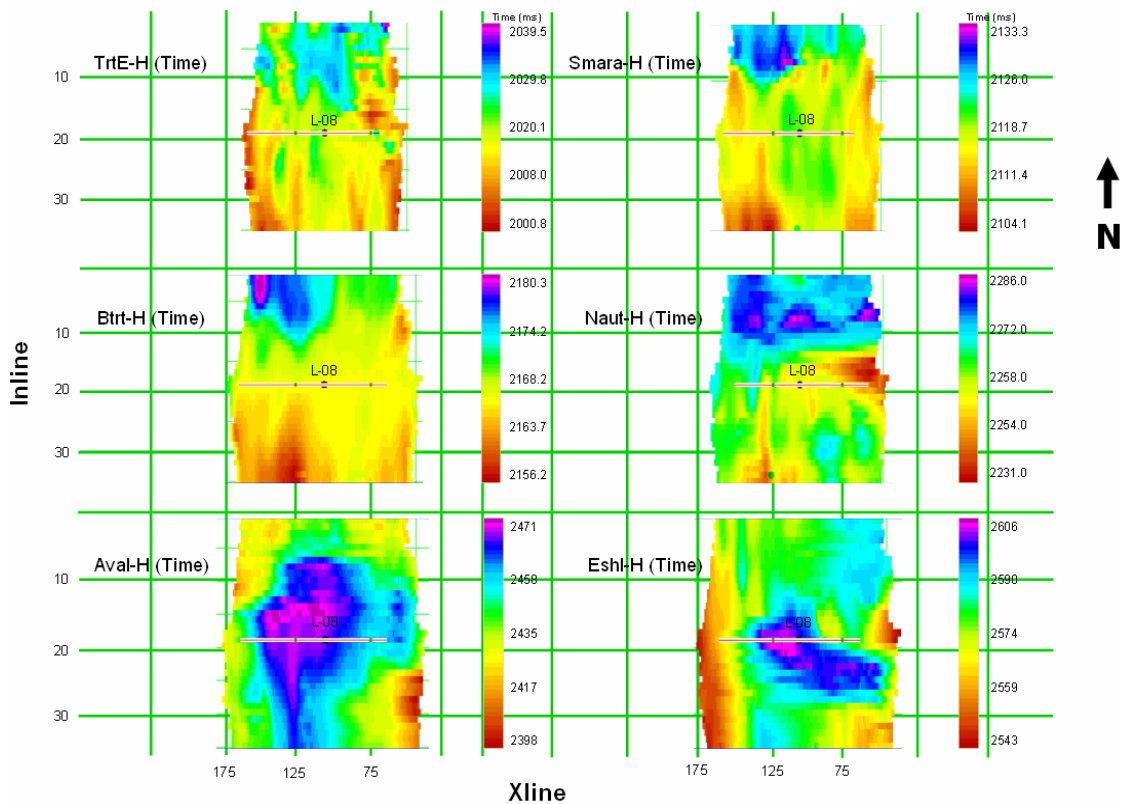


Figure. 4.20: Time slices of each of the events interpreted on the hydrophone component seismic section. The horizons defined are Tertiary E, South Mara, Base of Tertiary, Nautilus, Avalon, and Eastern Shoals events. Well L-08 is shown on each time slice.

After tying up the L-08 well log to the OBS horizontal seismic data, we used the PS synthetic seismogram (4/8 25/30 bandpass wavelet, Figure 4.12, Panel (b)). Then horizons were defined as follows (the interpretation can be seen in Figure 4.22):

- **South Mara and Base of Tertiary unconformity:** Once the Base of Tertiary event has been identified, the South Mara can be placed as the strong event above it. These events appear to be flat, as was observed on the vertical component. The Base of Tertiary event is not as strong as it is on the vertical component. This factor allows us to obtain an improved image of the reflections from the Avalon Formation. The South Mara is not a continuous event in the north section of the survey.
- **Nautilus:** This is a strong event that is difficult to follow, despite its strong seismic signature. This event is faulted and irregular in most of the area.
- **Avalon:** On the PP section, this event is difficult to define; on the PS section it is difficult to see any continuity of the event in the north section of the survey. Of all the previous events, the Avalon event is the most affected. However, the interpretation of this event along the south section of the survey is possible. The difficulty of seeing the event clearly in the north section could be due to the presence of noise and faulting affecting the area. The amplitude of the event varies along the survey.
- **Eastern Shoals:** Comparing the results from the Avalon top, this event, shows a small continuity of the horizon. It is still not a strong peak, but gives some kind of continuity of the event. The amplitude of this event changes constantly making it difficult to define the horizon.

The results from the comparison between the seismic radial component data and the PS synthetic (Figure. 4.22) are encouraging. The correlation of the Nautilus, Avalon and Eastern Shoals events are improved in the PS analysis. However, we have to bear in mind that the continuity on the radial section sometimes makes it difficult to follow the events (Avalon and Eastern Shoals Formations) along the seismic section. Despite this the results are reasonable.

Figure 4.23 shows the PS time slice for each event on the radial component. The general behaviour of the events along the survey can be seen. The general trend of the Tertiary events (Tertiary E, South Mara, and Tertiary Unconformity) is a subtle uplift on the west side of the survey. The Cretaceous events (Nautilus, Avalon and Eastern Shoals) are difficult to define as trend. This could be due to noise in the data.

The different thickness maps for the PS seismic section are shown in Figure 4.24. Tertiary E (~141–202 ms), Base Tertiary (~87–153 ms), Avalon (~62–193 ms) and Eastern Shoals (~66–196 ms) thickness maps have a very similar time variation. South Mara (~48–111 ms), with a small time variation, is the thinnest horizon. The Nautilus map thickness shows the largest time variation at ~206–300 ms.

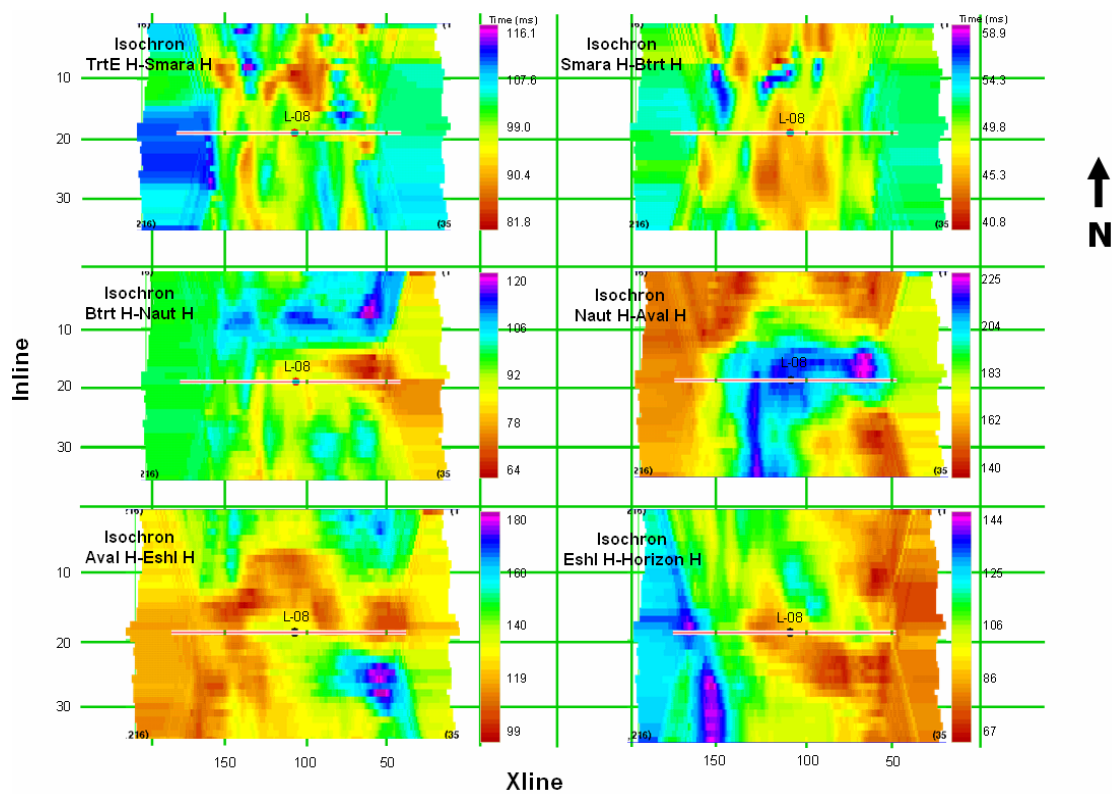


Figure. 4.21: Hydrophone time thickness maps on P time between the main horizons (Tertiary E, South Mara, Base of Tertiary, Nautilus, Avalon and Eastern Shoals) of the survey. Well L-08 is shown on each time thickness map.

Comparing the three-component (vertical, radial, and hydrophone) time thickness maps, the largest time variation is on the radial component. The vertical and hydrophone have a similar time variation range. In general, the Nautilus horizon has the largest time variation on the three components (~300 ms). South Mara horizon is the thinnest on the different components (~111 ms). Tertiary E, Base of Tertiary, Avalon, and Eastern Shoals have time thicknesses up to ~200 ms.

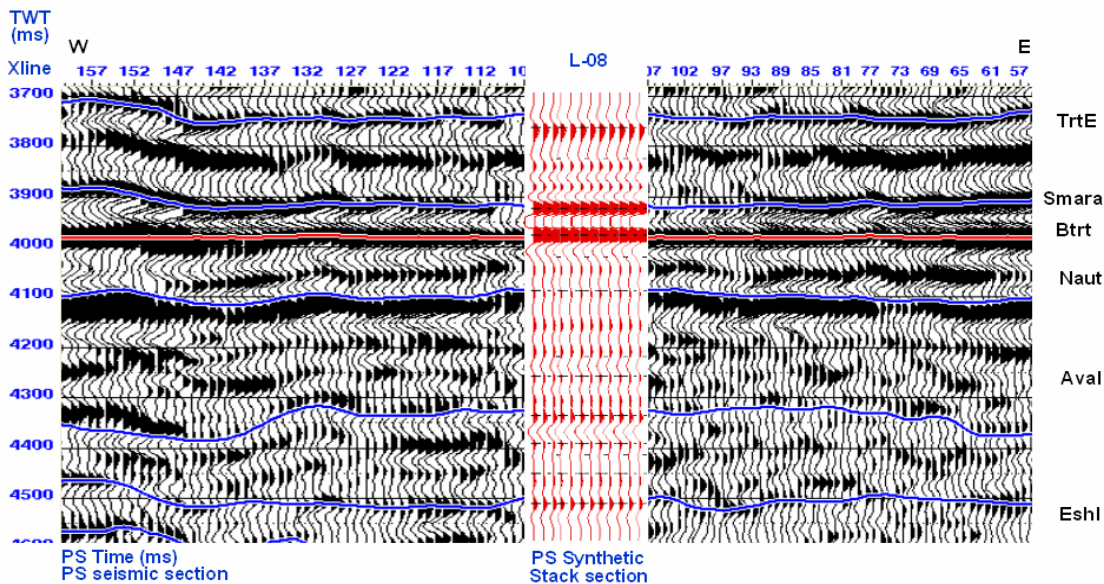


Figure 4.22: Well L-08 PS synthetic and radial component section showing Inline 19. The horizons were defined (TrtE, South Mara, Base of Tertiary, Nautilus, Avalon, and Eastern Shoals) after tying well L-08 with the seismic. The data was flattened at the Base of Tertiary unconformity to facilitate the interpretation.

4.2.4 Correlation

Before the correlation it was necessary to pick all the events (Tertiary, South Mara, Base of Tertiary, Nautilus, Avalon, and Eastern Shoals and Horizon) on both PP (vertical) and PS (radial) seismic sections, with the help from the well log data. The PS data is transformed into PP time using the velocity information from the well log (L-08). For this case it was assumed a V_p/V_s value of 2.0. In the process of horizon matching, a link is established between traces (all PS events are forced to

match the same events in PP time). As a result of this time adjustment the Vp/Vs is calculated (Figure 4.28).

► **PP (Vertical component OBS data) - PS (Radial component OBS data)**

Once the radial component is mapped into PP time, we can correlate it with the vertical component seismic section (Figure. 4.25). It is observable that all the different events involved in the interpretation (TrtE, South Mara, Base of Tertiary, Nautilus, Avalon and Eastern Shoals, Horizon) have a reasonably good match, although there is still some ambiguity with the Nautilus and Avalon events. There are some problems to correlate these Formations but despite this the results show a great advance in imaging the reservoir.

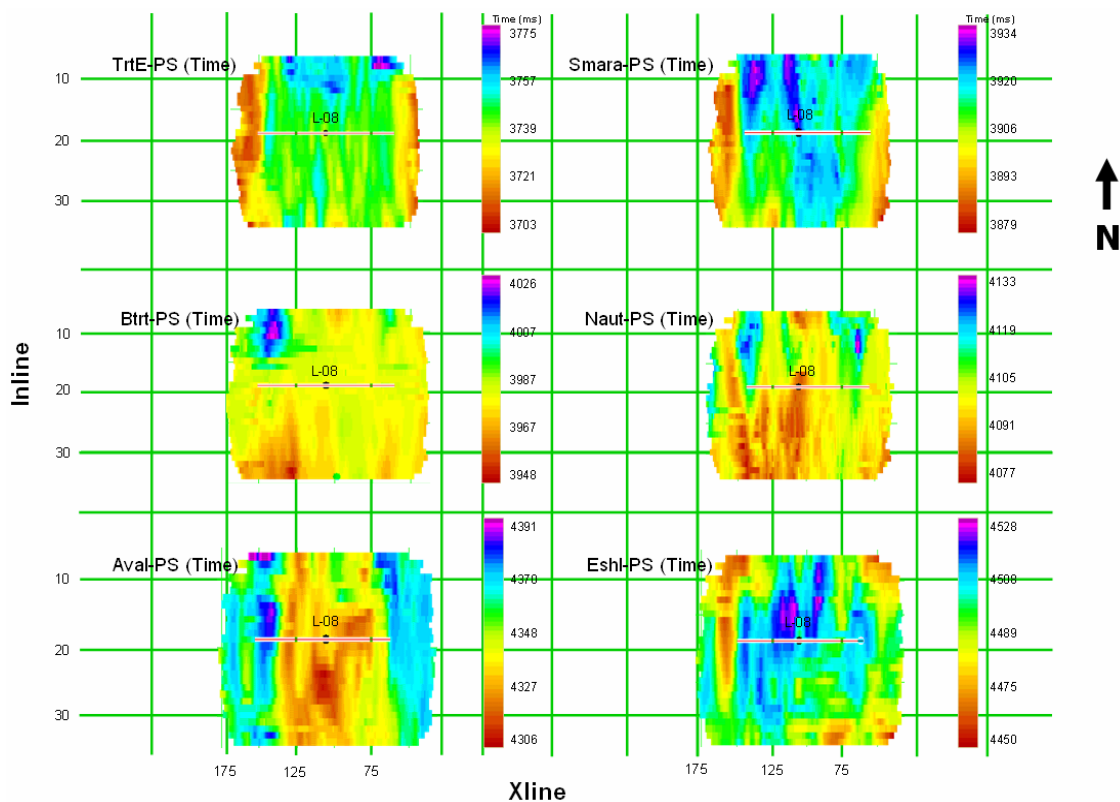


Figure 4.23: Time slices of each of the events interpreted on the radial component (PS-wave) seismic section. The horizons defined are Tertiary E, South Mara, Base of Tertiary, Nautilus, Avalon and Eastern Shoals events. Well L-08 is shown on each time slice.

► **PP (Vertical component OBS data) – Streamer P data 1997**

During the summer of 1997, a streamer seismic survey (the White Rose PGS 97, Figure 4.17) was acquired over a hexagonal area of 311 km². This survey was done to understand the structural and tectonic framework, to correlate stratigraphy, and locate delineation and development wells for interpreting the White Rose Field (Husky Oil Operations Ltd, 2001).

There was a good correlation between the P streamer data and the OBS P data (Figure 4.26). The match of the different horizons (South Mara, Base of Tertiary, Nautilus, Avalon and Eastern Shoals) was reasonable.

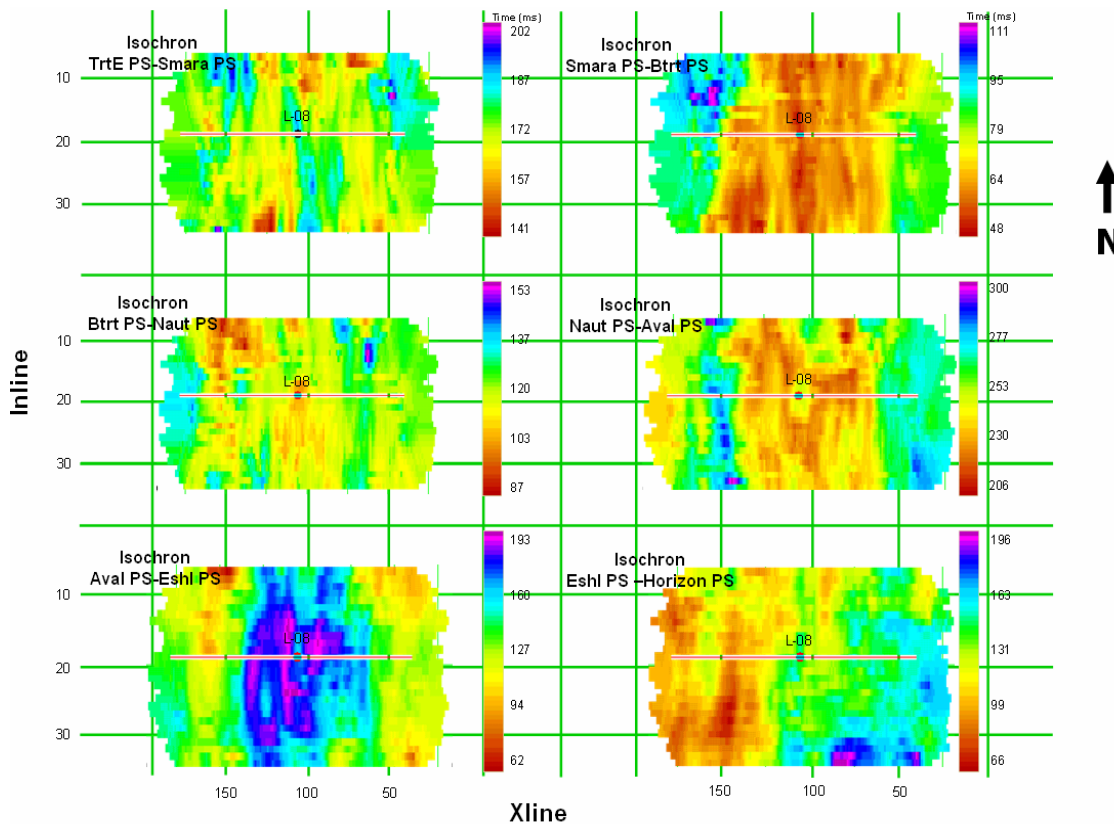


Figure 4.24: PS time thickness maps between the main horizons (Tertiary E, South Mara, Base of Tertiary, Nautilus, Avalon, and Eastern Shoals) of the survey. Well L-08 is shown on each time thickness map.

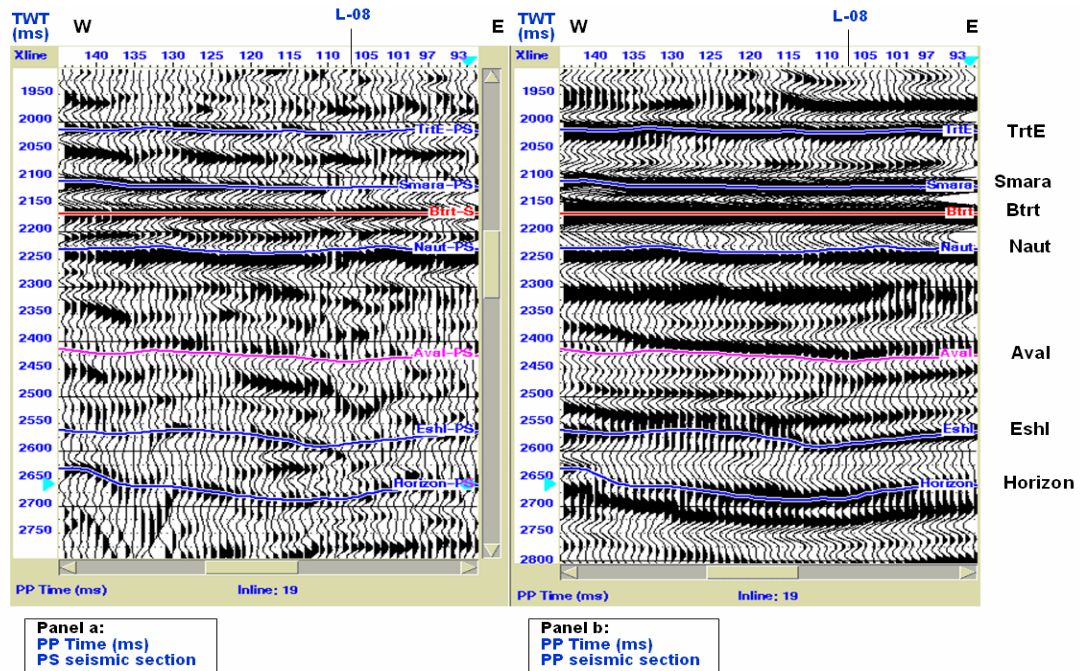


Figure 4.25: Radial component (Panel a) and vertical component (Panel b) seismic sections mapped on PP time, showing the different horizons defined (TrtE, South Mara, Base of Tertiary, Nautilus, Avalon, and Eastern Shoals) after tying the GR well log. Well L-08 is annotated on the seismic, showing Inline: 19 for both sections.

► **PS (Radial component OBS data) - Hydrophone (Pressure component OBS data)**

The pressure component and the radial component seismic sections (Figure 4.27), shows a reasonable correlation for the Tertiary events (South Mara and Base of Tertiary). The TrtE event is shifted. The Cretaceous events do not show good correlation. The Nautilus and Avalon events can be followed from component to component. There is no correlation for the Eastern Shoals and the Horizon events.

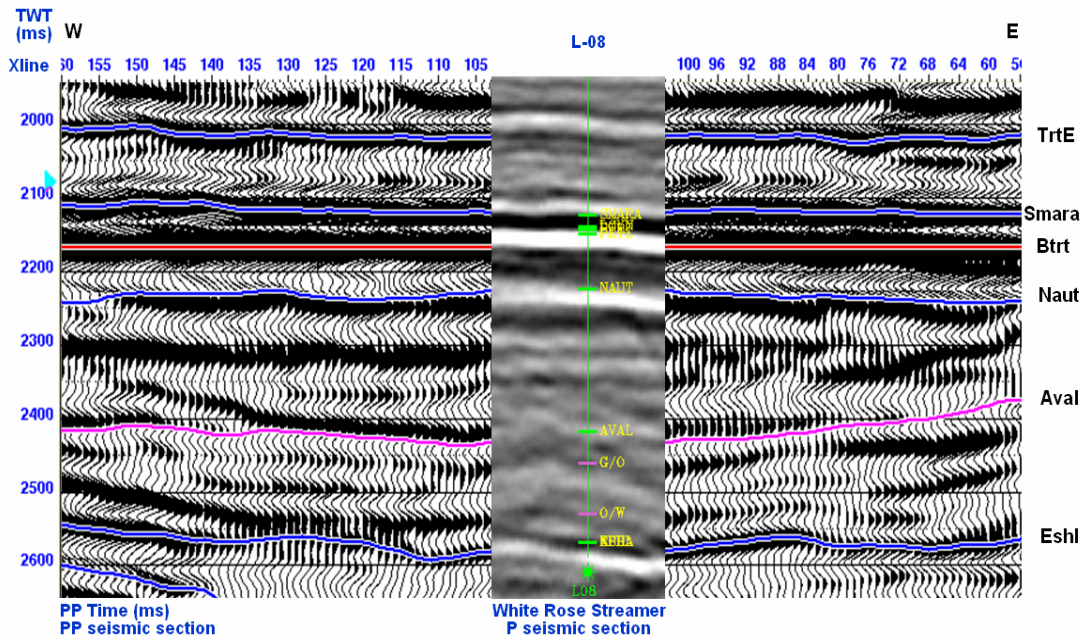


Figure 4.26: Correlation between the OBS P data and the Streamer P data. Showing the correlation between the different horizons (TrtE, South Mara, Base Tertiary, Nautilus, Avalon and Eastern Shoals) with well L-08.

4.2.5 Vp/Vs analysis

After mapping the PS data into PP time, the horizons from the vertical and the radial components were correlated, making it possible to see the Vp/Vs values used on the matching process of the seismic sections (Figure 4.28).

Figure 4.28 shows that for the Tertiary E horizon there is a Vp/Vs of ~ 1.84 – 3.59 , interpreted as shales, while South Mara, with a Vp/Vs ~ 1.81 – 2.21 , is interpreted as sandstones and siltstones. The horizon directly beneath the Tertiary unconformity is comprised of sediments of Petrel limestone; the values found in the seismic section are ~ 1.81 – 2.23 . Nautilus has approximate values of 1.67 – 1.98 for shales and sandstones. The Avalon horizon has a range of values from ~ 1.52 – 1.91 . Eastern Shoals has a wide range of values from ~ 1.7 – 1.81 , interpreted as calcareous sandstone-siltstone.

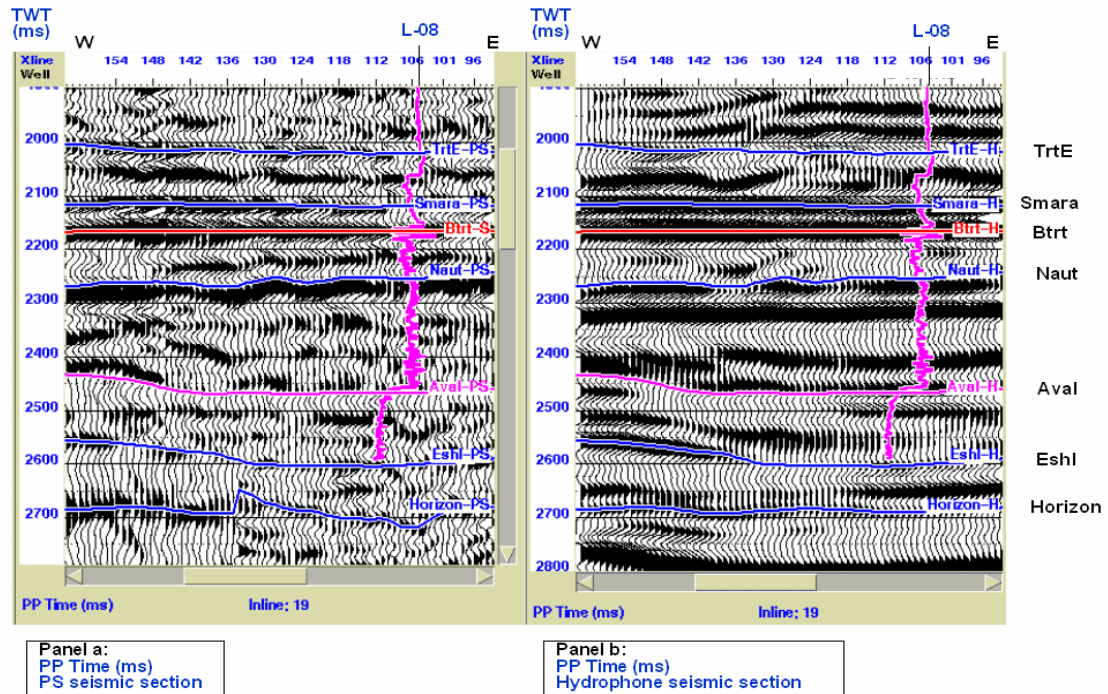


Figure 4.27: Radial component (Panel a) and pressure component (Panel b) seismic sections mapped on PP time, showing Inline 19 for both sections and with the different horizons defined (TrtE, South Mara, Base of Tertiary, Nautilus, Avalon, and Eastern Shoals) after tying the GR well log. Well L-08 is annotated on the seismic.

The use of average interval V_p/V_s maps aid in interpreting the V_p/V_s values (Figure 4.29). The area in general shows V_p/V_s values that decrease with depth. During the interpretation of each horizon, V_p/V_s lateral variations were found (Figures 4.30 and 4.31). These variations could be indicative of changes in lithology, porosity (distribution of pore and crack shape), the presence of fluids (liquid or gas), and other parameters related to the rock type (Tatham, 1982). Pickett (1963b) determined V_p/V_s values for different lithologies as follows: 2.0-3.0 for shales; 1.9 for limestones; 1.8 for dolomites; and 1.6-1.75 for sandstones.

The V_p/V_s analysis of the different horizons is explained as follows, beginning with an analysis of the V_p/V_s values from the well log data (Figure 2.5, Panel (b)) and following with an analysis of the average interval V_p/V_s maps for each horizon from the seismic section (Figure 4.29).

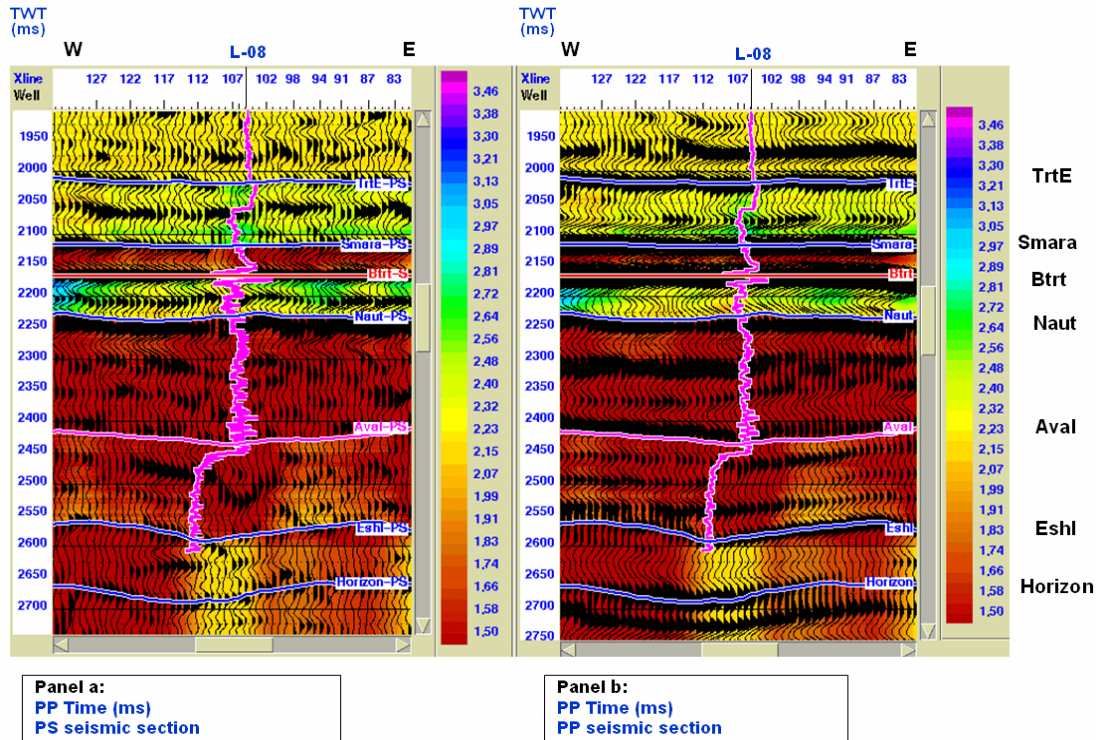


Figure 4.28: Vp/Vs analysis after matching the PP section with the PS seismic section, showing the horizons (Tertiary E, South Mara, Base of Tertiary, Nautilus, Avalon, and Eastern Shoals) and well L-08 with the gamma ray log.

- Tertiary E Horizon (TrtE).** Most of the Tertiary sediments are shales (Figure 2.5, Panel (b)). Tertiary E shale is about ~149.88 m thick (from well log data). This Formation could be divided into three sections where the upper section shows decreasing Vp/Vs values with depth from ~3.59–1.9; the middle section (at ~2155 m) shows increasing Vp/Vs value with depth (~2.0–2.35); and the lower section (at ~2254 m) has Vp/Vs values decreasing drastically with depth (~2.35–1.84).

From the Vp/Vs map (Figure 4.29) the main range of values is ~1.9–3.12 interpreted as shales and some sandstones. These values are reasonably distributed along the area of the study. On the NW section there are some higher values ~3.37 interpreted as high shaly areas.

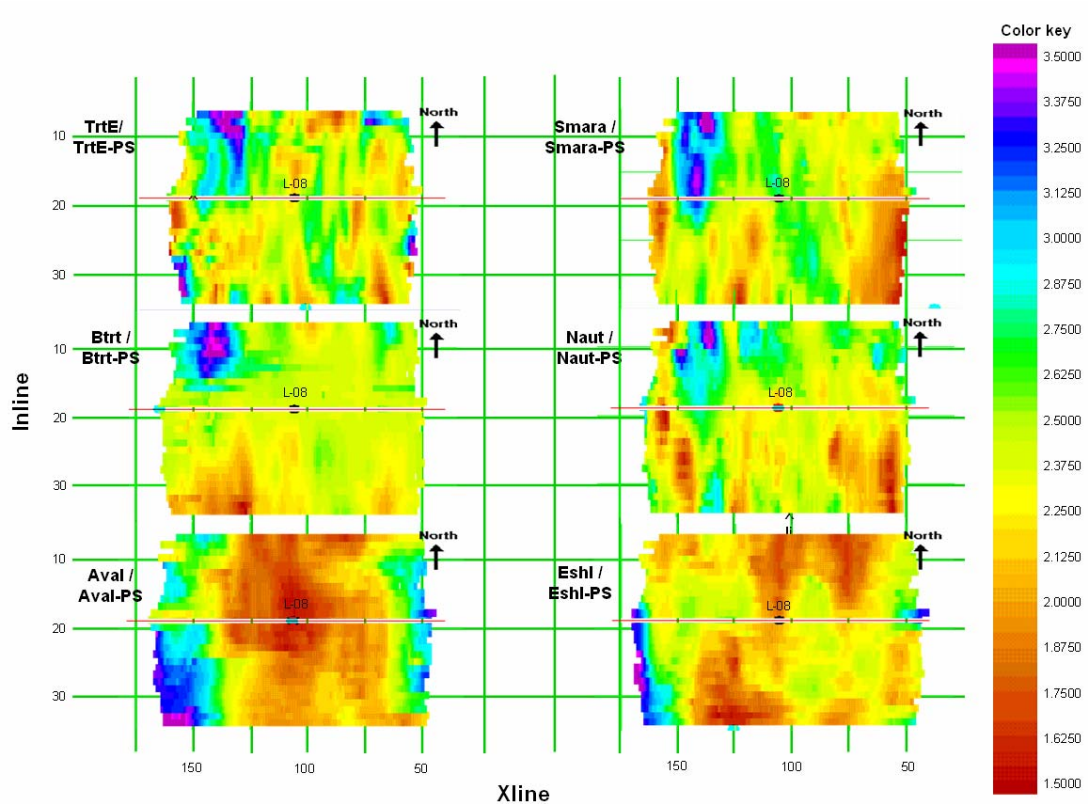


Figure 4.29: Apparent average interval V_p/V_s maps for each horizon (Tertiary E, South Mara, Base of Tertiary, Nautilus, Avalon, and Eastern Shoals). Well L-08 is shown on each V_p/V_s map. The inline and xline are gridding onto 25x25 bin spacing. Refer to Table 4.1 for V_p/V_s comparison.

- South Mara Horizon (Smara):** This sandstone-siltstone Formation is about ~55.88 m thick (Figure 2.5, Panel (b)). There are anomalous V_p/V_s values; this could be due to its proximity to the Tertiary unconformity at the bottom of the Formation. The upper section of the Formation increases values with depth (~1.8–2.21). At ~2300 m the values of V_p/V_s decrease with depth (~2.21–1.8).

Figure 4.29 shows an average interval in the main area of ~1.74–2.15 which could be interpreted as sandstones and siltstones. Anomalous values ~3.37 on the NW side of the area were found.

- **Base of Tertiary Horizon (Btrt):** Directly beneath the unconformity there is the Petrel limestone with ~148.88 m of thickness (Figure 2.5, Panel (b)). At the top of the Formation the values increase with depth drastically (~1.8–2.23); this could be due to the unconformity. Below ~2320 m, the values decrease as we go deeper in the well (2.23–1.8). The presence of anomalous values is noticeable on the well log data.

The average interval Vp/Vs map for this horizon (Figure 4.29) shows a main trend of ~1.9–2.25 that could be interpreted as limestones. Some anomalous values ~2.87–3.37 are to the NW.

- **Nautilus Horizon (Naut):** The Nautilus shale at 350.38 m has a general trend of decreasing Vp/Vs values with depth (~1.98–1.67). There are anomalous values. The Nautilus Formation is subdivided into three units of silty sandstones to siltstones, with limestone also present.

The average interval map (Figure 4.29) shows a general trend of ~2.0–2.62. This range can be interpreted from sandstones to siltstones including limestones. Also of note are the anomalous values in the NW (~2.87–3.37) and along the south section of the map (~1.75–2.12).

- **Avalon Horizon (Aval):** This horizon has a range from sandstones to shales. The approximately thickness is ~279.38 m (well log data). In general, Vp/Vs values increase with depth. According to the Φ_D (sandstone matrix) analysis, the range of percentage porosity is from ~0–20% in the Formation. There are several events that help to divide the Formation into three units (Figure 4.30 and Figure 2.5, Panel (b)). From the top of the Formation to the Gas-Oil Contact (GOC), the Vp/Vs values range ~1.52–1.75. At the very top the values are low; here we have the shale section with low Φ_D values; from the GOC to the Oil-Water Contact (OWC), the values of Vp/Vs increase from a range ~1.6–1.91. From the

OWC to the bottom of the Formation the range of values reduce to ~1.65–1.75.

Figure 4.29 shows the main range of Vp/Vs in this horizon ~1.6–2.87. These values can be interpreted from sandstones to shales. There are anomalous values which in this case could be due to the image of the discontinuous event on the PS seismic section. During the early Cretaceous, the Avalon sandstones were deposited as shoreface sands along a north-south trending shoreline roughly parallel to the eastern margin of the Jeanne d’Arc Basin (Husky Oil, 2001). It is possible to perceive a general north-south trend to the sandstones (Figure 4.29) in the apparent average interval Vp/Vs Avalon map. It is important to see that the regional trend is observable in a local area.

- **Eastern Shoals Horizon (Eshl):** The Eastern Shoals calcareous sandstone-siltstone horizon has 21 m of thickness (Figure 2.5, Panel (b)). The general trend of the Formation (well log data) is decreasing Vp/Vs values (~1.81–1.70) with depth.

The average interval Vp/Vs map (Figure 4.29) shows a main trend of ~1.7–2.5 values, according with sandstones and siltstones. Anomalous values are present to the NE and SW sides of the area. On the PS section, this horizon is not a continuous event which could be due to the presence of anomalous values in this horizon and in the Avalon horizon.

Table 4.1 summarizes the Vp/Vs analysis. The values from the well L-08 data are related to the Vp/Vs values from the OBS seismic (Jaramillo et al, 2004). The presence of higher values in the seismic section could be due to the extension of the area analyzed or difficult picks through low signal/noise events; also, with the OBS analysis, it was possible to see lateral Vp/Vs anomalies in the area.

Formation	Lithology	Vp/Vs	
		Well L-08	OBS
Tertiary E	Shales	~1.84–3.59	~1.9–3.12
South Mara	Sandstone-siltstone	~1.8–2.21	~1.74–2.15
Petrel Member ♦	Limestone	~1.81–2.23	~1.9–2.25
Nautilus	Shale-mudstone	~1.67–1.98	~2.0–2.62
Avalon	Sandstone-shale	~1.52–1.91	~1.6–2.87
Eastern Shoals	Calcareous sandstone-siltstone	~1.70–1.81	~1.7–2.50

Table 4.1: General behaviour of Vp/Vs, showing the general trend found in each Formation for well L-08 and for the OBS seismic data. Key: ♦ indicates the Formation that is directly beneath the Base of Tertiary unconformity.

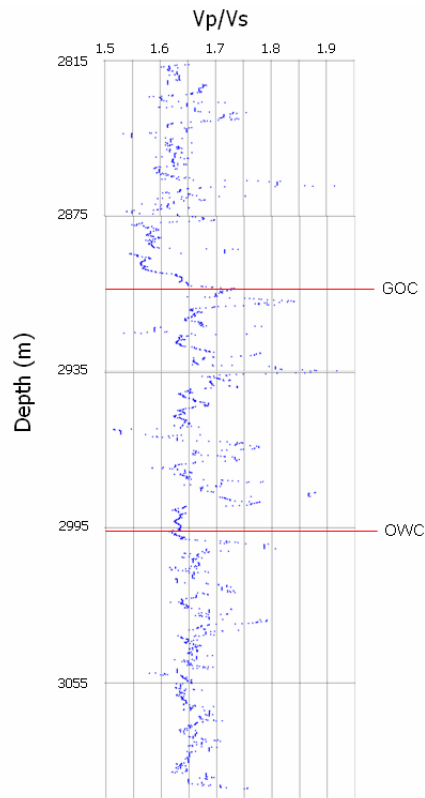


Figure 4.30: Vp/Vs versus depth Avalon Formation, from well L-08.

5. CONCLUSIONS

5.1 Well-Log Analysis

Vp and Vs generally increase with depth.

Vp/Vs decreases with depth.

Faust is the better predictor for Vp.

Castagna is better predictor for Vs.

Castagna's limestone relationship works better than Pickett's limestone relationship.

Gardner prediction of r should be take with caution.

Velocity decreases as porosity increases.

Empirical relationships apply with variable level of accuracy.

5.2 VSP interpretation

The P-P synthetics seismograms match well with the Offset VSP (PP) field data, with the Walk-above VSP (PP) and the seismic section (PP).

The P-S synthetic seismograms match well with the Offset VSP (PS) field data.

Comparing the PS to the PP synthetic seismograms and comparing the field results of the Offset VSP (PS) to the offset VSP (PP), the PS images improve the top of the Avalon Formation.

PS (synthetic and offset VSP data) shows less amplitude loss at the top of

the Tertiary unconformity leaving more energy to image below.

5.3 OBS interpretation

Detailed correlation information from the wells L-08 and H-20 enabled the interpretation of the low impedance contrast between the Avalon and Nautilus Fms on the synthetics.

A reasonable data match was found for:

- PP synthetics & PP vertical component seismic section (OBS).
- PS synthetics & PS radial component seismic section (OBS).

Vp/Vs values from the seismic and the well L-08 are related, presence of lateral Vp/Vs anomalies is evident on the seismic.

Acquiring converted wave with the help of an OBS survey, should help address the different image challenges of White Rose field.

6. FUTURE WORK

The conclusions of this study could be further enhanced through the release of additional datasets that currently remain proprietary to the data owners for analysis.

All the different relationships studied in this work with wells A-90, E-09, H-20, J-49, L-08 and N-22, should be explored on the rest of the wells (N-30, L-61, A-17, F-04 and F-04Z) of the area.

The acquisition of another OBS survey in the area would help to define the Avalon reservoir image and gain a better understanding of all the different analyses related to the geophysical interpretation.

7. REFERENCES

- Asquith, G. B., 1990, Log evaluation of shaly sandstones: a practical guide: Continuing Education, Course note series #31, The American Association of Petroleum Geologists, 59.
- Avseth, P., Mukerji, T., and Mavko, G., 2001, Rock physics and AVO analysis for lithofacies and pore fluid prediction in a North Sea oil field: The Leading Edge, April, 429-434.
- Caldwell, J., 1999. Marine multicomponent seismology. The Leading Edge, November, 1274-1282.
- Castagna, J.P., Batzle, M.L. and Eastwood, R.L. 1985. Relationship between compressional-wave and shear-wave velocities in clastic silicate. 50 4, 571-581.
- Castagna, J. P., Batzle, M. L., and Kan, T. K., 1993, Rock physics; the link between rock properties and AVO response: in J. P. Castagna and M. M. Backus, Eds., Offset-Dependent Reflectivity - Theory and Practice of AVO Analysis, Society of Exploration Geophysicists.
- Cary and Stewart, 2003, Processing Ocean-Bottom Seismic (OBS) Data from the White Rose oilfield, offshore Newfoundland, CREWES Research Report, Volume 15, 26 pages.
- DeAngelo, M. V., Backus, M., Hardage, B.A., and Murray, P., 2003, Depth registration of P-wave and C-wave seismic data for shallow marine sediment characterization, Gulf of Mexico: The Leading Edge, February, 96-105.
- Dewan, J. T., 1983, Essentials of modern open-hole log interpretation, PennWell Publishing Company, 361.
- Draper, N. R. and Smith, H., 1966, Applied regression analysis, John Wiley & Sons, Inc, 407 pages.
- Emery, D., 2001, Application of converted wave potential at the White Rose oil and gas discovery, presentation prepared for the University of Calgary course GOPH699.07.

- Enachescu M. E., Meehan, P. J., Smee, G. W., Emery, D., Hodder, J., Deutsch, K. and Mayo, L. 1999, White Rose Oil Field, Offshore Newfoundland (part 1): Drilling History, Geophysical Characterization and Structural Setting. Husky Oil Operation Ltd., Calgary, Alberta Canada.
- Faust, L.Y., 1951, Seismic velocity as a function of depth and geologic time: *Geophysics Journal*, 16 (2), 192-206.
- Faust, L.Y., 1953, A velocity function including lithologic variation: *Geophysics, Journal* 18, 271-288.
- Gardner, G.H.F., Gardner, L. W., and Gregory, A.R., 1974, Formation velocity and density – the diagnostic basis for stratigraphic traps: *Geophysics*, 39, 770-780.
- Garotta, R., 2000, Shear waves from Acquisition to Interpretation, Society of Exploration Geophysicists, 2000 Distinguished Instructor Short Course, Distinguished Instructor Series, No. 3.
- Grant, A. C. and McAlpine, K. D., 1990, The continental margin around Newfoundland; Chapter 6 in *Geology of the Continental Margin of Eastern Canada*, Keen, M. J., and Williams, G. L., (ed.); Geological Survey of Canada, *Geology of Canada*, No. 2, 239-292.
- Hall, K. W., and Stewart, R. R., 2002, Survey design and acquisition of a 4-C ocean-bottom seismometer survey over the White Rose oilfield, offshore Newfoundland, CREWES Research Report — Volume 14, 9 pages.
- Hanson, R., MacLeod, M., Bell, C., and Thompson, C., 1999, Multi-component seismic interpretation: data integration issues, Alba Field, North Sea. *SEG Exp. Abst.* 4 pages.
- Hilchie, D. W., 1982a, Applied open-hole log interpretation for geologists and engineers, Department of Petroleum Engineering, Colorado School of Mines.
- Hilchie, D. W., 1982b, Advanced well log interpretation, Department of Petroleum Engineering, Colorado School of Mines.

- Hoffe, B.H., Lines, L.R., Stewart, R.R., Wright, J.A., and Enachescu, M.E., 2000, A proposed 4C Ocean Bottom Cable (OBC) experiment in the White Rose field, Jeanne-d'Arc basin, offshore Newfoundland, 32 pages.
- Husky Oil Operations, 2001, White Rose oilfield development application volume 2 development plan.
- Isaac, J.H., and Lawton, D.C., 1995, Converted-wave processing and interpretation at Cold Lake, Alberta. CREWES Research Report. Volume 7. 24 pages.
- Jackson, R., Asprey, K., Chapman, B., Goold, S., Girouard, P., Johnston, L., and Loudon, K., 2002, Hudson 20002-011 cruise report. Flemish Cap Margin Transect. Geological Survey of Canada, Open file # 1234. 40 pages.
- Jaramillo, S. J., Stewart, R. R., and Emery D. 2002, Interpretation of well log, VSP, and streamer seismic data from the White Rose oilfield, offshore Newfoundland, CREWES Research Report Volume 14, 15 pages.
- Jaramillo, S. J., and Stewart, R. R., 2003, Analysis of well-log data from the White Rose oilfield, offshore Newfoundland. CREWES Research Report, Volume 15, 16 pages.
- Jaramillo, S. J., and Stewart, R. R., 2004, Interpretation of PP and PS seismic data from the White Rose oilfield, offshore Newfoundland. CREWES Research Report, Volume 16, 22 pages.
- Johnson, D. E., and Pile, K. E., 2002, Well logging in nontechnical language. 2nd Edition, PennWell Publishing Company, 289.
- Larsen, J.A., Margrave, G.F., and Foltinek, D.S., 1997, New developments in the SYNTH algorithm. CREWES Research Report Volume 9. 9 pages.
- Louden, K.E. and Funck, T., 2000, SCREECH: Study of continental rifting and extension on the eastern Canadian shelf, Cruise Report OC359-2. 105 pages.
- McAlpine, K.D., 1990, Mesozoic stratigraphy, sedimentary, evolution and petroleum potential of the Jeanne d'Arc Basin, Grand Banks of Newfoundland. Geological Survey of Canada, 89:17.

- MacLeod, M., Hanson, R., Hadley, M., Reynolds, K., Lumley, D., McHugo, S., and Probert, T., 1999, The Alba Field OBC seismic survey. SEG Exp.Abst. 3 pages.
- Pickett, G. R., 1963a, Acoustic character logs and their applications in formation evaluation: In Mavko, G., Mukerji, T., and Dvorkin, J., 1993, The Rock Physics Handbook: Tools for Seismic Analysis in Porous Media, Cambridge University Press.
- Pickett, G. R., 1963b, Acoustic character logs and their applications in formation evaluation: In Potter, C. C., and Foltinek, D. S., 1997, Formation elastic parameters by deriving S-wave velocity logs. CREWES Research Report Volume 9. 10 pages.
- Rider, M. H., 2002, The geological interpretation of well logs, 2nd edition, Rider-French Consulting Ltd, 280.
- Russell, B. 2004, The application of multivariate statistics and neural networks to the prediction of reservoir parameters from seismic attributes: Ph.D. thesis, University of Calgary, Department of Geology and Geophysics.
- Schlumberger Educational Services, 1987, Log interpretation principles/applications, 2nd edition, 198.
- Sheriff, R. E., 1999, Encyclopedic dictionary of exploration geophysics, Third Edition, Society of Exploration Geophysicists.
- Stewart, R.R., Gaiser, J. E., Brown, R. J., Lawton, D. C., 2003, Converted-wave seismic exploration: applications. Geophysics, 68 (1), 40-57.
- Stewart, R. R., Jaramillo, S. J., and Nieto, C., 2001, 4-C ocean-bottom seismometer data from the 2000 SCREECH, CREWES Research Report, Volume 13, 10 pages.
- Stewart, R. R., 2001, In Special Report - on seismic technologies, December 2001, Sea Change, Multi-Component Seismic Survey Designed For White Rose Using Ocean Bottom Seismometers. New Technology magazine.
- Tatham, R., 1982, Vp/Vs and lithology: Geophysics, 47 (3), 336-344.
- Western Atlas, 1985, Log interpretation charts. Atlas Wireline Services, Western Atlas International, Inc., 203 pages.

Yilmaz, 2001, Seismic data analysis: Soc. Expl. Geophys.

Web pages

World Atlas, 2004, www.encarta.msn.com

Dalhousie Seismic Group, 2002, <http://www.phys.ocean.dal.ca/seismic/>

Geological Survey of Canada (Atlantic), <http://agcwww.bio.ns.ca/>, 2000

Husky Energy, 2002, <http://www.huskyenergy.ca/whiterose/default.asp>

Husky Energy Inc, 2003, 2004, 2005, <http://www.huskywhiterose.com/>

Ocean Drilling Program, <http://www-odp.tamu.edu>

APPENDIX A. Introduction

Jeanne d'Arc Basin's Stratigraphy

- **Sequence 1. Aborted Rift (Late Triassic to Early Jurassic: ~225–197 Ma).** Presence of continental red beds, and restricted marine evaporites and carbonates (McAlpine, 1990). The depositional environments for these deposits consist of arid continental, restricted evaporite basins, followed by coastal sabkhas, tidal flats and restricted lagoons, and finally, a shallow neritic sea. In addition, late Triassic subaerial basalt flows (southern part of the basin) are present and are related to an early rifting (Grant and McAlpine, 1990).

The main structures include large half-grabens, steps and horsts; tilted block arrays; roll-overs; trap-door faults; immature to overmature salt diapirs; transfer faults; rift shoulders; inner and outer ridges (Hoffe et al., 2000).

- **Sequence 2. Epeiric Basin (Early to Late Jurassic: ~197–153 Ma).** Conformed by shallow marine shales and carbonates and some fine-grained deltaic sediments (McAlpine, 1990). These sediments were deposited in a broad epeiric sea that flooded the old rifted topography. Local unconformities may be present due to mobilization of the underlying salt (Grant and McAlpine, 1990).

The structures included in this stage are small fault blocks; draping over underlying highs; locally formed differential compaction structures; salt domes and diapirs; peripheral sink synclines; sedimentary wedges (Hoffe et al., 2000).

- **Sequence 3. Late Rift (Late Jurassic to Neocomian: ~153–118 Ma).** Now the sequence is of sandstones and siltstones. The base of this sequence is a major unconformity of middle Kimmeridgian age (Late

Jurassic). The environment of deposition ranges from dominated clastic-rift depositional systems such as fluvial fan, fan-delta, coastal plain-delta top, delta front-prodelta, interdistributary bay, shallow marine shoreface facies, and estuarine to tidal flat (Grant and McAlpine, 1990).

The principal structures consist of large half-grabens; steps and horsts; titled block arrays; roll-overs; trap-door faults; immature to overmature salt diapirs; transfer faults; rift shoulders; inner and outer ridges (Hoffe et al., 2000).

- **Sequence 4. Transition to Drift, Phase I (Barremian to Cenomanian: ~118–105 Ma).** Shallow to deep estuarine sandstones and shales, conglomerates, marls and siltstones were deposited in a continental to marginal marine environment (Grant and McAlpine, 1990).

The structures involved in this sequence, include large half-grabens; steps and horsts; titled block arrays; roll-overs; trap-door faults; immature to overmature salt diapirs; transfer faults; rift shoulders; inner and outer ridges (Hoffe et al., 2000).

- **Sequence 5. Transition to Drift: Phase II (Late Cretaceous and Paleocene: ~105–58 Ma).** The sequence is comprised of open marine shelf sediments overlapping deltaic deposits, distal turbidites, chalky limestones, shales, and siltstones. The environment of deposition was related to neritic to outer neritic and delta front to prodelta environments (Grant and McAlpine, 1990).

The principal structures are related to small roll-over anticlines associated with fault slip reversal; monoclinal folds; forced folds above antithetic faults; possible flower structures (Hoffe et al., 2000).

- **Sequence 6. Passive Margin (Tertiary to Quaternary: ~58–3 Ma).** Deposits of shales, siliceous mudstone, and minor chalk. The

environment of deposition was from deep neritic, bathyal to shallow conditions (Grant and McAlpine, 1990).

The structures observed in this sequence were small fault blocks; draping over underlying highs; locally formed differential compaction structures; salt domes and diapirs; peripheral sink synclines; sedimentary wedges (Hoffe et al., 2000).

White Rose field's Reservoir Lithologies

This lithological description also includes a brief explanation of the South Mara Unit, due to its importance in the development of the synthetics.

- **Hibernia Formation (223 m — Tithonian to Berriasian).** Composed of alternating thick sandstones and thinner interbedded shales. It is possible to subdivide the formation into two units:

Lower unit (161 m) consists of thick, stacked, fining upward sequences of arenites.

Upper unit (62 m) interbedded sandstones, silty shales, and siltstones.

The contact of the formation with the Fortune Bay Shale is defined as the first thick sandstone-dominated sequence conformably overlying the shale sequence. The contact with the Hebron Well Member is sharp but usually conformable with massive limestone of the "B" marker. The formation has a gradational contact with the Whiterose Shale. The Hibernia Formation is best developed in the Hibernia field / Hebron I-13 / and Terra Nova field region of the Jeanne d'Arc Basin. The depositional conditions of the Hibernia Formation are interpreted as prograding deltaic sediments of a fluvial system (<http://agcwww.bio.ns.ca/>, 2000).

- **Catalina Formation, (207 m — Late Berriasian to Valanginian).** The Catalina Formation is defined as the initial laterally persistent sandstone/carbonate sequence directly overlying the "B" marker limestone. Thinly bedded sequence of sandstones, siltstones, shales, and minor limestones conformed the Catalina Formation. The lower boundary of the formation is a sharp but apparently conformable contact with the "B" marker limestones. The upper boundary with the Whiterose Shale is gradational. The Catalina Formation is present only in the southern part of the Cretaceous depocentre of the Jeanne d'Arc Basin. The depositional conditions of these sediments are interpreted as interdistributary bay and marginal-marine facies deposited away from the strongly wave-influenced open shoreface (McAlpine, 1990).
- **Eastern Shoals Formation (815 m — Hauterivian to Barremian).** A massive calcareous sandstone/oolitic limestone sequence and a thick sequence of interbedded sandstone and siltstone compose the Eastern Shoals Formation. The environment of deposition was a shallow-marine to marginal-marine setting. The contact of the formation with the underlying and laterally equivalent Whiterose Shale or the Catalina Formation is conformable and gradational. The upper contact with the Avalon Formation is sharp and unconformable to disconformable. This contact on seismic sections is an important and broadly correlatable reflector (Barremian reflector), usually referred as the "A seismic marker". The Formation appears to be confined to that part of the Jeanne d'Arc Basin between the Egret Fault and the Whiterose field. It is thickest on the western side of the basin, apparently due to tilting of the basin during deposition, but may also develop substantial thicknesses near the eastern side of the basin, north of the Hibernia-to-Ben Nevis trans-basin fault zone (<http://agcwww.bio.ns.ca/>, 2000).

- **Avalon Formation (125 m — Barremian to late Aptian).** This Formation is a complex and variable siliciclastic series, subdivisible into 3 subunits, displaying a coarsening upward pattern:

Basal subunit (42 m): "red mudstone" sequence characterized by varicoloured shales containing a few thin interbeds of sandstone.

Middle subunit (37 m): thicker sandstone beds, and interbedded grey shales.

Upper subunit (46 m): slightly coarsening upward, sandstone-dominated unit, with siltstone at the top.

The lower contact with the Eastern Shoals Formation is always sharp. The upper contact with the Ben Nevis Formation is sharp and unconformable at the basin margins and over major structures, becoming disconformable to conformable toward the basin axis. The Avalon Formation grades laterally into the Nautilus Shale. The environment of deposition is a flat, low-lying coastal plain containing brackish lagoons and swamps bordering a large, tide-dominated shallow estuary (McAlpine, 1990).

- **Ben Nevis Formation, (378 m — Late Aptian to Late Albian).**

Lower subunit (43 m): thinly interbedded shale and sandstone and local coal beds. This subunit, displays a low velocity signature on the sonic log, making it a distinctive log marker.

Upper subunit (335 m): sequence of fining upward sandstone.

The contact with the Avalon Formation is sharp and unconformable. The upper contact with the Nautilus Formation is abrupt. Seismically, the Ben Nevis sequence is distinguished from the Avalon sequence by its lower amplitude and weakness of internal reflections. Although the Ben Nevis

Formation was deposited during a period of important basin structuring and growth faulting, in general, the fining upward Ben Nevis sandstones is evidence a period of transgression (McAlpine, 1990).

- **Nautilus Formation (617 m — Late Barremian to Late Cenomanian-Turonian).** The formation is a monotonous unit dominated by grey calcareous shale or mudstone. This unit is subdivided in three subunits:

Basal subunit (70 m): intercalated beds of very fine-grained, silty sandstone that grade upward into siltstone.

Middle subunit (201 m) siltstone beds with sandstone stringers.

The upper subunit (179 m): very calcareous and argillaceous siltstone and argillaceous, silty, microcrystalline to chalky, limestone beds.

The lower contact, usually taken to be the Albian unconformity where the Ben Nevis Formation is present, is abrupt and unconformable to conformable. The upper contact is also abrupt but possibly conformable. The formation is almost everywhere in the Jeanne d'Arc Basin where middle Cretaceous strata were deposited and preserved. The unit was deposited in a transgressive (lower and middle units)/regressive (upper unit), low energy, open marine shelf environment. Clastic input was limited, especially during deposition of the middle unit (<http://agcwww.bio.ns.ca/>, 2000)

- **South Mara unit (Danian-Thantetian).** A basal transgressive shallow marine sandstone. The sediments were deposited during thermal subsidence. The sequence with a fining upward pattern of glauconitic silty fine to very fine grained sandstones (Husky Oil Operations, 2001).

APPENDIX B. Well log analysis

Actual Vp versus Vp estimated from Faust's relationship (from section 2.2.4).

As was explained in Chapter 2, the Faust empirical relationship (shown below in Equation 2.1) predicts compressional velocities as a function of geological time and depth of burial of the rock (Faust, 1951). In section 2.2.4 the relationship was explained using Faust's constant and the least square fit constant per well (E-09, H-20, J-49, L-08, and N-22). Now our approximation was done in two different ways:

- Using a constant per Tertiary Formations and a constant per Cretaceous Formations; and
- Using a constant per individual Formation

Each derived constant was obtained from the least-square fit using the actual Vp data and the Faust function ($ZT^{1/6}$). Also, we did an RMS error study to measure how accurate the analysis was.

$$V_p = C_p (TZ)^{1/6}, \quad (2.1)$$

where: V_p Compressional velocity (m/s)
 C_p Constant 125.3
 T Formation age
 Z Depth of burial (m)

The reasons for using different constants for the Tertiary Formations and Cretaceous Formations was to target Faust's relationship more closely on the area of interest. In this case (Figures B.1 to B.4), these two constants were based on the least square value that better fit the original data. Also the analysis of the RMS error value was acquired to corroborate the accuracy of these constants.

In Figures B.1 and B.2, the curve using the Faust constant ($C_p=125.3$) is compared with the derived Vp Faust using the least square constants (Table B.1). After comparing both percentage errors (Figures B.1 and B.2, Panels (b) and (c)), we

can conclude that derived C_p curve data constants (Tertiary and Cretaceous constants) work best for the younger Tertiary Formations. However, we could have a better fit for the Cretaceous Formations if we examined each Formation independently and then determined an independent constant for the Tertiary section. Tertiary sediments are mostly clastics. In the Cretaceous Formations, there is limestone present. In general, the results obtained from the clastic base Faust equation have to be looked at with caution since the Faust equation was formulated using clastic data.

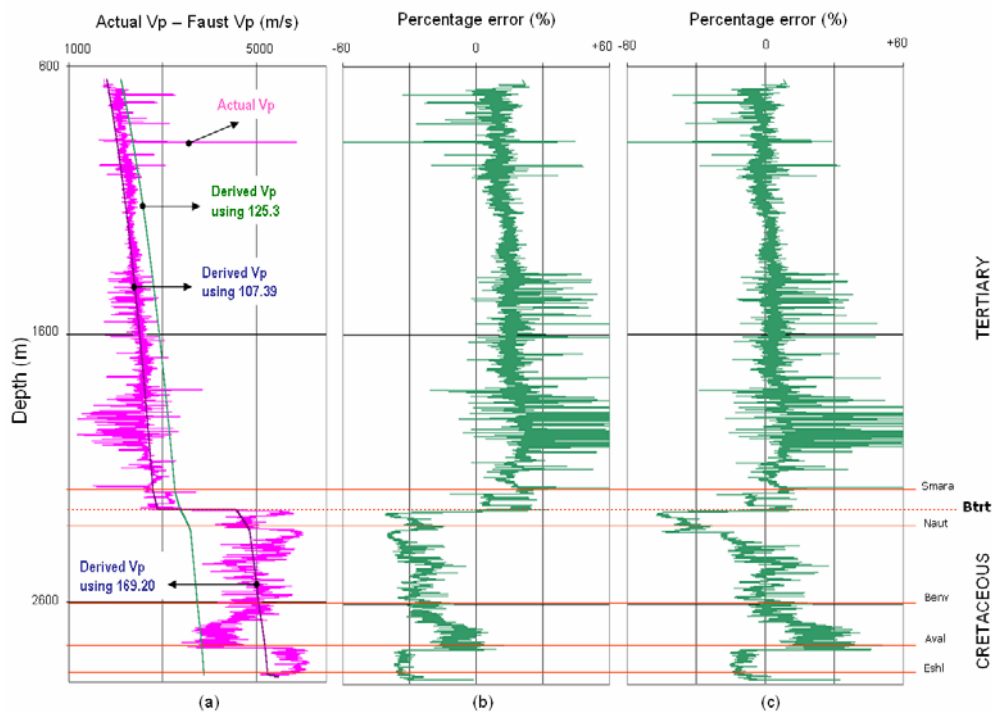


Figure B.1: Data from well A-90. Panel (a) — actual Vp and Faust Vp using 125.3 (for the entire well) and Vp using derived constants (a constant for the Tertiary Formations and a constant for the Cretaceous Formations) versus depth. Panel (b) — percentage error between the actual Vp curve and the Faust Vp (derived from the 125.3 constant). The RMS error is ± 1344.12 m/s. Panel (c) — percentage error between the actual Vp curve and the Faust Vp curve derived using two constants. The Tertiary Formations with constant $C_p=107.39$ and an RMS error of ± 238.79 m/s. The Cretaceous Formations with a constant $C_p=169.20$ and RMS error ± 631.71 m/s.

	A-90	E-09	H-20	J-49	L-08	N-22
Formation	Constants used in Faust equation					
Tertiary	107.39	108.61	116.89	108.71	108.87	110.12
Cretaceous	169.20	174.14	139.59	133.49	133.50	129.19

Table B.1: Constants used to predict Vp from Faust's relationship for all wells. There were just two constants per well (for the Tertiary and for the Cretaceous sections).

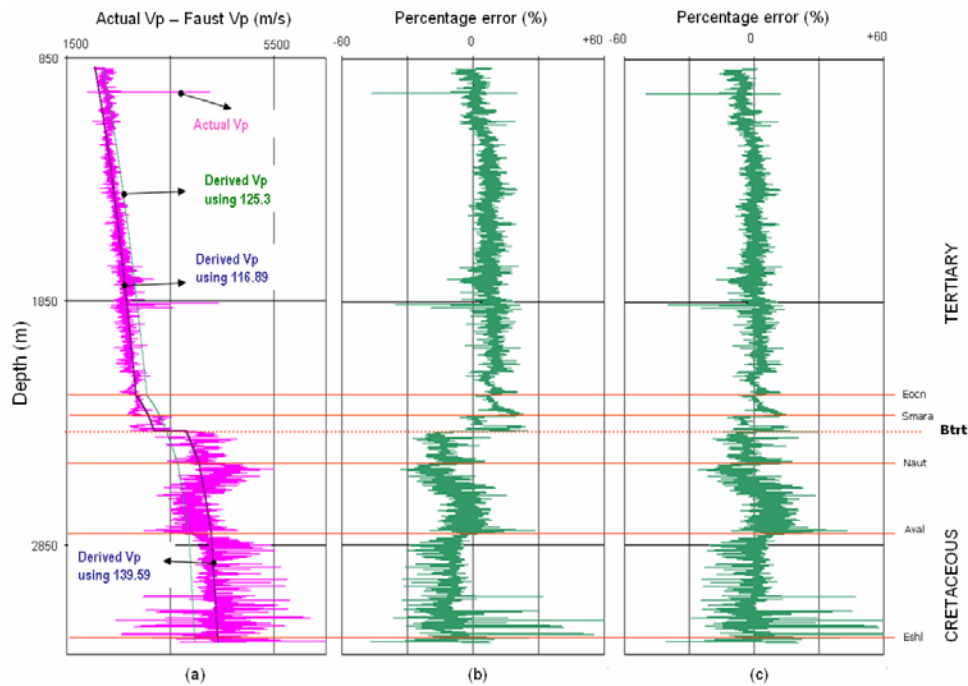


Figure B.2: Data from well H-20. Panel (a) — actual Vp and Faust Vp using 125.3 (for the entire well) and Vp using derived constants (a constant for the Tertiary Formations and a constant for the Cretaceous Formations) versus depth. Panel (b) — percentage error between the actual Vp curve and the Faust Vp (derived from the 125.3 constant). The RMS error is ± 398.01 m/s. Panel (c) — percentage error between the actual Vp curve and the Faust Vp curve derived using two constants. The Tertiary Formations with constant $C_p=116.89$ and an RMS error of ± 127.53 m/s. The Cretaceous Formations with a constant $C_p=139.59$ and an RMS error of ± 397.60 m/s.

The approach using a constant per Formation (Table B.2) gave good results (Figure B.3). With this approach, we are able to analyze the constants per lithology. We know that all the Formations have mixed lithologies; however, we categorized each Formation by the main lithology present:

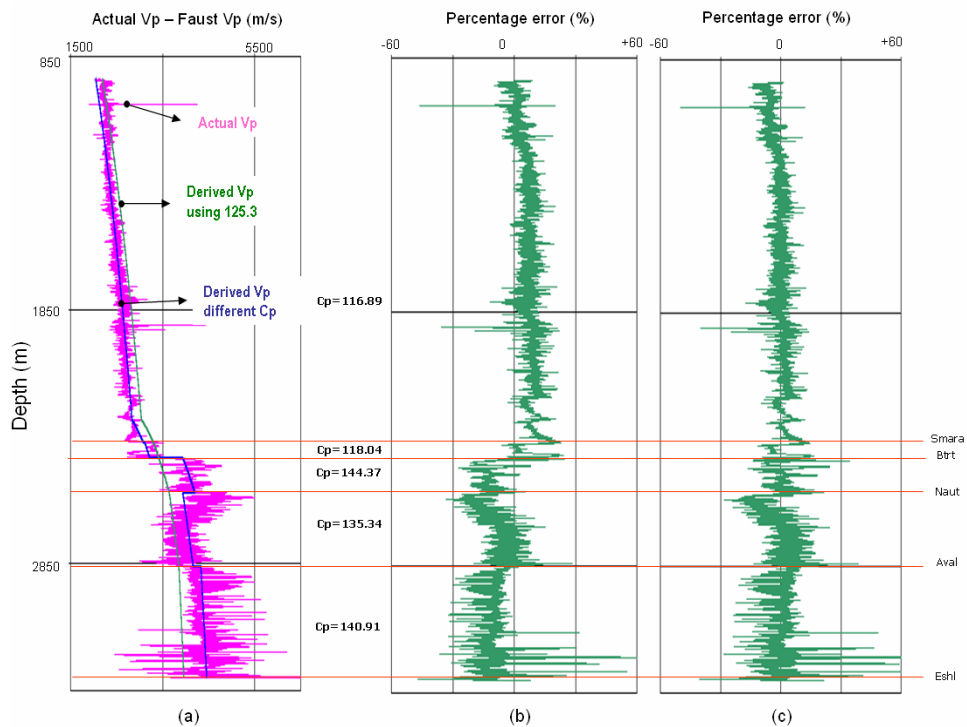


Figure B.3: Results from well H-20. Panel (a) — actual Vp, Faust Vp using 125.3 (for the entire well) and Vp using derived constants per Formation ($C_p=116.89$ Tertiary; $C_p=118.04$ South Mara; $C_p=144.34$ Petrel/Base of Tertiary; $C_p=135.34$ Nautilus; $C_p=140.91$ Avalon). Panel (b) — percentage error between the actual Vp curve and the Faust Vp (derived from the 125.3 constant). The RMS error is ± 398.01 m/s. Panel (c) — percentage error between the actual Vp curve and the Faust Vp curve derived using several constants. The RMS error is ± 120.23 m/s (Tertiary), ± 238.80 m/s (South Mara), ± 298.11 m/s (Petrel/Base of Tertiary), ± 398.63 m/s (Nautilus), and ± 401.59 m/s (Avalon).

- **Siltstone Formations (Hibernia).** In general the Formation has an approximate constant value ~ 127.86 – 135.46 .
- **Shale Formations (Tertiary, Dawson Canyon, Nautilus, White Rose and Fortune Bay).** The constants for these Formations, in general, range ~ 106.86 – 138.65 . There was just one constant that was above this range — the Nautilus Formation in well A-90 with a constant 173.58
- **Sandstone Formations (South Mara, Ben Nevis, Avalon, Eastern Shoals, Lower Hibernia, and Voyager).** The general trend of values is ~ 112.86 – 146.92 . An anomalous value was found in Avalon and Eastern

Shoals Formations in well A-90, where the values ranged between ~180.83–187.41.

- **Carbonate Formations (Petrel Member and Rankin)** have a trend (125.23–144.37) similar to the sandstone Formations trend.

		A-90	E-09	H-20	J-49	L-08	N-22
Age (my)	Formation	Constants used in Faust equation					
	Tertiary	106.86	107.99	116.89	108.61	108.65	109.88
55	South Mara	115.74	120.66	118.04	122.63	112.86	115.40
65	Wyandot	178.18	143.45	♦	131.66	♦	126.87
75	Dawson Canyon	♦	♦	♦	♦	114.52	121.59
88	Petrel Member	♦	♦	144.37	130.93	136.13	125.23
92	Nautilus	173.58	138.65	135.34	133.09	130.09	127.76
105	Ben Nevis	144.70	142.35	♦	141.22	♦	132.27
115	Avalon	187.41	146.92	140.91	146.25	136.32	132.97
118	Eastern Shoals	180.83	142.52	♦	♦	♦	127.93
118	White Rose	♦	♦	♦	132.14	♦	126.41
122	Hibernia	♦	135.46	♦	127.86	♦	135.50
125	Lower Hibernia	♦	♦	♦	130.01	♦	♦
128	Fortune Bay	♦	112.79	♦	♦	♦	111.91
138	Jeanne d'Arc	♦	♦	♦	♦	♦	126.03
152	Rankin	♦	♦	♦	♦	♦	136.48
152	Voyager	♦	♦	♦	♦	♦	♦

Table B.2: Faust's constants used to predict Vp for each well's Formations. Well N-22 had the closest results to the Faust constant (125.3) in the Wyandot, Petrel, Nautilus, Eastern Shoals, White Rose and Jeanne d'Arc Formations. Key: ♦ This Formation is not present on this well; • Formation at the bottom of the well.

In general, and with caution, we can say the shales have the lower values and the sandstones reach the higher values. The siltstone and carbonate Formations have values that are embedded between the shales and the sandstones values. The higher and lower values found in each lithology could be due to the mixed lithologies present in the Formations. These results can help us foresee with a

degree of certainty what constant value we should expect for given type of lithology. However, there were some anomalous high values related to Formations from well A-90. Well A-90 does not penetrate the reservoir section, which could explain the anomalous high values. Possibly the petrophysical properties are different from the other wells on the reservoir; also, the proximity to the Outer Ridge Complex Fault system could affect the rocks surrounding the well A-90.

The results from these approaches are reasonable, as are the RMS errors obtained; however the ideal situation is to have one constant for all the wells. In this case, these approaches helped to understand better the petrophysical behaviour of the rocks in the reservoir, even knowing that Faust relationship deals with changes in depth and time of burial of the rock.

Actual Vs versus Vs estimated from Faust's relationship (from section 2.2.5).

We explored the prediction of Vs using a relationship similar to the one used to predict Vp from Faust (1951; Equation 2.2). We explored attempts using the "Vs Faust equation" to predict shear velocities as a function of geological time and depth of burial of the rock. We explore this relationship in wells H-20 and L-08 where the shear velocity was acquired (Figures B.4 and B.5). The constants obtained to derive Vs have lower values than those obtained to derive Vp.

$$V_s = C_s (TZ)^{1/6}, \quad (2.2)$$

where: V_s Shear velocity (m/s)
 C_s Constant 70
 T Formation age
 Z Depth of burial (m)

The constants used per Tertiary and Cretaceous sections are in Table B.3. In this case, the results from both the Tertiary and Cretaceous Formations were reasonable (Figures B.4 and B.5 and Table B.3). The results from the Vs analysis on the Tertiary Formations have a better fit than those on the Cretaceous Formations; but the RMS errors (the values of which can be found on each Figure) from the Cretaceous Formations are still satisfactory. The results from the percentage error

analysis (Panels (b) and (c) in Figures B.4 and B.5) show the good fit obtained by this approach.

After analyzing the constants derived, the Tertiary Formations were found to have a lower value than the Cretaceous Formations; this trend was also observed in the approach using V_p derived from Faust.

	H-20	L-08
Formation	Constants used in Faust equation	
Tertiary	49.60	45.11
Cretaceous	79.79	75.96

Table B.3: Constants used to predict V_s for wells H-20 and L-08 Formations. There were just two constants per well.

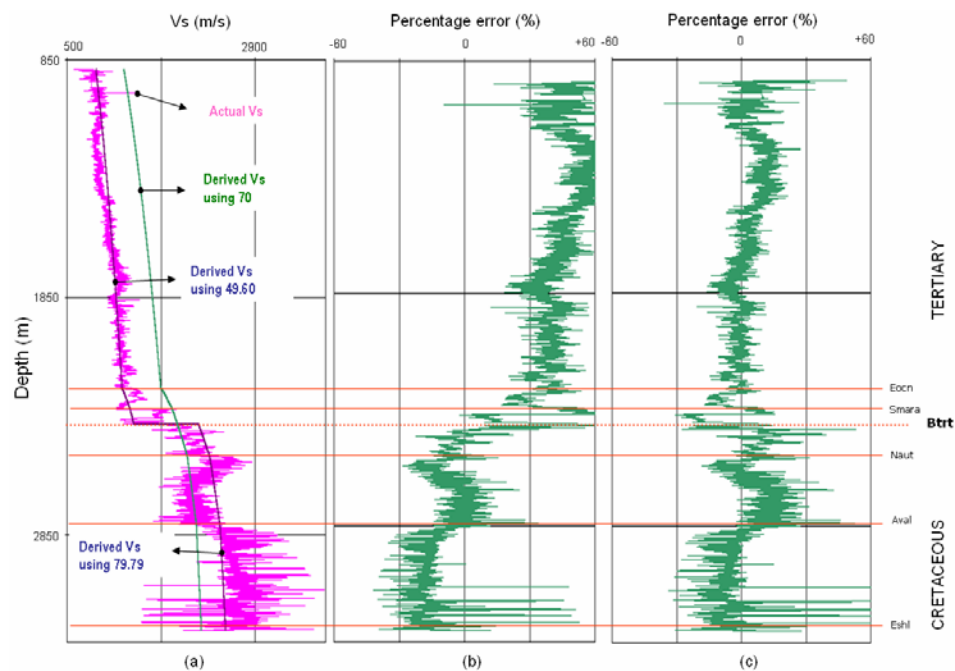


Figure B.4: Data from well H-20. Panel (a) — actual V_s and Faust V_s using 70 (for the entire well) and V_s using derived constants (a separate constant for the Tertiary and the Cretaceous Formations) versus depth. Panel (b) — percentage error between the actual V_s curve and the Faust V_s (derived from using 70 as the constant). The RMS error is ± 444.48 m/s. Panel (c) — percentage error between the actual V_s curve and the Faust V_s curve derived using two constants: the Tertiary Formations with constant $C_p=49.60$ and an RMS error of ± 98.26 m/s and the Cretaceous Formations with a constant $C_p=79.79$ and an RMS error of ± 299.74 m/s.

To see if we could improve the results, we broke down the wells (Table B.4) into their main Formations (as we did in our approach to the Vp curve). After this procedure, the results obtained were optimistic (Figure B.6).

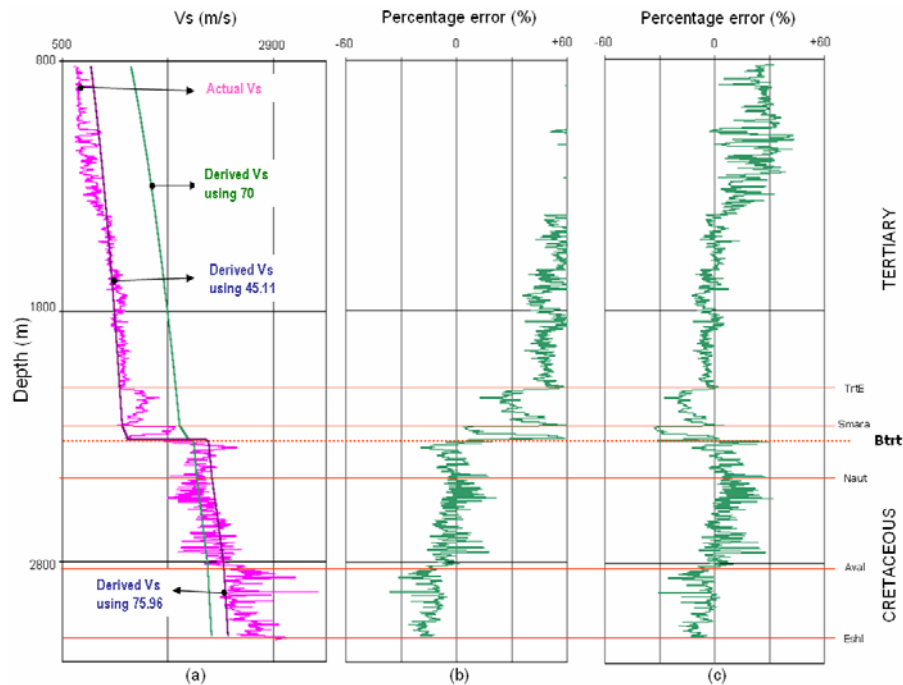


Figure B.5: Data from well L-08. Panel (a) — actual Vs and Faust Vs using 70 (for the entire well) and Vs using derived constants (separate constants for the Tertiary and Cretaceous Formations) versus depth. Panel (b) — percentage error between the actual Vs curve and the Faust Vs (derived from using 70 as the constant). The RMS error is ± 508.53 m/s. Panel (c) — percentage error between the actual Vs curve and the Faust Vs curve derived using two constants. The Tertiary Formations with a constant $C_p=45.11$ and an RMS error of ± 153.93 m/s. The Cretaceous Formations with a constant $C_p=75.96$ and an RMS error of ± 47.83 m/s.

When we review the results of the constant per Formation/lithology, we do not see any trend similar to that with the Vp analysis:

- **Shale Formations (Tertiary, Dawson Canyon, and Nautilus).** exhibit a range of values, $\sim 44.40\text{--}73.27$;
- **Sandstone Formations (South Mara and Avalon).** show a trend of $\sim 58.01\text{--}85.17$;

- **Carbonate Formations (Petrel Member)**. shows a trend of ~72.32–74.09.

Age (My)	Formation	Lithology	H-20	L-08
			Constants used in Faust's equation	
	Tertiary	Shale	49.03	44.40
55	South Mara	Sandstone-siltstone	58.13	58.01
75	Dawson Canyon	Sandstone-shale	♦	63.28
88	Petrel Member	Limestone	74.09	72.32
92	Nautilus	Shale-mudstone	73.27	72.04
115	Avalon	Sandstone-shale	85.17	82.21

Table B.4: Constants used to predict Vs for Formations in wells H-20 and L-08. Constants were derived for each Formation. Key: ♦ This Formation is not present in this well. These constants could be lithology indicators.

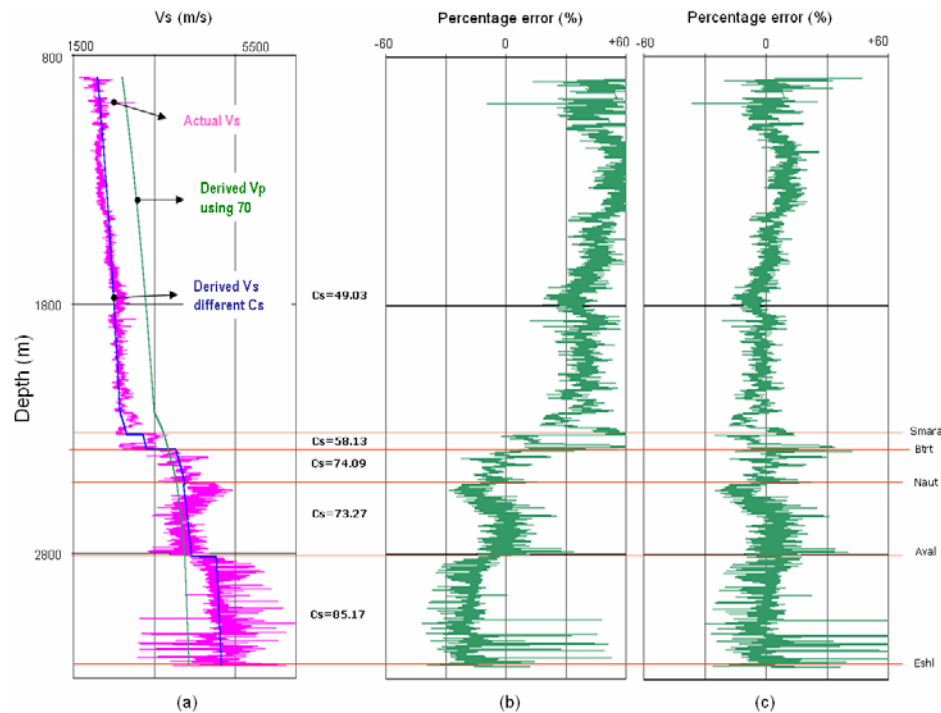


Figure B.6: Results from well H-20. Panel (a) — actual Vs, Faust Vs using 70 (for the entire well) and Vs using derived constants per Formation (Cs=49.03 Tertiary; Cs =58.13 South Mara; Cs =74.09 Petrel/Base of Tertiary; Cs =73.27 Nautilus; Cs =85.17 Avalon). Panel (b) — percentage error between the actual Vs curve and the Faust Vs (derived from the 70 constant). The RMS error is ± 444.48 m/s. Panel (c) — percentage error between the actual Vs curve and the Faust Vs curve derived using several constants. RMS errors are: ± 76.87 m/s (Tertiary), ± 199.92 m/s (South Mara), ± 173.76 m/s (Petrel/Base of Tertiary), ± 228.17 m/s (Nautilus), and ± 268.18 m/s (Avalon).

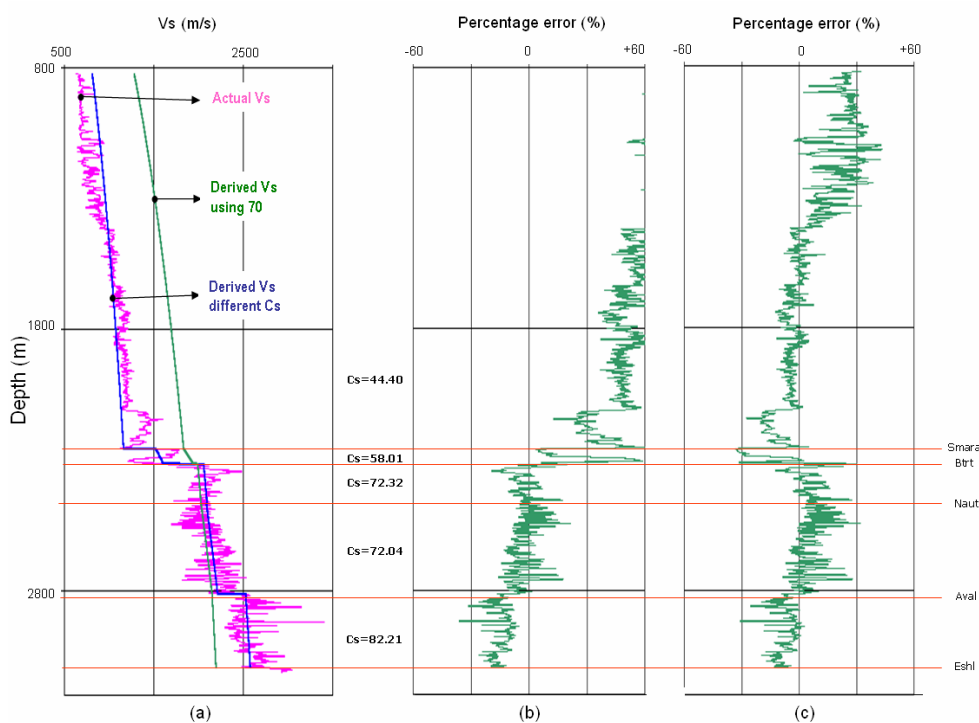


Figure B.7: Results from well L-08. Panel (a) — actual Vs and Faust Vs using 70 (for the entire well) and Vs using derived constants per Formation ($C_s=44.40$ Tertiary; $C_s=58.01$ South Mara; $C_s=72.32$ Petrel/Base of Tertiary; $C_s=72.04$ Nautilus; $C_s=82.21$ Avalon). Panel (b) — percentage error between the actual Vs curve and the Faust Vs (derived from the 70 constant). The RMS is error ± 508.53 m/s. Panel (c) — percentage error between the actual Vs curve and the Faust Vs curve derived using several constants. RMS errors are: ± 133.03 m/s (Tertiary), ± 222.02 m/s (South Mara), ± 150.52 m/s (Petrel/Base of Tertiary), ± 152.41 m/s (Nautilus), and ± 163.79 m/s (Avalon).

The results were good when we used a different constant per Formation. If there are trends consistent with lithologies, they are complicated by the velocity response to the lithology, to the fluids (gas or liquid) and solids (cement) present in the pores of the rocks, as well as the observation that the sequence is mainly clastic but still contains limestones that can affect the determination of the constant. The best results were found in well H-20 (Figure B.6). Well L-08 had a fair result for the Tertiary Formations (Figure B.7). The final results showed a suitable velocity average.

As we did with the V_p analysis, the most important reason for using different constants for each Formation was to see how precise the relationship could be for

the area of study; but it is still essential to have only one constant for the area as a replacement for several constants.

Actual ρ versus Gardner ρ derived from V_p (from section 2.2.8).

Gardner's equation (Equation 2.7), was used to derive ρ (density in kg/m^3) from V_p and Gardner's constants, a and m . Gardner (1974) gives values for a and m of 310 and 0.25, respectively. This section compares the predicted ρ from Gardner's equation with actual ρ values. We applied this relationship to each Formation in all well data where a ρ log was acquired.

$$\rho = a\alpha^m, \quad (2.7)$$

where: ρ Density (kg/m^3)
 a Constant of 310
 α Compressional velocity (m/s)
 m Constant of 0.25

Faust (1953) concludes that, in general, velocity and density will increase with increasing depth and age of formations. Gardner (1974) states that consecutively deeper layers may vary significantly in composition and porosity with additional marked local changes in velocity and density that will disrupt the gradual increase of velocity and density with depth. In our study, we did experience this situation, which is why we approached the relationship in a different way, as explained in this section.

Well A-90 did not have ρ log. For wells E-09 and H-20, the results after using one constant were reasonable. For wells J-49, L-08, and N-22 Gardner's equation had difficulties predicting ρ using 310 as constant. There was considerable scatter in the data. In this case, the wells were segmented into different Formations. The constants used on each Formation are shown in Table B.5. With these new constants we were able to fit the data. Also, with the help of the RMS error analysis and the percentage error plots, we were able to corroborate where the relationship did work better (Figure B.8).

Formation	Constants used in Gardner's equation									
	E-09		H-20		J-49		L-08		N-22	
	a	RMS error \pm (kg/m ³)	a	RMS error \pm (kg/m ³)	a	RMS error \pm (kg/m ³)	a	RMS error \pm (kg/m ³)	a	RMS error \pm (kg/m ³)
Tert	348.66	73.56	♦		280.41	249.35	319.29	66.63	325.88	87.08
Smara	329.48	44.93	♦		321.80	25.60	329.16	30.85	324.51	49.50
Wndt	328.69	33.18	♦		326.50	80.36	♦		299.45	47.94
DCyn	♦		♦		♦		318.00	9.76	328.12	40.88
Petl	♦		♦		327.31	128.96	329.52	51.05	328.28	169.80
Naut	328.19	45.86	321.88	133.14	324.85	89.27	329.98	35.50	326.35	48.68
Benv	301.49	87.24	♦		306.95	93.50	300.19	41.94	314.26	45.66
Aval	301.91	90.83	308.80	83.40	316.41	366.32	♦		293.75	127.66
Eshl	327.36	68.14	317.92	47.43	♦		312.83	24.46	327.38	50.93
Whtr	♦		♦		332.25	39.03	♦		329.45	64.31
Hibr	317.50	110.11	♦		332.37	42.18	♦		315.23	102.56
Lhibr	♦		♦		329.63	60.28	♦		♦	
Frtn	334.82	51.14	♦		332.91	42.00	♦		321.25	178.14
Jnda	318.74	114.70	♦		♦		♦		321.28	116.82
Rnkn	♦		♦		♦		♦		320.99	35.60
Vygr	♦		♦		♦		♦		327.61	50.05

Table B.5: Gardner constant used to predict p from V_p . Key: ♦ This Formation is not present on the well; blue shading: Good RMS results per Formation; yellow shading: Bad RMS results per Formation.

As was noted at the beginning of the section, the velocity and density properties depend on different factors. That is why, after breaking down the wells into their main Formations and our subsequent analysis, we can conclude that the results are adequate. In addition, the RMS values show that this approach to the relationship is good. The highest deviation in Table B.5 is about 366.32 kg/m³ (Avalon Formation, well J-49), but this high deviation still gives reasonable results. If we look closer at the RMS error results (Table B.5), the best outcome per formation is in wells L-08 and J-49, and the less good results are in well N-22. However, the general outcome is reasonable.

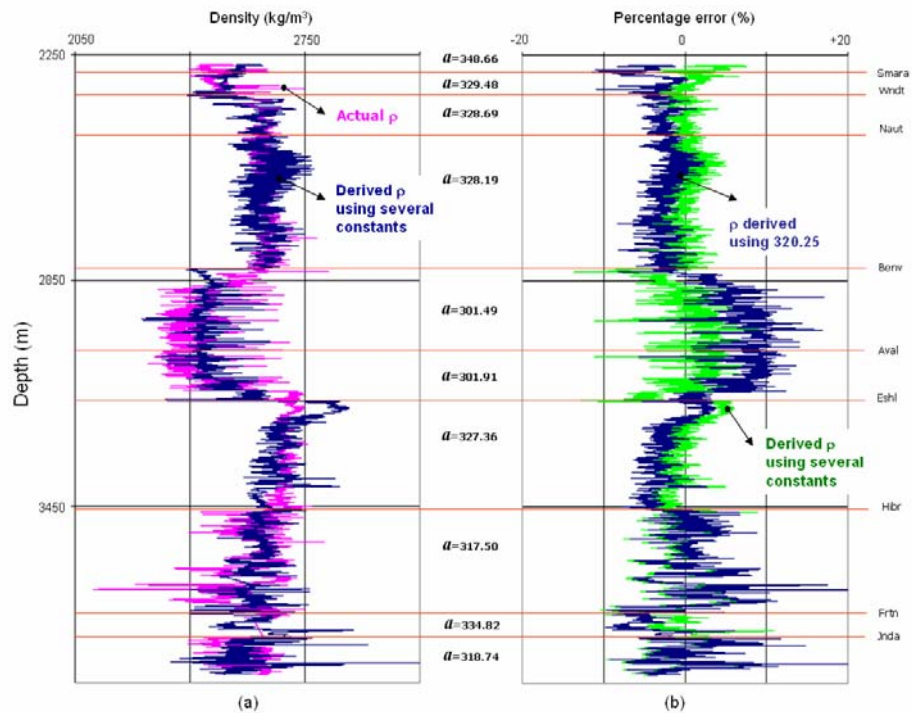


Figure B.8: Results from well E-09. Panel (a) — actual ρ , Gardner ρ (derived from V_p) using derived constants per Formation ($a=348.66$ (Tertiary), $a =329.48$ (South Mara), $a =328.69$ (Wyandot), $a =328.19$ (Nautilus), $a =301.49$ (Ben Nevis), $a =301.91$ (Avalon), $a =327.36$ (Eastern Shoals), $a =317.50$ (Hibernia), $a =334.82$ (Fortune Bay), and $a =318.74$ (Jeanne d'Arc)). Panel (b) — green curve shows the percentage error between the Gardner ρ curve and the Gardner ρ (derived from a least square constant of 320.25); dark blue curve shows percentage error between the Gardner ρ curve and the Gardner ρ curve derived using several constants. The RMS errors are: ± 73.56 kg/m³ (Tertiary), ± 44.93 kg/m³ (South Mara), ± 33.18 kg/m³ (Wyandot), ± 45.86 kg/m³ (Nautilus), ± 87.24 kg/m³ (Ben Nevis), ± 90.83 kg/m³ (Avalon), ± 68.14 kg/m³ (Eastern Shoals), ± 110.11 kg/m³ (Hibernia), ± 51.14 kg/m³ (Fortune Bay), and ± 114.70 kg/m³ (Jeanne d'Arc).

We can conclude that shale units tend to have higher values, up to ~ 348.66 . Sandstone Formations have the lowest value (~ 300.20).

Approaching the Gardner relationship with two constants per well (Tertiary and Cretaceous Formations) the results were reasonable (Table B.6, V_p section). The constants for the Cretaceous Formations show some similarity ~ 310 – 326 . Tertiary Formations do not behave similarly between wells: we found a broad range of values ~ 280 – 332 . Well H-20 shows the best outcome. The results should be

taken with adequate caution, keeping in mind the different lithologies that were involved in the analysis.

		Constants used in Gardner's equation									
		E-09		H-20		J-49		L-08		N-22	
	Formation	a	RMS error \pm (kg/m ³)	a	RMS error \pm (kg/m ³)	a	RMS error \pm (kg/m ³)	a	RMS error \pm (kg/m ³)	a	RMS error \pm (kg/m ³)
Vp	Tertiary	332.37	56.53	♦	♦	280.82	249.98	319.70	67.10	326.71	87.11
	Cretaceous	319.65	119.20	310.14	90.71	326.28	156.94	318.73	118.63	320.95	223.91
Vs	Tertiary			♦	♦			401.34	46.28		
	Cretaceous			352.73	109.01			367.11	149.68		

Table B.6: Constants used to predict ρ from Gardner's relationship for all wells using Vp and Vs. Two constants were derived per well (Tertiary and Cretaceous constants). Also the RMS value is shown for comparison between wells. Key: ♦ This Formation is not present on the well; blue shading: Good RMS results per Formation (Tertiary or Cretaceous); yellow shading: Bad RMS results per Formation (Tertiary or Cretaceous).

Actual ρ versus Gardner ρ derived from Vs (from section 2.2.9).

The prediction of ρ using Vs is a new approach (Equation 2.8) based on Gardner's equation (1974) (Equation 2.7). This section compares the predicted ρ from Equation 2.8 with the actual ρ value. We performed this comparison for all the data on well L-08 and for a portion of well H-20 (2272-3271 m) data.

$$\rho = aV_s^m, \quad (2.8)$$

where: ρ Density (kg/m³)
 a Constant of 350 or 370
 V_s Shear velocity (m/s)
 m Constant of 0.25

To improve results and better understand the relationship, we segmented the well data into lithological Formations and used a different constant per Formation. These constants and their corresponding lithologies are listed in Table B.7. Even though we used different constants (least square fit value) for each Formation, the product was fair. Due to the fact that there was not enough data for comparison between wells, we can state that all the RMS error values are good and the deviation

is reasonable. According to the percentage error plot (Figure B.10, Panel (b)), the error is between ~ -6 and $+6\%$.

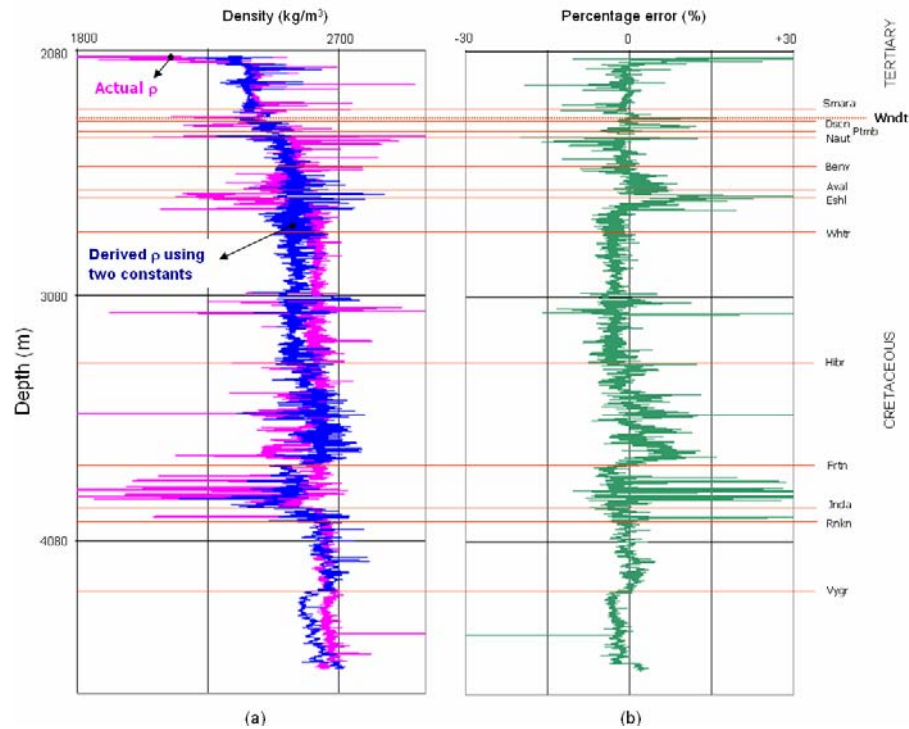


Figure B.9: Results from Well N-22. Panel (a) — actual ρ and Gardner ρ (from V_p) using derived constants (a separate constant for the Tertiary and Cretaceous Formations) versus depth. Panel (b) — percentage error between the actual V_s curve and the Gardner ρ curve derived using two constants. The Tertiary Formations with a constant of $a = 326.71$, and RMS error of $\pm 87.11 \text{ kg/m}^3$. The Cretaceous Formations with a constant of $a = 320.95$ and RMS error of $\pm 223.91 \text{ kg/m}^3$.

Formation	Constants used in Gardner's equation			
	H-20	RMS error \pm (kg/m^3)	L-08	RMS error \pm (kg/m^3)
Tertiary	♦		401.96	42.28
South Mara	♦		388.87	68.98
Dawson Canyon	♦		368.84	12.96
Petrel Member	♦		385.99	39.58
Nautilus	♦		382.59	53.52
Avalon	350.22	95.01	340.63	39.49
Eastern Shoals	369.14	47.00	362.01	28.74

Table B.7. Gardner's constant used to predict ρ from V_s . Key: ♦ data was not acquired on this Formation.

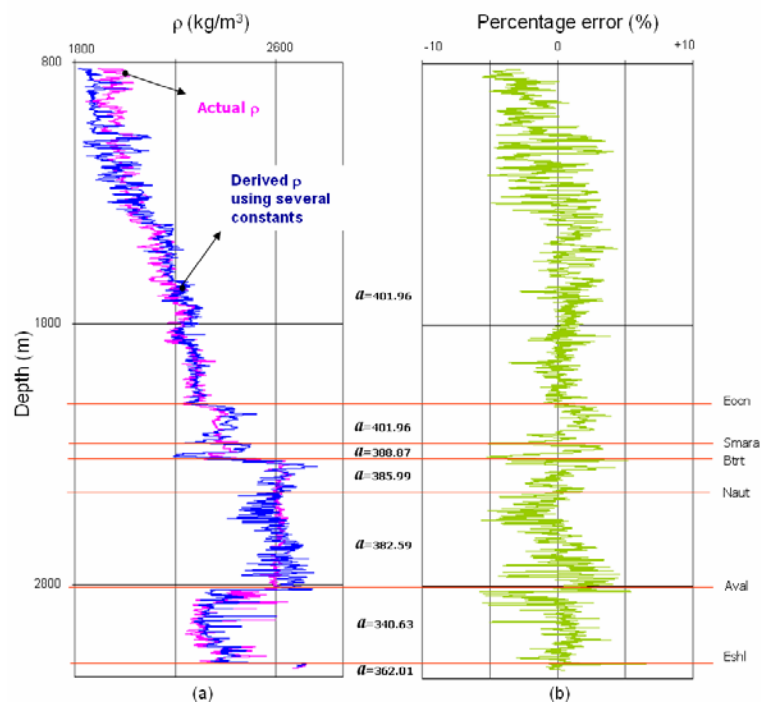


Figure B.10: Results from well L-08. Panel (a) — actual ρ and Gardner ρ (derived from Vs) using derived constants per Formation ($a=401.96$ (Tertiary), $a=388.87$ (South Mara), $a=385.99$ (Petrel/Base of Tertiary), $a=382.59$ (Nautilus), $a=340.63$ (Avalon), and $a=362.01$ (Eastern Shoals)). Panel (b) — percentage error between the Gardner ρ curve and the Gardner ρ (derived from several constants). RMS errors are: $\pm 42.28 \text{ kg/m}^3$ (Tertiary), $\pm 68.98 \text{ kg/m}^3$ (South Mara), $\pm 39.58 \text{ kg/m}^3$ (Petrel/Base of Tertiary), $\pm 53.52 \text{ kg/m}^3$ (Nautilus), $\pm 39.49 \text{ kg/m}^3$ (Avalon), and $\pm 28.74 \text{ kg/m}^3$ (Eastern Shoals).

Velocity and density properties depend on different factors, including type of rock, porosity, mineral composition, and fluid properties. These factors, in turn, depend on overburden pressure, fluid pressure, microcracks, age, and depth of burial (Gardner et al., 1974). This could explain the poor results from using Vs to derive ρ with a 310 constant. That is why, after our analysis from dividing the wells into their main Formations, we can conclude that we have reasonable results.

Using two constants (Figure B.11 and Table B.7) demonstrated that it worked for the Tertiary Formations but did not do the expected good job with the Cretaceous Formations. However, the RMS error (Table B.7) and the percentage error plot (Figure B.11, Panel (b)) show that the results should be treated with caution.

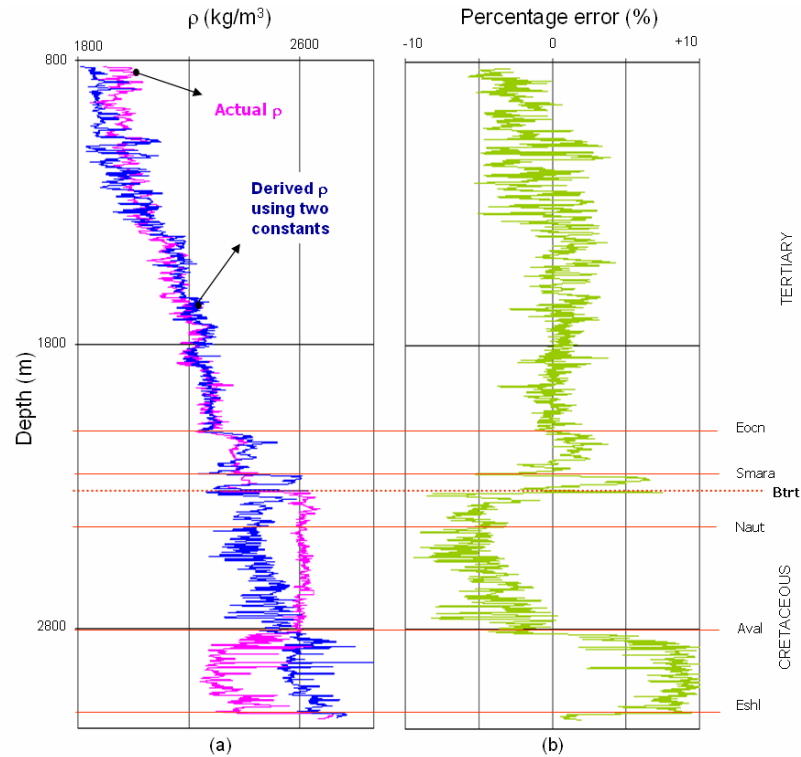


Figure B.11: Results from well L-08. Panel (a) — actual ρ and Gardner ρ (from V_s) using two derived constants (once constant for the Tertiary Formations and another for the Cretaceous Formations) versus depth. Panel (b) — percentage error between the actual ρ curve and the Gardner ρ curve derived using two constants. The Tertiary Formations with a constant $\alpha=401.34$ has an RMS error of $\pm 46.28 \text{ kg/m}^3$. The Cretaceous Formations with a constant $\alpha=367.11$ and an RMS error of $\pm 149.68 \text{ kg/m}^3$.

In general, we can see that V_s behaves differently. We can have a Formation that works fine with the constant derived from V_p but does not respond the same way when the relationship is derived using V_s .

Multivariate analysis (from section 2.2.14).

Multilinear regression processing was used to estimate a statistical relationship between several different well log properties. The input properties were V_p , V_s , GR, ϕ_N and ϕ_D . As a test, I chose a portion of well L-08 (2636-2675 m) where the V_s values were known. Assuming that I did not know the values of V_s , I used the multivariate analysis to estimate values of V_s in the above-mentioned zone. I then

compared the known Vs values to the estimated Vs values.

This technique involves finding the multilinear relationships (Draper and Smith, 1966) between the well log information available in this project (V_p , and V_s , GR, ϕ_D and ϕ_N). We want to find the V_s values. Each i^{th} sample of this property is modeled using the linear equation B.1 shown below. Equation B.1 is a generalized version of equations 2.13 and 2.14.

$$V_{si} = a_0 + a_1V_{pi} + a_2GR_i + a_3\phi_{Ni} + a_4\phi_{Di}, \quad (\text{B.1})$$

where: V_{si} Shear velocity (m/s)
 V_{pi} Compressional velocity (m/s)
 GR_i Gamma Ray (API)
 ϕ_{Ni} Neutron porosity (pu)
 ϕ_{Di} Density porosity (pu)
 a_0, a_1, a_2, a_3, a_4 Constants

When we use known V_s values, we are able to find the value of the constants. The constants (a_0, a_1, a_2, a_3, a_4) are derived by minimizing the mean-squared prediction error (Equation B.2)

$$E^2 = \frac{1}{N} \sum_{i=1}^N (V_{si} - a_0 - a_1V_{pi} - a_2GR_i - a_3\phi_{Ni} - a_4\phi_{Di})^2, \quad (\text{B.2})$$

where: E Error
 N Number of samples
 V_{si} Shear velocity (m/s)
 V_{pi} Compressional velocity (m/s)
 GR_i Gamma Ray (API)
 ϕ_{Ni} Neutron porosity (pu)
 ϕ_{Di} Density porosity (pu)
 a_0, a_1, a_2, a_3, a_4 Constants

The process applies equation (B.1) to each sample. This generates a set of N linear equations, which can be expressed in matrix form as shown below in equations B.3 or B.4.

$$\begin{bmatrix} V_{s1} \\ V_{s2} \\ V_{s3} \\ \vdots \\ V_{sN} \end{bmatrix} = \begin{bmatrix} 1 & V_{p1} & GR_1 & \phi_{N1} & \phi_{D1} \\ 1 & V_{p2} & GR_2 & \phi_{N2} & \phi_{D2} \\ 1 & V_{p3} & GR_3 & \phi_{N3} & \phi_{D3} \\ \vdots & \vdots & \vdots & \vdots & \vdots \\ 1 & V_{pN} & GR_N & \phi_{NN} & \phi_{DN} \end{bmatrix} \begin{bmatrix} a_0 \\ a_1 \\ a_2 \\ a_3 \\ a_4 \end{bmatrix}, \quad (\text{B.3})$$

where: V_s (1,2,3,...N) Shear velocity (m/s) i^{th} samples
 V_p (1,2,3,...N) Compressional velocity (m/s) i^{th} samples
 GR (1,2,3,...N) Gamma Ray (API) i^{th} samples
 ϕ_N (1,2,3,...N) Neutron porosity (pu) i^{th} samples
 ϕ_D (1,2,3,...N) Density porosity (pu) i^{th} samples
 a_0, a_1, a_2, a_3, a_4 Constants

$$V_s = PA, \quad (\text{B.4})$$

where: V_s Nx1 matrix
 P Nx5 matrix
 A 5x1 matrix

In equation B.4, V_s is an Nx1 matrix containing the known V_s values. P is an Nx5 matrix containing known V_p , GR , ϕ_D , and ϕ_N values. A is a 5x1 matrix with unknown constants, (a_0, a_1, a_2, a_3, a_4). Finally, equation B.5 is the least squares solution of equation (B.4) and this yields our unknown constants.

$$A = (P^T P)^{-1} P^T V_s, \quad (\text{B.5})$$

where: A Matrix with unknown constants
 P Matrix with known values
 P^T Transpose of matrix with known values (V_p , GR , ϕ_D , and ϕ_N)
 V_s Matrix with Vs values

Now that we have the constants, we can use the equation B.1 to estimate any unknown value of V_s , given a particular set of log properties V_p , GR , ϕ_N and ϕ_D . In the thesis, I also applied the same analysis to the V_p values using V_s , GR , ϕ_N and ϕ_D .

APPENDIX C. VSP Interpretation

Tying PP synthetic seismograms with PP offset VSP field data (from section 3.2.1).

As previously noted, the well H-20 ρ log was set to a constant value of 2642 kg/m³ for the upper section of the well (2772 m to 824 m). For the lower part (2772–3271 m), we applied Gardner' relationship and then applied this derived ρ log to derive the synthetic seismograms (Figure C.1). The results after tying the PP synthetic seismogram and the PP offset-VSP field data (Figure C.1) show that the derived ρ value (R_{hga}) from Gardner increases the amplitude on the synthetic seismogram, giving more definition to the events. See section 3.2.1 for further details.

Tying PS synthetic seismograms with PS offset VSP field data (from section 3.2.2).

With this tie, using the R_{hga} log curve (Figure C.2), we can see that the amplitude also increases on the synthetic seismogram, as with the results from the PP synthetic seismogram. This characteristic helped to identify events on the synthetic seismograms created with the actual R_{hob} log curve. See section 3.2.2 for further details.

Tying PP synthetic seismograms with the PP seismic section (from section 3.2.5)

Using this method with the synthetic seismogram derived from the R_{hga} log curve, shows that the correlation is as good (Figure C.3) as the one between the R_{hob} synthetic seismogram and the seismic section (Figure 3.9).

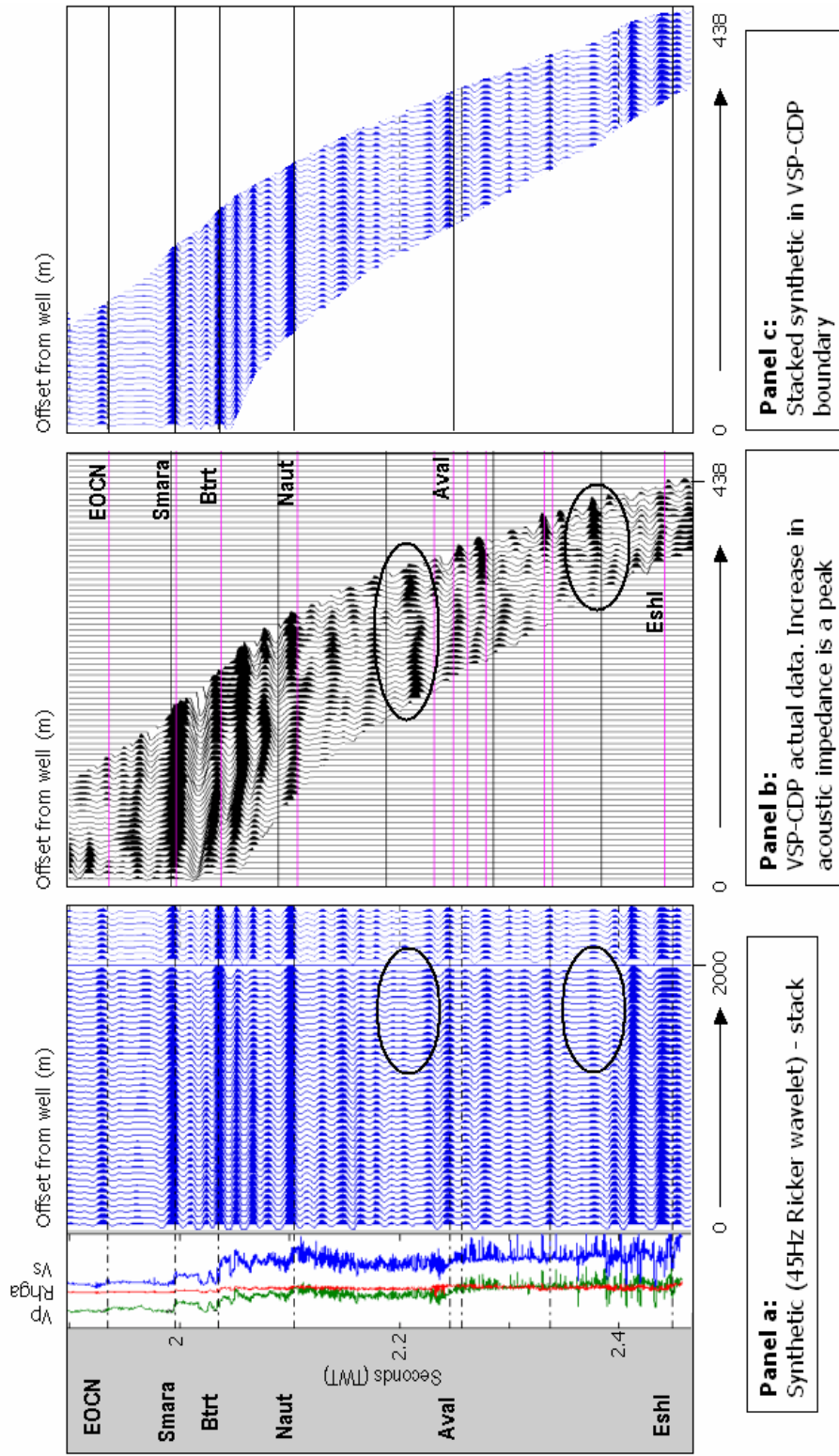


Figure C.1. Result from matching the PP synthetic seismogram and the offset VSP section, using the Gardner p value (curve RHGA in Figure 2.23). Key: Eocene EOCN, South Mara Smara, Base Tertiary Btrt, Nautilus Naut, Avalon Aval, Eastern Shoals Eshl.

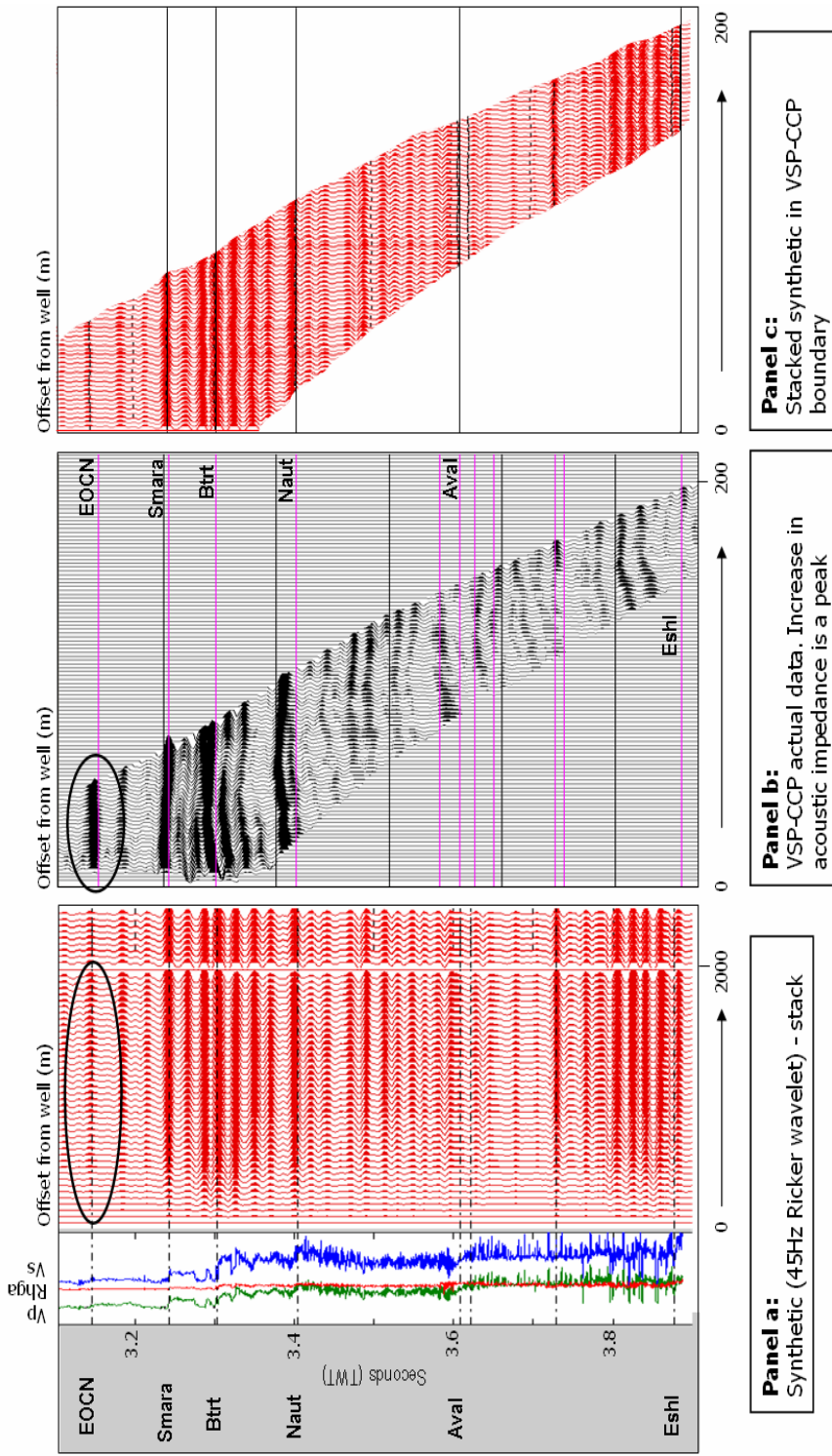


Figure C.2. Result from matching the PS synthetic seismogram and the Offset VSP section, using the Gardner ρ value (curve RHGA in Figure 2.23). Key: Eocene EOCN, South Mara Smara, Base Tertiary Btrt, Nautilus Naut, Avalon Aval, Eastern Shoals Eshl.

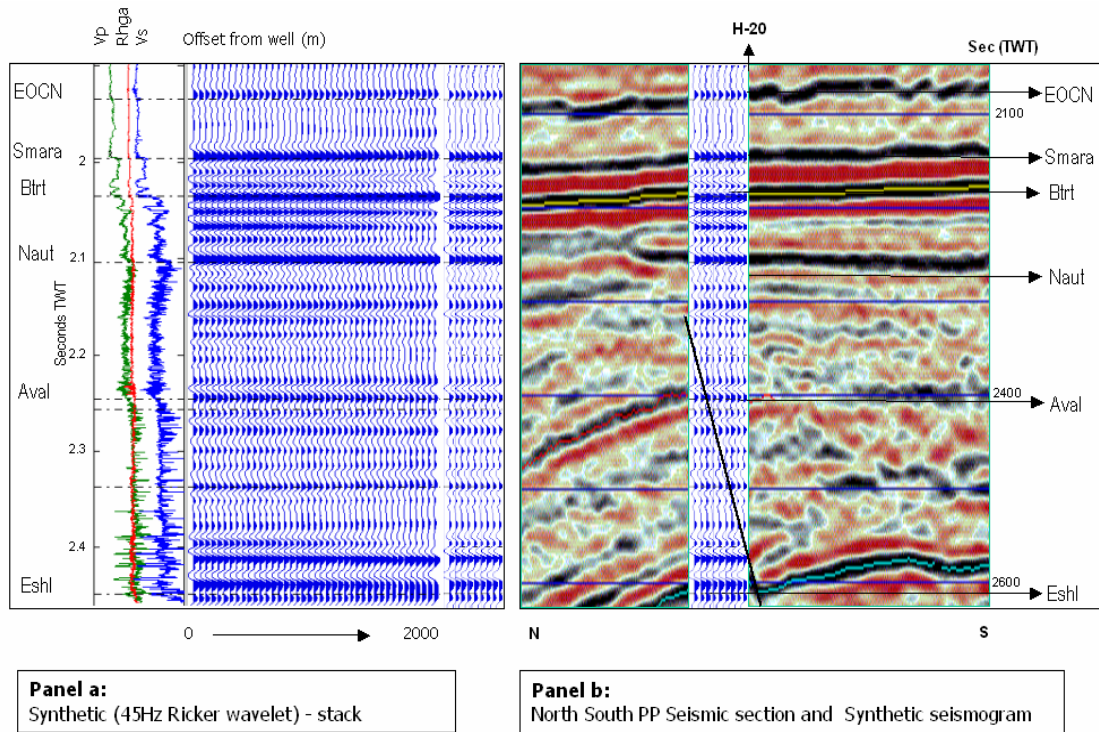


Figure C.3: Results from matching the PP synthetic seismogram and the PP seismic section, using the Gardner p value (curve RHGA in Figure 2.23). (Black is a peak and red is a trough.) Key: Eocene EOCN, South Mara Smara, Base Tertiary Btrt, Nautilus Naut, Avalon Aval, Eastern Shoals Eshl.

Appendix D. Converted-wave OBS interpretation

Interpretation (from section 4.1.3).

A preliminary analysis of four 4C receiver gathers on transect 3 (SCREECH survey) was conducted (Figures D.1). Several of the events could be interpreted as reflections. After analyzing the four channels of the OBS on the different locations of the transect 3 (Figures D.2. to D.5), the best signal-to-noise ratio data was recorded on the receiver at location #3090, and the lowest signal-to-noise ratio data was recorded at the receiver at location #3110. See section 4.1.

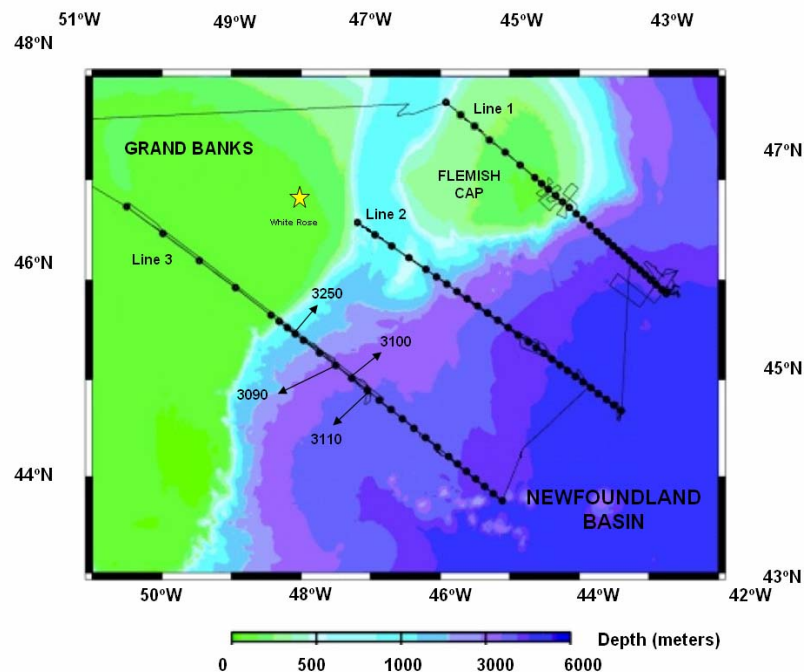


Figure D.1: Location of seismic lines and receivers 3090, 3100, 3110 and 3250 from the SCREECH survey. (Modified from Keith and Loudon, 2000).

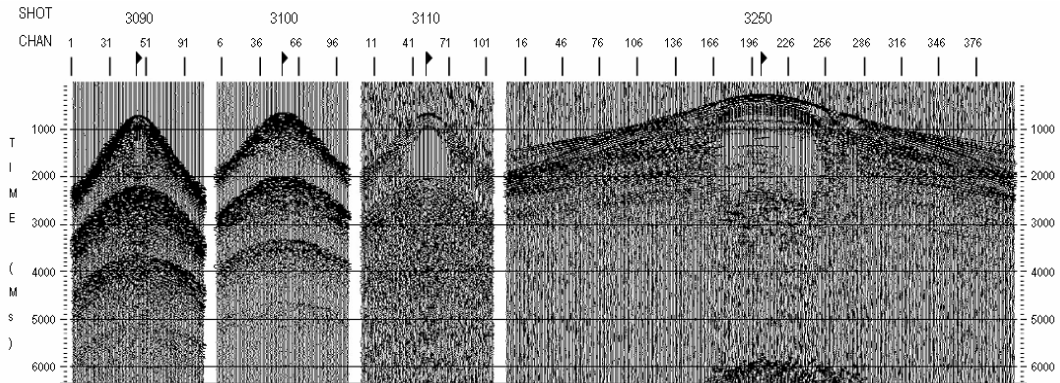


Figure D.2: Common receiver gathers for the hydrophone (pressure sensor) at locations 3090, 3100, 3110 and 3250. (Modified from Stewart et al., 2001).

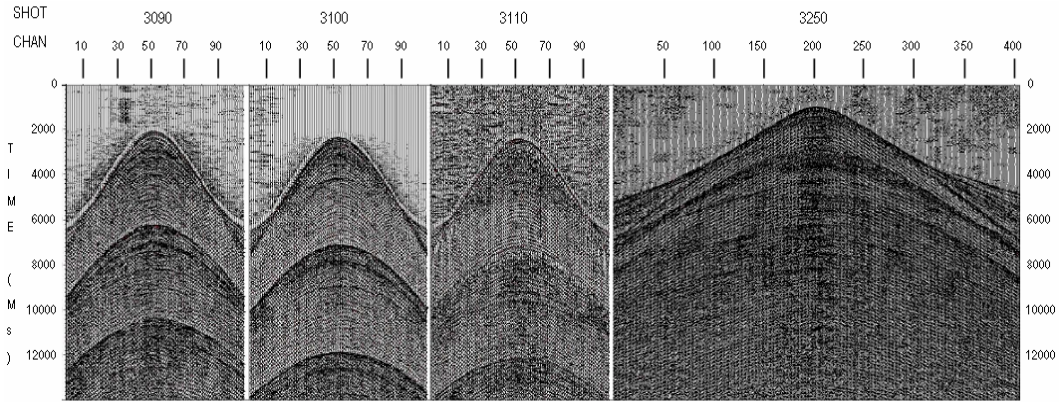


Figure D.3: Common receiver gathers for the vertical component (V1) at locations 3090, 3100, 3110 and 3250. (Modified from Stewart et al., 2001).

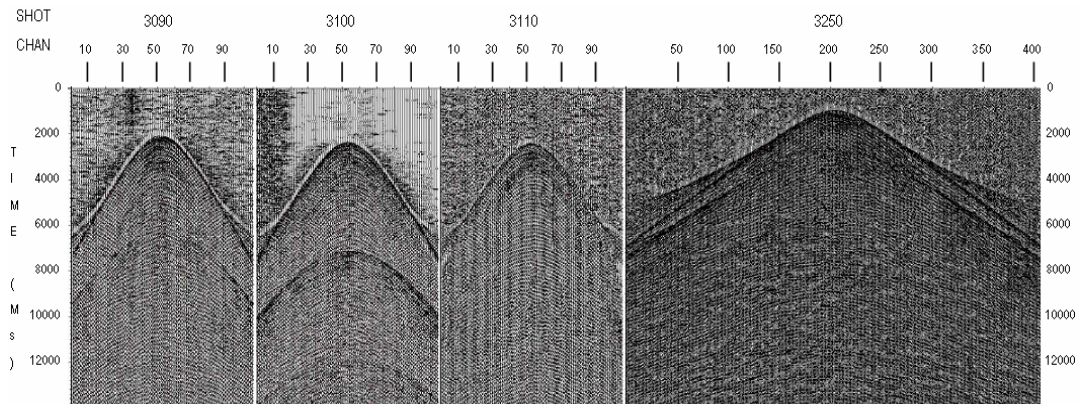


Figure D.4: Common receiver gathers for the horizontal component (H1) at locations 3090, 3100, 3110 and 3250. (Modified from Stewart et al., 2001).

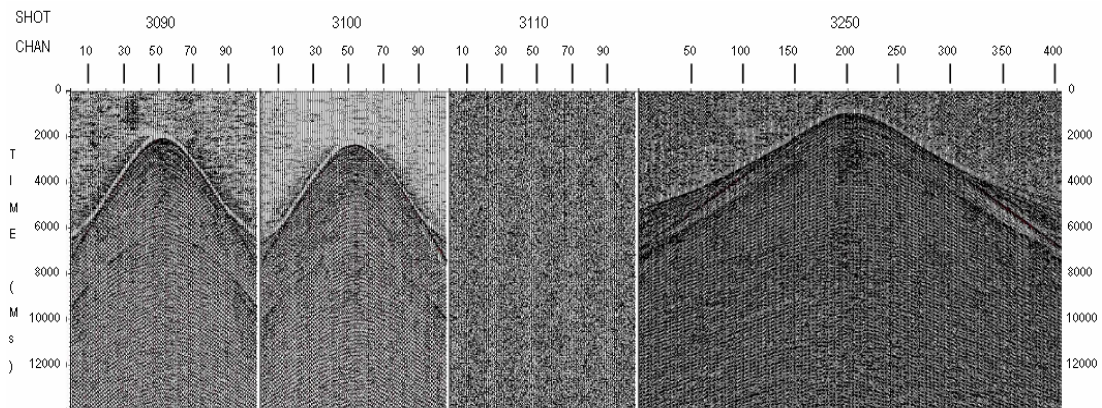


Figure D.5: Common receiver gathers for the horizontal component (H2) at locations 3090, 3100, 3110 and 3250. (Modified from Stewart et al., 2001).